Formation and evolution of vortex rings with weak to moderate swirl and their implications for enhancing vortex ring circulation

RIGOBERTO ORTEGA-CHAVEZ

Formation and evolution of vortex rings with weak to moderate swirl and their implications for enhancing vortex ring circulation

Rigoberto Ortega Chavez

A Thesis presented for the degree of
Doctor of Philosophy

Department of Engineering
Durham University
United Kingdom
January 2024

Abstract

The formation of swirling vortex rings and their early time evolution, resulting from the controlled discharge of an incompressible fluid into a stationary equivalent fluid bulk, is explored both numerically and experimentally for swirl number $S \in [0, 1]$. For the numerical work, two practically realisable inlet conditions are investigated with swirl simultaneously superposed onto a linear momentum discharge; the corresponding circulation based Reynolds number is 7500. The results reveal that, for $S > 1/2$, the addition of swirl promotes the breakdown of the leading primary vortex ring structure, giving rise to the striking feature of significant negative vorticity, or opposite sign vorticity (OSV), generation in the region surrounding the primary vortex ring core, whose strength scales with S^2. Through a non-linear interaction with the vortex breakdown, the radius of the primary toroidal vortex core is rapidly increased; consequently, the self-induced propagation velocity of the leading ring decreases with S and vortex stretching along the circular primary vortex core increases counteracting viscous diffusion effects. The latter governs the evolution of the peak vorticity intensity and the swirl velocity magnitude in the primary ring core, the circulation growth rate of this ring, as well as the vorticity intensity of the trailing jet and hence its stability. This combination of effects leads to an increased dimensionless kinetic energy for the primary ring with increasing S and results in an almost linearly decreasing circulation based formation number, F. In a rigorous complementary experimental investigation, OSV is observed by introducing swirl using a rotating pipe, varying the time period before the piston stroke to achieve the desired swirl strength at a Reynolds number of 1000. Rotating pipe is found to generate a secondary flow altering the inlet condition. Nevertheless, it is observed, using short periods of pipe rotation and higher angular speed, that it is possible to generate a swirling vortex ring with less OSV production and all the related effects discussed above. The relation between F and the radius of the vortex ring is investigated through manipulation of ring radius growth, achieved through its interaction with a preceding vortex ring. Reducing radius growth, facilitates an increase of the circulation of the vortex ring, which in turn affects its F value.

Declaration

The work in this thesis is based on research carried out at the Department of Engineering, Durham University, United Kingdom. No part of this thesis has been submitted elsewhere for any other degree or qualification and it is all my own work unless referenced to the contrary in the text.

Acknowledgements

I would like to thank my family, Rigo bigote, lulys, Liz y Marilu, for their support during this process and always. Muchas gracias, los quiero mucho familia. I would like to express my gratitude to my supervisor team, Dr. Lian Gan, for giving me the opportunity to work with him five years ago and introducing me to the fascinating world of vortex dynamics and experimental fluid mechanics. I am thankful for everything he taught me and for keeping me motivated throughout my journey, also I would like to extend my thanks to Professor Gaskell for his valuable advice, hinsightful comments, and especially for his immense patience in correcting my grammar mistakes and Spanglish. Thank you both for always being there to answer my questions and for providing support during my PhD. To the mechanical and electrical workshop which help was fundamental to perform my experiments, and Ruth and Louise for their guides in the department.

Also, I would like to express my gratitude to my eternal housemates, Paola and Joel, for making me feel in Chihuahua. Their company and care have meant a lot to me. I am also thankful to my office friends Aidan, Milad, and Adam, who have made my work days go by faster. Lastly, I must thank my Mexican gang, who have helped me avoid feeling homesick.

Finally, I would like to express my gratitude to CONACYT for their financial support, which made this experience possible. Muchas gracias.

Aaaah si! Special thanks to Rebecca for her support, motivation, and love – especially for showing me the best of the UK, her.

Contents

List of Figures

List of Tables

List of Symbols

L	Equivalent stroke length . 2
D_o	Orifice diameter . 2
$U_p(t)$	Instantaneous discharge velocity in the axial flow direction . 2
U_o	Time average discharge velocity . 3
Γ	Circulation . 3
Γ^*	Dimensionless circulation . 3
$\mathbf{u}$	Velocity vector in cylindrical coordinates . 3
r	Radial coordinate in a cylindrical system . 3
θ	Azimuthal coordinate in a cylindrical system . 3
z	Axial coordinate in a cylindrical system . 3 . 64
u_x	Velocity component in the x direction in a cartesian system . 64
u_y	Velocity component in the y direction in a cartesian system
ω_θ	Azimuthal vorticity, . 3
u_r	Radial velocity, . 3
u_z	Axial velocity, . 3
u_θ	Azimuthal velocity, . 3
$\partial\Gamma/\partial t$	Circulation flux, . 3

Ω Angular velocity of the flow at the inlet, . 3

$U_z(t)$ Velocity profile at the orifice exit, . 4

$U_p(t)$ Uniform velocity profile over the orifice cross-section, . 4

F Formation number, . 4

T^* Dimensionless time, . 5

Γ^*_{Total} Dimensionless circulation over the whole flow field, . 5

Γ^*_{Ring} Dimensionless ring circulation, . 5

T^*_{int} Dimensionless time at which the intersection of Γ^*_{Total} and Γ^*_r occurs , . 6

α Dimensionless kinetic energy, . 6

E kinetic energy, . 6

I Hydrodynamic impulse, . 6

Re Reynolds number, .7

S Swirl number . 9

u_i Induced velocity . 11

r_c Radial distance from the core centre . 11

Δt Time step . 23

ΔV Differential control volume . 23

ψ General parameter . 23

$\hat{u}$ Normal vector . 23

ϕ volumetric flux . 23

p Pressure . 23

p_i Point location . 23

β Interpolation factor . 24

M Matrix of known coefficients, . 24

Δp Pressure step, . 24

A Diagonal matrix of M , . 24

H Residual Matrix, . 24

ν kinematic viscosity, . 27

ν_{sub} Subgrid Kinematic viscosity, . 27

$\tilde{u_i}$ Filtered velocity, . 27

$\tilde{p}$ Filtered pressure, . 27

Δ Filter characteristic length scale, . 27

$\tilde{S_{ij}}$ Strain rate tensor, . 27

C_s Smagorinsky constan, . 27

R_i Radial lengths in the computation mesh , . 29

κ Resolved turbulence kinetic energy , . 29

κ_{sg} Sub-grid turbulent kinetic energy , . 29

$M(x,t)$ Ratio between sub-grid and resolved turbulent kinetic energy, . 29

u'_z Propagation velocity of the ring . 31

f Frequency . 44

ρ Flow density . 46

κ_{in} Inlet turbulent kinetic energy . 47

I_t Turbulence intensity . 47

R_o Orifice Radius . 48

u_x Cartesian velocity in the x direction . 78

u_y Cartesian velocity in the y direction . 78

R Radial position of the core centroid . 50

Z Axial position of the core centroid . 50

u_c Velocity distribution in the core in a frame of reference moving with the vortex ring. . 56

a Time-dependent characteristic core radius . 56

$\omega^*_\theta(max)$ Scaled peak vorticity in the ring core centre . 57

$V(t)$ Vortex ring volume . 58

A_c Vortex ring cross section area . 58

Δr Radial displacement . 61

De Dean number . 63

ω_r Radial vorticity . 64

ω_z axial vorticity . 64

Γ_T Circulation generated by the tilting . 65

γ Scaling factor . 69

sp Stagnation point in the vortex bubble . 71

Z_{sp} the difference between the z coordinate of sp and that of the vortex core centroid. 71

$\bar{u_\theta}$ spatial average azimuthal velocity within the core . 75

$F(r)$ Arbitrary initial distribution . 76

w Generic average velocity . 76

J_n Bessel function of the first kind and order n, . 76

λ_n positive roots of Bessel function . 76

$L(t)$ Angular momentum . 78

ϵ Ratio between the core radius and ring radius . 80

γ_c Circulation in the core as a function of r . 80

T_n Terms of the Saffman equation . 80

α_r Dimensionless ring kinetic energy . 86

$\omega_\theta(jet)$ Maximum vorticity in the trailing jet . 88

ϕ_c Positive constant obtained by continuity equation . 100

u_θ^* Dimensionless azimuthal time, . 77

$\overline{u_\theta}_p$ Average azimuthal velocity close to the wall, . 113

I_{acc} Acceleration impulse, . 126

I_{total} Total impulse, . 126

T_{off}^* Dimensionless time delay between vortex rings, . 126

T_{off}^* Dimensionless time when the piston is working, . 126

R_{cn} Radial position of one core centroid, . 133

Z_{cn} Axial position of one the core centroid, . 133

Δr_c Distance between ring A and B, . 133

u_{i-r} Induced velocity in the radial direction, . 139

u_{i-z} Induced velocity in the axial direction, . 139

$\bar{\omega}$ Approximate angular velocity in the vortex core, . 147

$\mathbf{s}$ Vector from a vortex line to a curve in the space . 10

$u_o^{'}$ vortex ring centre point . 143

Dedication

A mi tia Elvira.

CHAPTER 1

Introduction

Circular vortex rings, coherent toroidal shaped circular vortex structures characterised by closed vortex lines, often arise as a consequence of an impulsive or pulsatile discharge of momentum from a nozzle, or orifice, to an adjacent quiescent open or confined region. Examples include, a volcanic eruption (Pulvirenti et al., 2023; Taddeucci et al., 2021) and the exchange of blood from the left atrium to the left ventricle of the heart, via the mitral valve, during the ventricular diastolic phases of a cardiac cycle (Arvidsson et al., 2016; Gharib et al., 2006; Töger et al., 2012), as shown in Figure 1.1. Vortex rings are intriguing unsteady flows, which evolve and propagate forward at a self-induced velocity; they are comprised of closed (circular) vortex lines transporting a bubble volume of rotating fluid, determined by the formation process. It was not until the nineteenth century that related scientific research began to emerge, inspired by their spontaneity; since the experimental observations of Reynolds (1876) concerning the slowdown of a vortex ring's propagation velocity and the first simplified theoretical model of a circular vortex filament derived by Helmholtz (1858a), numerous investigations of vortex ring behaviour have appeared in the open literature. Only those of direct relevance to work reported here are reviewed and discussed below.

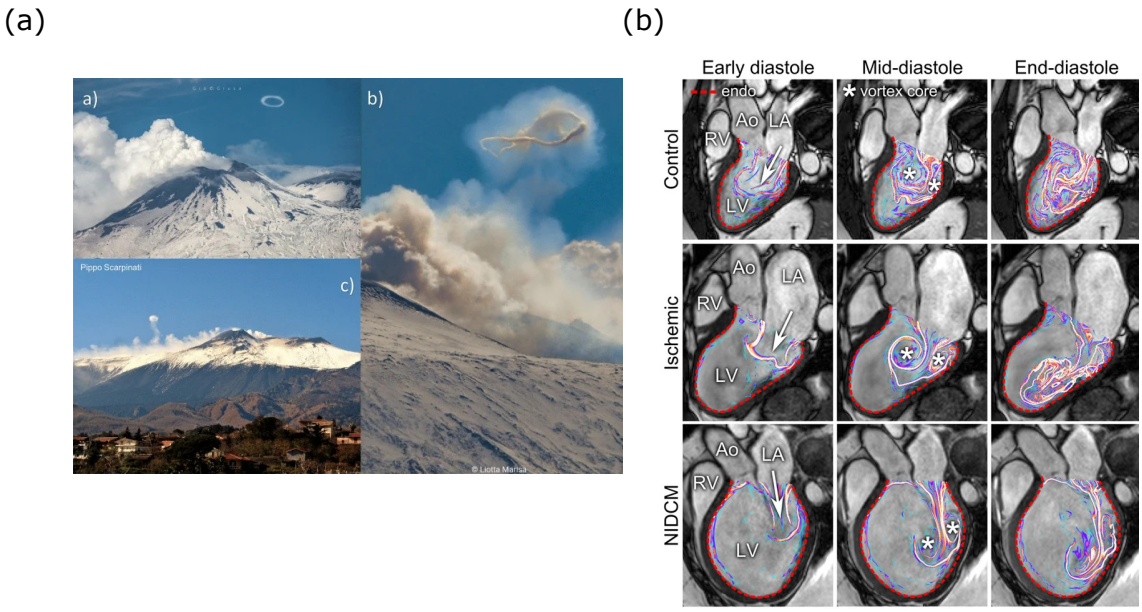

Figure 1.1: Example of the formation and propagation of vortex rings generated in: (a) volcano eruption and (b) the human heart. Figures taken from Pulvirenti et al. (2023) –left; Arvidsson et al. (2016) –right.

1.1 Formation process

When fluid is rapidly discharged from a nozzle or orifice, the azimuthal component of vorticity in the boundary layer present along the inner (circular) wall of a nozzle, or in the case of an orifice opening the shear layer present between the central jet which forms and the quiescent ambient fluid, rolls up during momentum discharge giving rise to the resultant toroidal vortex ring structure. The amount of volume and enstrophy from the discharged fluid delivered to the ring structure is proportional to the duration of the discharge (Lim and Nickels, 1995; Shariff and Leonard, 1992). In a controlled environment, the formation process that produces a vortex ring can be quantified by a simple parameter, namely the stroke ratio that represents the amount of flow discharged, and is defined as:

$$\frac{L}{D_o} = \frac{1}{D} \int U_p(t)\, \mathrm{d}t, \tag{1.1}$$

where $U_p(t)$ is the instantaneous discharge velocity in the axial flow direction and assumed uniform across the usually circular discharge plane of diameter D_o; L is

the equivalent stroke length (Figure 1.2).

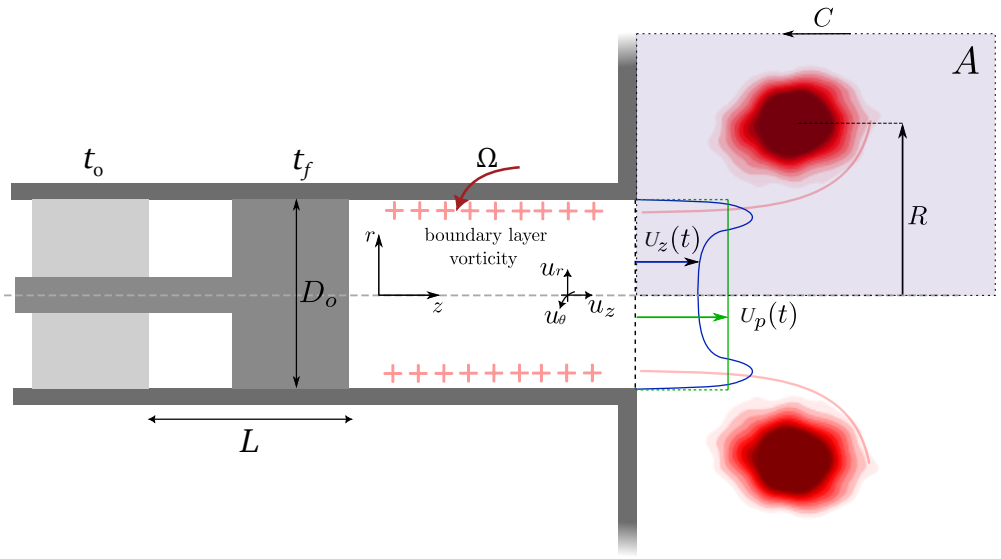

Figure 1.2: Illustration of flow discharge through an orifice and the subsequent formation of a vortex ring. $U_z(t)$ denotes the actual velocity profile at the orifice exit, while $U_p(t)$ represents the assumed velocity applied to the slug model. Ω is the angular velocity of the flow for the cases with swirl and L is the piston displacement from an initial time t_o to t_f.

Another important scalar used to describe the strength of any vortex flow is its circulation, Γ, around a closed curve C. It measures the vorticity flux through the area enclosed by the curve C (Saffman, 1995). In the literature pertaining to vortex rings, its dimensionless version Γ^* is often employed, which is defined as follows:

$$\begin{aligned}\Gamma^* = \frac{\Gamma}{U_0 D_o} = \frac{1}{U_0 D_o}\oint_C \mathbf{u}\cdot \mathrm{d}\mathbf{l} &= \frac{1}{U_0 D_o}\int_A (\nabla\times\mathbf{u})\ \mathrm{d}A \\ &= \frac{1}{U_0 D_o}\int_A \omega_\theta\ \mathrm{d}A, \end{aligned} \tag{1.2}$$

where $\mathbf{u} = (u_r, u_\theta, u_z)$ is the velocity vector in cylindrical coordinates (r, θ, z) – see Figure 1.2, $\mathrm{d}\mathbf{l}$ is the differential of the curve length C, $U_o = \overline{U_p(t)}$ is the time average discharge velocity, A is the area enclosed by C (Figure 1.2) and ω_θ is the azimuthal component of vorticity in cylindrical coordinates, namely:

$$\omega_\theta = \frac{\partial u_r}{\partial z} - \frac{\partial u_z}{\partial r}. \tag{1.3}$$

The Slug Flow Model is a simple technique used to predict the circulation generated by a piston-cylinder system. It can estimate the flux circulation for a specific L/D_o. However, certain assumptions must be considered, such as a constant velocity $U_p(t)$ over the orifice cross-section outside to the boundary layer and zero radial flow velocity, u_r, at the nozzle/orifice exit at all times. Under these assumptions, the circulation flux solely depends on U_p, as shown below:

$$\begin{aligned}\frac{\partial \Gamma_{slug}}{\partial t} = \int_0^{D_o/2} \omega_\theta U_z \mathrm{d}r &= \int_0^{D_o/2} \left(\cancelto{0}{\frac{\partial u_r}{\partial z}} - \frac{\partial U_z}{\partial r} \right) U_z \, \mathrm{d}r \\ &\approx \frac{1}{2} U_p(t)^2, \end{aligned} \tag{1.4}$$

where $U_z(t)$ denotes the actual velocity profile at the orifice exit.

However, as reported by Didden (1979), the slug flow model underestimates the circulation. At early times, the flow around the orifice edge accelerates due to the roll-up process of the vortex sheet, resulting in a more significant vorticity flux; Figure 1.2 provides a representation of the actual velocity profile, $U_z(t)$. As time progresses, the velocity profile approaches a parabolic shape, typical of flow in a pipe, where the maximum velocity remains larger than U_p and forms a thicker boundary layer, keeping the vorticity flux higher than that expected for the flow slug model. Didden (1979) through experimental work, proposed the following modified slug flow model equation:

$$\frac{\Gamma}{U_o D_o} = 0.16 + 0.57 \frac{L}{D_o}, \quad \frac{L}{D_o} > 0.6. \tag{1.5}$$

In their well-known experiment, Gharib et al. (1998) studied the formation of vortex rings generated by a piston-nozzle arrangement and found that when L/D_o is smaller than a limiting value, all of the fluid discharged from the piston motion is entrained into the rolled up vortex ring, with the circulation proportional to L, in agreement with the slug model. However, for larger L/D_o, only a fraction of the fluid discharged is entrained into the ring structure before it pinches off, with the remaining fluid giving rise to a trailing jet. This limiting L/D_o is the formation

number, F, which is typically about $3 \sim 4$ and, as stated by the above authors, is reached when "*The apparatus is no longer able to deliver energy at a rate compatible with the requirement that a steadily translating vortex ring has maximum energy with respect to impulse-preserving iso-vortical perturbations*".

Figure 1.3 shows flow visulaizations of three vortex rings with different L/D_o at the same dimensionless time $T^*(tU_o/D_o) = 8$, where t defines time (seconds), and F≈4. No trailing jet is apparent for the first ring (viewed from top to bottom) with $L/D_o = 2$, and the ring size is slightly smaller than the other cases. In the second ring with $L/D_o = 3.8$, the presence of a trailing jet is negligible close to the ring, indicating that the ring has already detached from the trailing jet. The last ring with $L/D_o = 14.5$ maintains a similar size to the previous case; however, a strong trailing jet remains attached to the ring, showing that the size of the ring remains constant after F is exceeded.

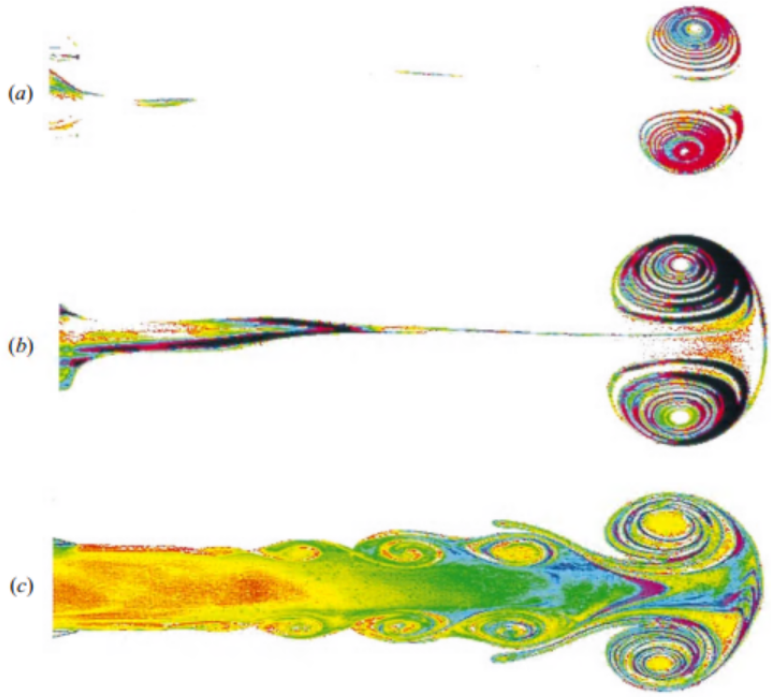

Figure 1.3: Visualization of vortex rings at a dimensionless time $T^* = U_o t/D_o = 8$ for different $L/D_o = 2, 3.8, 14.5$ and F≈ 4. Figure taken from Gharib et al. (1998).

The methodology proposed by Gharib et al. (1998) for determining the value of F is illustrated in Figure (1.4). It involves comparing the total circulation, Γ^*_{Total}, obtained by applying equation (1.2) over an area covering the vortex ring and the trailing jet, with the circulation of the ring Γ^*_{Ring}, where the area only covers the ring core after it detaches from the trailing jet – see Figure 1.2. The dimensionless time T^* at which both circulations intersect is denoted as F:

$$T^*_{int} = \frac{tU_o}{D_o} = \frac{L}{D_o} = \mathrm{F}, \tag{1.6}$$

where T^*_{int} represents the dimensionless time at which the intersection of Γ^*_{Total} and Γ^*_r occurs.

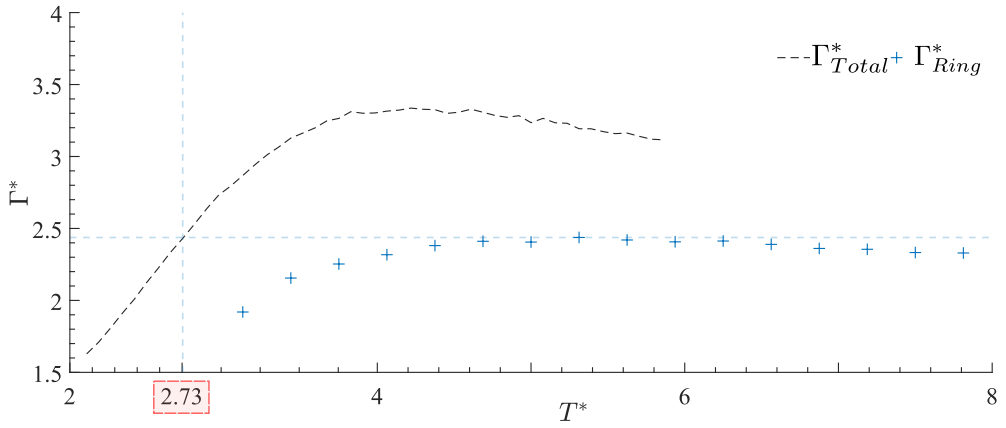

Figure 1.4: Determination of the formation number F based on the variation of the total, Γ^*_{Total} and the leading ring circulation, Γ^*_{Ring}, with T^*.

They also proposed a theoretical model to predict F, based on the intersection of the dimensionless kinetic energy, $\alpha(E, I, \Gamma)$, of the nozzle discharge (a decreasing function of time), and the limit for a steady vortex ring of $\alpha \approx 0.33$. The dimensionless kinetic energy α is defined as follows:

$$\alpha = \frac{E}{\sqrt{\rho I \Gamma^3}}, \tag{1.7}$$

where

$$E = 2\pi \int \int_A \left(u_z^2 + u_r^2\right) r dr dz, \tag{1.8}$$

$$I = \pi \int \int_A \left(\omega_\theta r^2\right) dr dz; \tag{1.9}$$

Γ represents the circulation defined in (1.2), I the hydrodynamic impulse and E is the kinetic energy. quantities are expressed for axisymmetric flow.

Shusser and Gharib (2000) presented an alternative explanation of the mechanisms involved in F. They showed that at detachment of the vortex ring from the trailing jet, the propagation velocity of the ring equals the trailing jet velocity in the fluid surrounding of the ring. This result aligns with Gharib et al. (1998) hypothesis that detachment happens because the apparatus can no longer provide the necessary energy for a stable vortex ring.

Subsequently, Gao and Yu (2010) highlighted that a vortex ring does not necessarily detach from an accompanying trailing jet when the formation number is reached, showing instead that α decays during the formation process and pinch-off occurs when $\alpha \lesssim 0.33$. Recently, Limbourg and Nedić (2021) have reported that kinetic energy, hydrodynamic impulse and circulation, which determine α, reach their asymptotic values at different times. Therefore, even when a leading ring acquires its maximum circulation, its energy and impulse continue to increase until the 'optimal formation time', which is larger than F, is reached.

The formation number reflects the main time scale for characterising the dynamics of vortex rings, and has been shown to be a fairly robust parameter with only a weak dependence on the Reynolds number (Gan, 2010; Gan et al., 2012; Gharib et al., 1998), defined as:

$$\mathrm{Re} = \frac{U_0 D_o}{\nu}, \tag{1.10}$$

where ν is the kinematic viscosity. Rosenfeld et al. (1998) reported a maximum difference of just 10% between a linear, trapezoidal and impulse velocity programme, but with a strong dependence on the axial velocity profile $U_z(r)$, viz. the discharge velocity distribution along the radial direction; for instance, it is decreased by 400% for a parabolic $U_z(r)$ profile compared to a uniform one.

1.2 Vortex rings with swirl

Superposing a swirl component $u_\theta(r)$ onto $U_z(r)$ is another effective way of manipulating F. Using both experiment and Large Eddy Simulation (LES), He et al. (2020b) showed that F decreases with increasing swirl strength almost linearly; this is primarily because the increased radial velocity of the ring core during the formation process weakens the delivery of vorticity from the nozzle to the leading vortex core. More importantly, if swirl strength is sufficiently strong, the flow structure during formation is changed remarkably; the convex vortex bubble surface is accompanied by a windward stagnation point, that is observed in the case of non- or weakly-swirling vortex rings, concaves inwards, similar to the breakdown mechanism of closed vortex lines to double spirals in a continuous jet with strong swirl (Billant et al., 1998; Brown and Lopez, 1990). Despite these valuable insights, the fundamental mechanism of vorticity evolution and the breakdown process remains to be revealed.

If a vortex ring is generated by axial momentum only, there is no mechanism to trigger the swirl velocity u_θ upon initiation, but weak swirl velocity will develop in the core of a well formed isolated vortex ring when it loses stability at large time and undergoes transition from a laminar state to a turbulent one (depending on the formation Reynolds number). This is coupled with azimuthal waves forming along the toroidal core due to instability (Gan et al., 2011; Maxworthy, 1977; Saffman, 1978), promoting energy decay.

Generating homogeneous and solid-body rotating swirl velocity flux in tandem with the axial velocity flux, and strictly confined within and through the desired discharge section, is not easily achievable in practice. Naitoh et al. (2014) studied swirling vortex rings experimentally by physically rotating the associated piston-nozzle system, similar to the mechanism used to generate a solid-body-rotating swirling jet by Liang and Maxworthy (2005). This arrangement invariably contaminates the ambient fluid in contact with the generator during rotation preparation. In He et al. (2020a,b), swirl was generated by installing static twisting vanes close to the exit of a piston-nozzle arrangement, similar to jet engine combustion chamber inlets. The strength of swirl was adjusted by vanes of different twist angles,

allowing the simultaneous onset of swirl linear momentum, but at the cost of turbulence 'contamination' from the complex boundary layer washed off the surface of the vanes.

From the point of view of related direct numerical simulation studies (Cheng et al., 2010; Gargan-Shingles et al., 2015; Virk et al., 1994), swirl has either been directly superposed onto a well-formed isolated Gaussian ring or generated by wrapping additional vortex lines around the toroidal vortex core in the azimuthal direction, without any practical consideration as to its generation.

The effect of additional swirl on flow field behaviour is striking. Naitoh et al. (2014) studied the long term evolution of a compact vortex ring for $L/D \in (1.25, 1.8)$ and swirl number S, defined here as:

$$\mathrm{S} = \frac{\Omega R_o}{U_o} = \frac{\Omega D_o}{2U_o}, \tag{1.11}$$

where $R_o = D_o/2$ is the orifice radius and Ω is the angular speed of the flow at the orifice, in the range $\mathrm{S} \in (0, 0.75)$. The above definition of S is in line with that adopted in Liang and Maxworthy (2005) for their continuous swirling jet experiment. Alternative definitions of S based on the ratio of swirl and axial momentum have been used in studies where rotation is not strictly of a solid-body rotation type (Candel et al., 2014).

Naitoh et al. (2014) found that increasing S resulted in faster decay of the ring propagation velocity, and speculated that it is related to the higher exchange rate with increasing S of the fluid material between the ring volume and the ambient surroundings. They also observed a pair of weak vortices' in the longitudinal central measurement plane, with oppositely signed (negative) vorticity in front of the leading ring, which grows during the formation process and decays quickly afterwards owing to the decay of swirl as illustrated in Figure 1.5(b). They also reported a decrease in the ring's circulation with increasing S, because of the so-called 'peeling off' of vortex lines around the ring core, which discharges vorticity from the leading ring to the wake. In addition to the effect of F, He et al. (2020a,b) found that although increasing swirl shrinks the vortex bubble length, which is the flow transported by

the vortex ring, along the symmetry axis, it increases the ring radius growth rate. For compact swirling rings $L/D = 1.5$, the onset of the azimuthal wave along the vortex core is also promoted with S at large time.

Cheng et al. (2010)'s simulation of rings for $S \in [0, 4]$ showed that a secondary ring like flow of negative azimuthal vorticity is formed ahead of the leading ring for $S > 0$; see Figure1.5 (a). The formation of this flow is a consequence of a secondary flow generated by the strong swirling flow in the primary vortex core, similar to the Dean vortex observed in a pipe section with non-zero curvature. The secondary flow consists of a pair of vortices of opposite sign whose strength increases with S. The positive vorticity merges with the primary ring increasing its strength, while the negative vorticity interacts with the primary ring in the sense of vorticity cancellation. This secondary flow makes a significant contribution to the dynamic behaviour of the overall vortex structure. For sufficiently large S, the propagation direction of the compact ring structure can be altered from one of moving downstream to upstream. Gargan-Shingles et al. (2015) also noticed a shear layer of opposite sign around the main vortex core in their simulations of rings for $L/D = 2.5$. By analysing the azimuthal component of the momentum equation, neglecting the viscous terms, they concluded that the convective acceleration of the azimuthal velocity plays a key role in the generation of this shear layer.

The vortex lines introduced in Virk et al. (1994) induce additional azimuthal velocity inside the vortex core analogous to a magnetic field induced by an alternating current in a toroidal coil invoking the Biot-Savart law, see Batchelor (1967) Chapter 2:

$$u_i = -\frac{\Gamma}{4\pi} \oint \frac{\mathbf{s} \times \mathbf{dl}}{|\mathbf{s}|^3}, \tag{1.12}$$

where u_i is the induced velocity, the vector $\mathbf{s}$ is taken from the vortex line to a point on a curve in space, and the differential arc length is represented by dl.

They showed the ring radius grew faster with larger azimuthal velocity stemming from the centrifugal effect, which is supported by He et al. (2020b). In Verzicco et al. (1996), swirl flow in compact laminar vortex rings with $L/D < 1$ results from the rotation of the whole flow field. They observed similar flow characteristics to those of other authors, such as decreased axial propagation velocity and secondary ring

formation with oppositely signed vorticity in front of the leading ring.

1.3 Interaction between vortex rings

A vortex ring induces an irrotational concentric velocity field (Batchelor, 1967). Following the Biot-Savart law in a 2D plane; see Figure 1.6, a vortex core generates a sequence of concentric streamlines, whose velocity magnitude depends on the strength, Γ_{Ring}, and radial distance from the core centre, r_c, with velocity u_i, namely:

$$u_{\mathrm{i}} = \frac{\Gamma_{Ring}}{2\pi r_c}. \tag{1.13}$$

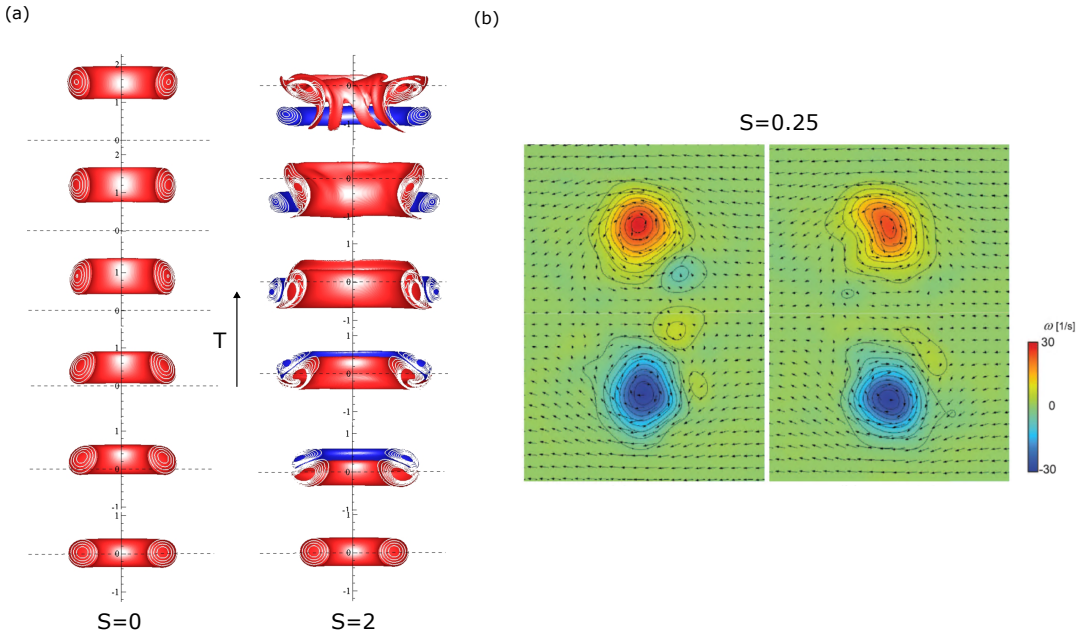

Figure 1.5: (a) Isosurfaces of ω_θ showing the evolution of a vortex ring for S=0 and 2. The red isosurface indicates $\omega_\theta > 0$ and blue isosurfaces indicated $\omega_\theta < 0$. (b) Contour plot of the vorticity field in Cartesian coordinates showing the formation of opposite sign vorticity ahead of the vortex ring for S=0.25. Figures taken from Cheng et al. (2010)–left; Naitoh et al. (2014)–right.

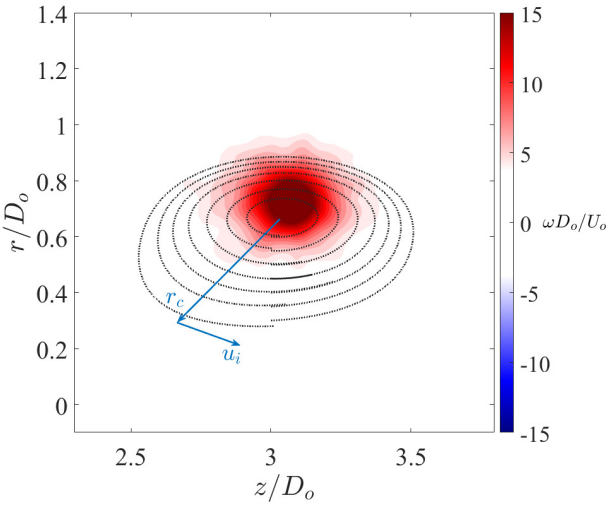

Figure 1.6: Vorticity contour plot of one vortex ring core and the streamlines formed around it representing u_i

The induced u_i from one core propels the other core downstream and vice versa, allowing the vortex ring to propagate. If another vortex ring is generated subsequently, the self-induced velocity of the initial ring will diminish the rear one, reducing its radius and increasing its propagation velocity. At the same time, the trailing ring's induced velocity will increase the radius of the one preceding it and reduce its propagation velocity. The phenomenon of a subsequently formed ring passing through is known as "leapfrogging" (Maxworthy, 1972); see in Figure 1.7.

The interaction of two coaxial vortex rings has been studied widely for decades. It began with the observations of Helmholtz (1858b) concerning the interaction of two vortex rings in his work on vortex dynamics, followed by the theoretical model proposed by Sommerfeld (1950). Subsequent to this several articles appeared dedicated to theoretically analysing a system of two or more coaxial vortex rings (Borisov et al., 2014; Davila et al., 2022; Mavroyiakoumou and Berkshire, 2020; Shariff et al., 1989; Tophøj and Aref, 2013). Most employ the point vortices method, which assumes an inviscid flow in which the whole vorticity is concentrated at points the space, achieving an infinite number of leapfrogging events for a specific set of parameters. However, experiments tell a different story.

Batchelor (1967), in his book "Introduction to fluid dynamics", made an "invita-

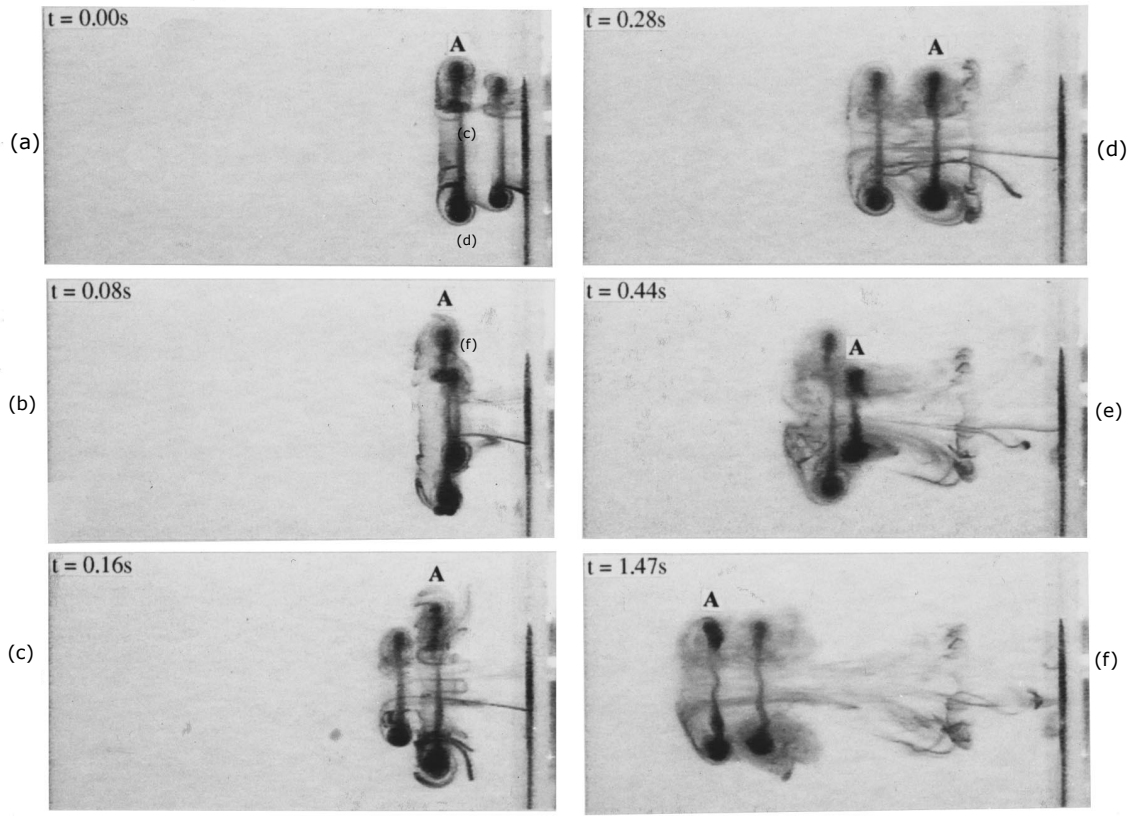

Figure 1.7: Visualisation of a leapfrogging. Figure taken from Lim (1997)

tion" to experimental scientists, suggesting the possibility of achieving two leapfrogs in a laboratory, namely two passages of one ring through the other before they merge. In one of the classic works associated with vortex rings, Maxworthy (1972) dedicated the last section of his paper to the interaction between two vortex rings. He was unable to achieve a single leapfrog with two rings having similar circulation and Re=600 (based on the initial ring propagation velocity). Information about the time delay between the formation of rings was not provided. He observed that the induced velocity from the leading ring distorts the following vortex ring, which was entrained by the leading one, forming a single large vortex ring.

Oshima et al. (1975) reported similar results, which used three different time delays between two rings with similar circulation and Re=150. For a time delay of 2.4 seconds, the following ring could not catch the leading one, and its propagation appeared unaffected by the induced velocity of the leading ring. With a 1.8 seconds

delay, the following ring reached the leading one, which engulfed it; finally, for a 1.5-second delay, the following ring engulfed the leading one immediately after passing through it. In summary, they suggested that the vortex cores of such rings should be smaller in comparison to the ring radius in order to reduce the deformation experienced and avoid their merger.

The first successful leapfrogging experiment in a laboratory was performed by Yamada and Matsui (1978), whose main change was to increase the Re to 1600 (based on the initial ring propagation velocity). They compared the trajectories of both rings from their experiments with those obtained by point vortex theory showing remarkable agreement. Finally, they mention that a second leapfrogging event was achieved, however, no figure is provided. Extending his previous work and including the findings of Yamada and Matsui (1978), Oshima (1978) constructed a diagram showing the region where leapfrogging is successful in two fluid, water and air, based on the Re number and the delay time, T, between the rings as presented in Figure 1.8(a). However, as is clearly it is not a universal region; every orifice diameter,D, used in this work reflects a different region. Besides, most of the successful areas were achieved when smoke rings were employed instead of water vortex rings, suggesting the existence of another dimensionless number that characterises leapfrogging. Another diagram, proposed subsequently by Lim (1997), Figure 1.8(b) in terms of the same parameters reveals a single region when leapfrogging is possible. In their diagram, as the Re decreases, the time delay, t^*, to achieve leapfrogging increases, unlike Oshima's diagram, where the time delay decreases with the Reynolds number.

From their numerical work, Shariff et al. (1989) suggest a connection between Re and successful leapfrogging depends on the vortex core size. A vortex ring generated with a low Re forms a thick vortex core susceptible to core distortion, making it hard to achieve leapfrogging. Following this idea, Satti and Peng (2013) performed experiments for vortex rings with different core sizes and different time intervals between the rings; The core size was determined by L/D_o and calculated from the cross-sectional area of the vortex core after applying a threshold of 5% the peak vorticity value. Double leapfrogging was observed for their middle-size core

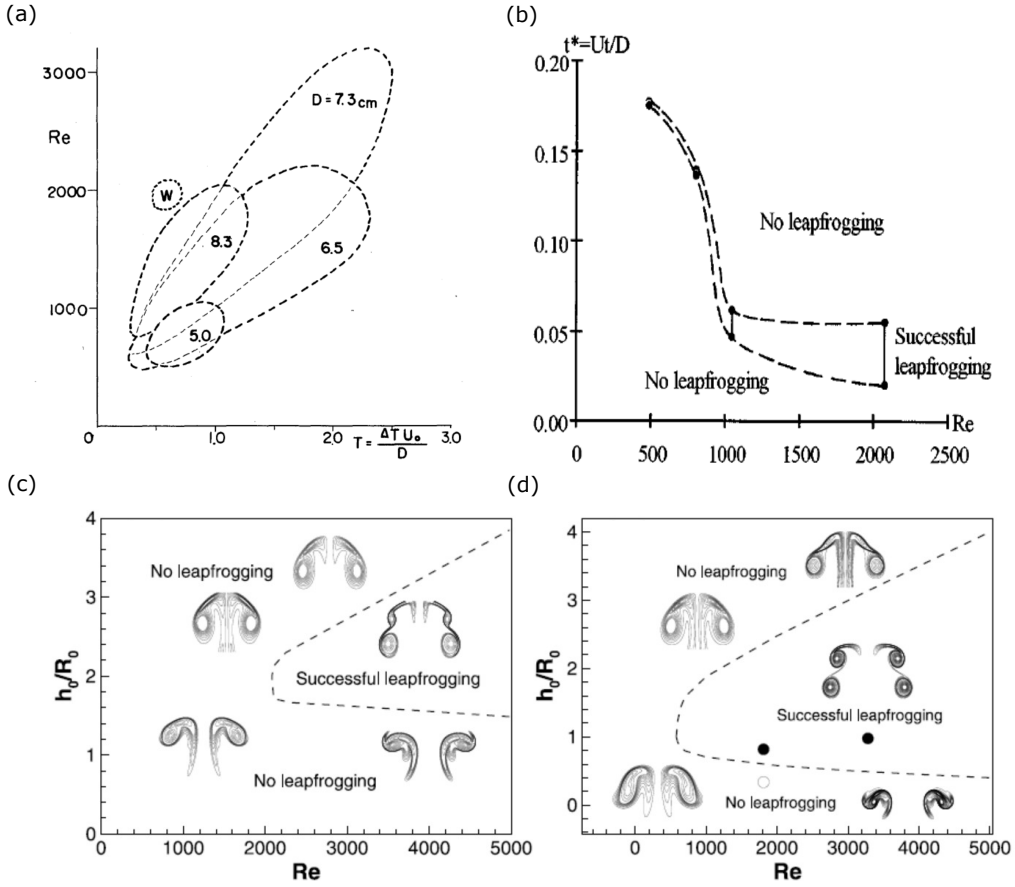

Figure 1.8: Evolution of diagrams showing regions of successful leapfrogging based on different parameters over the years; (a)Oshima (1978) where W denotes the case in water and D the nozzle diameter, (b) Lim (1997), (c,d) Cheng et al. (2015) for a core radius 0.2 and 0.1 times the initial ring radius respectively where h_o denotes the initial distance of the leadering vortex ring from the nozzle.

generated by $L/D_o = 1.5$, with a time interval between strokes equal to half of the stroke ratio ($t^* = 0.75$). They observed that the following ring experienced a higher shear, induced by the leading ring, increasing the shedding of vorticity to the wake. They also presented the evolution of each ring's circulation, where an evident decay is observed before the first leapfrog is achieved. The faster decay is attributed to vorticity cancellation when both rings are aligned radially, where the following ring cores are closer to each other. For a shorter time interval, the following ring merged with the leading one straight away, while for a longer time interval, just one leapfrog is achieved before the rings merge. Finally, for a vortex ring with a smaller core, the deformation of the following ring together with its

circulation decrease was found to be much smaller; however, only one leapfrog was possible due to the lower magnitude of the induced velocity field. Meanwhile, for their larger vortex ring core size experiments leapfrogging was not observed. Cheng et al. (2015), via a numerical investigation of viscous vortex rings, pointed out that a larger core requires a higher Reynolds number to achieve leapfrogging, presenting diagrams similar to those discussed above, but with Re plotted against the initial distance of the leading ring from the nozzle, h_o, and for two vortex core sizes, see Figure 1.8(c-d).

While most of the literature concerning the interaction between two or more vortex rings focuses on achieving leapfrogging, an interesting finding was made by Fu et al. (2014) and subsequently Fu and Liu (2015), that have studied the use of vortex rings as a locomotive force in nature. In their experiment, they created two consecutive vortex rings with the same stroke ratio and observed an increase in impulse of up to 50% for the second piston stroke for rings with $L/D_o = 1$. They found that as the stroke ratio was increased, this impulse augmentation decreased, reaching a 10% gain for $L/D = 4$. The same trend was observed when the time interval between piston strokes was increased. In both cases, the decrease in impulse augmentation was related to the distance between the rings. For small stroke ratios, the leading ring's propagation velocity is slow, resulting in a strong interaction with the following ring upstream. As the stroke ratio increases, the propagation velocity also increases, reducing interaction with the following ring. Although Fu et al. (2014) suggests that the additional impulse input may promote fluid entrainment, further discussion on the formation process of the following ring is needed.

Another important feature related to a series of successively generated vortex rings was observed by Qin et al. (2018), where the circulation of the last vortex ring generated in the vortex chain increases by up to 10%. Experimentally, they generated a chain of rings with the same stroke ratio and time interval. Two modes were reported: the formation enhancement mode (FEM) and the formation restraint mode (FRM). The latter one was observed when the vortex rings were generated consecutively with a minor or zero time interval when $L/D_o = 1$ or 2. As the number of generated rings was increased, the drop in ring circulation of the last ring also

increased compared to the circulation of an isolated ring. This loss of the ring's circulation seems to be more pronounced for rings with $L/D_o = 1$ than $L/D_o = 2$, where up to 20% of the ring's circulation is lost for the fifth vortex ring compared to an equivalent isolated ring. The formation enhancement mode, on the other hand, is observed when generating only two vortex rings, with a time interval higher than a half second for $L/D_o = 1$ and one second for $L/D_o = 2$. However, if this interval exceeds a specific time, the circulation gain decreases, approaching the equivalent isolated ring case as expected.

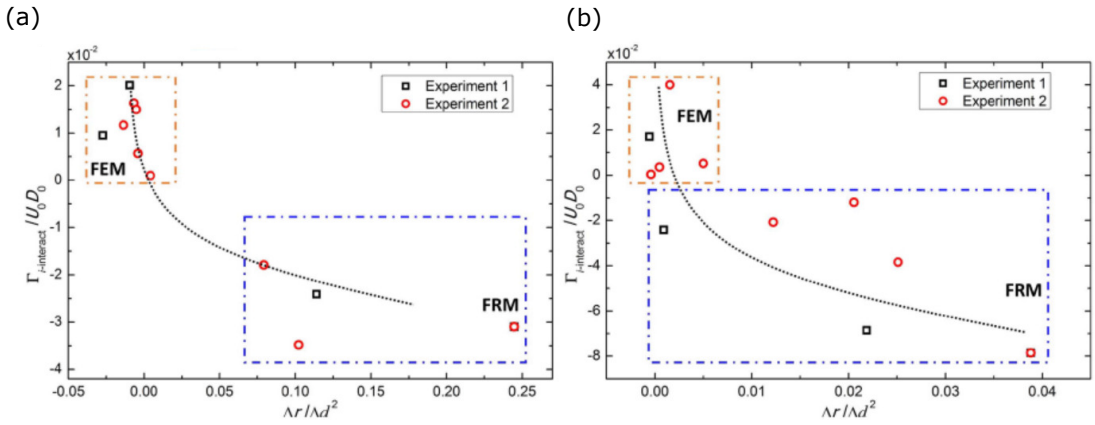

Figure 1.9: Circulation augmentation ($\Gamma_{interact} = \Gamma_{ring} - \Gamma_{ring-isolated}$) as a function to the parameter $\Delta r/\Delta d^2$ for (a) $L/D_o = 1$ and (b) $L/D_o = 2$. In experiment 1, several vortex rings were produced instantaneously, one after the other. For experiment 2, only two rings are generated with an interval time. Δr is the difference in the vortex radii, and Δd^2 is the square of the axial distance between the vortex rings. Figure taken from Qin et al. (2018)

According to Qin et al. (2018), the above two modes can be characterised and identified in terms of the ratio between the difference in the vortex radii, Δr, and the square of the axial distance between the vortex rings, Δd^2, as shown in the Figure 1.9 where the FEM occurs for small $\Delta r/\Delta d^2$. Even though it is clear that the induced velocity of the vortex ring is responsible for these modes, further investigation is needed as to its role during the formation process of vortex rings. Due to the vortex rings observed in the FEM having a L/D_o smaller than the formation number, there are two most likely hypotheses to explain the circulation enhancement. The first hypothesis is that the following ring engulfs some vorticity from the leading ring.

The second hypothesis is an increase in the vortex flux coming from the nozzle, which is consistent with the findings of Fu et al. (2014) and Fu and Liu (2015) regarding impulse augmentation.

The overarching aim of the present work is to study the influence of the addition of swirl on the global flow dynamics of impulsively generated vortex rings, in particular in relation to their formation process and early time evolution, features that have not been addressed sufficiently in the past. Additionally, based on observations made in the study of swirling vortex rings, it explores how the effect of a preceding vortex ring can enhance the formation of a vortex ring.

The thesis is structured in the following manner:

- Chapter 1, the fundamental properties of a vortex ring are explained, followed by an overview of previous numerical and experimental work that illustrate the characteristics observed when swirl is added to a vortex ring as well as the interaction between two or more vortex rings.

- Chapter 2 provides a comprehensive account of the numerical and experimental methods utilised in the research. The computational domain, flow conditions, discretisation technique, solution algorithm, and turbulent model employed in the numerical part as well as its validation, are explained in detail. Additionally, a precise description of the experimental rig, techniques performed, and devices involved is provided.

- Chapter 3 presents a comprehensive set of results obtained from the numerical analysis performed. It covers the nature of the three-dimensional flow field and the characterisation of the vorticity dynamics, with a particular focus on the mechanism behind the generation of negative vorticity. The chapter also explores the impact of swirl on the kinematic features of the flow field and concludes by addressing the dependence of F on the strength of the swirl.

- Chapter 4 focuses on the experimental analysis of swirling vortex rings. The feasibility of generating an inlet velocity with solid body rotation, as utilised in the numerical work, is tested using a rotating pipe. The experimental work is compared with features observed in Chapter 3 and confirms some of the

hypotheses. Also, it introduces a new method to generate swirling vortex rings faster and with different characteristics.

- Chapter 3, it was found that there is a correlation between the ring radius and F. Chapter 5 delves deeper into this relationship by examining how two collinear vortex rings with different strengths and separations interact. The main objective is to control the ring radius of the following ring during its formation by manipulating its interaction with the preceding vortex ring. This study also analyses the effect of the ring radius on important quantities such as circulation or strength, as well as the dimensionless energy of the ring and its impact on the core structure.

- Conclusions are drawn in Chapter 6 and suggestions for future work provided.

CHAPTER 2

Methodology

The work presented in this thesis consists of three investigations focused on understanding some exciting features regarding vortex rings. Each study was approached differently, starting with a rigorous numerical exploration and finishing using two detailed and thorough experimental investigations. The purpose of this Chapter is to introduce and describe the numerical and experimental methodology and techniques that were used to generate the findings discussed in Chapters 3, 4 and 5.

2.1 Governing equations

The Navier-Stokes equations, which are constrained by the continuity equation, are used to describe the formation and evolution of vortex rings. Despite being known for over a century, only a few flows can be solved analytically using these equations. Circular vortex lines and Hill spherical vortex models are the simplest for vortex rings, see Batchelor (1967) Chapter 7. Although both models are based on several assumptions, they provide useful information regarding the self-induced velocity of the ring. To analyse and comprehend the formation and evolution of a vortex ring, a numerical solution of the Navier-Stokes equations is necessary. The continuity equa-

tion and Navier-Stokes equations for an incompressible flow are written in Cartesian coordinates are:

$$\frac{\partial u_x}{\partial x} + \frac{\partial u_y}{\partial y} + \frac{\partial u_z}{\partial z} = 0, \tag{2.1}$$

$$\frac{\partial u_x}{\partial t} + u_x\frac{\partial u_x}{\partial x} + u_y\frac{\partial u_x}{\partial y} + u_z\frac{\partial u_x}{\partial z} = -\frac{\partial p}{\partial x} + \nu\left[\frac{\partial^2 u_x}{\partial x^2} + \frac{\partial^2 u_x}{\partial y^2} + \frac{\partial^2 u_x}{\partial z^2}\right], \tag{2.2}$$

$$\frac{\partial u_y}{\partial t} + u_x\frac{\partial u_y}{\partial x} + u_y\frac{\partial u_y}{\partial y} + u_z\frac{\partial u_y}{\partial z} = -\frac{\partial p}{\partial y} + \nu\left[\frac{\partial^2 u_y}{\partial x^2} + \frac{\partial^2 u_y}{\partial y^2} + \frac{\partial^2 u_y}{\partial z^2}\right], \tag{2.3}$$

$$\frac{\partial u_z}{\partial t} + u_x\frac{\partial u_z}{\partial x} + u_y\frac{\partial u_z}{\partial y} + u_z\frac{\partial u_z}{\partial z} = -\frac{\partial p}{\partial z} + \nu\left[\frac{\partial^2 u_z}{\partial x^2} + \frac{\partial^2 u_z}{\partial y^2} + \frac{\partial^2 u_z}{\partial z^2}\right], \tag{2.4}$$

where p is the kinematic pressure and p/ρ, ν is the kinematic viscosity. The flow can be assumed incompressible since the velocities are low, lower than 1 m/s. The second term on the left-hand side in equation (2.4) refers to the advective transport related to the inertia, and the second term on the right-hand side to the diffusive transport related to the viscous forces acting on the flow.

It is important to exercise caution when implementing numerical methods. The solutions obtained are only approximations of the Navier-Stokes equations, which means it's crucial to analyse the errors that occur during discretisation and iterative processes. Therefore, the quality of the grid and an appropriate interpolation scheme are the main fundamental steps to ensure the accuracy of numerical results.

Due to the complexity involved in solving the Navier-Stokes equations numerically, OpenFOAM®, which stands for Open-source Field Operation and Manipulation was employed in the work reported here. This software is a set of C++ libraries that enables problems from fluid mechanics to electromagnetism to be solved using a range of meshing tools, customisable numerical solvers and pre/post-processing utilities –see Figure 2.1(OpenCFD, 2024b). Additionally, a large global community continuously contribute to the number of resources available, which has made OpenFOAM very popular and widely accepted in the scientific community.

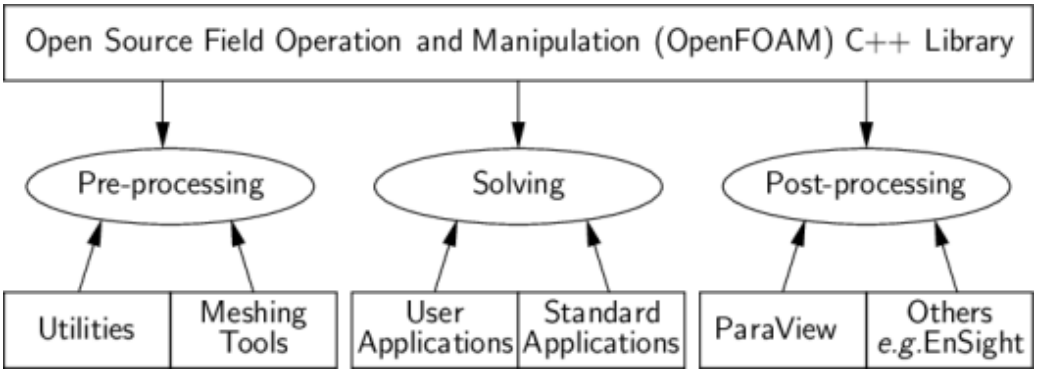

Figure 2.1: Overview of OpenFOAM's structure, Figure taken from OpenCFD (2024b)

2.2 Numerical Methodology

2.2.1 Method of solution

In order to apply numerical methods, it is necessary to discretise ordinary or partial differential equations. This involves dividing the continuous time into smaller time steps, denoted by Δt. Additionally, the space is divided into cells that contain relevant field values such as velocity and temperature. As a result of the discretisation method, solving partial differential equations is replaced by solving a set of linear equations using a variety of algorithms.

Finite Volume Method (FVM)

In OpenFOAM, the discretisation method used is the finite volume method (FVM). This method divides the computational domain into multiple connected polyhedral finite control volumes, where the conservation equations for mass, momentum and energy are formed by balancing the fluxes between the inflows and outflows at each volume's surfaces. For instance, when discretising the advection term $\nabla \cdot (u\Psi)$, where ψ is a general parameter, the integral surface obtained by applying Gauss's theorem to the finite control volume is broken down and approximated as a summation over its faces. Due to the small size of the faces, the flux calculation over them is

approximated as the value at the face centre, as (Greenshields and Weller, 2022) follows:

$$\nabla \cdot (u\Psi) = \lim_{\Delta V \to 0} \frac{1}{\Delta V} \int_S \vec{\mathbf{u}} \cdot \hat{\mathbf{n}} \Psi dS \sim \frac{1}{\Delta V} \sum_S \vec{u}_S \cdot \hat{n}_S \Psi_S = \frac{1}{\Delta V} \sum_S \phi_S \Psi_S \quad (2.5)$$

where $\hat{n}$ is the normal vector, ϕ_s the volumetric flux at the surface. In contrast to a staggered grid arrangement, where the velocity component values are stored at the face centres, OpenFOAM uses a co-located grid. This means that all the flow variables, such as $\vec{u}$, p, and T, are only stored at the finite volume centroids (Liu and Hinrichsen, 2014). In order to obtain the values at the face centroids, Ψ_S, an interpolation scheme is required. This scheme combines the values from the centroid of the control volume Ψ_O and its neighbour Ψ_N, as illustrated in Figure 2.2. OpenFOAM uses an interpolation scheme based on the Rhie & Chow interpolation, consisting of a linear interpolation and a correction term related to the pressure gradient. This correction term helps to avoid chequerboard oscillations that can arise with co-located grids, ensuring that the velocity remains oscillation-free (Bartholomew et al., 2018; Kärrholm, 2006; Rhie and Chow, 1983).

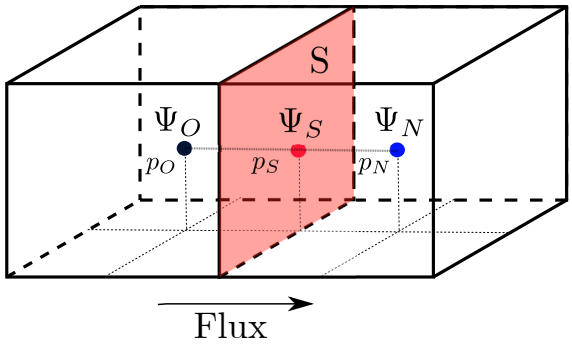

Figure 2.2: Sketch of two adjacent control volumes with their respective centroidS, P_O (owner cell), P_N (neighbour cell) highlighting the shared surface and its centroid. Ψ represents the quantity transported by the flux and S is the volume surface

The present study employs the central differencing/linear scheme to compute the gradient and Laplacian terms. This scheme is known for its second-order accuracy, which makes it highly precise. However, a linear interpolation scheme may lead to

unstable numerical results for the advection/divergence term, producing unbounded solutions. For this term, a LUST (Linear-Upwind Stabilised Transport) is used, which is a fixed blended scheme with 0.25 linearUpwind and 0.75 linear weights (OpenCFD, 2024a). The linear interpolation model takes the following form, where β is an interpolation factor(Ferziger et al., 2019):

$$\Psi_S = \beta\Psi_N + (1-\beta)\Psi_O \qquad \beta = \frac{|p_S - p_O|}{|p_N - p_O|} \qquad 0 \leq \beta \leq 1. \tag{2.6}$$

For temporal discretisation, an implicit second-order scheme named "backward" is implemented in OpenFOAM. It is important to note that this scheme is not the same as Euler backwards, named Euler in OpenFOAM. The backward scheme is defined as:

$$\frac{\partial \Psi_O}{\partial t} = \frac{3\Psi_O^{n+1} - 2\Psi_O^n - 2\Psi_O^n + \Psi_O^{n-1}}{2\Delta t} + O(\Delta t^2), \tag{2.7}$$

where n is the current time step and $n-1$ and $n+1$ the previous and forward time step, respectively (Marić et al., 2014). The value of Δt is set to 1×10^{-4} seconds. It is worth noting that since an implicit discretisation scheme is used, it is not necessary to satisfy the Courant–Friedrichs–Lewy (CFL) number condition to ensure numerical stability.

After discretising all the terms in the Navier-Stokes equations and arranging, a linear system is obtained that can be represented in the following matrix form, where M is a matrix of known coefficients:

$$\boldsymbol{M}u = -\Delta p. \tag{2.8}$$

Even though, for an incompressible flow, there are four equations (three from each velocity component of the momentum equation and the continuity equation) with four variables (u_x, u_y, u_z and p), there is no specific equation for pressure. This creates a problem known as pressure-velocity coupling.

PISO algorithm

In order to solve the pressure-velocity coupling problem for an incompressible transient flow, the PISO algorithm (Pressure Implicit with Splitting of Operators) proposed by Issa (1986) is implemented. The first step (not exclusive to the PISO algorithm) is to find an explicit expression to compute the pressure field. This can be achieved by extracting the diagonal from the matrix $\boldsymbol{M}$, named $\boldsymbol{A} = diag(\boldsymbol{M})$, to obtain:

$$\boldsymbol{M}u = \boldsymbol{A}u - \boldsymbol{H} \rightarrow \boldsymbol{H} = \boldsymbol{A}u - \boldsymbol{M}u, \tag{2.9}$$

where $\boldsymbol{H}$ is a residual matrix. The reason for extracting the diagonal from matrix $\boldsymbol{M}$ is to simplify the calculation of its inverse $\boldsymbol{A}^{-1} = 1/\boldsymbol{A}$. Subsequently, by multiplying equation (2.9) by $\boldsymbol{A}^{-1}$, gives:

$$u = \boldsymbol{A}^{-1}\boldsymbol{H} - \boldsymbol{A}^{-1}\Delta p, \tag{2.10}$$

named Momentum corrector. Finally, the continuity equation for incompressible flows ($\nabla \cdot u = 0$) is applied to obtain an explicit equation for the pressure field namely:

$$\nabla\cdot(\boldsymbol{A}^{-1}\Delta p) = \nabla\cdot(\boldsymbol{A}^{-1}\boldsymbol{H}). \tag{2.11}$$

The PISO algorithm involves the following overall steps:

1. Solve equation (2.8), also known as Momentum predictor, obtaining an initial guess of the velocity field from the previous iteration of the pressure field. However, u does not satisfy the continuity equation yet.

2. With the initial guess u, the residual $\boldsymbol{H}$ is computed using the equation (2.9).

3. The pressure field equation is solved via equation (2.11).

4. The corrected velocity field that satisfies the continuity equation is calculated explicitly using equation (2.10).

5. As the velocity field has changed, so too has $\boldsymbol{H}$. Therefore, step 2 and the following are repeated. This process is known as the inner loop and is one of

the primary differences between the SIMPLE and PISO algorithms. In SIMPLE, the iteration starts with the momentum predictor and is repeated until the pressure converges. However, in PISO, repeating the iteration process for every time step would be computationally expensive. Therefore, the momentum predictor is solved only once per time step. After the PISO loop, the improved velocity becomes the earlier time value in the next time step. This increases the accuracy of the time derivative of the momentum equation. Another difference is that SIMPLE requires under-relaxation due to the absence of a time derivative, which reduces the diagonal dominance. (Ferziger et al., 2019; Wimshurts, 2019).

2.2.2 Turbulence model

The turbulent model used in this work is Large Eddy Simulation (LES). This model is based on the "energy cascade" theory proposed by Richardson (1922) and subsequently developed by Kolmogorov (1941) and illustrated in Figure 2.3. According to this concept, the kinetic energy is initially introduced to the turbulent flow through production mechanics at the largest scales of motion. Subsequently, the energy is transferred to smaller scales, continuing the transfer process until viscous action finally dissipates the energy. In simpler terms, most of the initial kinetic energy is concentrated in large unstable eddies. These eddies break down and transfer their energy to smaller eddies until viscous processes dissipate the kinetic energy (Pope, 2000).

The energy cascade occurs primarily through an inviscid process where the mesh resolves the eddies of large and medium scales. When dealing with smaller scales, a problem arises as the minimum number of cells required to solve an eddy is four. However, if the viscous dissipation is not strong enough to break down these small eddies and convert them into heat, the eddies will remain in the flow field, increasing the flow's kinetic energy. To solve this issue, a sub-grid model is required for smaller eddies, whose purpose is to artificially increase the turbulence dissipation rate by adding a new term to the kinematic viscosity (equation 2.12), allowing it to dissipate

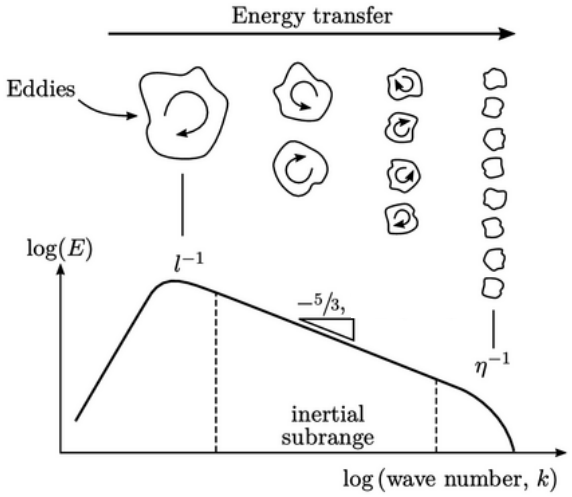

Figure 2.3: Plot of the kinetic energy from larger to smaller eddies, known as the energy cascade. l is the characteristic length of the flow and η the Kolmogorov length microscale. Figure taken from Greenshields and Weller (2022).

just the smallest eddies:

$$\nu = \nu + \nu_{sgs}. \tag{2.12}$$

In a Direct Numerical Simulation (DNS), the Navier-Stokes equations must be solved for all eddy scales, making it computationally expensive. However, a low-pass filtering procedure is executed for a Large Eddy Simulation (LES), where the filtered velocity field $\tilde{u_i}$ can be computed on a coarser grid. The unsteady and spatially filtered incompressible Naiver-Stokes equations that have been resolved numerically are:

$$\frac{\partial \tilde{u_i}}{\partial x_i} = 0, \tag{2.13}$$

$$\frac{\partial \tilde{u_i}}{\partial t} + \tilde{u_j}\frac{\partial \tilde{u_i}}{\partial x_j} = -\frac{\partial \tilde{p}}{\partial x_i} + \frac{\partial}{\partial x_j}\left[(\nu + \nu_{sgs})\frac{\partial \tilde{u_i}}{\partial x_j}\right], \tag{2.14}$$

which are expressed in a Cartesian coordinate that is the default coordinate system used by OpenFoam and where $\tilde{u_i}$ and $\tilde{p}$ are the filtered velocity components and the pressure (which includes the density term $1/\rho$), respectively, at the grid level. The sub-grid viscosity ν_{sgs} is approximated using the Smagorinsky model (Smagorinsky, 1963) as:

$$\nu_{sgs} = (C_s\Delta)^2\sqrt{2\tilde{S_{ij}}\tilde{S_{ij}}}, \tag{2.15}$$

where Δ is the filter characteristic length scale. $\tilde{S_{ij}}$ is the strain rate tensor and C_s is the Smagorinsky constant, which was set to 0.094. While the dynamic Smagorinsky model (Germano et al., 1991; Lilly, 1992), with the Smagorinsky constant computed in terms of the local flow conditions, is often used for jet flows, the classical Smagorinsky model has been shown to produce comparable accuracy in a number of recent investigations of vortex ring related flows at a similar Re employed here (e.g. New et al., 2021).

2.2.3 Mesh decomposition and validation

The distribution of grid points used to form the structured mesh employed to generate solutions is provided in Table 2.1. The computational domain is segmented into four coaxial, contiguous cylindrical volumes: three of radial length R_1, R_2 and R_3 (see Figure 2.4 (a)), and one associated exclusively with the nozzle volume for inlet Case A. The mesh in the axial and radial directions was carefully distributed to ensure sufficient spatial resolution in the vortex core region where velocity gradients are largest.

To avoid singularity issues at $r = 0$ associated with the mesh cells converging to a single point at the cylinder centre (Gullberg, 2017; Tucker, 2016), a smoothed square prism-like mesh structure, also know as a butterfly grid, is implemented in the vicinity of $r = 0$ as shown in Figure 2.4 (c), extending a distance $D_0/5$ from $r = 0$. Such a meshing approach was adopted by He et al. (2020b), ensuring the required level of accuracy for the current flow problem. Required also is a careful meshing strategy at the interface between the prismatic and contiguous adjacent cylindrical region, without which numerical artefacts can be triggered there, for example promotion of azimuthal instability. For the evolutionary time duration investigated in the present work, no pronounced effect, e.g. the appearance of a dominant azimuthal wave number of $m = 3$ along the primary vortex core, was detected for the associated physical quantities of interest.

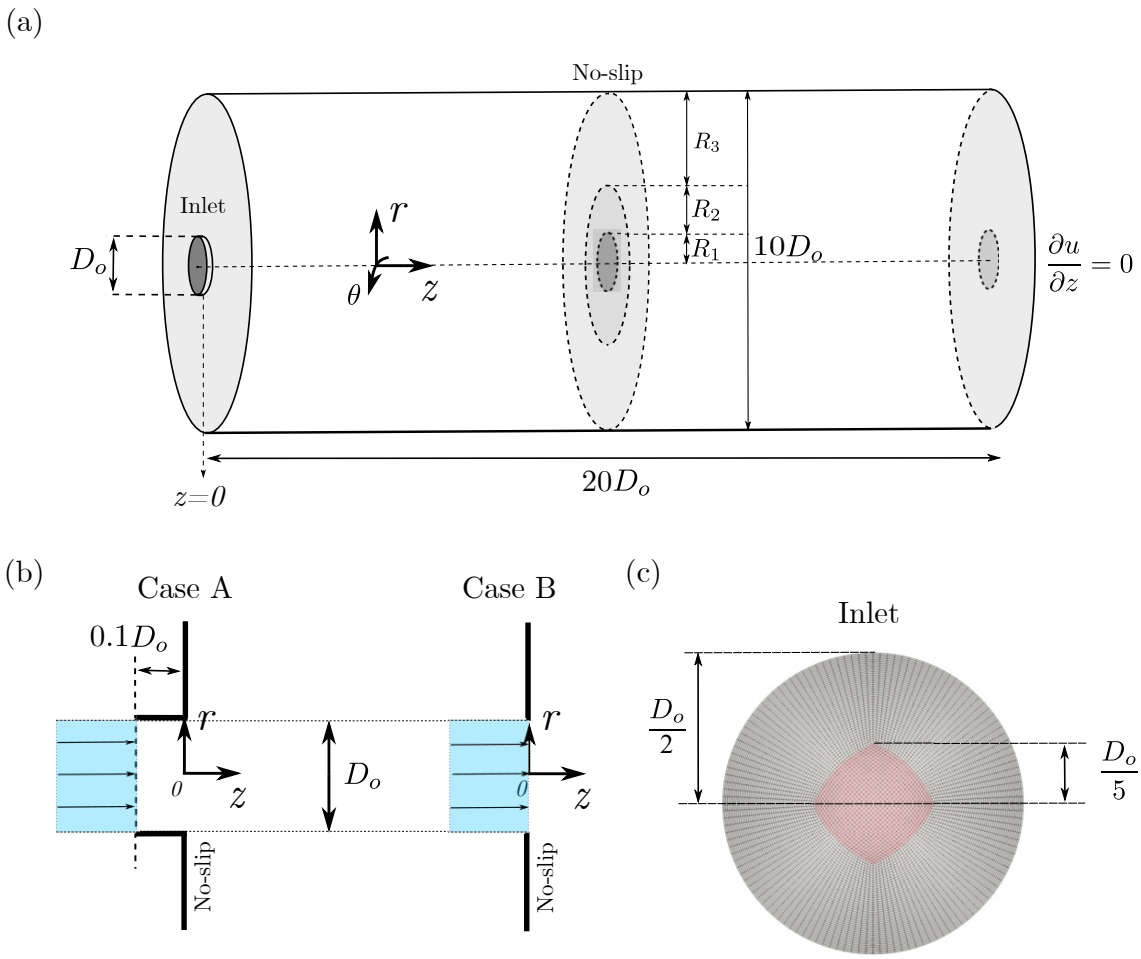

Figure 2.4: (a) Flow geometry (not to scale) and boundary conditions; shown also the mesh segmentation adopted for the accompanying computations, consisting of four adjoining contiguous coaxial cylindrical volumes (0, 1, 2 and 3) - one for inlet Case A only and three of radial length R_1, R_2 and R_3 - as detailed in Table 2.1. (b) Inlet geometries for Case A and Case B (not to scale) and associated coordinate system. (c) Cross-section(not to scale) showing the radially distributed structured mesh arrangement employed when $0 < r < D_o/2$ for all z.

The impact of the adopted meshing strategy and grid distribution on the accuracy of the LES solver were evaluated by resolving the turbulence kinetic energy (TKE), $M(x,t)$, see Pope (2004), as

$$M(x,t) = \frac{k_{sg}(x,t)}{k_r(x,t) + k_{sg}(x,t)}, \tag{2.16}$$

where k_r is the resolved TKE, and k_{sg} is the sub-grid energy. M and both k_r and k_{sg} are functions of space, x, and time, t. The histogram of M, presented in Figure 2.5

Case	Volume	Domain size		Number of grid points		
A	0	$-0.1 \leq z/D_o \leq 0$	$r/D_o \leq 0.5$	$25(z)$	$77(r)$	$128(\theta)$
	1	$0 \leq z/D_o \leq 20$	$r/D_o \leq 0.5$	$450(z)$	$77(r)$	$128(\theta)$
	2	$0 \leq z/D_o \leq 20$	$0.5 < r/D_o \leq 1.5$	$450(z)$	$80(r)$	$128(\theta)$
	3	$0 \leq z/D_o \leq 20$	$1.5 < r/D_o \leq 5$	$450(z)$	$30(r)$	$128(\theta)$
B	1	$0 \leq z/D_o \leq 20$	$r/D_o \leq 0.5$	$450(z)$	$77(r)$	$128(\theta)$
	2	$0 \leq z/D_o \leq 20$	$0.5 < r/D_o \leq 1.5$	$450(z)$	$80(r)$	$128(\theta)$
	3	$0 \leq z/D_o \leq 20$	$1.5 < r/D_o \leq 5$	$450(z)$	$30(r)$	$128(\theta)$

Table 2.1: Structured mesh distribution arrangement, detailing how the computational domain was segmented into 3 coaxial contiguous cylindrical volumes, 1, 2, and 3, of radial length R_1, R_2, R_3, respectively (see Figure 2.4 (a)). The contiguous axial cylindrical volume 0 is associated with inlet Case A only; see Figure 2.4 (b).

(a), confirms that at least 80% of the flow field TKE is resolved. The mesh grids having the lowest resolutions contributing to the other 20% of the TKE, are those along the outer cylindrical domain surface, which has negligible effect on the flow of interest. Given the unsteady nature of the flow under investigation, M here is the time averaged result over the entire piston stroke duration, which is equivalent to a dimensionless discharge duration $T^* \leqslant 6$ ($T^* = tU_o/D_o$) for the case of S = 1, where the strongest velocity gradient and turbulence occurs from among all the cases investigated and over the entire scrutinised duration. Accordingly, for all the other cases considered and later time, resolution is always better than 80%. This is similar to the resolution assessment applied in the pulse jet simulation of Coussement et al. (2012).

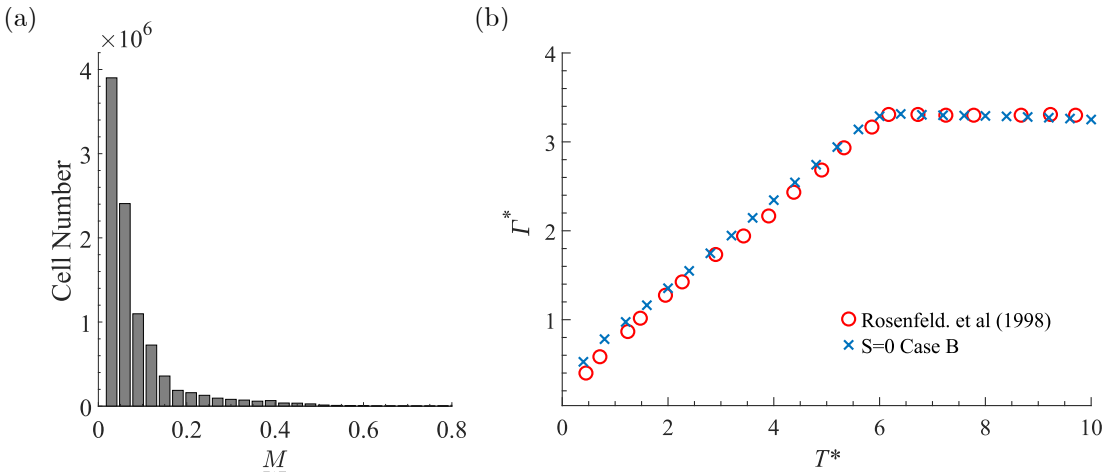

Figure 2.5: (a) Histogram of the mesh grid resolution of TKE when S = 1 and the inlet condition is Case A, averaged over $0 \leqslant T^* \leqslant 6$. (b) Comparison of the total circulation when S = 0 and the inlet condition is Case B, with that of Rosenfeld et al. (1998) for a similar flow condition; for both flows, Re = 2500, the equivalent discharge slug time is $L/D_o = 6$, and Γ^*.

In addition to the above, the resultant circulation for the case S = 0 is compared with that from the corresponding direct numerical simulation, in an axisymmetric domain, conducted by Rosenfeld et al. (1998) for non-swirl vortex rings issuing from an orifice geometry of the Case B type. Figure 2.5 (b) shows that Γ^* as calculated by Rosenfeld et al. (1998) is in very good agreement with the result generated using the computational approach outlined above, in terms of both the Γ^* growth rate and the asymptotic value after discharge terminates at $T^* = 6$, further validating the viscous dissipation model adopted in the current numerical methodology. Figure 2.6 shows important characteristic quantities such as ring trajectory, self-induced propagation velocity, u'_z, and vorticity distribution in the vortex core. These quantities were obtained by replicating the inlet velocity programme from the experimental work described in Chapter 5. The figure demonstrates a good agreement between the experimental and numerical results.

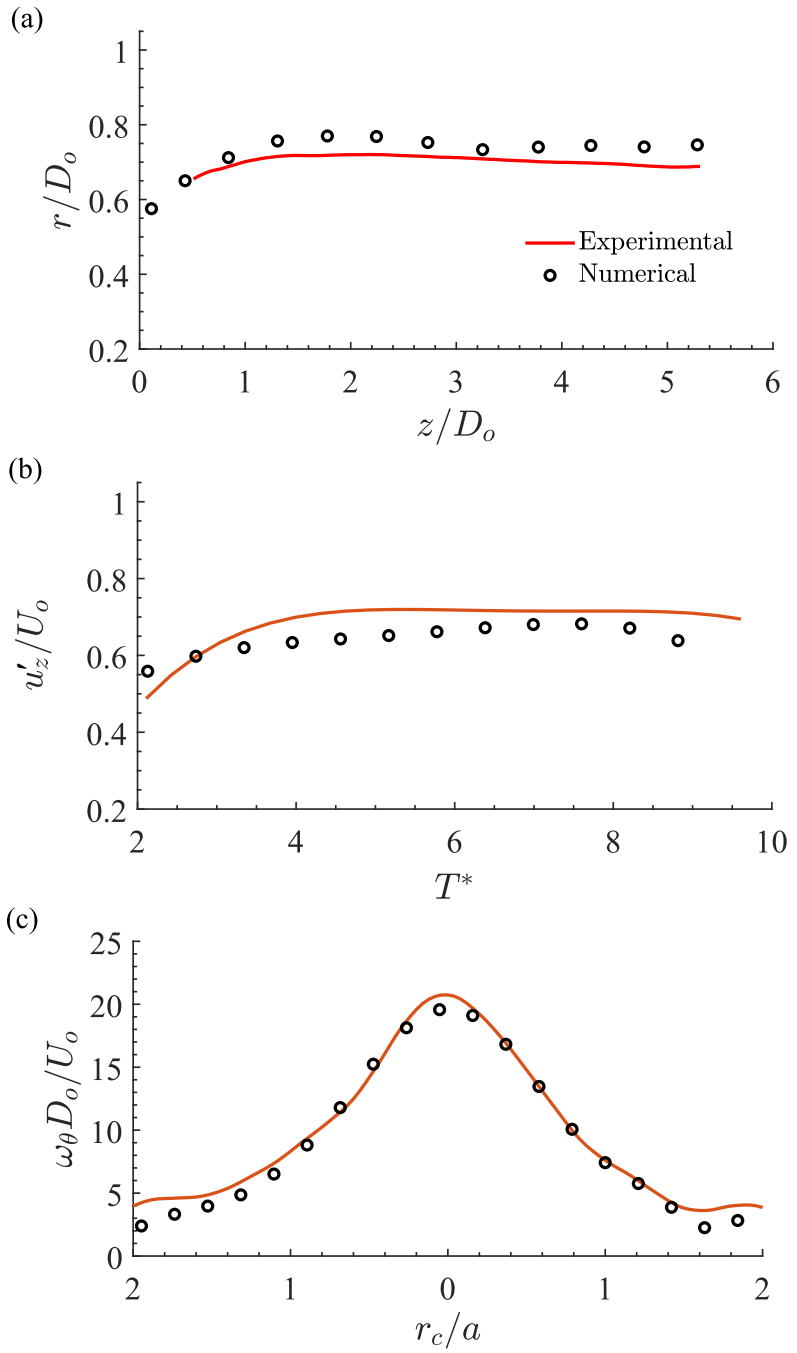

Figure 2.6: Comparison between numerical and experimental work, with inlet conditions and velocity program set to match experimental work for a single ring (L/D=4) as discussed in Chapter 5. (a) the trajectory of one of the vortex cores, (b) propagation velocity, and (c) vorticity distribution at the core at $T^* = 4.5$ and where r_c is the local radial coordinate with $r_c = 0$ at the core centroid; a is the time-dependent characteristic core radius, as defined in section 3.3.6

2.3 Experimental methodology

Few studies have been undertaken related to vortex rings with swirl primarily focused on theoretical or numerical analysis, while to the best of the author's knowledge only three experimental studies have been published addressing the production of swirling vortex rings, each utilizing different swirl arrangements. Chronologically, the first of them was conducted by Verzicco et al. (1996),see Figure 2.7 (a), who created a vortex ring by pushing a specific amount of fluid through an orifice plate located in the wall of a water tank. The entire apparatus was placed on a rotating table capable of achieving a range of angular velocities from 0.1 to 1 radians per second. Their study reports that rings produced with the above setup showed similar characteristics to those observed in previous theoretical or numerical investigations, such as a decrease in propagation velocity and the formation of negative vorticity[1] ahead of the ring. For rotation rates higher than a specific value, where the fluid discharged from the orifice no longer forms a vortex ring, Coriolis forces become dominant.

Later, Naitoh et al. (2014) produced swirling vortex rings with a piston-cylinder setup having an outer and inner acrylic cylinder as illustrated in Figure 2.7 (c). The outer cylinder, along which the piston moves, is fixed to the wall of the test tank; the inner rotating cylinder, which penetrates into the surrounding fluid bulk is connected by a timing belt to a stepper motor located at the top of the tank. A dividing screen was positioned close to the nozzle exit to isolate any unwanted vorticity generated by the timing belt.

For each experiment, the pipe was rotated at angular velocities ranging from 0 to 3π radians per second for 15 seconds before the piston stroke. Finally, He et al. (2020b) opted to utilize axial swirlers consisting of 12 vanes placed at the nozzle exit; Figure 2.7 (b), with the trailing angle of these vanes determining the angular velocity added to the flow. Even though the axial swirlers instantly produced a flow close to a solid body rotation, it simultaneously contaminated the flow leading to turbulent vortex rings.

[1]This refers to azimuthal vorticity with the opposite sign to that of the ring ($\omega_\theta < 0$).

The methods discussed above each have their own advantages and disadvantages, which influence the characteristics of the swirling vortex ring under investigation. Below, a different arrangement for the apparatus and experimental methodology employed in the work reported in this thesis –see Chapters 4 and 5– is reported that sets it apart from the above earlier studies.

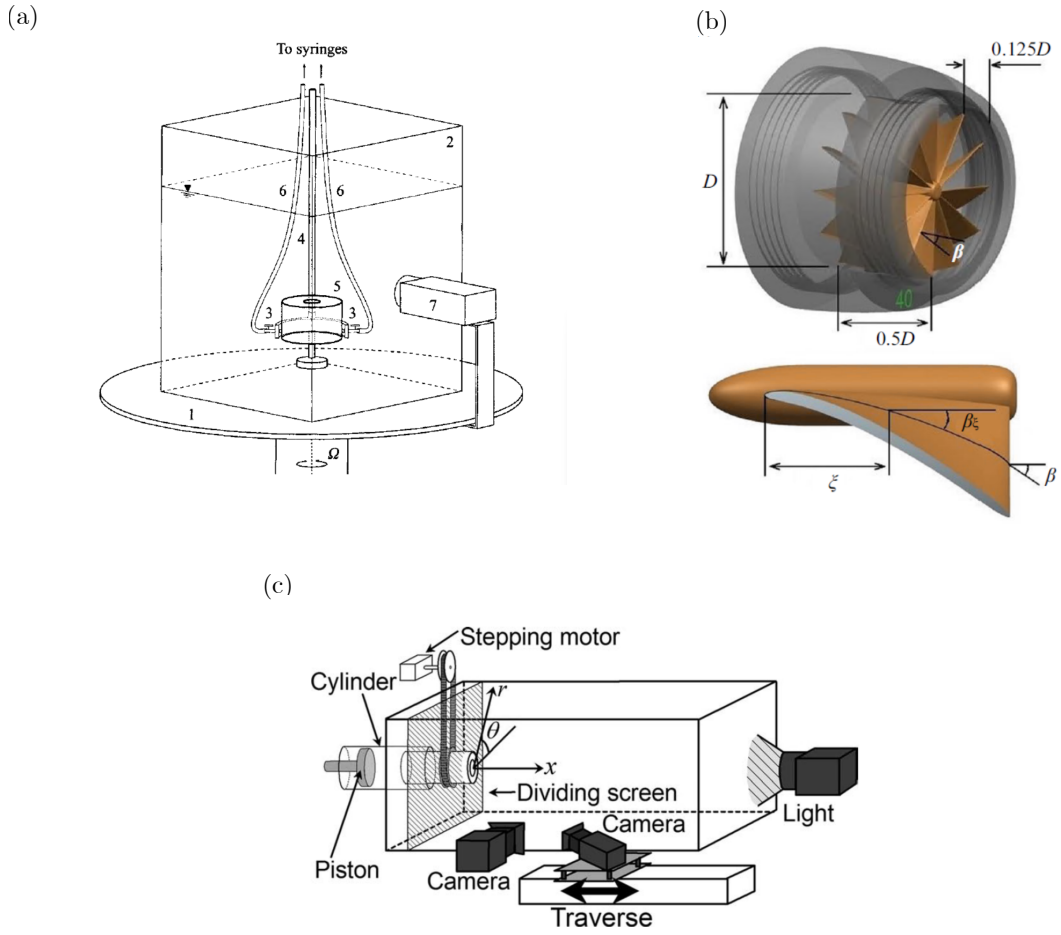

Figure 2.7: Schematic diagrams the rigs and swirlers of previous investigators (a) Verzicco et al. (1996); (b) He et al. (2020b); (c) Naitoh et al. (2014).

2.3.1 Apparatus

The experiments were performed in a stationary glass water tank of length 2400 mm, width 900 mm and height 800 mm, as illustrated in Figure 2.8. A piston-cylinder system, with a inner diameter of 40 mm and a thickness of 10 mm, was employed

to generate an impulsive fluid motion, but unlike previous associated experimental work, the system was not directly mounted in the water tank. Instead, it was connected to an external second system or swirl system, via two hoses that imparted azimuthal velocity to the discharged flow.

The swirl system, shown schematically in Figure 2.8 (b,c,d), consisted of a 450 mm long perspex tube of diameter of 42 mm and thickness 8mm passing through and fixed to the wall of the water tank. Inside the tube is an internal arrangement able to rotate smoothly and whose axis is concentrically aligned. The internal arrangement consists of four sections, as shown in Figure 2.8 (d).

- A rotor connected to a stepper motor, labelled M-2 in the Figure 2.8 (b,c).
- A 100 mm long pipe section with an outlet diameter of 25 mm containing a sequence of six holes distributed lengthwise on its surface and at 60° interval of rotation, through which enters the water from the piston-cylinder system to the rotation pipe.
- A 90 mm long and 32 mm inner diameter divergent nozzle whose purpose is to increase the azimuthal velocity by increasing the diameter of the rotating pipe.
- A perspex tube with the same inner diameter as the nozzle exit and a length of 200 mm whose purpose is to study the flow inside the rotating pipe.

Most of the swirl system sections are push-fit, except for the connection between the rotor and the 100 mm pipe. Two grub screws were placed between the perspex tube and the nozzle to ensure the system rotates homogeneously. To maintain alignment of the internal system, a PTFE bearing and rubber O-ring are placed within the 100 mm tube before the nozzle and 20 mm before the exit of the outer tube, respectively. These components also help to prevent fluid from the piston-cylinder system flowing into the gap between the outer tube and the 200 mm long perspex tube and reaching the water tank.

The swirl system protrudes approximately 250 mm into the tank, and to which a perspex disc of 320 mm diameter is attached to the exit of the outer tube via a

push-fit assembly at the edge. A 32 mm diameter orifice D_o was manufactured by laser cutting, ensuring concentricity with the orifice and proper alignment with the 200 mm perspex tube at the exit. A 1 mm gap was left between the inner perspex tube and the disc to allow free rotation. The use of a honeycomb was considered as an alternative because it facilitates faster establishment of the velocity distribution as a solid body rotation contrary to relying on diffusion from a rotating perspex tube (Liang and Maxworthy, 2005). However, the honeycomb was found to generate noise in the system resulting in unstable vortex rings; for that reason, it was ultimately discarded.

For the experiments, two stepping motors were utilized: one for the piston-cylinder system, M-1, and one for the swirl system, M-2 see Figure 2.8 (b). The M-1 motor governs the piston's movement, which in a previous study (He et al., 2020b) attained a speed of 0.5 m/s with an acceleration of 25 m/s^2. In the current experiments, the maximum speeds required were 0.04 m/s with a maximum acceleration of 0.4 m/s^2, which are significantly lower. The piston motion was controlled by the software Motion Perfect 5 from TRIO Ltd., which uses BASIC language to implement a velocity programme and add information from external devices. The communication between Motion Perfect and the stepper motor and the reading of external signals was performed by a Smartdrive Ltd. (SA28) driver. The M-2 used to create the solid-body rotation is controlled by an Arduino board Ldt. The Arduino interface uses C++ to handle the velocity program as well as reading and writing external signals. Communication with the M-2 is facilitated through the driver MA860H.

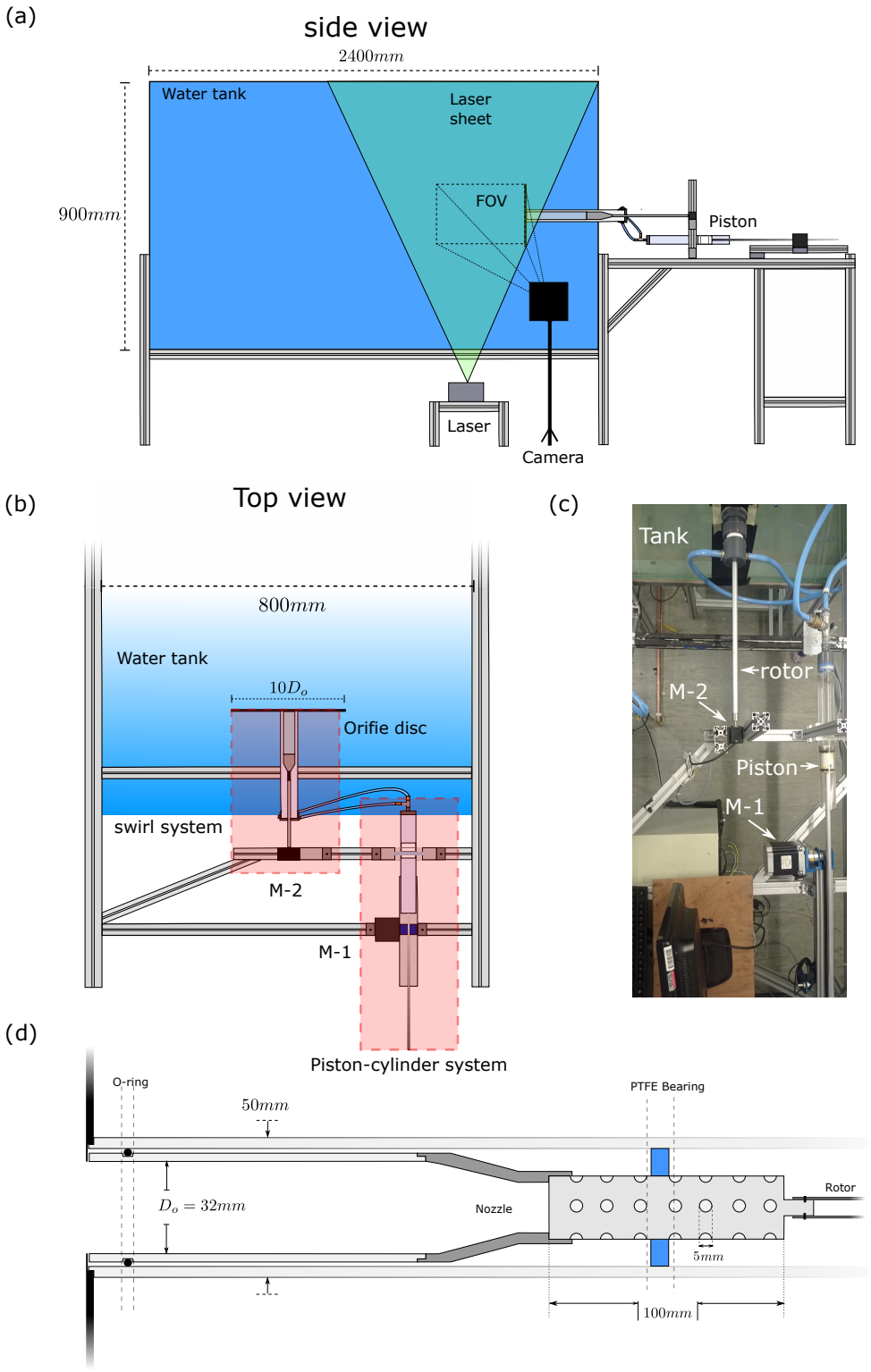

Figure 2.8: Illustrative schematics of the experiment setup. (a) Side view of the 2D PIV arrangement for the experiments discussed in Chapter 5, (b) Top view with the piston-cylinder and swirl systems highlighted in red, (c) picture of the top view, (d) internal arrangement of the swirl system.

2.3.2 Flow visualisation and PIV

The study employed two-dimensional and stereoscopic PIV (Particle Image Velocimetry) to obtain the velocity field with two and three components on a specific plane, in a non-invasive way. To achieve this, it requires an illumination source, one high-speed camera for two-dimensional and two cameras for stereoscopic PIV, seeding particles with a similar density to the working media and of a suitable size to minimize distortion in the flow, and a timing circuit. The precision of the method is primarily determined by the PIV's temporal resolution Δt, which is the time interval between successive frames used to calculate the velocity field.

To determine the displacement and velocity vector, particles from an interrogation window, which is obtained by gridding the field of view (FOV), with a time difference of Δt are compared through cross-correlation to find the best match between two-time steps. However, only one vector is calculated for each grid, with the interrogation window's size defining the spatial resolution of the PIV. If the Δt chosen is too big, or the interrogation window too small, particles at the initial time will not appear in the interrogation window at the next time step, leading to incorrectly calculated velocities vectors. This also emphasizes the significance of suitable particle seeding in the flow. Silver-coated hollow glass spheres with a diameter of $10\mu m$ were used as seeding particles for all experiments performed in the present work.

Two-dimensional PIV

This technique is used for the experiments discussed in Chapter 5 and the first section of Chapter 4 to obtain the velocity of the flow. The arrangement for the experiments in Chapter 4 is that of Figure 2.8 (a). A continuous laser (Beijing SUM Laser Technology Co. Ltd.) is used as an illumination source and located at the bottom of the water tank, emitting a beam of 532 nm wavelength (green) with a power of 5 Watts. A lens generates a laser sheet with an estimated thickness between $1-2$ mm covering the entire FOV at the central cross-section of the tank that runs parallel to the tank wall and intersects with the orifice. The tank was filled with tap water and kept at a temperature of around 18 $^{\circ}C$ during the experiments, having a

kinematic viscosity $\nu = 1.054\ mm^2/s$.

A four-megapixel high-speed camera Mini WX Photron Ltd. is used to obtain the images, providing up to 2048×2048 pixel resolution at 1080fps. This study used a 250 Hz frame rate, equating to a PIV Δt of 4 ms with a resolution of 2048×1536 pixels, giving a FOV of $7D_o$ x $4.4D_o$ as shown in Figure 2.8 (a). Estimation of the PIV Δt is based on the average velocity at the orifice U_o as well as an interrogation window of 16×16 pixels. The raw images were analysed by the software DaVis 7.2 to obtain velocity fields with an overlap size of 50%, giving a spatial resolution of 0.86 mm based on vector spacing. A 300 $mm \times 300\ mm$ metallic plate, as shown in Figure 2.9 (a), was used to calibrate the software. The plate is black and has a grid of white dots with a diameter of 2 mm distributed on its surface and separated by 20 mm each other, forming a 2D cartesian coordinate system. Even though it is not appreciated in Figure 2.9 (a), the calibration plate has two depths. For every couple of white dots columns, one is about 2 mm deeper. This allows the software to include all the particles illuminated by the laser sheet with approximately the same thickness.

The first set of experiments in Chapter 4 aims to study the flow inside the rotation pipe from the swirl system discussed in section 2.3.1. To achieve the desired FOV as is shown in Figure 2.9 (b), the camera had to be positioned no more than 1 meter away from the orifice disk. To make this possible, the water tank was emptied and a small tank was added around the pipe emerging from the main tank. In this case, FOV is represented by a square with a length of $2.17D_o$ and a resolution of 1024×1024 pixels, with the perspex tube at the centre (see Figure 2.9(b)). For the purpose of estimating the PIV Δt, the interrogation window previously utilized in the experiments from Chapter 4 is now applied. In this instance, the maximum azimuthal velocity $u_\theta(D_o/2)$ is being utilized instead as the characteristic velocity giving a Δt of 20 ms which means a 50 Hz frame rate with a spatial resolution of 0.54 mm based on vector spacing. A perspex disc of 30 mm diameter with a grid sticker was placed inside the 200 mm long tube to calibrate the software. For both experiments discussed above, each case studied had five repetitions, and the resulting vector fields were averaged to reduce the vorticity noise created in the

background.

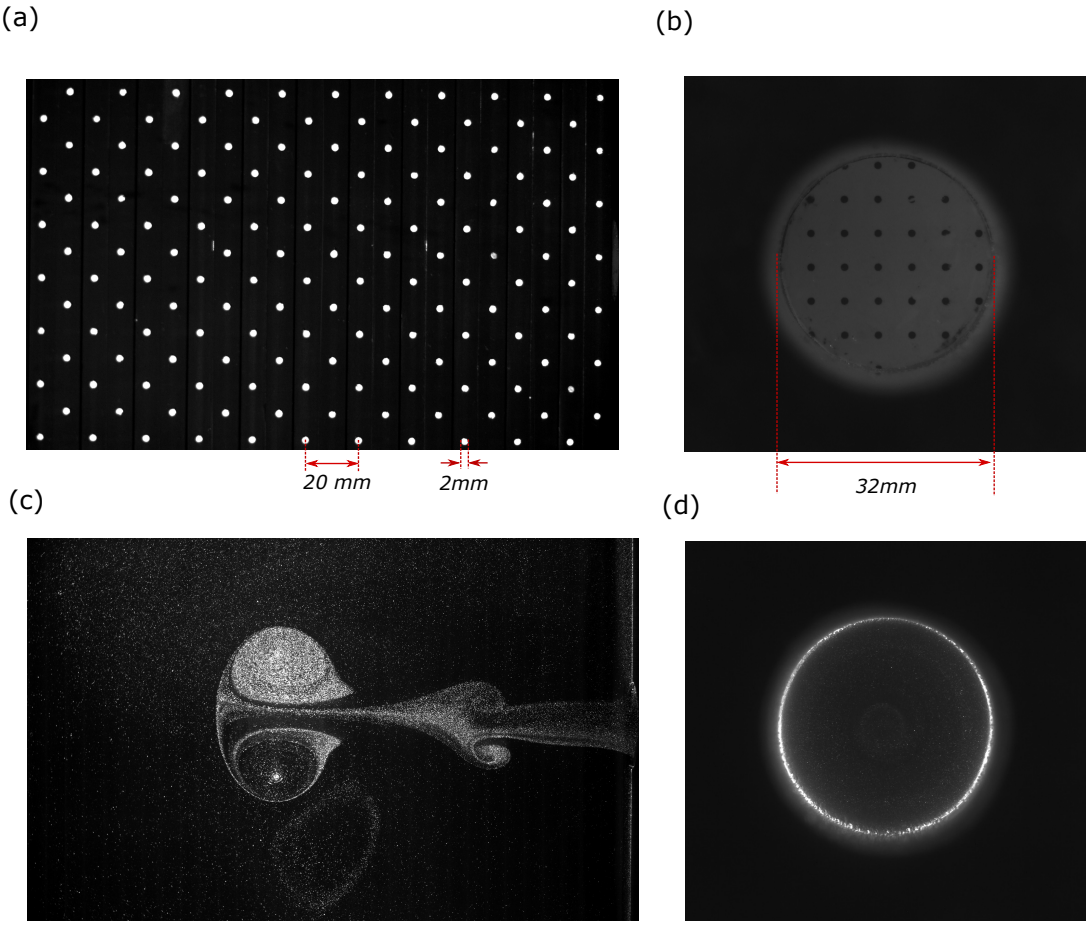

Figure 2.9: Calibration plates and FOV employed for the two-dimensional PIV, where the seed particles are illuminated by the laser. For the experiments in (a,c) Chapter 5 and (b,d) Chapter 4

In order to achieve a successful PIV, it is crucial to ensure that all devices involved are operating with the same clock. To accomplish this, a synchronizer NI BNC-2121 created by National Instruments Ltd. is utilized. This device can receive a Transistor-Transistor Logic, TTL, input signals and, with the assistance of LabVIEW, can control other devices through TTL output signals. For all the experiments performed in this work, the initial time is established through the movement of the piston. As explained in section 2.3.1, the driver used for M-1 has the ability to send digital outputs. A BASIC code in MotionPerfect is used to send an output signal 1 ms after the piston's initial displacement. This signal serves as the trigger that starts the time for the other devices connected to the synchronizer.

During the two-dimensional PIV experiments, the synchronizer produces two outlet signals in response to the trigger signal it receives as illustrated in Figure 2.11 (a). The first signal, a rectangular pulse lasting for 1 ms, has a chosen frequency based on the time step required to study the evolution of the flow. This signal is directed towards a high-speed camera set in "Random reset" mode. This mode captures three consecutive images with a time step equivalent to the chosen PIV Δt every time it receives a pulse. The second signal targets the continuous laser, but unlike the camera signal that acts as a trigger, the pulse length and frequency of the laser signal control when the laser works and, consequently, the amount of light captured by the camera. Another difference compared to the first signal is that the pulse frequency is the same as the inverse of PIV Δt. This means that the laser works even when the camera is not recording but ensures that the laser is on every time the camera works (Figure 2.11 (a)). Although two frames per pulse are sufficient to calculate the velocity field, three frames were compared in case the acceleration vector was needed. However, this was not to be the case, so only the velocity field obtained from the transition between the second and third frame is analysed in Chapter 4.

Stereoscopic PIV

Stereoscopic PIV is a technique similar to two-dimensional PIV. It calculates the velocity field on a plane (FOV) and also considers the velocity component that moves across the plane. This requires the use of a different laser that can resolve the third direction, as the laser sheet generated by the continuous laser is not thick enough. Additionally, a second high-speed camera is required. To track particles in the normal direction of the FOV, the cameras must be angled in relation to the surface of the water tank's normal vector, as illustrated in Figure 2.10 (b). Two perspex prisms were situated near the cameras on the side walls of the water tank. The surfaces of the prisms facing the camera were positioned parallel to the lens surface to reduce any refraction-related disruptions. The prisms were filled with water, including the tiny gap between the prism and the tank wall. It's important to note that the refractive indices of water and perspex are similar.

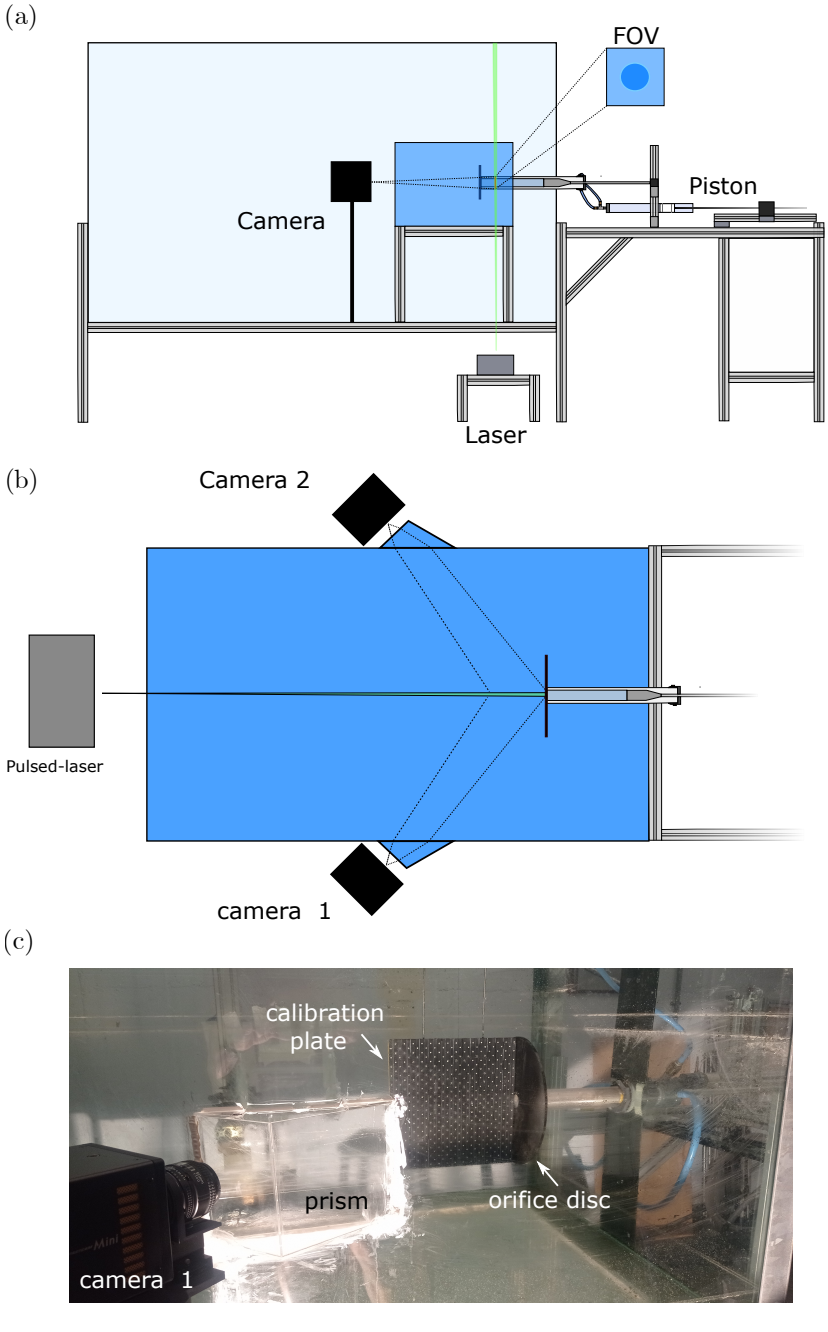

Figure 2.10: Illustrative schematic of the arrangement used to perform the experiments from Chapter 4: (a) to investigate the azimuthal velocity inside the rotating pipe via a 2D PIV whose FOV is shown in the top right; (b) to investigate vortex rings with swirl where two cameras were implemented to perform a stereoscopic PIV. (c) Picture of the arrangement used for the calibration in the stereoscopic PIV

The location of the FOV is the same as the one discussed above section 2.3.2, with a size of $6.8D_o \times 6.8D_o$ and a resolution of 1536×1536. In these experiments, the second motor (M-2) is utilized to impart azimuthal velocity to the vortex rings. To ensure synchronization between both stepping motors, a signal from the M-1 driver is sent directly to the Arduino board, which functions as a trigger for the M-2 motor. An illumination device (Oxford Lasers Ltd.) was used that can produce two pulsed laser beams with a power of 1.5 W and a wavelength of 532 nm (Green), with a pulse repetition rate of 15 Hz. Figure 2.11 (b) illustrates how the synchronizer generates four TTL signals for the laser device, with two signals per laser (trigger and Lamp).

The power of the laser beams is controlled by the time delay between each trigger and Lamp signals named Q, which was set to 0.19 ms for both lasers based on previous experiments (He et al., 2020b). The two laser beams are required because the pulse repetition rate of 15 Hz (60 ms) is too large to be considered as Δt. Therefore, each laser beam illuminates one of the two frames required to compute the velocity field. This is illustrated in Figure 2.11 (b), where the time difference between the laser's trigger signals has to match with the chosen Δt.

Two PIV Δt values were computed to establish the temporal resolution, one for axial displacement and another for the third direction. After analyzing both, the chosen PIV Δt was 20 ms, corresponding to the axial displacement with the lowest value. To ensure that the particles moving in the third direction were accurately measured during the PIV Δt selected, the laser sheet thickness was set at 4 mm, which allowed the particles to displace a quarter of the sheet's thickness (Gan, 2010). The interrogation window was configured to have dimensions of 32x32 pixels with a 50% overlap, resulting in a spatial resolution of 1.7 mm based on vector spacing. The same calibration plate discussed earlier was used. The white dot grid is present on both sides of the plate, which facilitates the calibration of both cameras. One specific dot must be selected on one side and its corresponding dot from the other side. This enables the software to merge both images and calculate the third velocity component that is perpendicular to the plate. For this experiment, six repetitions were performed for each case studied.

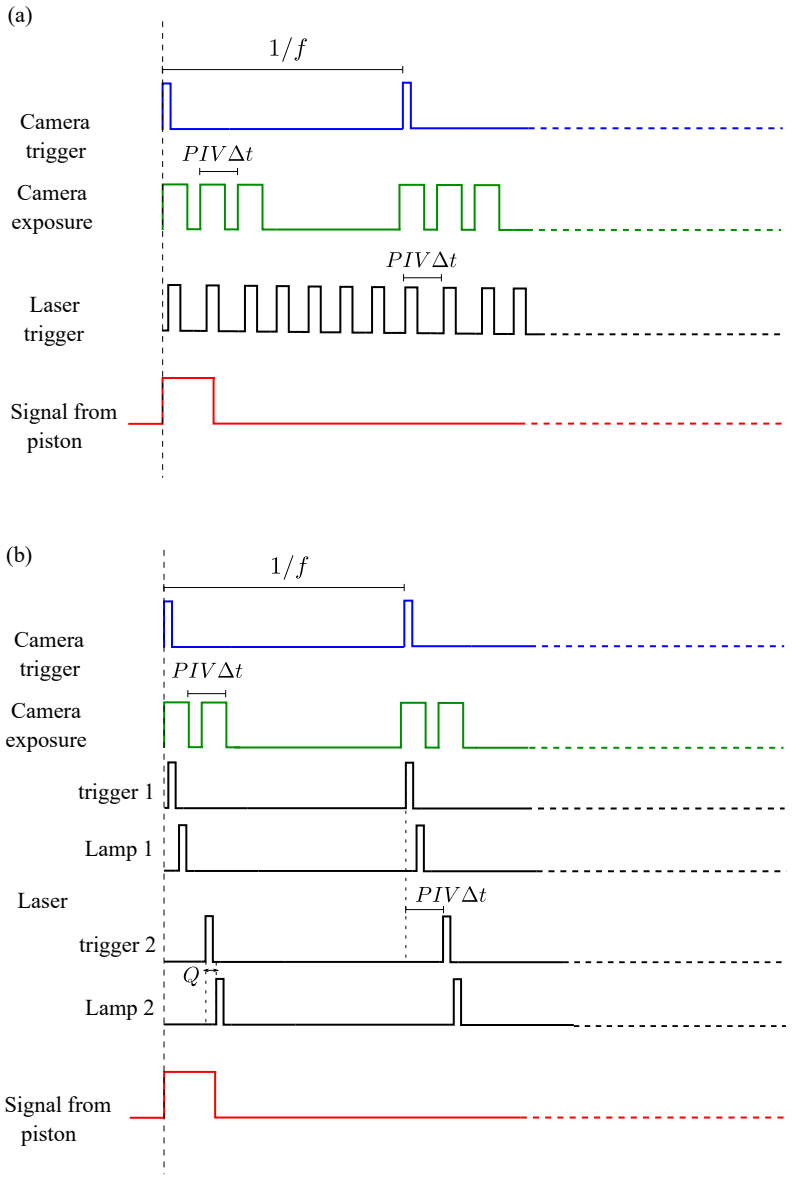

Figure 2.11: Timing programme controlled by the synchronizer for (a) Two-dimensional PIV and (b) Stereoscopic PIV. f is the frequency of the signal.

CHAPTER 3

Formation and evolution of vortex rings with weak to moderate swirl

3.1 Introduction

A swirling vortex ring exhibits certain characteristics, including an expansion of its radius while its propagation speed decreases, the creation of negative azimuthal vorticity in front of the ring, and a lower formation number F. Even though previous studies have examined each of these attributes, their origin and relationship to each other remain uncertain. The overarching aim of this Chapter is to study theoretically the influence of the addition of swirl on the global flow dynamics of impulsively generated vortex rings, in particular in relation to their formation process and early time evolution.

3.2 Problem formulation

3.2.1 Flow geometry and boundary conditions

The flow geometry employed in the investigation consists of a horizontally aligned cylindrical domain, open at one end, with a concentrically aligned inlet, centred on $r = 0$, at the other, as shown in Figure 2.4 (a), mimicking a sufficiently large but finite sized confinement typical of a corresponding laboratory-based experimental set-up. For reasons outlined subsequently, two different inlet geometries, denoted Case A and B – see Figure 2.4 (b) – are explored for the generation of swirling vortex rings.

Incompressible, Newtonian fluid (density, $\rho = 1000\ kg/m^3$, kinematic viscosity $\nu = 1 \times 10^{-6}\ m^2/s^2$) is impulsively discharged from the inlet, of diameter $D_o = 25$ mm, into the same bulk fluid at rest occupying an adjoining cylindrical domain, of diameter $10D_o$ and length $20D_o$. These dimensions are sufficient to ensure the proximity of the confining boundaries will have no effect on the solutions obtained (Danaila et al., 2015), the case S = 1 representing a worst case scenario. To this end the adequacy of the domain size is reinforced in Chapter 3 where it is shown that the growth rate of the vortex ring core radius increases with swirl strength. The maximum radial coordinate of the ring core for S = 1, is $\approx 1.5D_o$, for the time duration of interest, which is sufficiently far away from the confining surface of the cylindrical wall, i.e. the induced velocity on this surface from the ring circulation is negligible at this distance.

The geometry and dimensions of the computational domain used in the numerical work try to emulate a circular water tank where one of its plane walls has an inlet at the centre. Two inlet geometries are considered, named Case A and Case B, which will be discussed later.

At time $t = 0$ seconds, the fluid in the entire numerical domain is at rest. The inlet condition is solid body rotation, which means that $u_\theta = \Omega r$ (see Figure 3.1) where Ω is the angular speed (rad/s). Both axial, z, and swirl, θ, momentum at the inlet surface are initiated and terminated impulsively with infinite acceleration and deceleration, respectively. The velocity programme is illustrated in Figure 3.1.

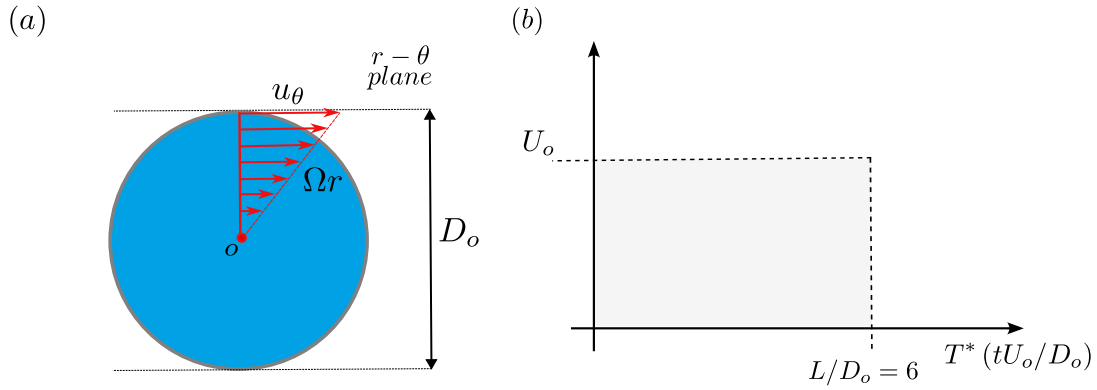

Figure 3.1: (a) solid body rotation velocity distribution at the inlet and (b) the impulsive velocity programme used to generate all the vortex rings analysed in this section.

For the axial component, uniform and constant velocity is applied over the inlet surface, $U_0 = 0.1\ m/s$, and independent of r or θ as shown in Figure 2.4 (b). The attendant boundary conditions comprise of no-slip everywhere other than at the inlet and outlet; for the latter, being sufficiently distant from the inlet, satisfaction of a zero-gradient constraint is specified. To compute the turbulent viscosity at the wall, the "nutUWallFucntion" was implemented based on y^+. Additionally, regarding the inlet turbulence, it should be noted that the initial estimation of κ_{in} is 2.5×10^{-5}, which is based on the following equation:

$$\kappa_{in} = \frac{2}{3}\left(|u|I_t\right)^2. \tag{3.1}$$

This estimation results in a turbulence intensity, I_t, of approximately 4%, which can be considered a medium intensity suitable for internal low-speed flows such as pipes (Greenshields and Weller, 2022). To investigate the formation process and the dependence of the vorticity entrainment capability of the leading ring on swirl strength, the fluid discharge time is set as equivalent to $L/D_o = 6$, a constant. L is computed as $L = U_o t_s$ where t_s is the stroke time. This produces a flow that is of a starting jet type, allowing determination of its influence on the roll-up of the trailing jet, or the wake flow behind the primary leading ring. Orifice based and slug circulation, Γ_{slug}, –see equation (1.4) based Reynolds numbers can be defined,

regardless of swirl strength, as:

$$\mathrm{Re} = \frac{U_0 D_o}{\nu} = 2500, \quad \text{or} \quad \mathrm{Re} = \frac{\Gamma_{\mathrm{slug}}}{\nu} = \frac{U_0^2 t_s}{2\nu} = \frac{U_0 L}{2\nu} = 7500, \tag{3.2}$$

respectively. Here, Re is taken to be 7500, the same as that in the work of Rosenfeld et al. (1998).

Swirl is generated as a solid-body rotation at a rate $0 \leq \Omega \leq 8$ (rad/s); based on which the dimensionless swirl number S is defined here as:

$$\mathrm{S} = \frac{\Omega R_o}{U_o} = \frac{\Omega D_o}{2U_o}, \tag{3.3}$$

where $R_o = D_o/2$ is the orifice radius. The above definition of S is in line with that adopted in Liang and Maxworthy (2005) for their continuous swirling jet experiment. The S spectrum investigated in the present work is S = 0 (non-swirl) and S = $1/4, 1/2, 3/4, 7/8, 1$, spanning the regimes of weak swirl to total vortex breakdown in a continuous swirling jet (Liang and Maxworthy, 2005).

Returning to the matter of the different inlet geometries investigated, Case A resembles the orifice exit geometry utilised in the experiments of Gan (2010), where a large no-slip circular surface is placed flush with the exit of a short nozzle at $z = 0$. The inlet surface is positioned at $z = -0.1D_o$ resulting in a nozzle length of $0.1D_o$. This length has been carefully chosen to imitate a realistic experimental configuration: on the one hand, since swirl is also fluxed through the inlet plane, rolling-up of the non-swirl fluid volume inside this nozzle at the start of the discharge needs to be minimised; on the other hand, the quiescent fluid in the region $z > 0$, before the start of discharge, should be minimally affected by momentum diffusion from the fluid in (solid-body) rotation preparation, which can often be realised by a physically rotating nozzle (Liang and Maxworthy, 2005; Naitoh et al., 2014).

In order to examine the impact of the short nozzle associated with Case A, on the swirl strength inside the rolled up ring structure, comparisons can be made with results obtained for a idealised inlet, an orifice with a nozzle of zero length, where the inlet surface is flush at $z = 0$, namely Case B (Rosenfeld et al., 1998). The source of vorticity in the vortex ring is different for the two cases. For Case A, it is from

the boundary layer which develops on the inner surface of the inlet nozzle section of length $0.1D_o$. Owing to Richardson's annular effect (Richardson and Tyler, 1929), in a typical pulsatile flow inside a short pipe this boundary layer is appreciably different from the one of a paraboloid velocity distribution in an otherwise fully developed and continuous flow in a long pipe. The superposed swirl component will also affect the boundary layer profile. In Case B, it is from the shear layer that develops between the discharge velocity (the vector sum of U_0 and ΩR_o) and the ambient fluid. In both cases, vorticity in the boundary layer that develops on the surface flush with the orifice exit plane (the $r - \theta$ plane) will also be washed out and entrained into the ring structure attributable to the induced velocity of the leading primary ring core during its early development, before it propagates away. These important features and their impact on the forming of the ring are discussed in section 3.3.2.

3.3 Results and discussion

The simulations were conducted on Durham University's supercomputer, Hamilton, using 24 processors and each second of simulation required approximately 40 hours of CPU time. It took 60 days to run all the cases discussed.

OpenFoam operates in Cartesian coordinates, but using cylindrical coordinates for this problem is more convenient. Matlab was used to transform the velocity and vorticity vectors from Cartesian to cylindrical coordinates. The equation below demonstrates how the value of u_θ was calculated, which can also be applied to find the value of ω_θ:

$$u_\theta = -u_x sin\left(\theta\right) + u_y cos\left(\theta\right), \tag{3.4}$$

where θ is the azimuthal angle in the x-y plane, u_x and u_y are the velocity components in a Cartesian coordinate system, (z, y, z).

3.3.1 Vortex structure comparison

Figure 3.2 provides a comparison of the associated vortex structure at different times during the evolution of the flow for swirl numbers S = 0 and 1, and inlet Case A; in which the leading, toroidally shaped primary ring is clearly identifiable together the wake, or trailing jet. Figure 3.2, lef-hand column, reveals that the primary ring core, when S = 0, remains almost perfectly axisymmetric for the duration of the simulation, and the absence of any negative vorticity ($\omega_\theta < 0$) in that $\omega_\theta > 0$ everywhere (denoted as red isosurfaces) – the opposite of what is observed in the remaining images, Figure 3.2, right-hand column, when S = 1, and which display a number of distinguishing features. First, significant regions of negative vorticity (denoted as blue isosurfaces) are found to exist surrounding the main vortex core at the times shown, and is indeed found to be present from the outset. Second, the flow structure loses stability at large time, Figure 3.2(d), manifesting as a wavy primary vortex core and a broken vortex structure in the azimuthal direction and featuring both positive and negative vorticity outside of the vortex core. At $T^* = 12$, a secondary vortex ring can also be seen which rolls up at the downstream end of the trailing jet when discharge stops. As discussed later, in section 3.3.6, the strength of this secondary ring depends on S, and has non-trivial impact on the growth of the leading ring circulation.

The amplitude of the wave along the vortex core can be estimated in terms of the degree of asymmetry of the core centroid, whose coordinates (R, Z) for a given θ plane can be obtained from:

$$R(\theta) = \frac{\iint \omega_\theta(\theta) r \, \mathrm{d}r\mathrm{d}z}{\iint \omega_\theta(\theta) \, \mathrm{d}r\mathrm{d}z} \quad Z(\theta) = \frac{\iint \omega_\theta(\theta) z \, \mathrm{d}r\mathrm{d}z}{\iint \omega_\theta(\theta) \, \mathrm{d}r\mathrm{d}z}, \tag{3.5}$$

where regions in which $\omega_\theta \geqslant \omega_\theta(\max)e^{-1}$ in the primary vortex core are assumed to contribute; here $\omega_\theta(\max)$ is the maximum ω_θ in the vortex core centre. the vorticity $\omega_\theta < 0$ is not considered for this calculation. Figure 3.3 examines the time evolution of the standard deviation, σ_R, of $R(\theta)$ for different representative swirl numbers and inlets Case A and B. σ_R is defined as:

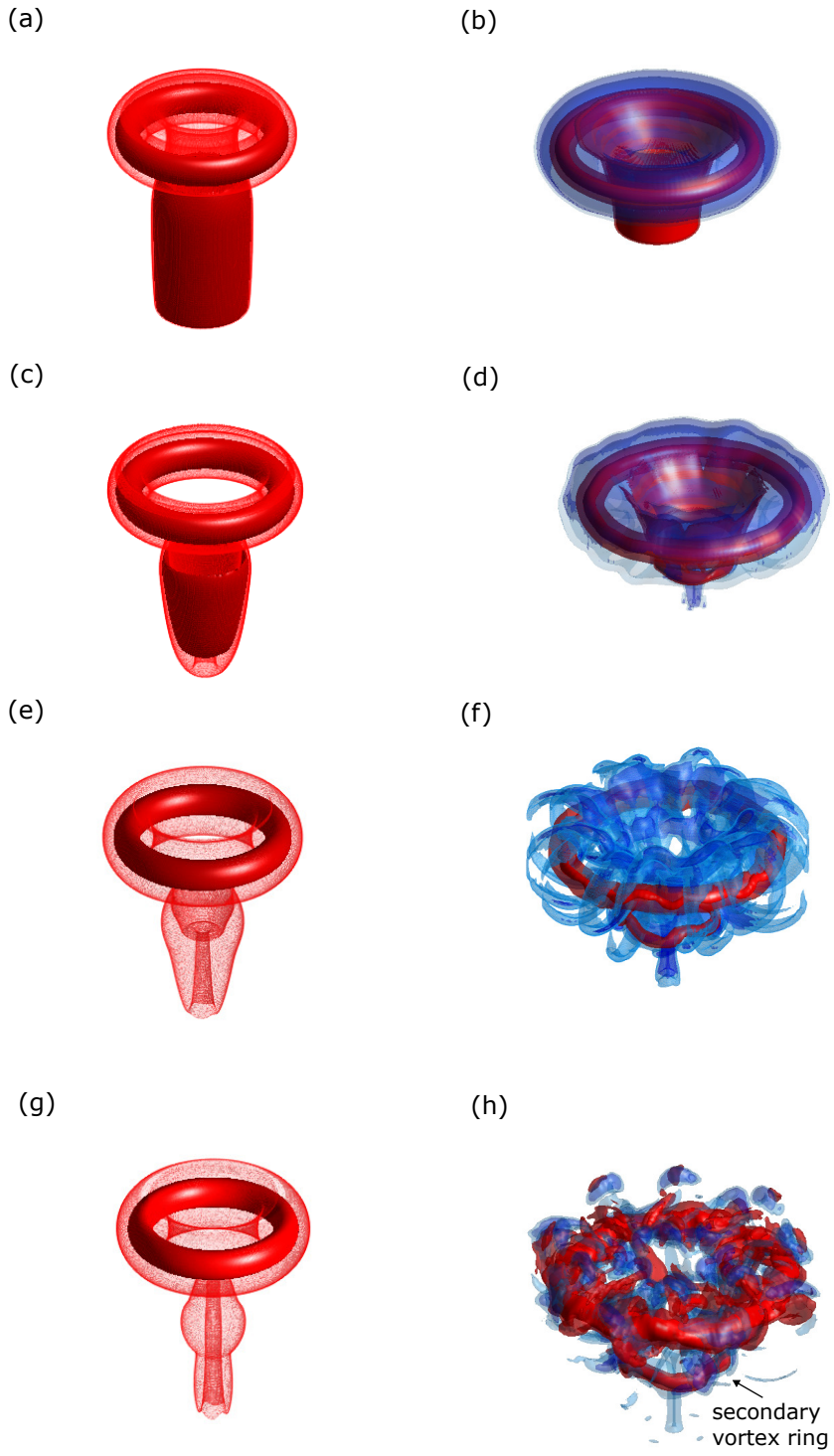

Figure 3.2: Vortex structure visualized, for swirl numbers S = 0, 1 and inlet Case A, as isosurfaces of $\omega_\theta D_o/U_o = [\text{levels} : -2.5, -1.25, 2.5, 5]$, with red and blue denoting positive and negative values of vorticity, respectively. (a) S = 0 at $T^* = 6$; (b) S = 1 at $T^* = 6$ (the moment the discharge stops), (c) S = 0, $T^* = 8$, (d) S = 1, $T^* = 8$, (e) S = 0, $T^* = 10$, (f) S = 1, $T^* = 10$, (g) S = 0, $T^* = 12$, (h) S = 1, $T^* = 12$.

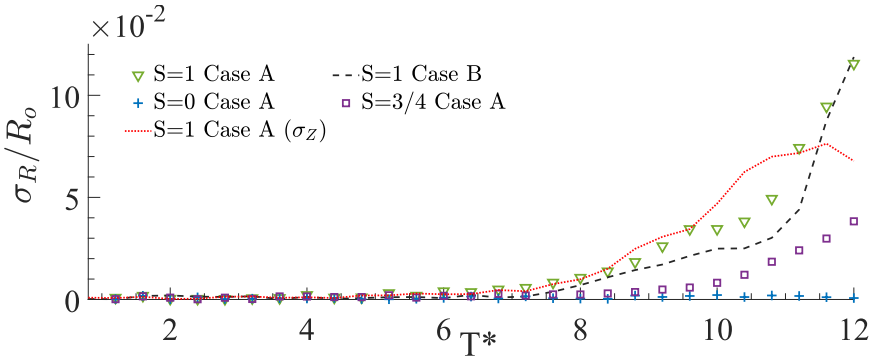

Figure 3.3: Evolution of vortex core asymmetry, expressed in terms of the standard deviation, σ_R, of $R(\theta)$ given by equations (3.5) (3.6) and for different S values and both inlets Case A and B. The dotted line represents the standard deviation of the axial position $Z(\theta)$.

$$\sigma_R = \sqrt{\sum_{i=1}^{n} \frac{\left(R(\theta) - \bar{R}\right)^2}{n}}, \tag{3.6}$$

where $\bar{R}$ is the azimuthal average ring radius and n represents every plane. Waviness is also reflected in the $Z(\theta)$ component, which is consistent. Note that the absolute ring radius R increases rapidly over time as S increases, as discussed in section 3.3.3, in particular for the case $T^* > 6$ and S $\geqslant 3/4$.

The primary core in Figure 3.2 (d) exhibits a wave number for the azimuthal asymmetry of $m = 3$, which is determined by spectral analysis of $R(\theta)$. The time dependence of the magnitude of the primary spectral peak also agrees well with that of σ_R. Accordingly, Figure 3.3 reveals that for the Re under investigation, core waviness develops to a noticeable level for $T^* > 8$, other than when S = 0 with experiments showing that azimuthal waviness does not develop until after very large time (Maxworthy, 1977). The corresponding temporal behaviour for S = 1 and inlet Case B, confirms that the loss of azimuthal symmetry is instability induced, which is not driven by the choice of inlet geometry. The amplitude of the waves, reflected by σ_R, increases with time, as well as S. Although the azimuthal instability will eventually lead to turbulence and breakdown of the vortex core; before this occurs the leading primary ring propagates downstream as a coherent structure – which is typically isolated and compact after it detaches from the trailing jet.

The dominant wave number m induced by instability depends non-linearly on S, and could also be time dependent. However it only becomes important at relatively large time (see the experiment of He et al., 2020a). The present study considers small time only; that is, before core waves develop significantly. As such, for $T^* \leqslant 12$, axisymmetric flow is a reasonable assumption, permitting the process of azimuthal averaging to reflect the global behaviour of these flows in their axisymmetric $r-z$ planes.

3.3.2 Distribution of azimuthal vorticity ω_θ

Regions of $\omega_\theta > 0$

As the dominant vorticity component in a non-swirling vortex ring, regions of $\omega_\theta > 0$ in a swirling ring reflect a weak dependence on S. They mainly originate as a consequence of a ω_θ flux from a modified boundary layer profile at an orifice exit, as in Case A. Figure 3.4(a) shows the dependence of the axial velocity u_z on r at the $z = 0$ plane when $T^* = 0.4$, which correctly replicates the Richardson's annular effect similarly observed in starting jets, where u_z becomes a maximum ($\approx 1.2U_0$) at $r \approx 0.95R_o$ outside of the boundary layer and a minimum ($\lesssim U_0$) at $r = 0$ satisfying mass conservation (Didden, 1979; Lim and Nickels, 1995). It also is related to the acceleration of u_z close to the orifice edge induced by the rolled-up vortex core at an earlier time, which increases the magnitude of $\partial u_z/\partial r$ and in turn that of ω_θ; see equation (1.3).

The flux of circulation associated with ω_θ through the orifice exit can be calculated, using equation (1.3), as:

$$\begin{aligned} \frac{\partial \Gamma}{\partial t} = \int_0^{R_o} \omega_\theta u_z \mathrm{d}r &= \int_0^{R_o} \left(\frac{\partial u_r}{\partial z} - \frac{\partial u_z}{\partial r} \right) u_z \, \mathrm{d}r \\ &= \underbrace{\int_0^{R_o} \frac{\partial u_r}{\partial z} u_z \, \mathrm{d}r}_{\Gamma(u_r)} + \underbrace{\frac{1}{2} u_z^2 \Big|_{r=0}}_{\Gamma(u_z)}. \end{aligned} \tag{3.7}$$

The second term in equation (3.7) is related to the slug model and is only connected to u_z at the axis ($r = 0$), since $u_z = 0$ at $r = R_o$. The dependence of u_r on r is

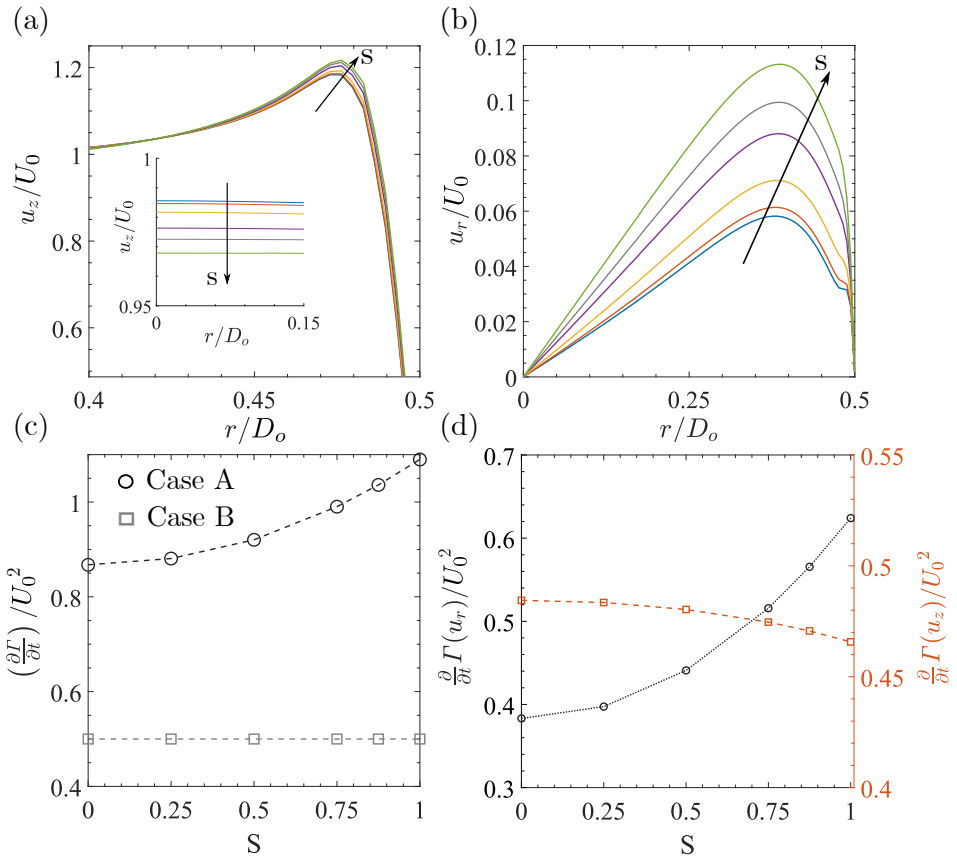

Figure 3.4: (a) Dependence of u_z on r at $z = 0$ [Case A]; for Case B, $u_z = U_0$, and independent of S. (b) Dependence of u_r on r [Case A]. (c) Dependence on S of the total circulation flux $\partial\Gamma/\partial t$ at $z = 0$ [Case A and B]. (d) Dependence on S of the total circulation components Γ_{u_r}, Γ_{u_z} defined in equation (3.7) [Case A]. The plots all correspond to $T^* = 0.4$ and the direction of the arrow in (a) and (b) indicates increasing S.

shown in Figure 3.4(b), where u_r is clearly non-zero at $z = 0$ owing to the velocity induced by the rolled-up vortex core (Didden, 1979). Nevertheless, it is an order of magnitude smaller than u_z. The total circulation flux $\partial\Gamma/\partial t$ through the orifice plane, shown in Figure 3.4(c), reveals a weak dependence on S for Case A only. Figure 3.4 (d) further reveals the effect of S on the production of $\partial\Gamma/\partial t$ for Case A. It can be seen also from equation (3.7) that adding swirl diminishes the contribution from $\Gamma(u_z)$, but increases that from $\Gamma(u_r)$. Although the contribution of $\Gamma(u_r)$ can be significant if the u_r profile is purposely manipulated (see Krieg and Mohseni, 2013, for example), the straight nozzle in Case A implies that it is moderate here.

For the idealised orifice, Case B, no surface is present for a boundary layer to develop, unlike Case A, and the $u_z(r)$ profile is independent of S at $z = 0$ which is exactly the inlet plane. Therefore no swirl induced ω_θ flux effect exists, as evidenced in Figure 3.4 c, where only the $\Gamma(u_z)$ term in equation (3.7) contributes. It is a constant for Case B and of similar magnitude to the same term for Case A. However, immediately outside the exit (e.g. at $z = 0.1D_o$) the primary ring core introduces a $\Gamma(u_r)$ effect which results in a similar dependence on S, as shown in Figure 3.4 (d), rendering the overall $\partial\Gamma/\partial t$ similar to that of Case A.

Profiles of the kind provided in Figure 3.4 (u_z, u_r and their associated circulation contributions $\Gamma(u_z)$ $\Gamma(u_r)$) are transient. The ones shown in this figure are for $T^* = 0.4$; a time when the primary ring is in the early stages of being formed and its location is very close to the orifice exit. The primary core imposes a strong influence on these quantities, which feeds back to the vorticity flux. This is a mutual process. When the leading ring propagates away (in both the z and r direction depending on S), its influence, especially the $\Gamma(u_r)$ component, fades as does $\partial\Gamma/\partial t$; hence, the growth of the total Γ in the flow domain (discussed later in section 3.3.6), tends to be steady. Compared to Case A, the steady shear layer (or trailing jet) outside of the orifice exit in Case B is thinner in general owing to the absence of the boundary layer effect present in the former, which results in slightly smaller $\partial\Gamma/\partial t$ and, more importantly, is more prone to instability (Zhao et al., 2000).

The overall effect also implies that the peak ω_θ in the vortex core centre is smaller for Case B than Case A and is less sensitive to S; for Case A, it increases weakly with

S at early formation time. This is supported by the findings shown in Figure 3.6, even after the absolute peak vorticity is scaled by the instantaneous ring radius $R(t)$; the rationale of choosing this scaling parameter is discussed next.

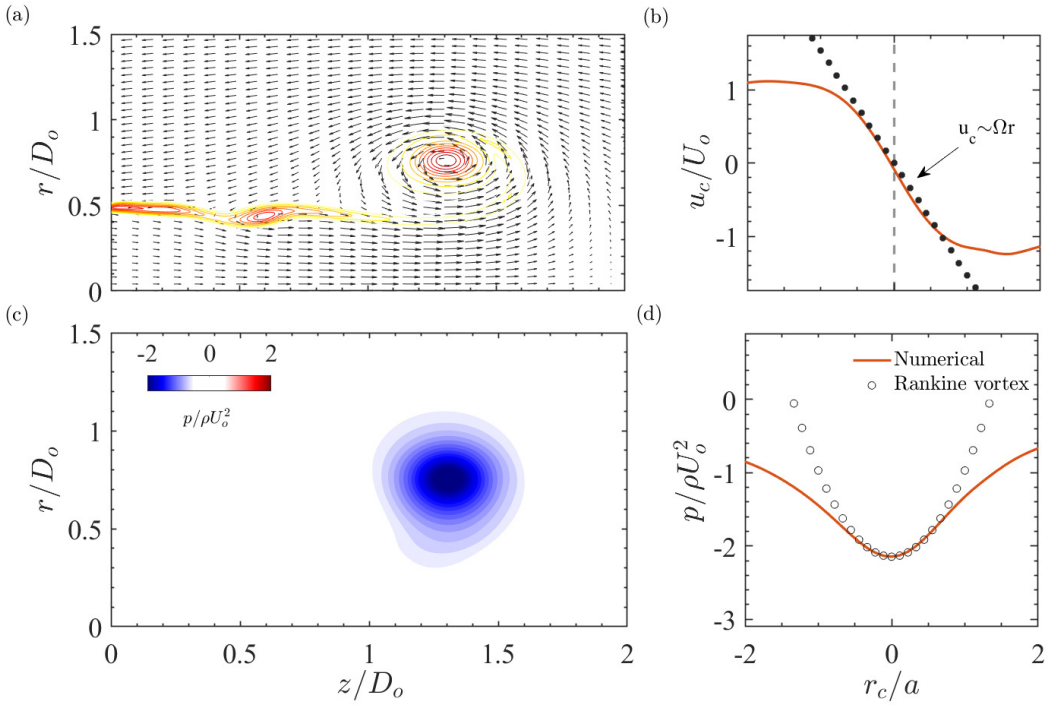

Figure 3.5: (a) Vector field and vorticity contour plot at $T^* = 3.8$ and $S = 0$. (b) Velocity distribution within the vortex core from a frame of reference moving with the ring and where r_c is the local radial coordinate with $r_c = 0$ at the core centroid; a is the time-dependent characteristic core radius, as defined in section 3.3.6 and Ω is the angular speed for the approximate solid body rotation velocity. (c) pressure contour plot. (d) Comparison between the Pressure distribution within the vortex core and the Rankine vortex.

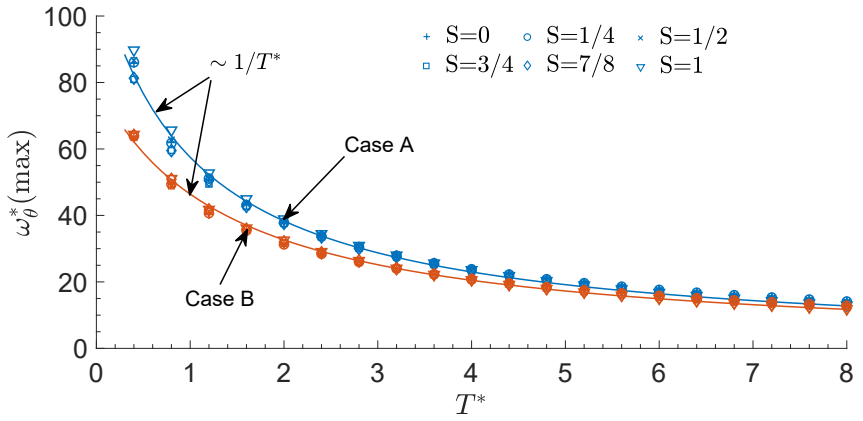

Figure 3.6: Evolution of $\omega_\theta^*(\max)$, the scaled peak vorticity in the ring core centre, for different S. The solid lines are fitting function $\omega_\theta^*(\max) \sim (T^* - T_0^*)^{-1}$, where $T_0^* = -1$ and -1.37 for Case A and B, respectively, are virtual time origins.

Soon after the vortex core is formed, roll-up of ω_θ in the vortex sheet from the orifice wraps around the outside of the core, leaving the core largely unaffected and remaining Gaussian like (Saffman, 1975, 1995). The flow distribution within the vortex core exhibits similar characteristics to a Rankine vortex. Although the vorticity distribution is not constant like in the Rankine vortex, it has a solid body velocity distribution as observed from the velocity field in Figure 3.5(a) and plotted in Figure 3.5(b). A region of low pressure – see Figure 3.5(c) – generates the centripetal force to maintain this distribution, as per the equation:

$$\frac{\partial p}{\partial r} = \rho \frac{u_c^2}{r} \sim \rho \Omega^2 r, \tag{3.8}$$

where u_c is the velocity distribution in the core in a frame of reference moving with the vortex ring and whose origin is at the core centre. Ω denotes the angular speed that corresponds to the approximate solid body rotation distribution. The pressure distribution within the core shows good agreement with the Rankine vortex model compared in Figure 3.5(d) for $r_c/a \leq 1$, where a is the core radius defined in section 3.3.6.

In the absence of swirl and assuming the curvature of the toroidal core to be negligible (i.e. R large), the distribution of $\omega_\theta(r,t)$ in the moving frame of reference centred at the core for an infinitely long vortex tube can be approximated by a Lamb-

Oseen vortex (Fukumoto and Moffatt, 2000; Saffman, 1978; Weigand and Gharib, 1997), which is a solution of the generalised vorticity equation:

$$\frac{\partial \omega}{\partial t} = \nu \left(\frac{\partial^2 \omega}{\partial r^2} + \frac{1}{r} \frac{\partial \omega}{\partial r} \right). \tag{3.9}$$

following the initial and boundary conditions:

$$\omega(0,0) = C_o, \quad \omega(0,t) = 0, \quad \omega(\infty,t) = C_o, \tag{3.10}$$

equation 3.9 lead to an exact solution of the form:

$$\omega(r,t) = \frac{C_o}{4\pi\nu t} \exp\left(-\frac{r^2}{4\nu t} \right) = \omega(0,t) \exp\left(-\frac{r^2}{r_c^2} \right), \tag{3.11}$$

where $\omega(0,t)$ is the peak ω_θ in the core centre and r_c the core radius. Here a local coordinate system is adopted with $r = 0$ at the centre of the vortex core, instead of the orifice geometry. Assuming that the circulation of the vortex core Γ_c, which is related to the peak vorticity $\omega(0,t)$ via

$$\Gamma_{Ring} = \int_0^{r_c} 2\pi\omega(0,t) \exp\left(-\frac{r^2}{r_c^2} \right) r \, \mathrm{d}r = \pi r_c^2 \left(1 - e^{-1} \right) \omega(0,t), \tag{3.12}$$

is constant, implies that there is no dissipation of vorticity.

The time varying volume $V(t)$ of this toroidal core, if assumed to remain toroidal by neglecting the azimuthal wave which develops at larger time, is written as

$$V(t) = 2\pi R(t) A_c(t) \sim 2\pi^2 R(t) r_c^2 \sim V(0)t, \tag{3.13}$$

where $A_c(t)$ is the cross-sectional area of the circular core, $R(t)$ the ring radius as a function of time and $V(0)$ is the initial volume of the core at $t = 0$. The (inviscid) stretching effect alone does not change $V(t)$; this can be seen from Kelvin's circulation theorem, which states that in an ideal fluid where only conservative body forces are exerted, there is a constant circulation about any closed material filament moving with the flow. In simple terms, this means that the vorticity in a material filament of length $\delta\mathbf{l}$ obeys $\boldsymbol{\omega}(t)/\delta\boldsymbol{l}(t) = C$ for constant C. $V(t)$ only grows under

the effect of viscous diffusion, i.e. $r_c \sim \sqrt{\nu t}$, which results in the last term of equation (3.13).

Equation (3.12) and equation (3.13) results in the following relationship:

$$\omega(0,t) \sim \frac{\Gamma_{Ring}}{r_c^2} \sim \frac{R(t)}{V(t)} \sim \frac{R(t)}{t}, \tag{3.14}$$

which shows that as the ring radius increases, the peak vorticity also increases and decreases with time. The evolution of the scaled peak vorticity, ω_θ^*, in the ring core centre is then

$$\omega_\theta^*(\max) = \left[\frac{\omega_\theta(0,t)}{R(t)}\right]\left(\frac{D_o^2}{U_0}\right) \sim \frac{1}{T^*}. \tag{3.15}$$

This relationship is demonstrated in Figure 3.6 for inlet Cases A and B. It can be seen from equation (3.14) that without vortex stretching (constant R), $\omega(0,t) \sim t^{-1}$; in which case Figure 3.6 essentially manifests the decay of $\omega_\theta(0,t)$ due to viscous diffusion, after the vortex stretching effect is scaled. It further suggests that the R behaviour, i.e. the stretching of the toroidal vortex core, is an important influential factor induced by swirl on top of viscous diffusion. Figure 3.6 also reveals that the difference between the decay profiles of $\omega_\theta^*(\max)$ diminishes as T^* increases, becoming almost indistinguishable once discharge terminates at $T^* = 6$.

As to the overall circulation of the leading ring, the differing swirl strength does not impact the similarity of the ω_θ roll-up process in the core area during the formation process. This is confirmed by the almost universal Gaussian like ω_θ distribution, regardless of S or orifice geometry (as discussed in section 3.3.4). Nevertheless, swirl weakly affects the evolution of the leading ring circulation, as evidenced in Figure 3.8, where Γ^*_{Ring} is the circulation of the leading ring normalised in accordance with equation (1.2). The algorithm used to produce this figure was designed specifically to isolate only the leading ring area, excluding the trailing jet which is not fully rolled into the ring core area. Previous experimental studies achieved this through a high vorticity field threshold, which removed most of the trailing jet or, Γ^*_{Ring} is computed only after the ring had detached from the trailing jet. The algorithm used in this work is described as follows:

- A reference point is determined based on the flow field's maximum or minimum

vorticity (depending on the core), corresponding to a point close to the core centroid; see Figure(3.7)(a).

- The vorticity field is interpolated onto lines expanding radially from the reference point.

- For every line, a displacement radially outward, Δr, is made while evaluating the vorticity magnitude at each step. As the vorticity has a Gaussian distribution, it decreases as Δr moves farther from the centre. The process continues until an increase in vorticity is detected for three consecutive radial steps, which indicates the presence of the trailing jet. The point where the increase started is labelled as P1 in Figure 3.7(b). If there is no increase in vorticity, the process stops and records the point where the vorticity becomes zero and is labelled as P2.

- The vortex core is enclosed by a closed curve formed by the points register, which separates it from the trailing jet. All vorticity outside this region is removed.

It shows that during discharge ($T^* \leqslant 6$) the mechanism of ω_θ delivery to the leading ring volume is fairly universal, with Γ^*_{Ring} increasing subtly with S due to higher ω_θ flux. For $T^* > 6$, the behaviour of Γ^*_{Ring} for Case A and B begin to deviate from one another. With reference to Figure 3.8(a), for S = 0 and 1/4, Γ^*_{Ring} continues to increase by ingesting vorticity ($\omega_\theta > 0$) from the trailing jet to the leading ring , whilst for S $\geqslant 1/2$, Γ^*_{Ring} increases until $T^* \gtrsim 8$, before decaying at a rate proportional to S. This is due to the stronger vorticity cancellation between the ring core ($\omega_\theta > 0$) and the peripheral region of $\omega_\theta < 0$ (as discussed in section 3.3.2), which increases with S and overwhelms the vorticity ingested from the trailing jet.

Figure 3.8 (b) examines the impact of orifice geometry on the evolution of Γ^*_{Ring}. For clarification purpose, only S = 0 and 1 are shown, the behaviour of other S cases being consistent. In line with ω^*_θ(max) in Figure 3.6, Case B displays an appreciably smaller Γ^*_{Ring} for the same S owing essentially to the absent ω_θ flux effect at the orifice exit illustrated in Figure 3.4, but the overall dependence on T^* is similar to that of Case A.

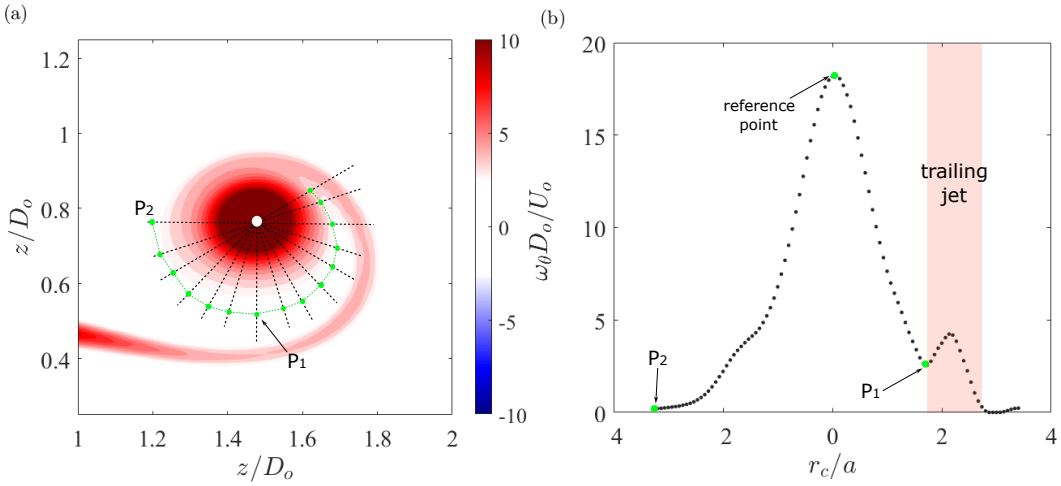

Figure 3.7: (a) Vorticity contour plot showing the line where ω_θ is interpolated and the curve formed by points P_1 or P_2 of each line that separates the ring core from the trailing jet. (b) ω_θ distribution of the ring core and the area around it. where the reference point as well as the points P_1 and P_2 are pointed out. r_c is the local radial coordinate with $r_c = 0$ at the core centroid; a is the time-dependent characteristic core radius, as defined in section 3.3.6

Regions of $\omega_\theta < 0$

A striking consequence of the presence of swirl in the flow of interest, is the generation of significant regions of $\omega_\theta < 0$ (negative vorticity) from the start of the formation process, as reported by Gargan-Shingles et al. (2015); Naitoh et al. (2014), Cheng et al. (2010) and He et al. (2020b); although in the case of the latter it is uncertain whether the negative vorticity originates from the boundary layer washed off the surface of the vanes creating the swirl velocity component. From figure 3.9(a), S = 1 and inlet Case A, three distinct regions of $\omega_\theta < 0$ can be identified. Region I stems from $\omega_\theta \sim \partial u_r/\partial z$ in the boundary layer developed by the inward flush of fluid induced by the circulation of the leading vortex core ($\omega_\theta > 0$); Region II issues from the orifice and is related to the imposed axial velocity profile, i.e. $\omega_\theta \sim -\partial u_z/\partial r$; Region III is the main contributor of $\omega_\theta < 0$ and is formed ahead and in the proximity of the main vortex core (see also Figure 3.2 (b)), as observed in the above studies. Note that for inlet Case B the intensity in Region II is much weaker than that in Case A, in accordance with the u_z profile imposed at the orifice exit; see

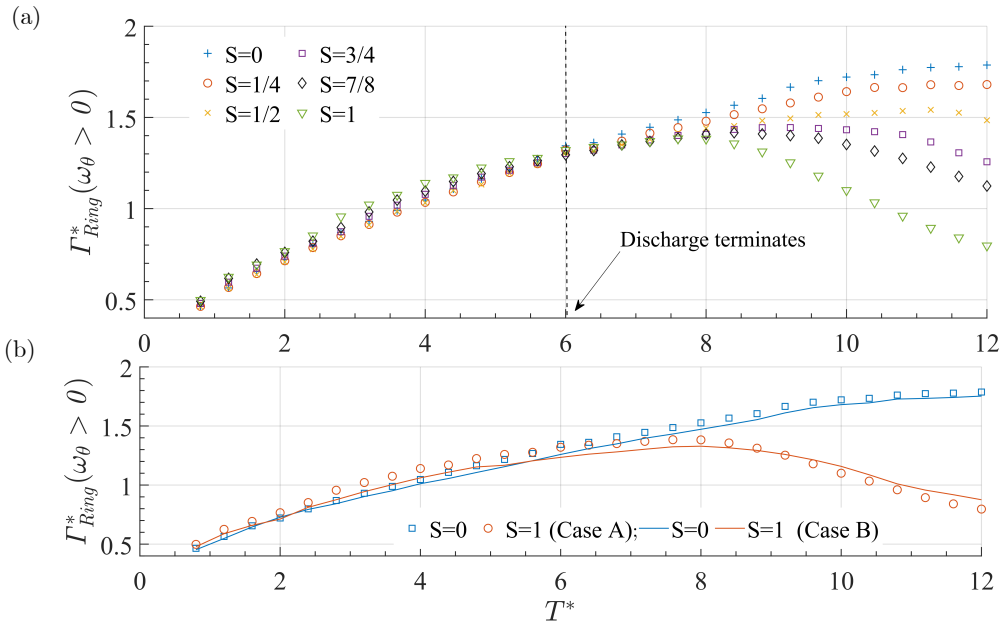

Figure 3.8: Evolution of the leading ring circulation Γ^*_{Ring}. (a) All S [Case A]; (b) comparison of Case A and B for S = 0 and 1.

Figure 3.4 (a).

The magnitude of ω_θ in Regions I and II increases slightly with S; for the former this is attributed to the increment of Γ_{Ring} Figure 3.8), hence the stronger u_r induced on the vertical wall outside the orifice; for the latter it is due to the slight increase of $\partial u_z/\partial r$ on the inner side of the jet at the orifice exit (Figure 3.4 (a)). They are both weaker than that in Region III, where $\omega_\theta(< 0)$ is of the same order of magnitude as $\omega_\theta(> 0)$ in the leading vortex ring core, as shown in Figure 3.9 (a).

Cheng et al. (2010) attributes the formation of negative vorticity observed in their work to the secondary flow induced by u_θ in the toroidal core, by a mechanism analogous to the secondary flow induced inside a curved pipe. In their study, this secondary flow is characterized by the formation of a vortex pair commonly known as Dean vortices, within which, positive vorticity feeds the primary vortex ring having the same vorticity sign, increasing its circulation; meanwhile, the negative vorticity interacts with the primary ring, forming complex vortex structures. A suitable dimensionless number that characterizes this phenomenon is the Dean number De, the ratio of the product of centrifugal and inertia forces to the viscous force (Berger

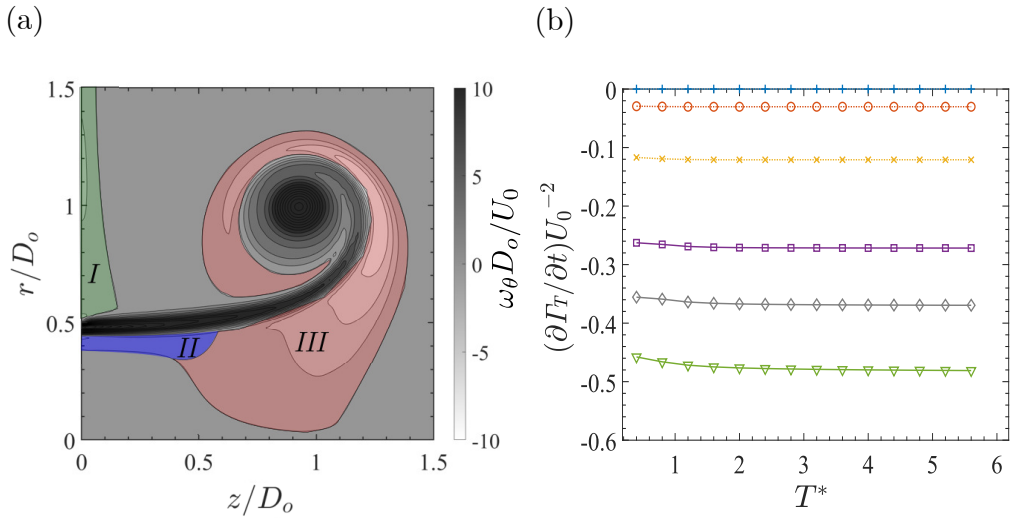

Figure 3.9: (a) ω_θ contours for S=1 at $T^* = 4$; Regions I, II and III indicate the presence of negative vorticity [Case A]. Distribution of ω_θ for Case B at the same S and T^* is very similar albeit the absence of Region II. (b) Dependence on time of the production rate of $\omega_\theta < 0$ due to vortex tilting, for different S [Case A]. [Symbol legend is the same as that for Figure 3.8 (a).]

et al., 1983), given by

$$\begin{aligned} \mathrm{De} &= \left[\frac{2a(t)u_\theta(t)}{\nu}\right]\left[\frac{a(t)}{R(t)}\right]^{\frac{1}{2}} \\ &= \left[\frac{2a(t)}{D_o}\right]^{\frac{3}{2}}\left[\frac{u_\theta(t)}{U_0}\right]\left[\frac{D_o}{2R(t)}\right]^{\frac{1}{2}}\mathrm{Re}; \end{aligned} \tag{3.16}$$

where $a(t)$ is the core radius. In the toroidal vortex core, both the radius r_c and swirl velocity $u_\theta(t)$ are time dependent, as well as the ring radius $R(t)$. The order of magnitude of the maximum De for the cases investigated, viz. S = 1, can be estimated, by taking $2a(t) \sim D_o/10$, $u_\theta \lesssim \Omega R_o/2 = U_0/2$ (as detailed in section 3.3.4), $D_o \lesssim 2R(t)$. It turns out that typically De < 40 (in the range of 20 to 55) for $0.4 < T^* < 6$, whilst for the swirling rings in Cheng et al. (2010), De ~ 640, an order of magnitude greater. Note that the swirl component in Cheng et al. (2010) was superposed onto a well formed Gaussian ring and has a very different u_θ distribution in the ring core, which is discussed in section 3.3.4.

According to Berger et al. (1983), secondary flow is induced at De > 36 and remains laminar until De ≈ 176. On the one hand, a Dean vortex pair similar

to that of Cheng et al. (2010) is not observed in the present study; on the other, the intensity of the negative vorticiy in their study is appreciably lower, albeit at a De one order of magnitude larger. This suggests that when the swirl component is generated simultaneously with ring formation, some other mechanism dominates the generation of negative vorticity in Region III.

Inspired by the work of Brown and Lopez (1990), Darmofal (1993) adopted a theoretical approach to explain that for a continuous swirling jet, negative vorticity originates from the tilting of ω_z, which eventually leads to vortex breakdown. It is an inviscid process. This can be seen from the ω_θ component of the inviscid vorticity equation:

$$\frac{D\omega_\theta}{Dt} = \omega_r \frac{\partial u_\theta}{\partial r} + \omega_z \frac{\partial u_\theta}{\partial z} + \frac{u_r \omega_\theta}{r}, \tag{3.17}$$

where D/Dt is the standard material derivative in cylindrical polar coordinates and:

$$\omega_z = \frac{1}{r}\frac{\partial (r u_\theta)}{\partial r}, \quad \omega_r = -\frac{\partial u_\theta}{\partial z}. \tag{3.18}$$

The production of negative vorticity in Region III is postulated to originate from the tilting terms (the first two terms on the *rhs* of equation (3.17)); while the vortex stretching term (the last term) amplifies its intensity at a rate proportional to u_r, as expected. For vortex rings without swirl, $u_\theta = 0$, the contribution from vortex tilting is zero and therefore negative vorticity is never observed in Region III in this case. The production of negative vorticity from the tilting terms can be quantified by substituting equation (3.18) into the first two terms of equation (3.17), resulting in:

$$\left(\frac{\partial \omega_\theta}{\partial t}\right)_{\mathrm{T}} = -\frac{\partial u_\theta}{\partial z}\frac{\partial u_\theta}{\partial r} + \frac{1}{r}\frac{\partial (r u_\theta)}{\partial r}\frac{\partial u_\theta}{\partial z}; \tag{3.19}$$

$$\left(\frac{\partial \omega_\theta}{\partial t}\right)_{\mathrm{T}} = -\frac{\partial u_\theta}{\partial z}\frac{\partial u_\theta}{\partial r} + \left(\frac{u_\theta}{r} + \frac{\partial u_\theta}{\partial r}\right)\frac{\partial u_\theta}{\partial z}; \tag{3.20}$$

$$\left(\frac{\partial \omega_\theta}{\partial t}\right)_{\mathrm{T}} = \frac{1}{2}\frac{\partial}{\partial z}\left(\frac{{u_\theta}^2}{r}\right); \tag{3.21}$$

the subscript 'T' on the *lhs* denoting vortex tilting. Since the term on the *rhs*, which is the gradient with respect to z, is negative in the leading area and approximately coincides with Region III (figure not shown, but can be inferred from the u_θ distri-

bution in the $r-z$ plane, as discussed in section 3.3.4), negative ω_θ is generated there, regardless the direction of u_θ. According to the distribution of $\partial\left({u_\theta}^2/r\right)/\partial z$ (figure not shown), strong tilting initiates on $r=0$ closer to the windward stagnation point in the moving frame (this is discussed further in section 3.3.3). Fluid having negative vorticity is then transported and stretched around the vortex core; u_θ inside the core does not contribute directly to the generation of negative vorticity. This supports the finding of Gargan-Shingles et al. (2015) that the gradients of u_θ are the source terms of the negative ω_θ. The rate at which the total circulation, Γ_T, is produced by vortex tilting can be obtained from:

$$\frac{\partial \Gamma_\mathrm{T}}{\partial t} = \int_A \left(\frac{\partial \omega_\theta}{\partial t}\right)_\mathrm{T} \mathrm{d}A = \frac{\partial}{\partial t}\int_A \left(\omega_\theta\right)_\mathrm{T} \mathrm{d}A = \frac{1}{2}\int_A \left[\frac{\partial}{\partial z}\left(\frac{{u_\theta}^2}{r}\right)\right] \mathrm{d}A, \tag{3.22}$$

where the constant integration area A is the same as that in equation (1.2), which is the entire flow domain. Figure 3.9 (b) shows the change in $\partial\Gamma_\mathrm{T}/\partial t$, over the discharge duration ($0 < T^* \leqslant 6$), calculated using equation (3.22) with the u_θ distribution over A; confirming that for S = 0, no negative vorticity is generated due to zero u_θ everywhere. The rate of production of negative vorticity from vortex tilting appears to be constant for a given S for $T^* > 2$, and mainly contributed by Region III. It suggests that even though u_θ intensity in the vortex core decreases over time due to viscous diffusion (see section 3.3.4), the production rate is maintained, since the gradient w.r.t. z is contributed to from the peripheral area of the core. The production rate is also a non-linear function of S, as evidenced by the uneven spacing between the lines in Figure 3.9 (b).

Thus, the dependence of Γ_T on time can be evaluated as

$$\Gamma_\mathrm{T}\left(t\right) = \frac{1}{2}\int_0^t \int_A \left[\frac{\partial}{\partial z}\left(\frac{{u_\theta}^2}{r}\right)\right] \mathrm{d}A\, \mathrm{d}t, \tag{3.23}$$

which suggests that Γ_T scales like

$$\Gamma_\mathrm{T} \sim u_\theta^2 \sim \left(\mathrm{S}U_0\right)^2 \sim \mathrm{S}^2. \tag{3.24}$$

Figure 3.10 (a) presents the time variation of the circulation associated with the

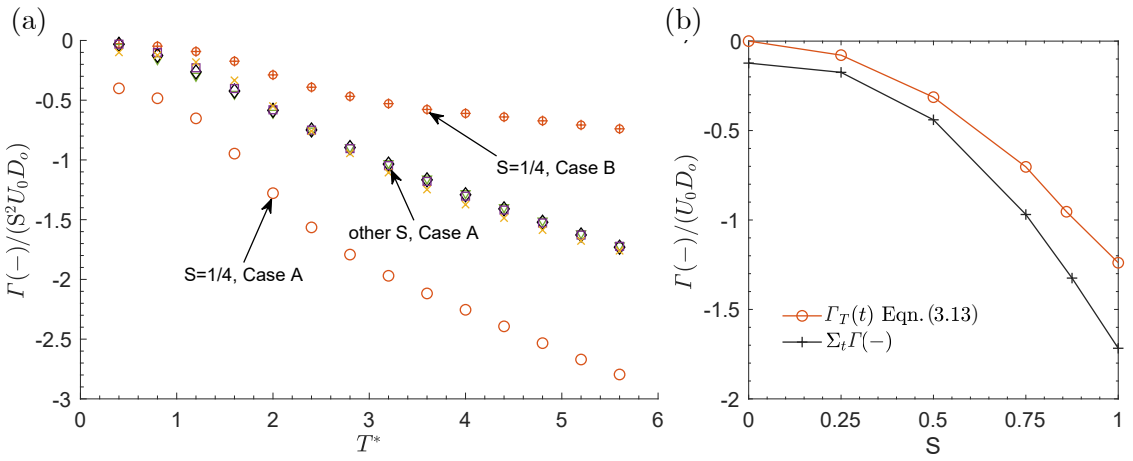

Figure 3.10: (a) Time variation of $\Gamma(-)$, the circulation associated with $\omega_\theta(< 0)$ in regions II and III of Figure 3.9 (a). Inlet Case B, for S $> 1/4$, shows behaviour consistent with that for Case A. [Symbol legend is the same as that for figure 3.8 (a)]. (b) Dependence on S of the total circulation $\sum_t \Gamma(-)$ associated with $\omega_\theta < 0$ in Regions II and III, integrated over $0 < T^* \leqslant 6$, and that contributed by vortex tilting calculated via equation (3.23); although these results are for inlet Case A, those for inlet Case B show consistent behaviour, but are roughly 3% higher for each S.

negative vorticity in Regions II and III, excluding Region I. This circulation is denoted $\Gamma(-)$, and calculated by integrating ω_θ over the two Regions. It suggests that for S $\geqslant 1/2$, Region III (vortex tilting Γ_{T}) is the main source of negative vorticity generation, and $\Gamma(-)$ scales with S^2 according to equation (3.24). For S $= 1/4$ and both inlet Case A and B, the main contribution to $\Gamma(-)$ is Region II, and therefore the scaling does not hold; for S $= 1/4$ and Case B, the weaker $\partial u_z/\partial r$ diminishes the magnitude of $\Gamma(-)$ compared to that for Case A. Note that the stretching term in equation (3.17) does not contribute to the generation of $\Gamma(-)$ in an inviscid flow, according to Kelvin's circulation theorem.

In addition, Figure 3.10 (a) shows that the production of negative vorticity starts in tandem with the formation of the primary ring. Unlike the flow studied in Brown and Lopez (1990) and Darmofal (1993), where vortex breakdown is caused by flow instability, for the vortex ring flow considered here, which is a starting swirling jet, the roll-up of the primary vortex core triggers the breakdown from $t = 0$. For any S > 0, $u_\theta^2 > 0$, and the u_r induced by the primary core promotes the generation of negative ω_θ by tilting ω_z.

The total negative vorticity produced from vortex tilting during formation can also be calculated from equation (3.23) by setting the upper integration limit to $T^* = 6$, the total discharge time. The result is shown in figure 3.10 (b) in terms of S dependence. The variation of the total Γ_T is consistent with that of $\Gamma(-)$, with the difference contributed by Region II, which in general increases appreciably with S.

It is worth noting that Naitoh et al. (2014) reported low intensity negative vorticity in Region III, which dissipates quickly without much interaction with the primary ring structure where $\omega_\theta > 0$. The important difference in their flow field is the low piston stroke ratio of $L/D < 2$, where almost all the vorticity flux through the nozzle exit was able to be entrained into the primary ring volume. Small L/D gives rise to a reduced circulation of the primary ring, and subsequently diminishes the negative vorticity production rate by weakening vortex tilting (as discussed further in section 3.3.3). Thus, it can be argued that the formation of regions of $\omega_\theta < 0$ is related more to the vortex tilting mechanism triggered by the swirling primary vortex ring structure.

3.3.3 Growth of the primary ring radius R

In Figure 3.11 (a), the dependence of the trajectory of vortex's centroid on S, calculated via equation (3.5) for inlet Case B, is compared; the background image shown is the ω_θ contour for S = 0 at $T^* = 8$. It reveals an unequivocal incremental trend for the ring radius R in the r-direction, accompanied by a strong decrease of the ring core penetration distance in the z-direction as S increases. This is in agreement with the experimental findings of He et al. (2020b) for a similar inlet condition, although at a Re an order of magnitude higher and swirl not strictly of solid-body rotation type. For S $\leqslant 1/2$, trajectory dependence on S appears to be weak; for S $> 1/2$, this dependence becomes clearly stronger and seems to have a more-or-less linear dependence (equal spacing) on S. For inlet Case A, similar trajectories and contour plots arise, with a clear secondary ring arising in the wake for S> 0; unlike Case B, no secondary ring is present when S = 0.

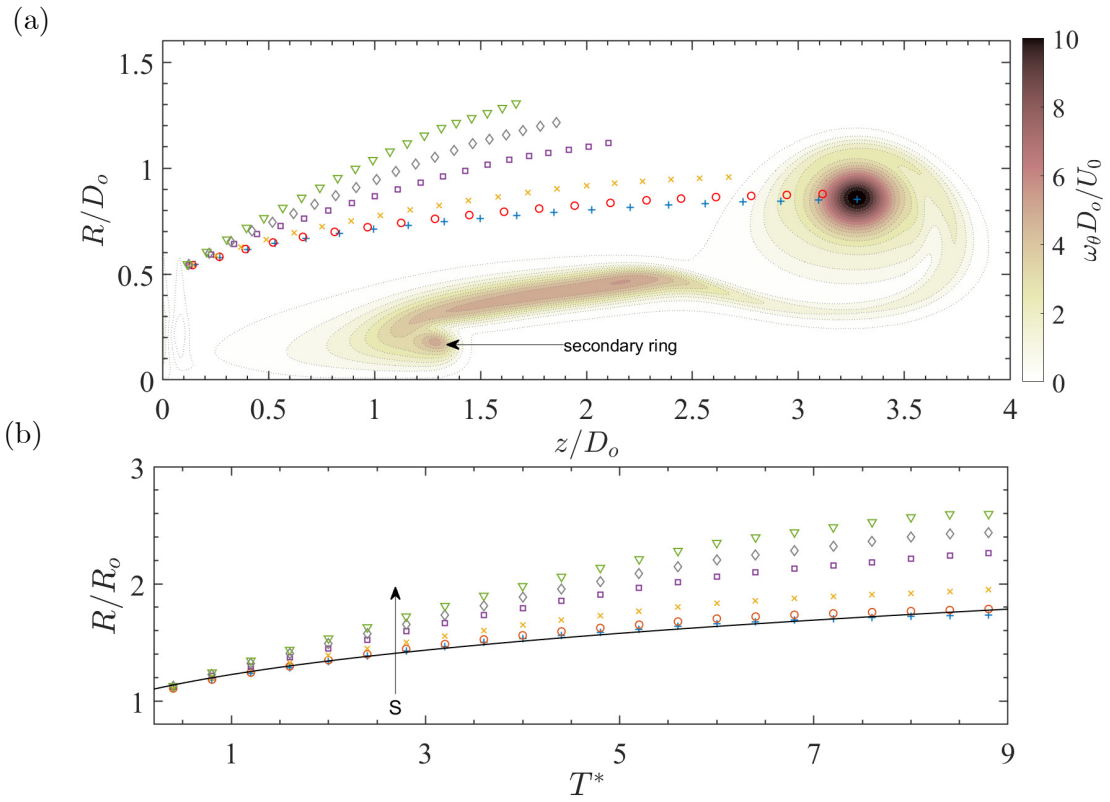

Figure 3.11: (a) Swirl number specific vortex core centroid trajectories for $T^* \leqslant 8$ [Case B]; shown also is the ω_θ contour plot associated S = 0 at $T^* = 8$. (b) Evolution of the ring radius R [Case A]; the solid line is the fitting function $R \sim (T^*)^{1/4}$ for S = 0. The direction of the arrow in (b) indicates increasing S. [Symbol legend is the same as that for Figure 3.8 (a).]

In previous studies, growth of the ring radius in the presence of swirl has commonly been attributed to the centrifugal force associated with u_θ in the core but has not been discussed in any detail. In Virk et al. (1994), where u_θ peaks in the ring core, the ring growth rate is much smaller ($\approx 4\%$); since the swirl in their work is parameterised according to the degree of polarization, it is difficult to directly compare their swirl intensity with that of the present work. The isolated Gaussian ring prior to the superposition of u_θ can effectively be considered as being formed after a sufficiently small discharge time. Alternatively, in the experimental study of Naitoh et al. (2014), for a similar physical formation process, the growth rates of R for similar S values are also smaller. This discrepancy is likely owing to the smaller discharge ratio, which was $L/D = 2$, compared to the value 6 in the present study. It suggests that whilst the centrifugal effect is indubitably responsible for the radial growth of an isolated and well-formed swirling ring, it is not the dominant factor during the vortex roll-up process, not least for long discharge times.

In Figure 3.11 (a), a secondary ring is seen to be forming at the far end of the trailing jet, as highlighted; see also Figure 3.2 (d). Typically one (sometimes two) secondary ring(s) can be observed to form just after discharge terminates, due to shear layer instability, but they should not be confused with a stopping vortex having the opposite sign to the leading ring. Their characteristics depend strongly on S. The only exception is for S = 0 and Case A, where no clear secondary ring is seen. This is because this case has the most stable shear layer of all the cases under investigation; it has zero swirl and its shear layer is also thicker than for S = 0 and inlet Case B, as mentioned in section 3.3.2.

For inlet Case A, Figure 3.11 (b) shows that for a ring without swirl, S = 0, the behaviour of R can evidently be described by a power law in T^*, viz. $R \sim (T^*)^\gamma$ with $\gamma \approx 1/4$. It stems from dimensional analysis by considering the conservation of the specific hydrodynamic impulse, I, of the isolated leading ring when S = 0 at high Re where viscous effects are unimportant (Gan, 2010; Glezer and Coles, 1990)

$$R(t) \sim (t - t_0)^{\frac{1}{4}} (I)^{\frac{1}{4}}, \tag{3.25}$$

where t_0 is some virtual time origin to account for the orifice radius R_o. By neglecting the effect of added mass and the trailing jet:

$$I = \frac{1}{2}\int_V \mathbf{x} \times \omega \, \mathrm{d}V \approx \pi \int_{A_c} r^2 \omega_\theta \, \mathrm{d}A, \tag{3.26}$$

which is unidirectional in z. $\mathbf{x}$ is position vector in cylindrical coordinates $\mathbf{x} = (r, \theta, z)$. The small discrepancy between the fitted line and the data points in Figure 3.11 (b) can be attributed to the effect of the trailing jet as well as the moderate Re. For S > 0, no reasonable corresponding power law relation is found due to a non-linear mechanism associated with swirl, which is discussed below.

Figures 3.12 (a) and (b) compare ω_θ contour plots when S $= 0$ and 1 for inlet Case A, together with instantaneous *in-plane* streamlines in the moving frame of reference travelling at the instantaneous propagation velocity of the leading primary vortex ring, u'_z, in the axial, z-direction (this is discussed further in section 3.3.5). The stagnation point, denoted as *sp*, is determined to lie at the axial position where $u_z = 0$ at $r = 0$ in this moving frame. For S $= 0$, figure 11 (a), the primary vortex core essentially moves in the axial direction with the radial velocity of the core $u'_r \ll u'_z$. The primary vortex is surrounded by the classical-shaped bubble (with wake) as revealed by the streamlines. The stagnation point is always located upstream of the vortex core as shown in Figure 3.12 (c), with Z_{sp}, the difference between the z coordinate of *sp* and that of the vortex core centroid, slowly increasing with time. This reflects the growth of the ring bubble volume due to entrainment of surrounding ambient fluid into the bubble (Gan, 2010). Although not shown, similar behaviour is observed for S $= 1/4$ and $1/2$.

In contrast, for S $= 1$, Figure 3.8(b), the vortex bubble breaks down as if the ring is about to pass over a (moving) bluff body. The relative position of the stagnation point, as shown in Figure 3.8(c), suggests that initially at $T^* = 0.8$, the shape of the bubble is similar for all the S cases, but for S $\geqslant 3/4$, the stagnation point gradually moves towards the primary core, passing through ($Z_{sp} = 0$) at $T^* \approx 4$ and 5.6, when S $= 1$ and $7/8$, respectively. This upstream translation (in the moving frame) implies a deceleration of u_z at $r = 0$ around the stagnation point, which, in turn,

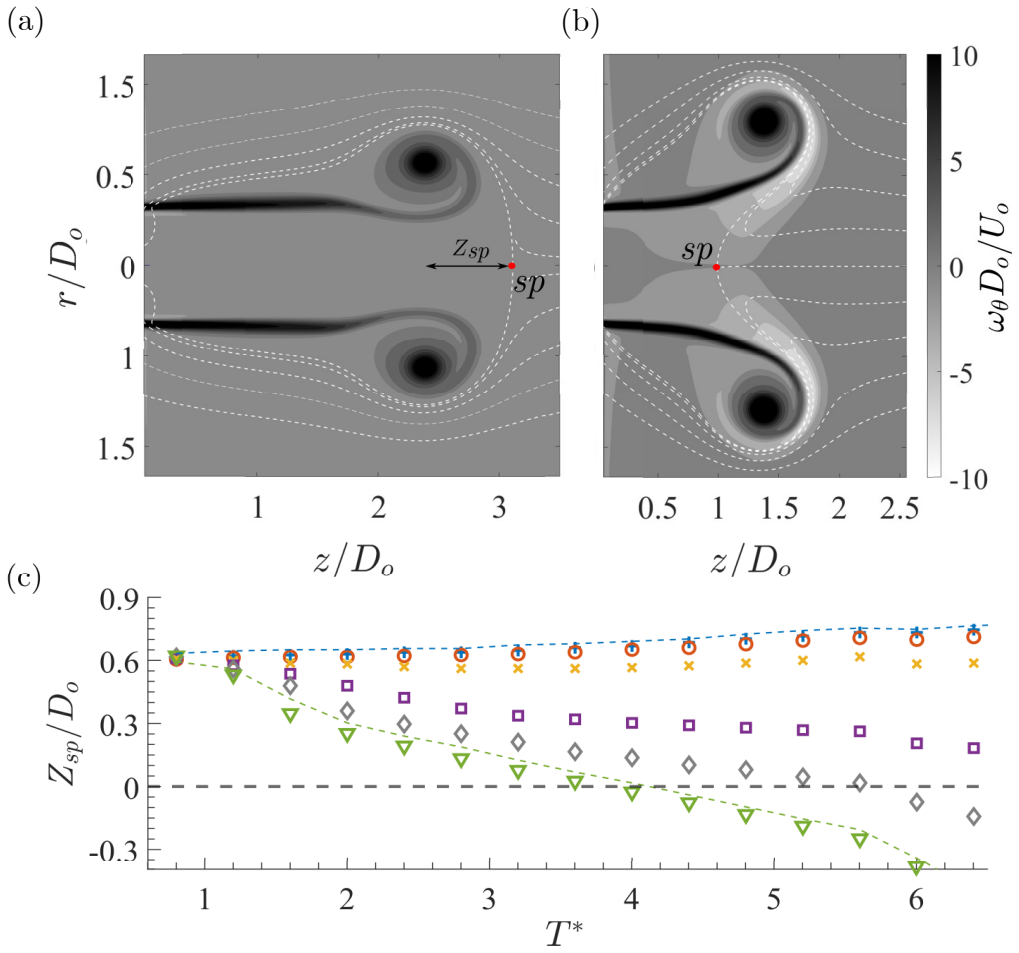

Figure 3.12: Instantaneous ω_θ contour plots at $T^* = 6.4$ for (a) S = 0, (b) S = 1 [Case A]; the overlaid dashed lines are the *in-plane* instantaneous streamlines in the frame of reference moving at the instantaneous u_z'. *sp* indicates the location of the stagnation point on $r = 0$ in this moving frame and Z_{sp} is the distance between *sp* and the vortex core centroid. (c) Dependence of Z_{sp} on time [Case A]; the corresponding dashed lines shown are for Case B and S = 0 and 1 only, since the remaining S cases follow a pattern consistent with Case A. [Symbol legend is the same as that for Figure 3.8 (a).]

accelerates u_r as a consequence of satisfying continuity, similar to the breakdown mechanism in a continuous swirling jet (Billant et al., 1998; Darmofal, 1993). This is associated with the formation of the $\omega_\theta < 0$ region, as can be clearly observed in Figure 3.12 (b) echoing Figure 3.9 (a), and can be interpreted via the Biot-Savart integral (Brown and Lopez, 1990):

$$u_z\left(0,z\right) = \frac{1}{2}\int_{-\infty}^{\infty}\int_{0}^{\infty} \frac{r^2\omega_\theta}{\left[r^2+(z-\acute{z})^2\right]^{3/2}}\,\mathrm{d}r\,\mathrm{d}\acute{z}. \tag{3.27}$$

That is, regions of $\omega_\theta < 0$ must be responsible for the deceleration of u_z near the stagnation point and hence the behaviour change of Z_{sp} with S. The S dependent accelerated u_r, induced by the primary vortex core in the present case, further promotes the generation of negative vorticity, creating a non-linear feedback for it (Darmofal, 1993), as well as for the behaviour of R in Figure 3.11 (b) and the downstream movement of the stagnation point in Figure 3.12 (b). This complex mechanism explains the difficulty in identifying a single working scaling law for R and all S.

Likewise, Figure 3.12 (c) also shows that the behaviour of Z_{sp} varies non-linearly as a function of S, showing an abrupt change between S = 1/2 and 3/4, suggesting the existence of a critical (or minimum) swirl number $1/2 \lesssim \mathrm{S}_c < 3/4$ for breakdown to occur. Finding this critical S_c is left as topic for future investigation.

3.3.4 Distribution of azimuthal velocity u_θ

In previous numerical studies (Cheng et al., 2010; Hattori et al., 2019), swirl was superposed onto a well-formed circular Gaussian vortex ring (in terms of the ω_θ distribution) as an axisymmetric and Gaussian distributed $u_\theta(r)$, with maximum intensity at the core centre. However, in practice, such a distribution of u_θ is hard to realise, if indeed possible; instead, it is more practical to introduce it via the roll-up process of the swirling vortex sheet in inlet geometries like Case A and B, as demonstrated in Figure 3.13 (a) which shows the swirling fluid material in the vortex core region appears to be diluted by engulfing the non-swirling ambient fluid at this early roll-up stage. The weaker u_θ in the core centre for Case A can plausibly

be attributed to the roll-up of the non-swirling fluid in the short $0.1D_o$ long nozzle section (see Figure 2.4) at the beginning of the formation process, which is equivalent to $T^* \in (0, 0.1]$.

The distribution of $u_\theta(r)$ through the vortex core centre is plotted in Figure 3.13 (b) together with the distribution of $\omega_\theta(r)$. The vortex core can clearly be identified as the classical Gaussian like ω_θ distribution centred at $r \approx 0.6D_o$ for both inlet Cases A and B. It can be observed that at the core centre where ω_θ peaks, the magnitude of u_θ is only about 1/5 and 1/2 of the maximum input swirl velocity ΩR_o, or SU_0, for Case A and B, respectively. This is approximately a local minima, instead of a local maxima. The peripheral region at $r \approx 0.55D_o$ and $0.7D_o$, having larger u_θ, is the trace of the rolled-up layer from the edge of the orifice (see Figure 3.13 (a)), which does not diffuse towards the core centre in an efficient manner to make it Gaussian even over the entire scrutinised duration. In contrast, the viscous diffusion leads to a more homogeneously distributed $u_\theta(r)$ in the core area for both cases, diminishing their initial inhomogeneity. This is illustrated in Figures 3.13(c) and (d), where the time dependence of the u_θ distribution in the core is presented. By $T^* \approx 4$, approximate homogenisation is reached and the geometrical dependence fades out thereafter in a manner of similarity. The local minima at $r_c/a \approx 1.8$, separating the shear layer and the core area, also appears to persist.

In Figure 3.13 (b), the inner shear layer can also be seen as a second ω_θ peak centred at $r \approx 0.5D_o$, aligned with the orifice edge. The ω_θ intensity of the second peak for Case A is also larger, in line with the primary peak. The shear layer associated with u_θ is also consistent with this second peak. This is reflected by an almost linearly rapid drop of u_θ over the range $0.45D_o \lesssim r \lesssim 0.53D_o$, at almost the same rate for both orifice geometries. For $r \lesssim 0.45D_o$, $\omega_\theta \approx 0$ and solid-body rotation manifests in both cases as a constant gradient $\partial u_\theta/\partial r$, with that of Case B appreciably larger as expected.

The typical ω_θ distribution shown in Figure 3.13 (b) largely replicates that of a non-swirling vortex ring with a Gaussian core during formation (figure not shown), which suggests that introducing swirl does not significantly alter the similar ω_θ distribution in the core area, and hence the fundamental roll-up process. However,

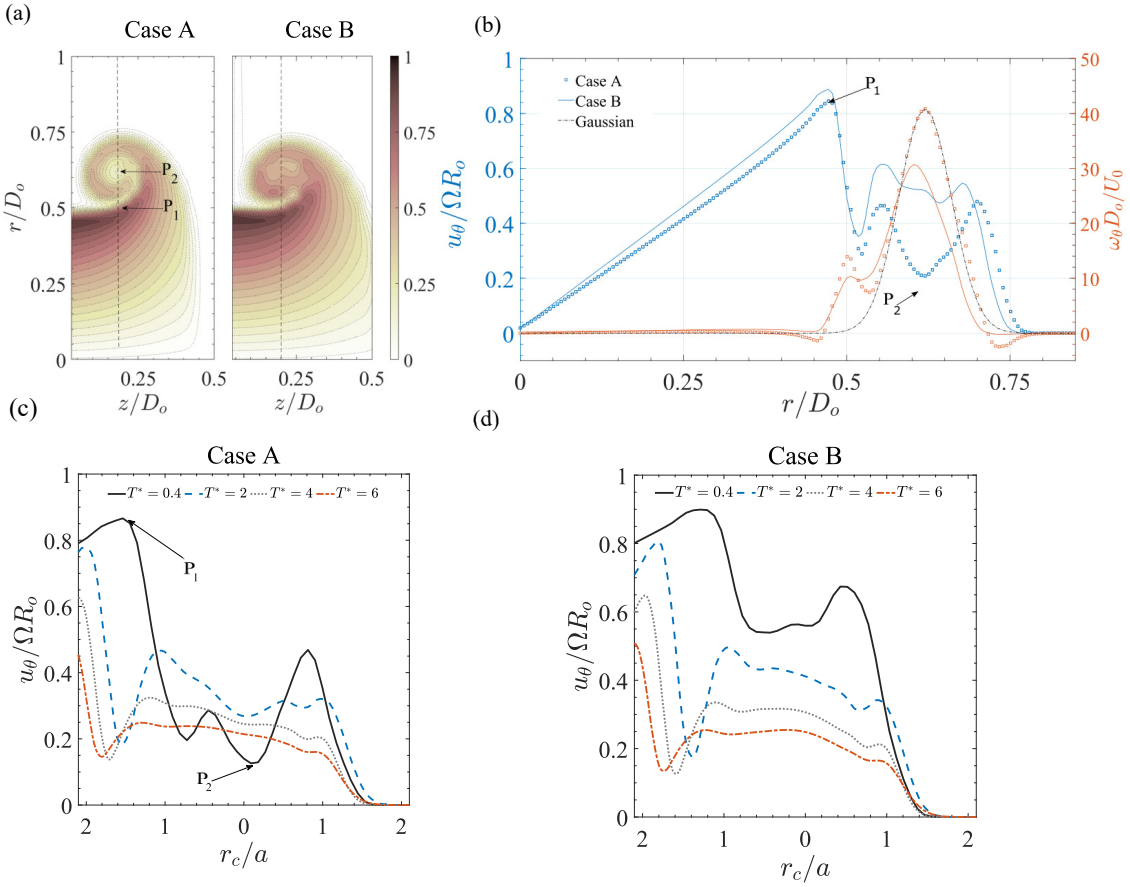

Figure 3.13: (a) Contour plot of the magnitude of u_θ in the $r-z$ plane for S = 1 at $T^* = 0.8$ [Case A and B]: the vertical dashed lines shown pass through the vortex core centroid based on ω_θ (point P_2), determined by equation (3.5); point P_1 marks the maximum u_θ along the dashed lines. (b) Distribution of u_θ and ω_θ along the dashed lines in (a). (c-d) Variation of $u_\theta(r)$ distribution, at different times, in the core area [Case A and B], where r_c is the local radial coordinate with $r_c = 0$ at the core centroid; a is the time dependent characteristic core radius, as defined in section 3.3.6.

different orifice geometries do have a clear impact on the peak ω_θ. That is, whilst Case B results in stronger u_θ in the vortex core, ω_θ there is weaker, as also shown in Figure 3.6.

Figure 3.14 presents the evolution of the averaged swirl intensity $\overline{u_\theta}$ over the core area where $\omega_\theta \geqslant \omega_\theta(\max)e^{-1}$:

$$\bar{u}_\theta = \frac{2\pi}{a}\int_o^{r_c} u_\theta r dr. \tag{3.28}$$

A key feature is the dependence of $\overline{u_\theta}$ on orifice geometry. Owing to the discharge of an initially non-swirling fluid volume contained within the short $0.1D_o$ nozzle section, the maximum $\overline{u_\theta}$ attainable in the core centre for Case A is $\approx 0.35\Omega R_o$. In the absence of such a non-swirling volume, the maximum $\overline{u_\theta}$ in Case B is $\approx 0.5\Omega R_o$. The non-swirling volume in Case A also leads to a gentle increment of $\overline{u_\theta}$ but of short duration (for $T^* \lesssim 1.2$) before decay starts, whilst Case B displays a monotonic decay of $\overline{u_\theta}$ in the core centre. The difference between the $\overline{u_\theta}$ intensity as well as its decay rate for the two geometries becomes fairly small after discharge terminates at $T^* = 6$. Comparing the dependence of $\overline{u_\theta}$ on S, it is clear that stronger swirl has lower resistance against $\overline{u_\theta}$ decay, for both inlet geometries. The decay of $\overline{u_\theta}$ can be well described by an exponential function of the form

$$\frac{\overline{u_\theta}}{\mathrm{S}U_0} \sim C_1 \exp\left(-C_2 T^*\right) + C_3, \tag{3.29}$$

where C_1, C_2 and C_3 are coefficients which are obviously S dependent even after the scaling factor S is incorporated. Figure 3.13 infers that the swirl component u_θ in the vortex core originates from the rolling up of the swirling shear layer outside the inlet orifice's edge. It then diffuses according to the effect of viscosity. The distribution of $u_\theta(r)$ around the vortex core can be considered as a canonical diffusion problem of the axial velocity w inside a circular zone of infinite length (assuming zero curvature, $R \to \infty$). The diffusion process is governed by an equation of the same form as equation (3.9) with the variable ω replaced by w.

The boundary and the initial conditions are

$$\left.\frac{\partial w}{\partial r}\right|_{r_c=a} = 0 \qquad w(r,0) = F(r), \tag{3.30}$$

the first of which can be inferred with reference to Figure 3.13 (c,d); a approximates the radius of the core area and $F(r)$ is the arbitrary initial distribution of w which stems from the roll-up process. Again, a local coordinate system is adopted where $r_c = 0$ is at the centre of the circular core area. Being analogous to the equation of heat conduction in cylindrical coordinates with an insulated boundary, the exact solution (Hahn and Özişik, 2012) for w is

$$w(r,t) = \frac{2}{a^2}\int_0^a rF(r)\mathrm{d}r + \sum_{n=1}^{\infty} C_n J_0\left(\lambda_n r\right)\exp\left(-\nu\lambda_n^2 t\right), \tag{3.31}$$

where J_0 is a Bessel function of the first kind of order zero and λ_n is one of the positive roots of $J_0(\lambda) = 0$. The coefficient C_n is given by:

$$C_n = \frac{\displaystyle\int_0^a rF(r)J_0\left(\lambda_n r\right)\mathrm{d}r}{\displaystyle\int_0^a rJ_0^2\left(\lambda_n r\right)\mathrm{d}r}. \tag{3.32}$$

Relaxing the boundary condition in (3.30), or including the curvature effect of the finite ring radius R, in general, should only alter the dependence of $w(r,t)$ on r, but not on t.

Naitoh et al. (2014) suggests that the decay of u_θ in the vortex core is attributable to the exchange of fluid between the ring and the ambient non-swirling fluid, the rate of which increases with S. Even though this effect could play an important role, it appears that u_θ behaviour is related to the combined effect of viscous diffusion (as shown) and the increment of ring radius R. As the initially irrotational free vortex flow outside a vortex undergoing solid-body rotation, which in this case is the jet rotating in the $r-\theta$ plane issuing from the orifice, is similar to a Rankine vortex albeit of a finite length and influenced by the primary vortex roll-up, $\overline{u_\theta}$ in the ring core approximately decreases as R^{-1} at a given time. Accordingly, a dimensionless

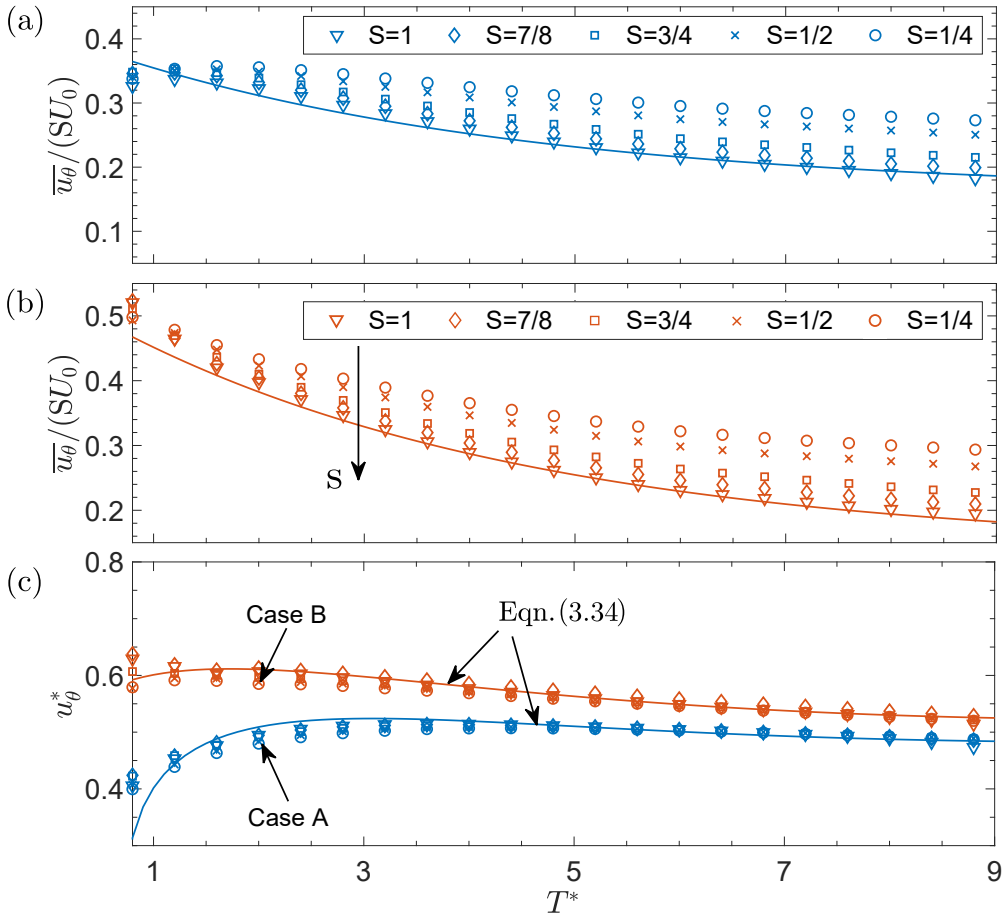

Figure 3.14: Spatially averaged azimuthal velocity $\overline{u_\theta}$ in the core area, (a) Case A, (b) Case B; the solid lines are fitting functions for S = 1 of the form of equation (3.29). (c) Dependence of u^*_θ on T^* scaled as per equation (3.33); the fitting lines follow equation (3.34). The direction of the arrow in (b) indicates increasing S.

swirl velocity u_θ^* can be defined as:

$$u_\theta^* = \frac{\overline{u_\theta} R(t)}{\Omega R_o^2} = \frac{\overline{u_\theta} R(t)}{\mathrm{S} U_0 R_o}. \tag{3.33}$$

The dependence of u_θ^* on T^* is shown in Figure 3.14 (c). The effectiveness of the scaling factor $R(t)$ is clear as it removes the effect of S for a given orifice geometry, which is a dominant factor for the early time evolution of u_θ^*. The decay rate of u_θ^* becomes almost geometrically independent after discharge terminates at $T^* = 6$. Taking equations (3.25) and (3.29), the time dependence of u_θ^* can well be described by:

$$u_\theta^* \sim (T^*)^\gamma \left[\exp\left(-\mu T^*\right) + \mathcal{F}\right], \tag{3.34}$$

which is S independent. For the fitting lines shown in figure 3.14 (c), γ takes a universal value of $1/4$, which seems to be attributed to the constant I in the z direction applied to all the cases tested. The fact that $\mu = 1/4$ ($= \gamma$, which could be a coincidence) suggests that the u_θ diffusion rate depends only weakly on the inlet orifice geometry. $\mathcal{F}$, representing the behaviour of the initial roll-up of u_θ into the core area, see equation (3.31), is apparently geometrically dependent, with a value 0.16 and 0.22 for inlet Case A and B, respectively. In general, the power law term in equation (3.34) dominates at early time, $T^* \lesssim 4$, with the exponential term dominating subsequently.

Physically, the scaling of equation (3.33) simply confirms that the strength (circulation) of the Rankine vortex mentioned above is proportional to S, as expected, and the decay of this circulation becomes asymptotically similar for the two orifices, following the specified function of time in equation (3.34).

The behaviour of the time dependent (specific) angular momentum $L(t)$ of the toroidal vortex core can also be inferred from equation (3.33), which can be written as:

$$L(t) = \int_V \mathbf{x} \times \mathbf{u} \, \mathrm{d}V \sim V(t) R(t) \overline{u_\theta}(t) \sim f(t, \mathrm{S}), \tag{3.35}$$

where $V(t)$ is the volume of the toroidal vortex core at time t and $f(t, \mathrm{S})$ denotes

some function describing the evolution of L. It is not difficult to see that:

$$L\left(T^*\right) \sim \mathrm{S}\ \left(T^*\right)^{\gamma+1}\left[\exp\left(-\mu T^*\right)+\mathcal{F}\right]. \tag{3.36}$$

It can be deduced that for the range plotted in Figure 3.14, L remains an increasing function of T^*, and increases according to viscous diffusion; i.e. the vortex ring entrains u_θ from the shear layer to the peripheral area around the core, which then diffuses towards the core centre. For $T^* \gg 9$, entrainment of u_θ from the shear layer terminates, and the decay rate of u_θ^* is much greater and becomes S dependent. This later stage is governed by viscous dissipation (figure not shown).

3.3.5 Propagation velocity u_z' of the primary vortex ring

The leading primary ring structure propagates downstream as a compact coherent structure soon after the vorticity delivered by the shear layer outside the inlet orifice rolls up forming the vortex core. The magnitude of the propagation velocity is influenced by the self induced velocity of the toroidal core, the shear layer in the trailing jet, as well as the swirl component. The dependence of this propagation velocity in the axial direction, u_z', on both time and swirl strength is presented in Figure 3.15; u_z' is calculated based on the azimuthal average of the core centroid $z-$coordinate as in equation (3.5).

Evidently, additional swirl decreases u_z', which is supported by previous numerical and experimental studies (He et al., 2020b; Naitoh et al., 2014; Virk et al., 1994). The effect of S is weak at small time but gradually becomes more pronounced. The effect also appears to be stronger for larger S, i.e. $u_z'(\mathrm{S}=0) \approx u_z'(\mathrm{S}=1/4) \gg u_z'(\mathrm{S}>1/2)$; $u_z'(\mathrm{S}=0) \approx 2.35u_z'(\mathrm{S}=1)$. For $\mathrm{S} \leqslant 1/2$, despite the different absolute magnitude, the dependence of u_z' on T^* appears similar to that of a vortex ring without swirl. That is, u_z' tends to a constant maximum value, before pinch-off, as a monotonic function. For $\mathrm{S} \geqslant 3/4$, the behaviour of u_z' changes appreciably. For example, u_z' for $\mathrm{S}=3/4$ is a maximum at $T^* \approx 3$, and then decreases to a stabilised value at $T^* \gtrsim 6$ when discharge terminates. $\mathrm{S}=7/8$ and 1 display additional complexity of u_z' behaviour after $T^*=6$; this is related to the influence of the stronger

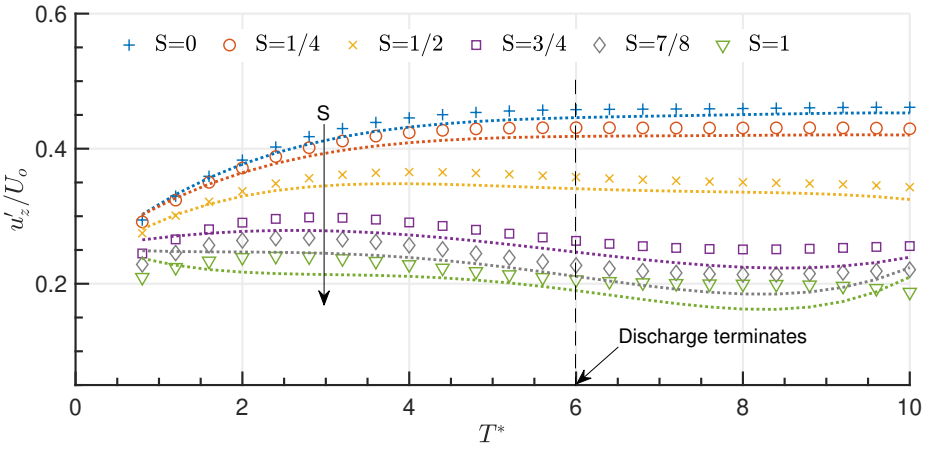

Figure 3.15: Leading vortex ring propagation velocity in the axial direction, u_z'. Symbols denote inlet Case A and dotted lines Case B. The direction of the arrow indicates increasing S.

secondary ring after discharge ends, as shown in Figure 3.11 (a).

Comparing the overall behaviour of u_z' for Case A and B, it is evident that except for very early time, $T^* \lesssim 1$, the values obtained for Case A are consistently larger than for Case B. Their difference, $\Delta u_z'$, is relatively small for S $\leqslant 1/2$, but greatly increases as S becomes larger. Dependence of $\Delta u_z'$ on T^* also appears to be more complex for large S. Plausibly, this is owing to the non-linear influence on S of the ω_θ flux, viz. $\partial\Gamma/\partial t$, leading to a larger Γ_{Ring} (see Figure 3.8) and hence u_z' in Case A, as well as the more unstable shear layer of the trailing jet in Case B.

Saffman (1995) provided a comprehensive model of u_z' for an isolated and perfectly circular thin core ring with swirl, which can be written as:

$$u_z' = \frac{\Gamma_{\text{Ring}}}{4\pi R}\left[\underbrace{\ln\left(\frac{8}{\epsilon}\right)}_{T_1} - 0.5 + \underbrace{\frac{1}{\Gamma_{\text{Ring}}^2}\int_0^a \frac{\gamma_c^2(r)}{r}\,\mathrm{d}r}_{T_2} - \underbrace{\frac{8\pi}{\Gamma_{\text{Ring}}^2}\int_0^a u_\theta^2 r\,\mathrm{d}r}_{T_3}\right] + f(w), \tag{3.37}$$

where $\epsilon = a/R$ is the ratio of the core radius a (which is discussed again in section 3.3.6) to the ring radius R calculated via equation (3.5). Term T_1 is the canonical estimation of u_z' for a (thin-cored) vortex ring without swirl, which is proportional to the leading ring circulation Γ_{Ring}; term T_2 is the additional correction factor which

involves the detailed distribution of ω_θ in the core, viz

$$\gamma_c(r) = 2\pi \int_0^r r\omega_\theta(r)\mathrm{d}r \quad \text{where} \quad \gamma_c(a) = \Gamma_{\text{Ring}}. \tag{3.38}$$

In the above equation, and in terms T_2, T_3 of equation (3.37), a local coordinate system is applied such that $r = 0$ is at the vortex core centroid and a perfectly circular core cross-section is assumed. Term T_3 quantifies the contribution from the azimuthal flow u_θ. The last term $f(w)$ accounts for the effect of the trailing jet and the regions of $\omega_\theta < 0$, which are not included in Saffman's model.

Equation (3.37) shows that if $f(w)$ is neglected, for a given Γ_{Ring} and R, introducing u_θ slows down u_z'. Based on a force-balance argument, Lim and Nickels (1995) suggests that this is related to the balance between the following forces, see Figure 3.16:

- The concept of vortex line tension, denoted as F_{sv}, refers to the curve of the vortex line that creates a ring where the velocity inside the curve is higher than the velocity outside the curve. This generates a pressure difference that tends to reduce the size of the ring.

- Kutta lift F_{kl} is a force generated by a body in relative motion to the ambient fluid.

- F_r is the force caused by the rotational flow, u_c in the core, resulting in a drop in pressure that contracts the ring.

- F_S is the force related to the addition of swirl, u_c that increases the centrifugal force.

Therefore, to preserve the force balance, the Kutta lift has to decrease with the additional u_θ and consequently the propagation velocity u_z' of the ring. The effect of swirl-induced vortex tilting and breakdown further complicates matters.

The contribution from each of the three terms in equation (3.37) is evaluated and presented in Figure 3.17, which unequivocally shows that T_1 dominates the other two, regardless of S. The direct influence of T_3, which is associated with u_θ generated by the mechanism in this study, is one order of magnitude smaller. Its

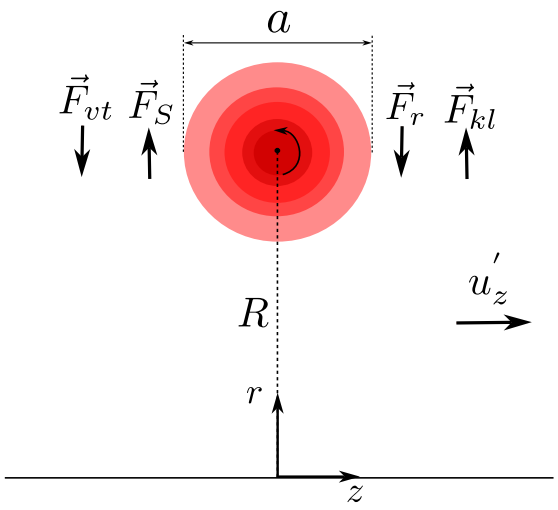

Figure 3.16: illustration of the vortex core and the force-balance argument where F_{st} stands for the vortex line tension, F_S is force related with the swirl, F_r is the force related to the flow within the core, u_c and F_{KL} is the Kutta lift.

contribution is indirectly reflected by R, hence ϵ in T_1, as well as the common factor $\Gamma_{\text{Ring}}/(4\pi R)$. In this respect, the detailed $\gamma(r)$ distribution in equation (3.38) is least important. Figure 3.17 (a) also suggests that the contribution when S = 1 to T_1 is larger than when S = 0, owing to smaller ϵ, but the overall u_z' is significantly smaller as demonstrated in Figure 3.15, because of the smaller common factor. It shows that the radius of the leading ring R is the key parameter determining u_z'. Figure 3.17 (b) demonstrates that $T_3(A) < T_3(B)$, inline with the findings for the spatially averaged u_θ in the vortex core discussed in section 3.3.4. Influence from both diminishes, as u_θ decays under viscous diffusion.

3.3.6 Formation process of the leading ring

Determination of the formation number F, according to the definition of Gharib et al. (1998), is illustrated in Figure 3.18 (a), which is the value of T^* when the total circulation Γ delivered by the orifice attains the maximum possible circulation of the leading ring, Γ_{Ring}, following pinch-off. Despite the three-dimensional nature of the flow, i.e. the instantaneous streamlines around the vortex core are of helical type owing to the swirling component, and discharge time also impacts on the detailed

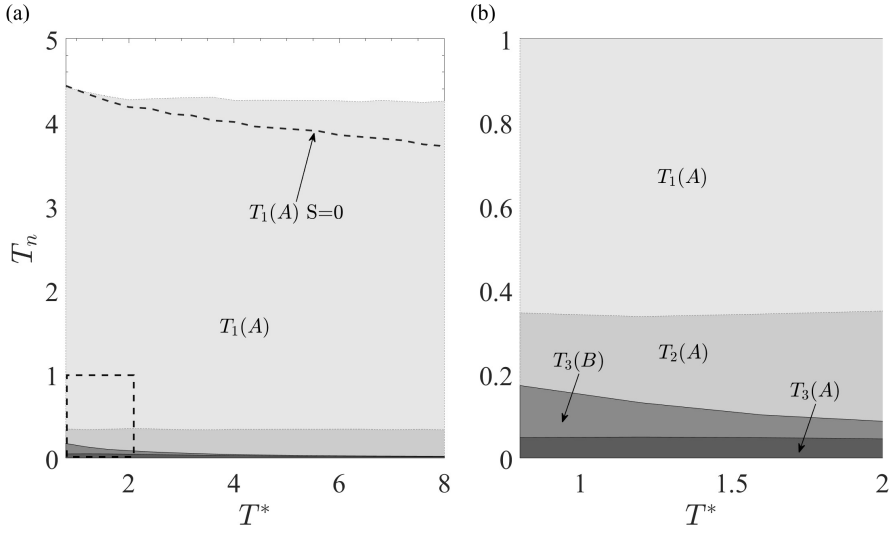

Figure 3.17: (a) Comparison of the relative contribution, T_n, to u_z' from the three terms in equation (3.37) for S = 1, where (A) and (B) denote inlet Case A and B, respectively. The shades of grey increases from T_1 to T_3, T_1 being the lightest shade. The area under the dashed line in (a) is for the T_1 term for the case S = 0. (b) is a magnified view of the area in (a), represented by the dashed box in the bottom left hand corner.

formation process as discussed in Limbourg and Nedić (2021), here the classical circulation based formation number evaluated in the $r-z$ plane is investigated, since the enstrophy of the flow is dominated by ω_θ. However, only $\omega_\theta > 0$ is included when calculating the circulation for both the total domain and the leading ring Γ_{Ring}. As demonstrated in section 3.3.2, regions of $\omega_\theta < 0$ originate from the tilting of ω_z (the swirl component). It is not produced by the inlet orifice directly, and its influence is taken into account in terms of interaction and cross-cancellation with the region of $\omega_\theta > 0$. As S increases, the contribution from the negative vorticity becomes significant as shown in Figure 3.10. For comparison purposes the total circulation is calculated, including $\omega_\theta < 0$, and also displayed for S = 1; including the negative vorticity, leads to the total circulation dropping to zero at $T^* = 8$ when the leading ring just gains maximum positive ω_θ. For S = 0, the total circulation is largely unaffected in the absence of $\omega_\theta < 0$ production.

The total circulation in Figure 3.18 (a) shows that even though the Γ flux at the orifice exit increases with S, see equation (3.7), cancellation of positive and negative vorticity leads to a similar growth rate for the different S cases, especially at early

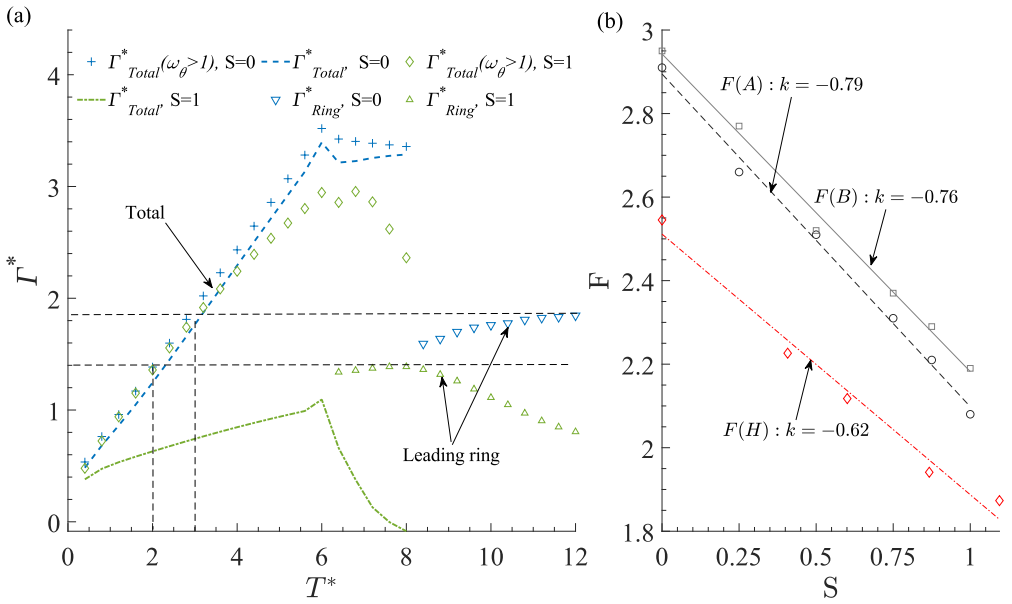

Figure 3.18: (a) Determination of the formation number F based on the variation of the total, Γ_{Total}, and the leading ring, Γ_{Ring}, circulation with T^* for inlet Case A. The leading ring circulation value Γ_{Ring} is taken from Figure 3.8 (b). Symbols are for Γ calculated from positive ω_θ (with a small threshold) only; dashed lines represent Γ obtained without applying a threshold (including $\omega_\theta < 0$). (b) Dependence of formation number on swirl number S. $\diamondsuit$ $F(H)$, $\bigcirc$ $F(A)$, $\square$ $F(B)$ where $k = \text{dF/dS}$. (A), (B) and (H) signify Case A, Case B, and He et al. (2020b), respectively.

time. Also because of such cancellation, the growth rate of the total circulation when S = 1 decreases, unlike that for S = 0 where the growth rate remains constant in accordance with the constant ω_θ flux at the orifice exit. The total circulation maximises when the discharge terminates at $T^* = 6$, as expected. After that the total circulation when S = 1 decreases dramatically because of cancellation by the strong negative vorticity, but Γ_{Ring} continues to grow until $T^* \approx 8$. The dependence of F on S is essentially determined by the maximum Γ_{Ring} alone, which is detailed in section 3.3.2, because of the insensitivity of S to the total circulation magnitude.

F determined in this way is presented in Figure 3.18 (b) for Case A and B, together with the experimental results in He et al. (2020b). For S = 0, F ≈ 3, which is similar to the simulation result of Rosenfeld et al. (1998). The values of F in the experiment of He et al. (2020b) are smaller but in a consistent way at a given S, plausibly owing to the higher turbulence levels introduced by the swirl generating vanes and the slightly different ways of determining F. Figure 3.18 (b) reflects a remarkably similar linear relation between the behaviour of (the circulation-based) F with S, excluding and offset by the value at S = 0. It is insensitive to Re, turbulence level, and the detailed u_θ distribution in the vortex core from a practical swirl generation mechanism. In particular, the two orifice geometries result in very similar gradients, k.

A second method proposed by Gharib et al. (1998) for the determination of F uses the generic dimensionless kinetic energy α defined as:

$$\alpha = \frac{E}{\sqrt{\rho I \Gamma^3}}, \tag{3.39}$$

where Γ and I are calculated from equation (1.2) and (3.26), respectively. In energy terms, pinch-off occurs when α delivered by the nozzle (decreases with time) drops to the asymptotic value of an isolated ring α_r. For rings with S = 0, the leading ring reaches an asymptotic status at $T^* \approx 12$, as shown in Figures 3.8 and 3.18 (a). This occurs when the leading ring pinches-off from its trailing jet, and the corresponding limiting energy for the leading ring is $\alpha_r \approx 0.33$. As swirl u_θ induces $\omega_\theta < 0$ for the S > 0 cases, no asymptotic status is reached, due to vorticity cancellation.

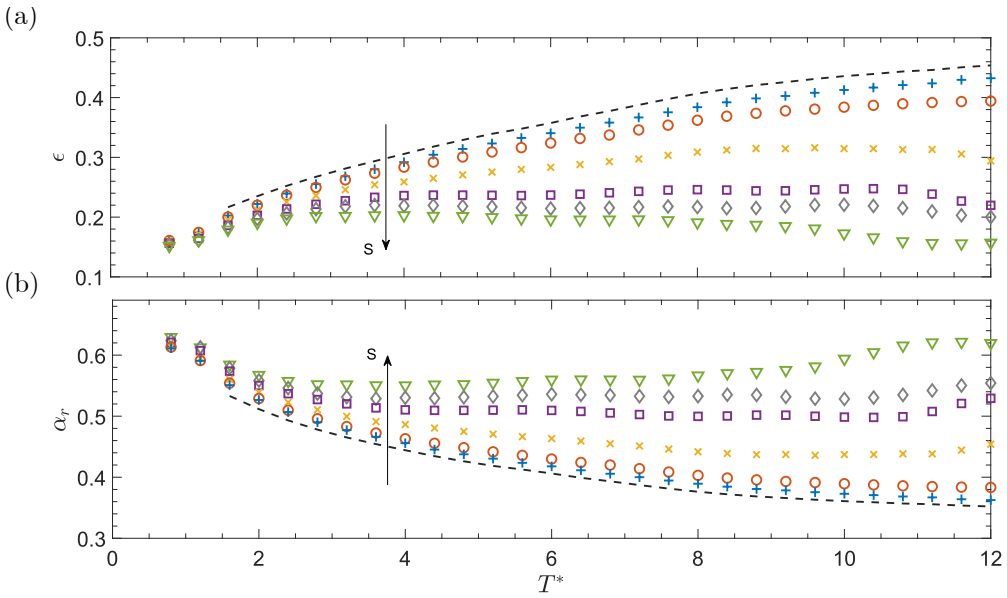

Figure 3.19: The dependence of (a) $\epsilon = a/R$ and (b) α_r calculated using equation (3.40), with time for inlet Case A. Similar behaviour is found for inlet Case B – the dashed curve shown on both figures is for this case and S = 0. The direction of the arrow indicates increasing S. [Symbols legend is the same as that for figure 3.15.]

Approximating the ring as a member of the Norbury-Fraenkel family (Fraenkel, 1972; Norbury, 1973), Shusser and Gharib (2000) proposed an expression for α_r as a function of a single parameter ϵ, defined as the ratio of core radius a to ring radius R, such that:

$$\alpha_r = \frac{\ln\left(\frac{8}{\epsilon}\right) - \frac{7}{4} + \frac{3}{8}\epsilon^2 \ln\left(\frac{8}{\epsilon}\right)}{2\sqrt{\pi\left(1 + \frac{3}{4}\epsilon^2\right)}}. \tag{3.40}$$

The core radius a is taken as the equivalent radius for an area of $\omega_\theta \geqslant \omega_\theta(\max)e^{-2}$, and $\epsilon = a/R$ is plotted in Figure 3.19 (a). As discussed above, the consequence of adding swirl is reflected in the $r - z$ plane in the promotion of ring radius growth. This tends to reduce a because of the stretching of the vortex core, which in turn significantly reduces ϵ. In comparison, the slow incremental change of ϵ for S = 0 is the result of (viscous) diffused core area counteracting the growth of R; see Figure 3.11. Thus, α_r increases with S as shown in Figure 3.19 (b). Consequently, the minimum rate of energy delivered by the orifice, necessary to support the formation of the vortex ring, is reached early, which leads to a decreased F.

The variation of α_r, with the resultant formation number is in line with that reported in Dabiri and Gharib (2005) where their α_r is manipulated by an iris nozzle whose exit diameter can be varied during ring formation. For an expanding exit, α delivered from a nozzle discharge increases, which tends to delay the pinch-off of the leading ring and increase F (Gharib et al., 1998). This however is counteracted by the higher R growth rate of the ring, increasing α_r by 25%, reducing the gain of circulation, which results in only a small increment of F. For a reducing exit, α delivery from a nozzle is basically unaffected but the modified ω_θ distribution in the vortex core diminishes α_r to a value close to Hill's spherical vortex and consequently F is up to 70% higher than for a static nozzle exit diameter. This is consistent with what is shown in Figure 3.18 (b) and 3.19 (b) for a given inlet geometry. Additionally, comparing the two S = 0 cases, the slightly smaller α_r in Case B also leads to a larger F.

To better understand the Γ_{Ring} growth in Figure 3.8 (b), Figure 3.20 (a) examines its time derivative for S = 0 and 1, revealing a decreasing functional relationship with time. This agrees with the decrease over time of energy delivery from the orifice to the leading ring (Gharib et al., 1998). S = 0 for inlet Case A shows a mild $\partial\Gamma_{Ring}/\partial t$ decrease with time up to $T^* \approx 9$; whilst for S = 1, the decrease is roughly two-fold faster on average for $T^* \leqslant 6$ and is similar for both orifice inlet geometries. This can be plausibly explained by the larger α_r for S = 1, see Figure 3.19 (b), where energy delivery by the orifice is relatively less efficient.

The additional u_θ does not seem to contribute efficiently to the energy supplied from the inlet orifice to the leading ring, where the swirl component of the kinetic energy, u_θ^2, is a small fraction (20% for $T^* < 2$ to 6% for $T^* = 4$ for S=1) of the $r - z$ plane components, $u_z^2 + u_r^2$, in the core area. In contrast, its contribution is adverse, in terms of the generation of $\omega_\theta < 0$ regions (from vortex tilting) leading to cross-cancellation of $\omega_\theta > 0$ (originating from the orifice) in two regions as shown in Figure 3.9 (a) and 3.12 (b). The first is in the trailing jet, especially the part close to the ring core in Region III, which strongly affects the last stage of vorticity delivery to the core. The second is over a large area surrounding the primary ring core, which modifies the ω_θ distribution from Gaussian-like on the core edge in contact

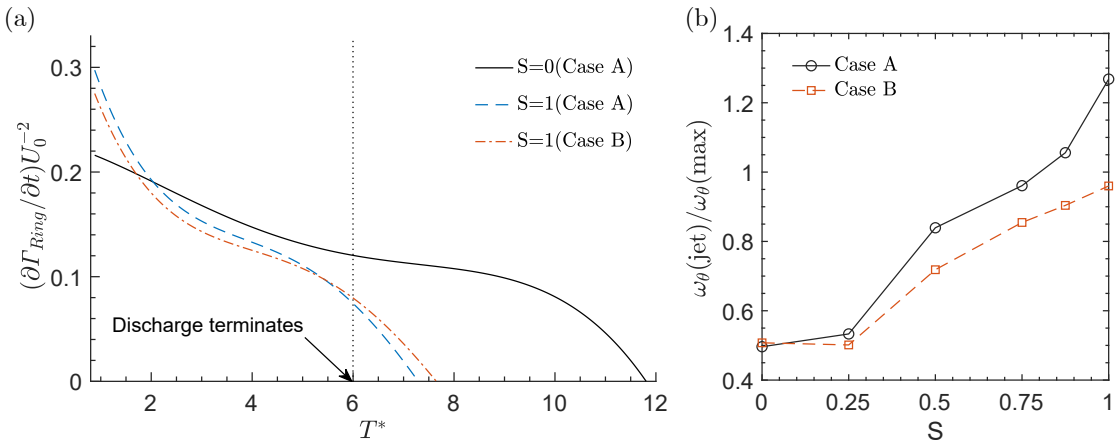

Figure 3.20: (a) Dependence of the time derivative of the ring circulation for S = 0 [Case A] and 1 [Case A and B], with time. (b) Ratio between the maximum ω_θ in the trailing jet and the maximum ω_θ of the primary vortex ring at $T^* = 8$ [Case A and B].

with the region of $\omega_\theta < 0$, reduces the core radius slightly and further diminishes ϵ and hence increases α_r.

Finally, in Figure 3.20(a) when $T^* \geq 6$, a faster decay of $\partial\Gamma_{Ring}/\partial t$ is observed for both inlet cases with S=1. This is attributable to the formation of Kelvin-Helmholtz-like instability in the shear layer promoted by the addition of swirl that amplifies as a secondary ring forming at the downstream end of the trailing jet after discharge terminates at $T^* = 6$, as discussed in section 3.3.3. The secondary ring engulfs the surrounding vorticity in the shear layer and, therefore, diminishes the vorticity delivered to the leading vortex ring affecting its formation process (see also Gao and Yu, 2010; Zhao et al., 2000). This is observed in the slight difference between cases A and B ($T^* \geq 6$) where the former decreases faster due to the formation of a stronger secondary ring as shown in Figure 3.20(b). It is also evident that ω_θ(jet) increases with S non-linearly, which even exceeds the ω_θ(max) of the primary ring for Case A and S > 3/4. This agrees with the stronger shear layer delivered by Case A discussed in section 3.3.2, even though it is less prone to instability than for inlet Case B (section 3.3.2).

3.4 Conclusion

In the present study, the physical effects of additional swirl, for swirl numbers $S \in [0, 1]$, on orifice generated circular vortex rings have been investigated over their formation process, together with their subsequent further development soon after discharge terminates. The formation of strong negative azimuthal vorticity $\omega_\theta < 0$ is a striking feature observed to surround the primary vortex ring core from time zero; the associated circulation $\Gamma(-) \sim S^2$. This is believed to be generated by the tilting of ω_z, which acquires a projection in the θ direction generating the gradient of $\partial u_\theta / \partial z$, eventually leading to a vortex breakdown type of mechanism for $S > 1/2$ given sufficient discharge supply. The breakdown effect is manifested by the displacement of the windward stagnation point downstream of the primary ring core position. The region of $\omega_\theta < 0$ surrounding the primary vortex ring plays an important role for rings with $S > 0$. Firstly, it displaces the windward stagnation point (in a moving frame), further promoting the vortex breakdown process; secondly, it reduces vorticity delivery to the ring core by cross-cancellation of $\omega_\theta > 0$ at the edge of the primary vortex core.

Another important feature is the dependence of the non-linear growth of the ring radius R on S, which is a direct consequence of vortex breakdown. R, which is responsible for the stretching of the toroidal vortex core in the θ direction, is shown to be a key scaling factor for the intensified peak vorticity in the primary core, $\omega_\theta(\max)$, and the diminishing swirl intensity in the core centre, $\overline{u_\theta}$, at a particular moment in time. Viscous diffusion, on the other hand, significantly contributes to the time evolution of these two quantities. The increased R is also the dominant factor for the reduced self-induced leading ring propagation velocity, u_z', with increasing S. Compared to R, the direct contribution from u_θ to u_z' appears to be unimportant.

Increased R growth with increasing S is a critical factor in understanding the formation process. The circulation based formation number F is shown to be a decreasing function of S, following a linear relationship whose coefficients appear to be insensitive to the detailed vortex roll-up process. The decreasing dependence of F on S is mainly caused by: firstly, the decreased core size to R ratio increasing the dimensionless ring energy α_r; secondly, cancellation between positive and the

negative ω_θ in the region peripheral to the ring core; thirdly, the adverse influence of a secondary ring that forms on vorticity delivery to the leading ring at the end of the discharge period.

Finally, comparing the same S, the short nozzle of inlet Case A provokes an appreciably larger vorticity intensity in the centre of both leading and secondary rings, but smaller swirl intensity in the leading ring core area. Nonetheless, this does not appear to have significant impact on other physical quantities.

CHAPTER 4

Experimental study of swirling vortex rings

In Chapter 3, it was noted that the distribution of u_θ from the swirling jet during the formation process of the vortex ring is the primary source of the negative azimuthal vorticity characteristic of swirling vortex rings. Its generation is related to its gradient:

$$\frac{1}{2}\frac{\partial}{\partial z}\left(\frac{{u_\theta}^2}{r}\right), \tag{4.1}$$

which value is higher around the centre of the swirling jet. This negative vorticity leads to the radial expansion of the vortex ring, which in turn results in a decrease in its formation number.

In the previous chapter, a solid-body rotation velocity distribution was applied at the inlet. However, in a laboratory setting, achieving the same condition requires a tangential stress applied by a rotating cylinder. This stress is dissipated through viscosity and transferred towards the centre of the cylinder. This phenomenon is described by the partial differential equation:

$$\frac{\partial u_\theta}{\partial t} = \nu\left(\frac{\partial^2 u_\theta}{\partial r^2} + \frac{1}{r}\frac{\partial u_\theta}{\partial r} - \frac{u_\theta}{r^2}\right), \tag{4.2}$$

its solution for a flow inside a single rotating cylinder of radius, a, with a zero initial angular velocity, $u_\theta(r,0) = 0$, and a cylinder with a constant angular speed, $u_\theta(a,t) = \Omega$, is:

$$u_\theta(r,t) = \Omega r + \Omega D_o \sum_{n=1}^{\infty} \frac{J_1\left(\lambda_n \frac{2r}{D_o}\right)}{\lambda_n J_0(\lambda_n)} \exp\left(-\lambda_n^2 \frac{4\nu t}{D_o^2}\right), \tag{4.3}$$

where J_0 and J_1 are Bessel functions of the first kind of order zero and one, and λ_n are the value where $J_1(\lambda) = 0$ (Batchelor, 1967). The velocity evolution corresponding to equation (4.3) is shown in Figure 4.1. The flow is assumed to be a solid-body rotation only when the tangential stresses inside the cylinder are zero everywhere, which theoretically takes around 1 minute to establish. Even though using a rotation cylinder requires some time to have a flow fully established, using a partially established velocity distribution could reduce the formation of negative vorticity due to u_θ close to the centre, where most of the negative vorticity is generated, being negligible.

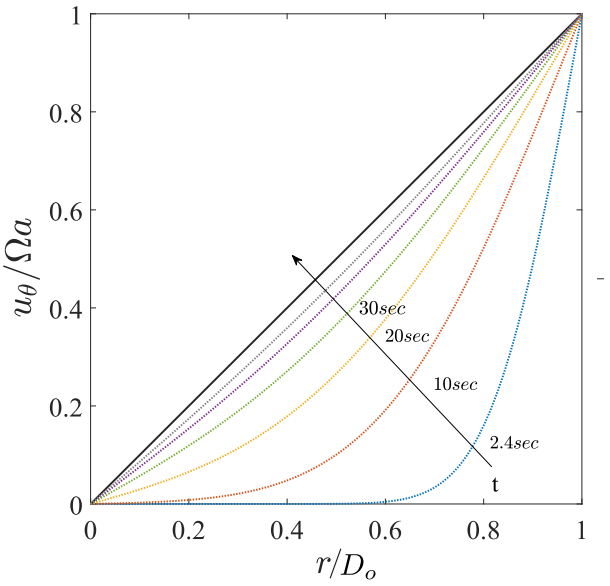

Figure 4.1: Velocity evolution of a flow inside a single rotating cylinder. The black line represents the solid-body rotation velocity distribution.

This chapter is divided into two parts. The first part discusses the challenges of forming swirling vortex rings using a rotating cylinder. The second aims is to reduce the formation of negative vorticity and its consequences by using partially

established solid body rotation velocity distributions.

4.1 Results and discussion

4.1.1 Addition of swirl

As part of the experiment, M-2 generated three angular speeds of $\Omega = 2$, 3.9, and 5.85 rad/s. These speeds were then tested at three different positions within the acrylic cylinder, which conforms to the swirl system discussed in Chapter 2. The positions tested were located at $l = D_o$, $2D_o$, and $3D_o$ from the orifice exit in the upstream direction. u_θ was computed from the experimental data as follows:

$$u_\theta = u_y cos\theta - u_x sin(\theta), \tag{4.4}$$

where θ is the polar angle in which the coordinate centre coincides with the centre of the disc. In the figures presented below, a spatial average u_θ is used. This average was obtained by interpolating the u_θ field into different concentric circles with radii $r \in (0, D_o/2]$ as illustrated in Figure 4.2 (a), and calculating the u_θ average from each circle.

After 60 seconds of continuous cylinder rotation, Figure 4.1 demonstrates that the flow is fully established. However, in reality, the flow does not achieve a velocity distribution similar to that of a solid-body rotation. Comparing Figures 4.2 (a) and (b), it is observed a significant difference in the central region of the tube, where u_θ is almost zero for $0 < r < D_o/4$, for the latter. Figure 4.2 (a) shows the velocity distribution of solid-body rotation, while Figure 4.2 (b) shows the actual distribution of u_θ for $\Omega_1 = 2$ rad/s and $l = 2D_o$ after 78 seconds of rotation. In Figure 4.2 (c), the velocity profiles in the rotating tube are compared to the theoretical model represented by dashed lines. The experiment agrees with the mathematical model during the first 12 seconds. However, at $t = 24$, the experimental results show a lower u_θ, and this difference increases as r approaches the tube centre, and it is more pronounced as the rotation time increases. The experimental flow never reached the solid body rotation velocity distribution.

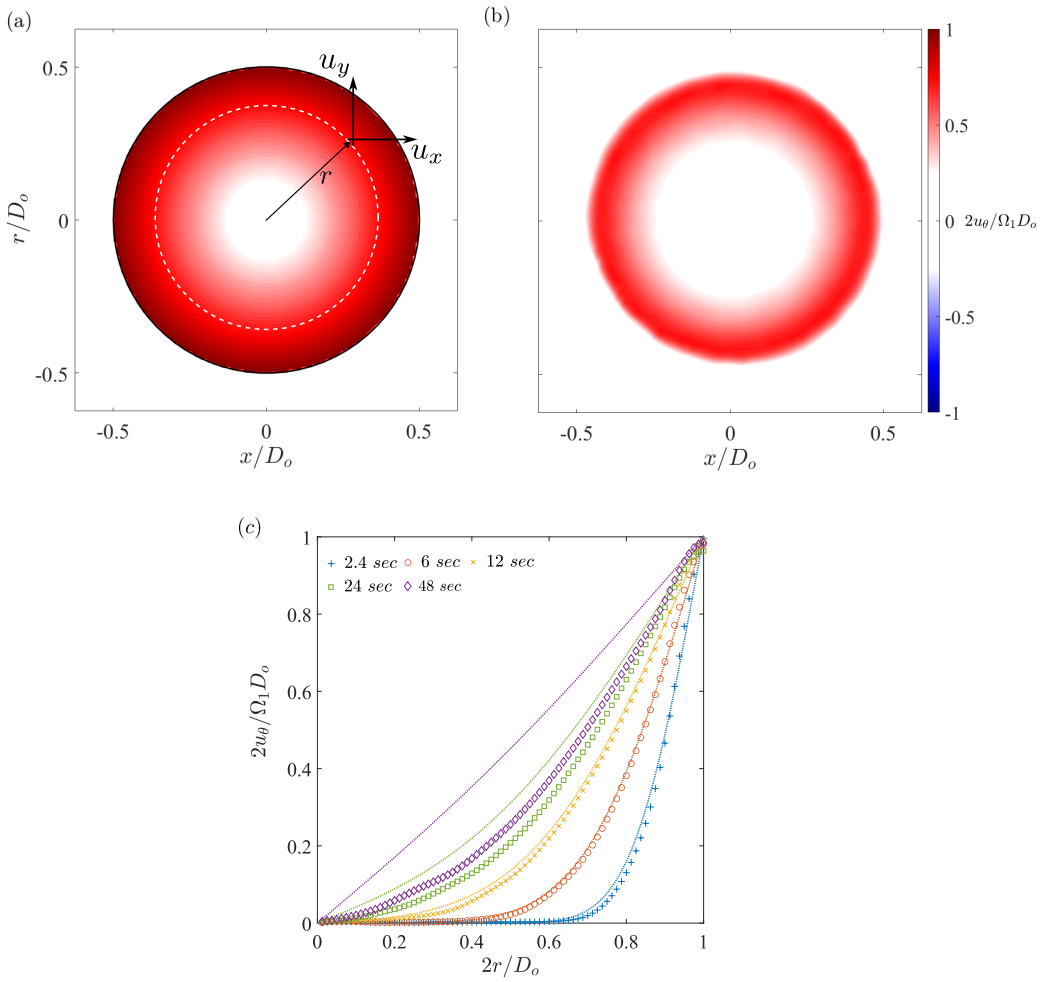

Figure 4.2: u_θ distribution for (a) a solid-body rotation, (b) experimental results for $\Omega_1 = 2\ rad/sec$ and $l = 2D_o$ after 78 seconds of rotation. (c) Evolution of the velocity profile, theoretically represented in dash lines and experimentally for the same parameters as (b) (Batchelor, 1967). The velocities used in equation (4.4)are illustrated in (a).

The angular velocity of the rotating cylinder is another factor that affects the development of the u_θ distribution. In Figure 4.3 (a), the u_θ profiles are shown for a higher angular speed of $\Omega_2 = 3.9\ rad/s$. Discrepancies with the theoretical model can be observed even before the first 12 seconds. Moreover, there is an unexpected decay of u_θ near the rotating tube wall, which contradicts the no-slip condition. These observations suggest the presence of a secondary flow that constrains the development of u_θ. The same graph also shows a curve for $\Omega_3 = 5.8\ rad/s$ and 12 seconds, which demonstrate an even more significant impact of the secondary flow on

the u_θ profile both towards the centre and close to the rotating pipe. Furthermore, Figure 4.3 (b) illustrates the velocity profiles for Ω_1 at $l = D_o$ and $2D_o$, revealing a faster decay for u_θ in the former case. These observations show the correlation between the secondary flow and the u_θ magnitude, as well as a stronger influence near the orifice exit.

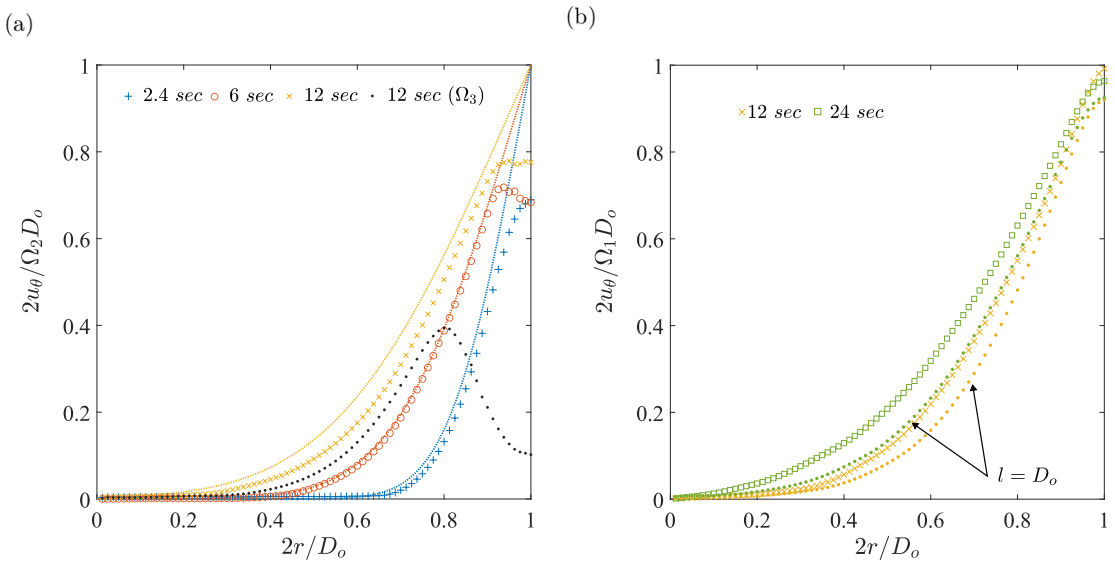

Figure 4.3: Evolution of the velocity profile for (a) $\Omega_2 = 4$ at $l = 2D_o$ where $\Omega_3 = 5.8$ rad/s and (b) for $\Omega_1 = 2$ at $l = D_o$ and $l = 2D_o$. The former are represented by dots and pointed out.

In order to study the characteristics of the secondary flow, an axi-symmetric laminar simulation was conducted in OpenFoam. The computational domain is depicted in Figure 4.4 (a), which is similar to the one that was utilized in Chapter 3. The domain comprises a cylindrical tank of length $15D_o$ and radius $5D_o$. A $10D_o$ long pipe with a diameter of $D_o = 32$ mm is located at the centre of the tank representing a section of the swirl system. It meets the no-slip condition and rotates with an angular speed of $\Omega_2 = 3.9$ rad/s, which is the only source of movement in the system. Based on this angular speed, the Reynolds number is defined as:

$$Re = \frac{D_o^2 \Omega}{2\nu} \approx 1000. \tag{4.5}$$

A total of 26000 grid points are distributed mainly in the pipe and around the orifice exit within the computational domain.

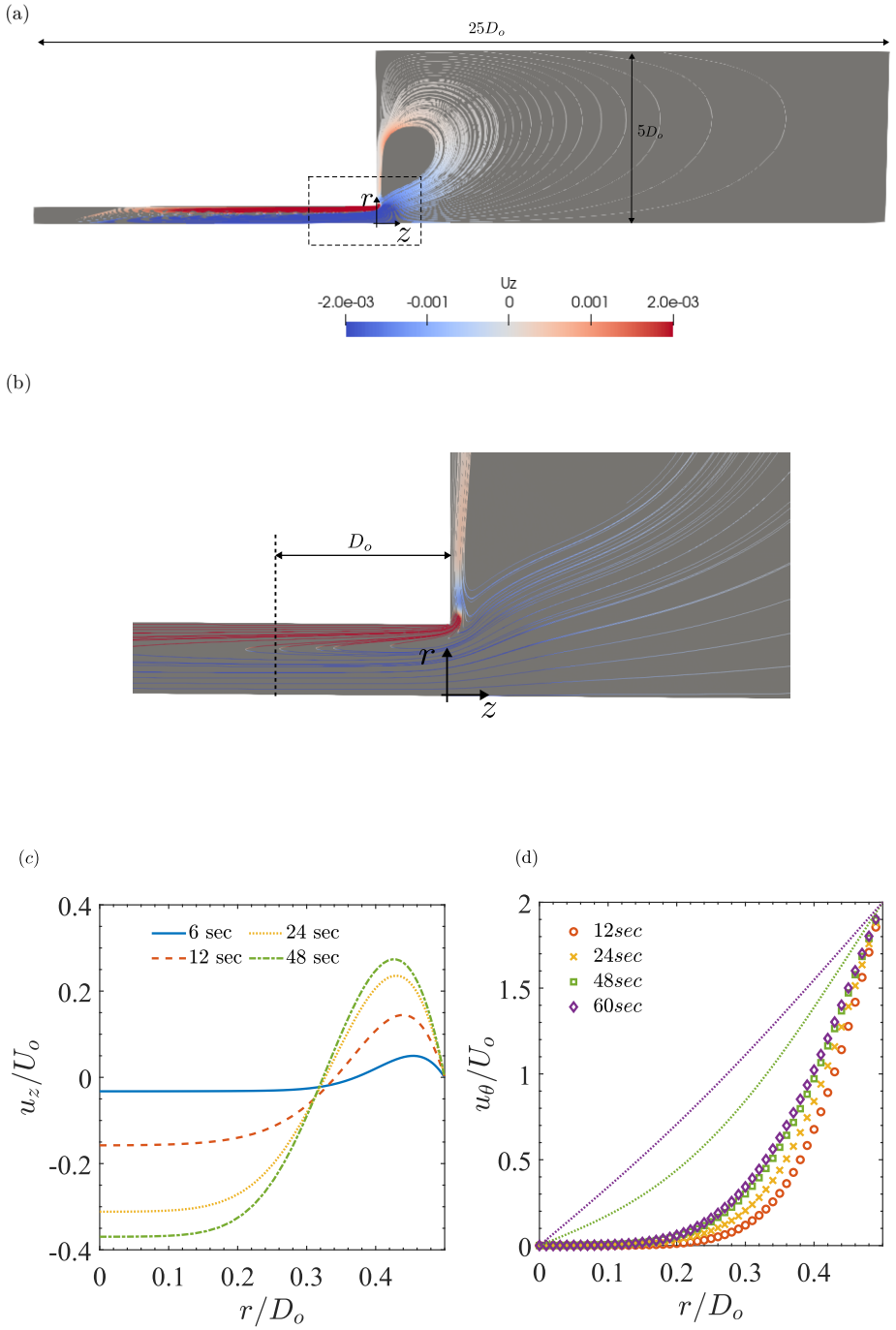

Figure 4.4: (a) Computation domain of the axi-symmetric simulation showing the streamlines in the r-z plane generated by the rotation of the pipe. (b) A closer look at the exit of the orifice. A dashed line marks the location where u_θ and u_z were obtained, (c) evolution of u_z and (d) u_θ profiles where the dash lines represent the theoretical velocities (Batchelor, 1967) and the symbols the numerical velocities. U_o is the discharge velocity defined in equation 4.8

In Figure 4.4 (a,b), it is entrained that the rotation of the pipe, in addition to u_θ,

also generates an axial flow, u_z, inside the pipe. Near the pipe wall, u_z is positive, where the flow is discharged in the tank. But, close to the pipe centre, u_z is negative, where the flow from the tank is absorbed into the pipe. The source of this flow is the pressure difference inside the pipe and the tank. It is a known fact that the pressure in a streamline increases outwards from the centre of curvature, and this can be expressed by the following equation:

$$\frac{\partial p}{\partial r} = \frac{u^2}{r}, \tag{4.6}$$

where R is the radius of curvature, creating a zone of high pressure near the pipe wall. Due to the fluid being expelled from the pipe, fluid around the orifice exit with initially zero u_θ is entrained to replace it, forming a recirculation zone along the pipe illustrated by streamlines In Figure 4.4 (b), it can be seen that the entrained flow occupies the central region of the pipe, decreasing u_θ.

The velocity profiles of u_z and u_θ are shown for $\Omega_2 = 3.9\ rad/s$ and at $l = D_o$ in Figure 4.4 (c) and (d). Initially, u_z is negligible for the first 6 seconds. Then, at $t = 12s$, a velocity profile is formed where u_z has a similar magnitude in both directions. Subsequently, The velocity of the flow entrained almost doubles the flow discharge velocity, increasing to above 30% of the characteristic discharge velocity U_o defined in equation (4.8). The velocity profiles obtained from u_θ exhibit differences with equation (4.3) similar to the experiments, where the solid-body rotation velocity distribution is not attained. However, there is a difference near the pipe wall. In the experiments, there was a sudden decrease of u_θ in that zone, which was not observed in the simulation. This suggests that the anomalies observed close to the pipe wall when the rotation speed increases may be due to an error in the PIV technique, as it did not consider u_z to estimate PIV Δt.

As the flow with $u_\theta \sim 0$ from the tank moves inside the pipe, its strength diminishes, which explains the faster deviation from the theoretical model observed for $l = D_o$ compared to $l = 2D_o$ in Figure 4.3 (b). This is further supported by the numerical work in Figure 4.5 (a), where u_θ was obtained from various positions inside the pipe, revealing a significant difference between the orifice exit profile and a position one orifice diameter (D_o) inside the pipe. Moreover, increasing the angular

speed of the rotating pipe results in more fluid being entrained by the pipe, leading to a greater decrease in u_θ, as demonstrated in the experiments, Figure 4.3, (a) and numerically Figure 4.5(b).

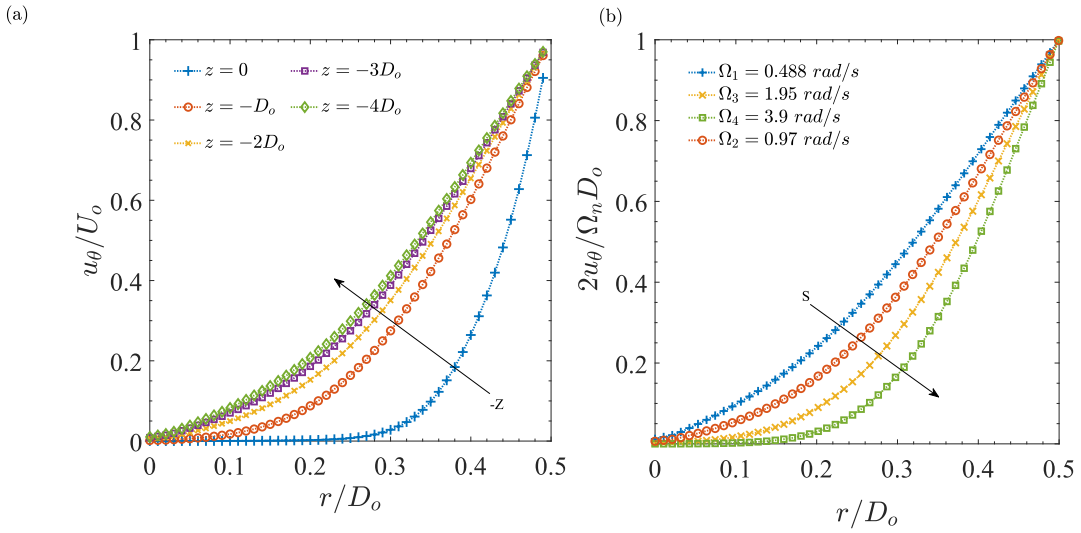

Figure 4.5: u_θ profiles (a) at different positions inside the pipe and (b) different angular speeds after 75 seconds of pipe rotation.

It is worth noting that the u_θ profiles shown earlier in Figure 4.2,4.3,4.4 and 4.5 are still valid solutions of the equation 4.3 regardless of an increase in the angular speed or the proximity to the orifice exit where measurements were taken. For example, the velocity profile at $l = 2D_o$ for 12 seconds matches with the curve at $l = D_o$ after 24 seconds; see Figure 4.3 (b). The effect of the secondary flow on $u_\theta(r,t)$ only affects the exponential term, consequently delaying the time evolution of the solution. A new solution that takes into account the influence of the secondary flow would look like the equation (4.7), where η is a function of z and u_z:

$$u_\theta(r,t) = \Omega r + \Omega D_o \sum_{n=1}^{\infty} \frac{J_1\left(\lambda_n \frac{2r}{D_o}\right)}{\lambda_n J_0(\lambda_n)} \exp\left(-\lambda_n^2 \frac{4\nu t}{D_o^2}\right) \exp\left(f(\eta)\right), \tag{4.7}$$

However, further work is needed to determine $f(\eta)$.

An interesting feature observed during the experiments was a recirculation zone formed at the orifice exit, similar to the one in Figure 4.4, but on a smaller scale. This occurred during the rotation of the pipe and before the piston stroke. As

the secondary flow developed, the fluid near the pipe wall was discharged to the tank, as mentioned earlier. However, instead of dissipating in the tank due to viscosity, it was entrained by the pipe, as shown in Figure 4.6, forming a recirculation zone at the orifice edge. But, it is only observed for the highest angular velocity $\Omega(S = 1) \geq 2\ rad/s$ at the bottom section of the orifice exit. This could be related to an alignment problem in the swirl system that, as is shown in Figure 4.9 (f), creates some instabilities in the bottom vortex core.

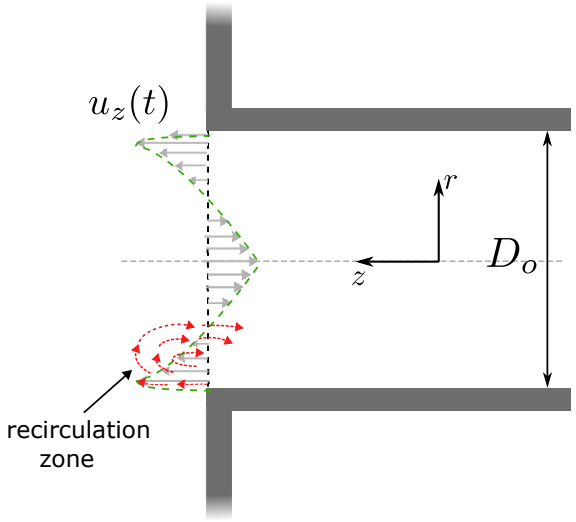

Figure 4.6: Illustrative schematic of the orifice exit, where a recirculation zone is generated due to pipe rotation.

4.1.2 Clean vortex rings

As mentioned at the beginning of this chapter, a partially established distribution of u_θ could help in reducing the generation of negative vorticity and its related consequences[1]. The objective is to create vortex rings with an azimuthal velocity corresponding to different swirl numbers, S, while minimizing vorticity production with an opposite sign. However, before that, it is essential to create a benchmark case of swirling vortex rings after 70 seconds of pipe rotation that ensures a fully established velocity profile.

[1]For both this chapter and the next one summarizing the experimental work, the vorticity is expressed in Cartesian coordinates. Instead of using the term "negative vorticity," the term " OSV' which stands for opposite sign vorticity, is used.

Fully established swirling vortex rings

A maximum angular speed of $\Omega_1 = 2\ rad/s$ was selected for the pipe. This choice was made because it closely matched the theoretical model for up to 12 seconds and reduced the intensity of the recirculation zone at the orifice exit. Furthermore, in order to achieve a maximum swirl number of $S = 1$, the discharge velocity was set to $U_o = 0.03125\ m/s$, which gives a $Re(D_o U_o/\nu) \approx 1000$. A trapezoidal velocity program, $U_p(t)$, was employed, with an acceleration of $0.07 m/s^2$ and a deceleration of $0.035 m/s^2$. The former lasted for 20% of the piston stroke time, Δt, while the latter lasted for 40%. The maximum speed of U_p was $0.029\ m/s$ with a piston stroke time of 2.05 *sec*. Das et al. (2017) suggested this program to minimize the formation of stopping vortices. This is discussed in further detail in the following chapter. The value U_o is the average discharged velocity at the orifice exit:

$$U_o = \frac{1}{\Delta t} \int_0^{\Delta t} \phi_c U_p(t) dt, \tag{4.8}$$

where ϕ is a positive constant that accounts for the different pipe diameters in the piston-cylinder and swirl systems as per the continuity equation. The stroke ratio used is $L/D_o = 2$, and with $\mathrm{S}(2\Omega D_o/U_o) = 0$, 0.25, 0.5 and 1.

Opposite sign vorticity (OSV) and ring circulation

The velocity field and vorticity contour plots for $S = 0.25$, 0.5 and 1 are shown in Figure 4.7. The vorticity is calculated from the velocity field by applying the central difference scheme to equation:

$$\omega = \frac{\partial u_y}{\partial z} - \frac{\partial u_z}{\partial y}, \tag{4.9}$$

expressed in Cartesian coordinates $\mathbf{u} = (u_x, u_y, u_z)$. The difference in the production of OSV is quite evident, particularly between $S = 0.25$ and 0.5. Although the OSV is weak for $S = 0.25$, its location, which is close to the centre, agrees with the finding from Chapter 3 concerning the relationship between OSV and the distribution of u_θ. This is also observed for $S = 0.5$ and 1 where the onset of OSV formation

occurs at the centre and then moves around the vortex core interacting with it and causing destabilization and vorticity cancellation. Also, the velocity field allows us to observe the vortex breakdown reported in Chapter 3.

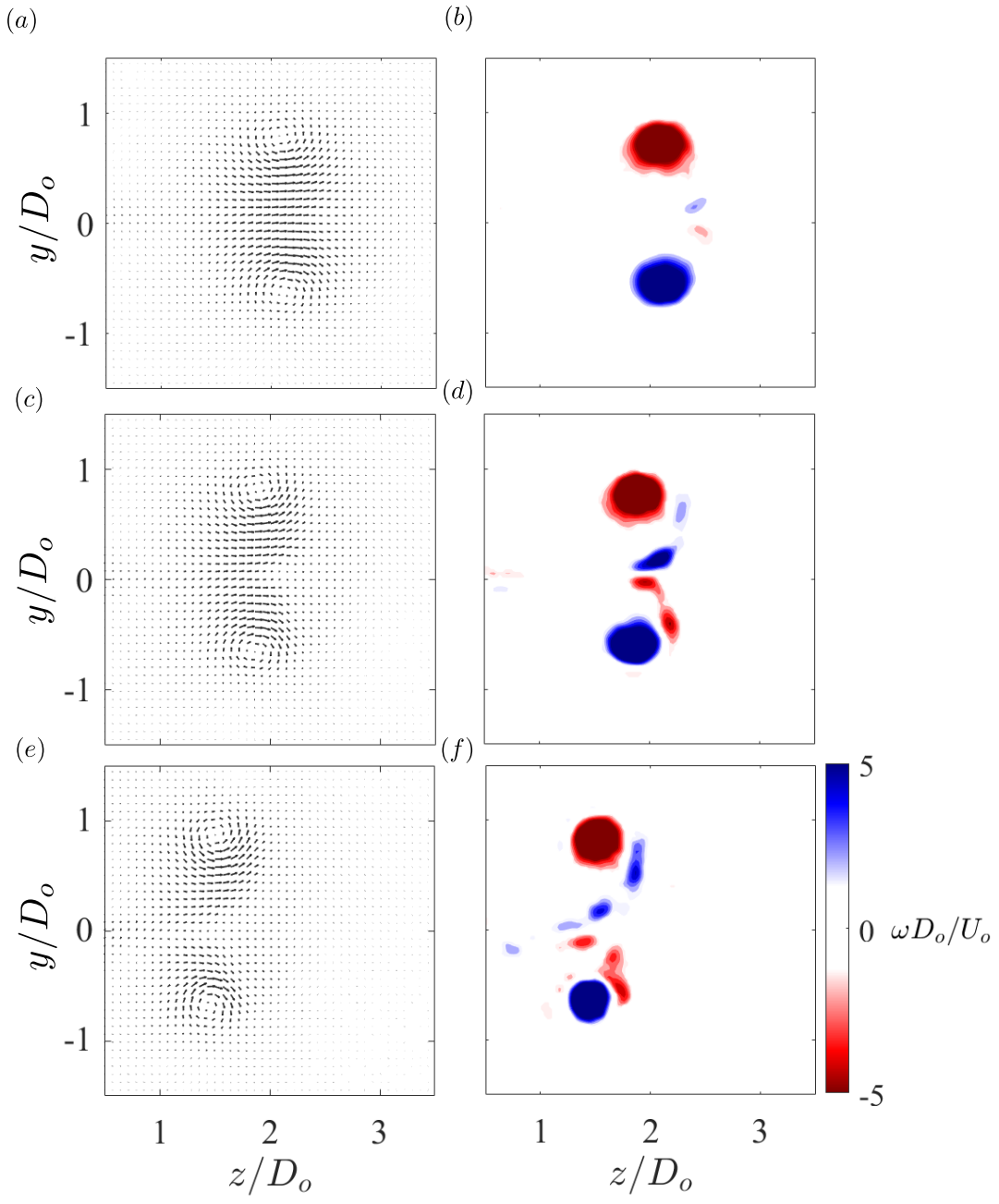

Figure 4.7: Velocity field (first column) and vorticity contour (second column) plot at $T^* = 5$ for (a,b) $S = 0.25$, (c,d) $S = 0.5$ and (e,f) $S = 1$, with a threshold of $|\omega| > 0.25\ s^{-1}$ for all the cases.

To measure the production of OSV, Figure 4.8 (a) compares the circulation

generated by the OSV at different S values. The threshold $|\omega| > 0.25\ s^{-1}$ is applied to remove background noise from the cross-correlation process. As expected, the circulation increases as S increases. For $T^* < 5$, the increase in circulation is directly proportional to the increment in S. Specifically, when S is raised from 0.25 to 0.5, the resulting Γ^* doubles that $S = 0.25$. When S is further increased to 1, the resulting Γ^* is roughly twice that $S = 0.5$. However, the threshold applied is not enough to remove most of the background noise with a magnitude, $|\omega| \sim 1\ s^{-1}$, but applying a threshold with that value would remove regions of OSV that are not related to the background noise. To discard the noise, the time-average circulation of the OSV for the $S = 0$ case was calculated and subtracted from the other S cases. This time-average circulation includes the OSV from the background noise and the regions I and II; see Chapter 3. The circulation after subtraction is shown as dashed lines in Figure 4.8 (a). The difference is small for $S = 0.5$ and $S = 1$ but larger for $S = 0.25$, where the time-average circulation is even greater in some periods given positive circulations.

In Figure 4.8 (b) and (c), the same dimensionless circulation is shown as in Chapter 3, Figure 3.10. The numerical simulation revealed that for $S = 0.25$, the circulation magnitude was higher than in the other swirl numbers studied, which collapsed into a single curve. This difference was attributed to a different source of OSV for $S = 0.25$, related to the discharge velocity profile rather than the u_θ distribution. The threshold $|\omega| > 0.25\ s^{-1}$, shown in Figure 4.8 (b), also has a higher value for the $S = 0.25$ case, but it was not separated from the other cases, being similar to the curve for $S = 0.5$. As a result, the conclusion from Chapter 3 about the source of OSV for $S = 0.25$ is not applicable since it has the same dimensionless circulation as the $S = 0.5$ case, where there is a strong production of OSV which comes from u_θ. In Figure 4.8 (c), the time-average circulation of the $S = 0$ case was subtracted, which decreased the circulation significantly, especially for $S = 0.25$. The maximum value of circulation for $S = 0.25$ dropped from around 2.5 to 1.5. However, it is still close to the circulation obtained from $S = 0.5$. Additionally, regardless of the method used to remove the background noise, the dimensionless circulation for $S = 1$ had the lowest magnitude. This is explained by

Figure 4.5 (b), which shows that for higher swirl numbers, the magnitude of u_θ is closer to zero as it approaches the centre. This reduction would also decrease the formation of OSV observed in Figure 4.8(b) and (c).

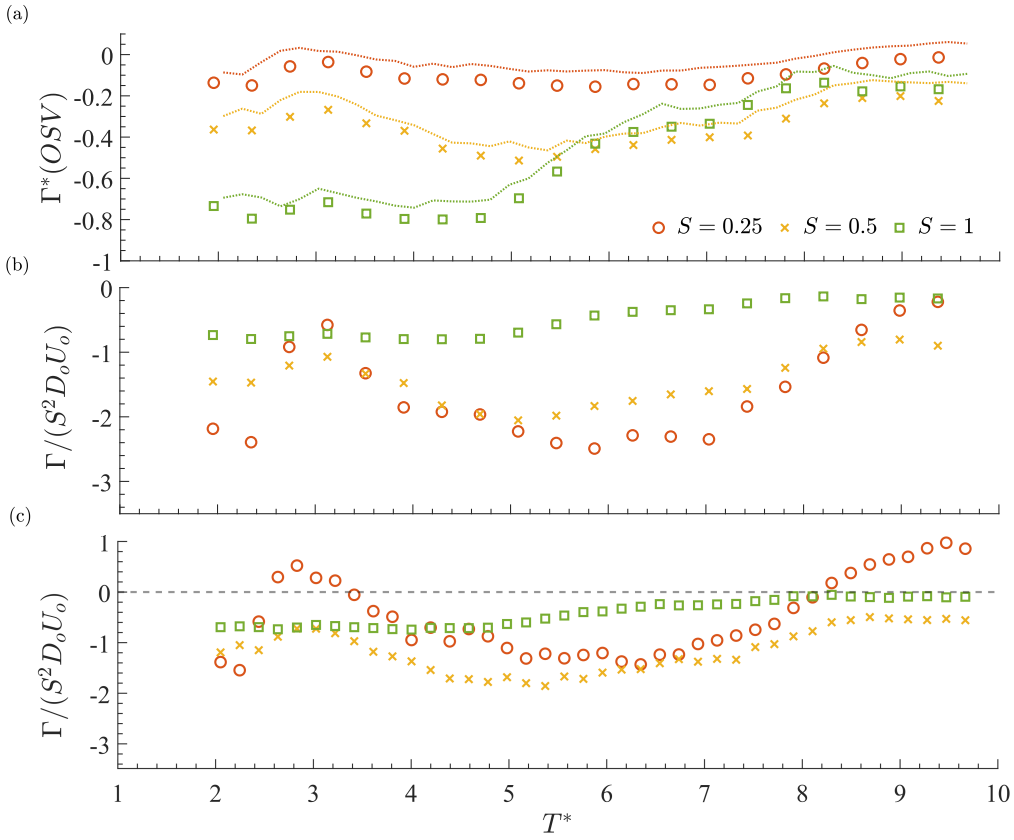

Figure 4.8: Evolution of the dimensionless circulation is shown in (a) using equation (1.2) with a threshold of $|\omega| > 0.25$ represented by marks and subtracting the time-average circulation for $S = 0$ represented by dashed lines. (b) and (c) show the dimensionless circulation, as defined by equation (3.24), for different values of S. The former uses a threshold of $|\omega| > 0.25$, while the latter subtracts the time-averaged circulation for $S = 0$.

When T^* is greater than 5, there is a sudden decrease in the circulation for $S = 1$. This drop occurs because of the strong interaction between the vortex ring and the OSV, leading to vortex cancellation. As a result, the circulation values become similar to those observed for the $S = 0.5$ case. Figure 4.9 shows the vorticity contour plots for $S = 0.5$ (first row) and $S = 1$ (second row) at different T^* values of 4, 5, and 6. At $T^* = 4$ and $S = 1$, the OSV has surrounded the vortex core, destabilizing it and leading to vorticity cancellation. At $T^* = 5$, it is not possible to distinguish

between the two swirl numbers. Still, a zone of high OSV concentration is formed for $S = 0.5$, causing a delay in the cancellation process as a low vorticity magnitude zone dissipates faster. At $T^* = 6$, most of the OSV has been dissipated or cancelled for $S = 1$. This cancellation can be observed in the shape of the vortex core, particularly the one with negative vorticity, see Figure 4.9 (f). This vortex interacts with the OSV as well as the recirculation flow at the orifice exit discussed earlier. Vorticity cancellation can be observed through an alternate method: the vortex

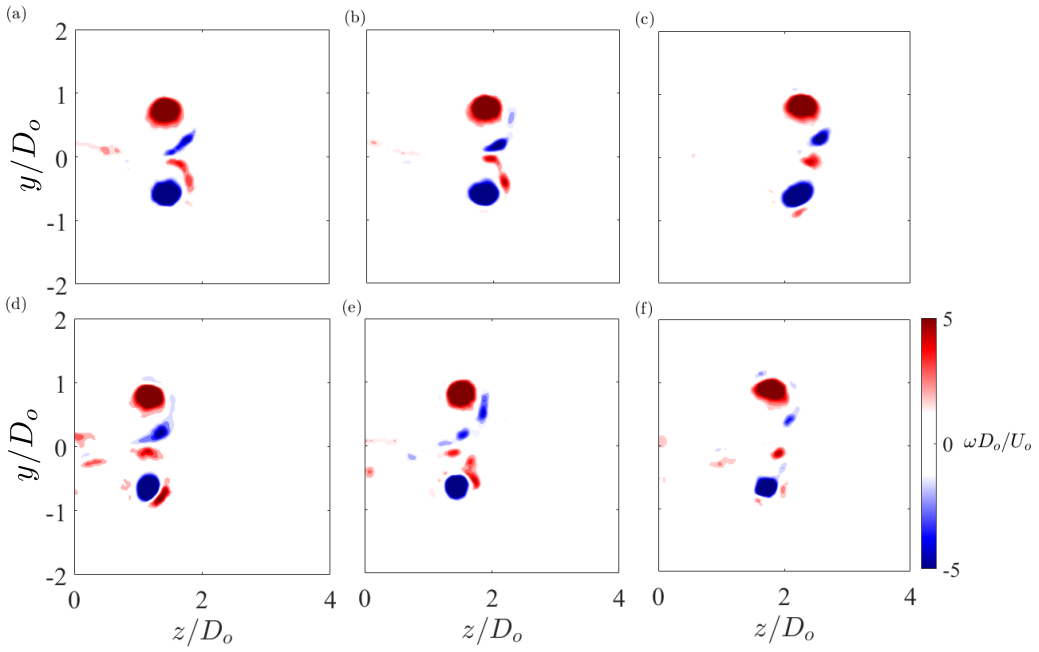

Figure 4.9: vorticity contour plots for $S = 0.5$ (first row) and $S = 1$ (second row) at different T^* values of 4 (a,d), 5 (b,e), and 6 (c,f).

ring circulation. Figure 4.10 compares the evolution of the vortex ring circulation for different values of S. In all cases, there is a decay in Γ^*_{Ring}, which increases as S grows due to the effects of viscosity dissipation and vorticity cancellation. After $T^* = 5$, the rate of decline for $S = 1$ increases due to a stronger interaction with the OSV, also observed in Figure 4.8 (a). Although the ring vorticity and OSV both decrease, the decrease is more pronounced for the OSV because of its weaker vorticity magnitude. As mentioned before, with reference to Figure 4.9 (f), the negative vortex core is more unstable than the positive one due to its early interaction with the recirculation flow at the orifice exit. The dotted line in Figure 4.10 captures this

effect, showing a faster decrease in its circulation than the positive vortex core. It is for this reason that all Γ_{Ring} and Γ_{OSV} values presented in this section come from the positive vortex ring core. Due to its short stroke ratio, $L/D_o = 2$, Γ_{Ring} was not determined by any method, but only by a threshold of $\omega > 1$.

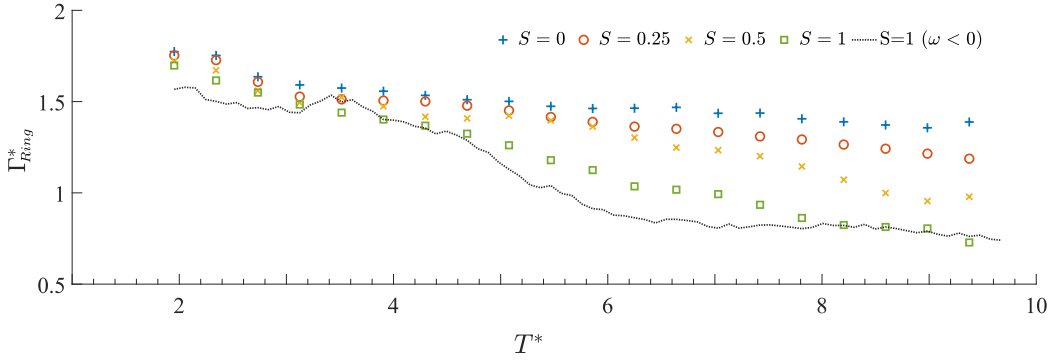

Figure 4.10: Evolution of the ring circulation Γ^*_{Ring} for all S. The dotted line $(\cdots)$ refers to the circulation of the negative core shown in Figure 4.9 (f)

Propagation

Based on Chapter 3, it was concluded that the formation of OSV close to the centre of the vortex ring results in an axial velocity that moves in the opposite direction to the ring's propagation velocity. This leads to the formation of a stagnation point, which, following the continuity equation, enhances the radial velocity of the vortex ring. Figure 4.11(a) shows the evolution of the ring radius, R for different S values. R was determined using the vortex core centroids defined as follows:

$$R = \frac{\iint \omega y \, \mathrm{d}y\mathrm{d}z}{\iint \omega \, \mathrm{d}y\mathrm{d}z} \quad Z = \frac{\iint \omega z \, \mathrm{d}y\mathrm{d}z}{\iint \omega \, \mathrm{d}y\mathrm{d}z}. \tag{4.10}$$

As the swirl number increases, there is a significant increase in the vortex ring radius. At $S = 1$ and $T^* \approx 6.5$, there is a 30% growth compared to a non-swirling ring. The cases with S=0.25 and 0.5 show a positive increase rate throughout the studied period. However, for $6.5 < T^* < 7.5$, the radius of the ring with S=1

decreases, reaching the same values as $S = 0.5$. This change in radial propagation is due to the instabilities triggered by the interaction with the OSV. To observe this behaviour in more detail, Figure 4.12 shows the trajectories of the cores for a vortex ring with $S = 1$ as well as the vorticity contour plots starting from $T^* = 5$, in steps of 0.5, up to $T^* = 8$. It can be seen that the negative core radius (blue) does not increase, but rather the opposite happens for $6.5 < T^* < 7.5$. The same is observed for the positive core (red) but for $T^* > 7.5$.

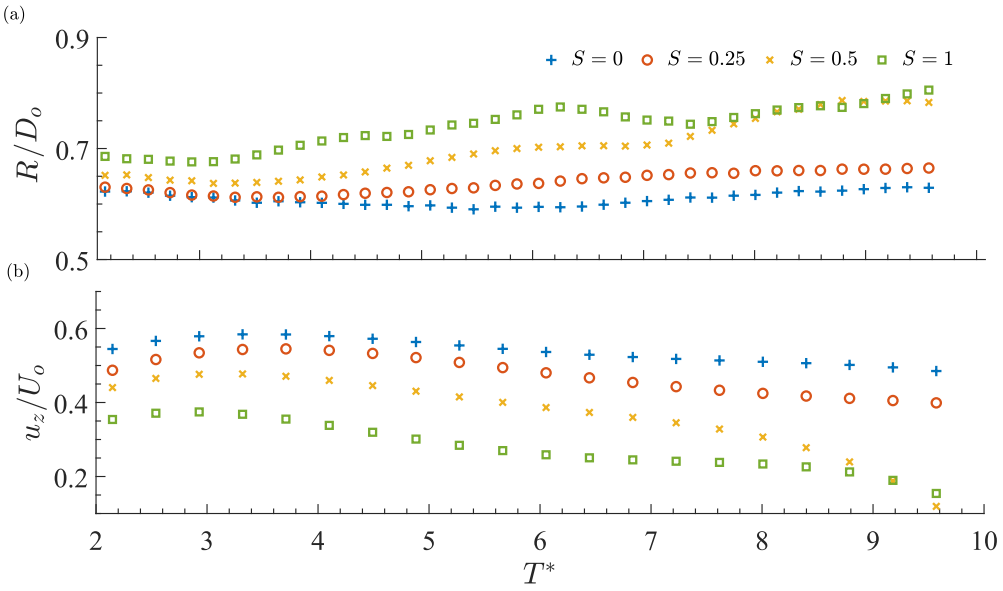

Figure 4.11: (a) Evolution of (a) the ring radius and (b) propagation velocity for different S.

Figure 4.11 (b) shows the different propagation velocities, $u_z^{'}$ for every S, which confirms the relation between the ring radius and propagation velocity given by:

$$u_z^{'} \sim \frac{\Gamma_{Ring}}{4\pi R}. \tag{4.11}$$

In the case where $S = 1$, the rate at which the velocity decays changes when $T^* = 6$. The speed then stays relatively constant until $T^* = 8$. During this same time interval, the radius of the ring drops and then begins to increase again after $T^* > 8$. As expected, the propagation velocity decreases during this time. The same pattern is observed with the $S = 0.5$ vortex ring, where there is faster radius growth for

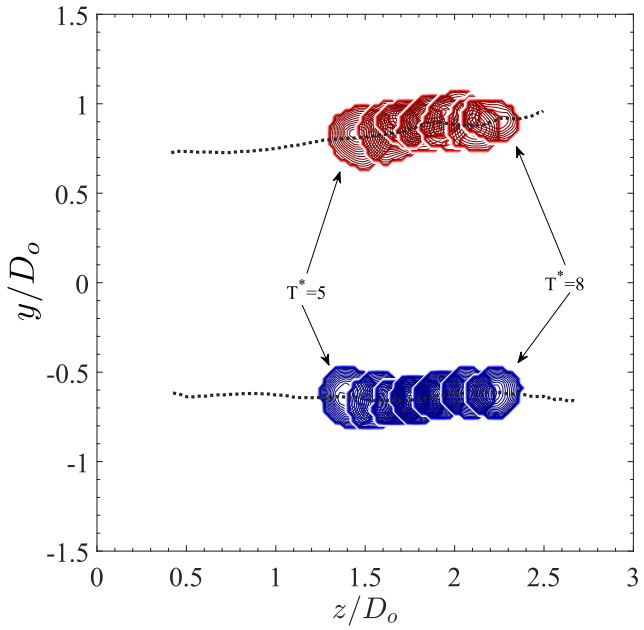

Figure 4.12: Trajectories of the core centroids obtained from equation (4.10) and the vorticity contour plots, from $T^* = 5$ to 8, with 0.5 time steps increments.

$T^* > 7.5$, leading to a faster decay of the propagation velocity.

Azimuthal velocity u_θ

As described in Chapter 2, the implementation of stereoscopic PIV enables the examination of the distribution of u_θ for different S values as well as the vorticity contour plot for $|\omega| = 1$ represented by dashed lines. Figure 4.13 displays the u_θ distribution for S=0.5 at $T^* = 4, 5, 6, 7, 8$ and 9.

Initially, the vortex sheet carries u_θ from the orifice to the vortex core through the roll-up process. After the formation of the vortex ring is complete, when the trailing jet is no longer present at $T^* \approx 6$, the u_θ that was not engulfed by the ring forms a wake which is stretched and dissipated as the vortex ring moves downstream. These contour plots illustrate that only a small percentage of the u_θ delivered from the swirl system ends up in the vortex rings. This u_θ is mostly derived from the boundary layer that is formed in the swirl system when the fluid is discharged. This ensures that the ring engulfs the u_θ with the highest magnitude. It is interesting to note in Figure 4.13 (e) how opposite sign u_θ (in comparison with the u_θ in the

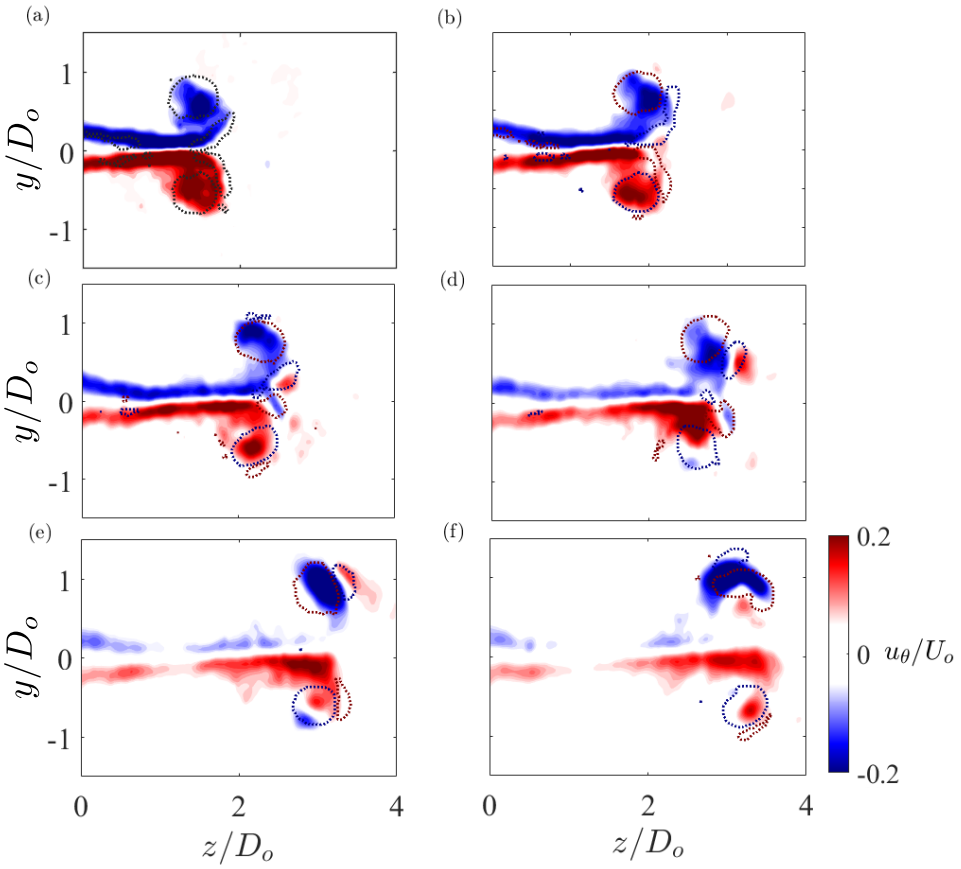

Figure 4.13: u_θ distributions for $S = 0.5$ at (a) $T^* = 4$, (b) $T^* = 5$, (c) $T^* = 6$, (d) $T^* = 7$, (e) $T^* = 8$ and (f) $T^* = 9$. The dashed lines represent a vorticity contour plot for $|\omega| = 1$.

closer vortex core) moves around the vortex core. This u_θ is transported by OSV, as shown in Figure 4.13 (b) at $T^* = 5$, where two regions of OSV are present around the centre. Since the u_θ distribution is not perfectly symmetric, the corresponding OSV, for every core, transports u_θ that correspond to the other vortex core, as seen in Figure 4.13 (c) at $T^* = 6$. Another feature only observed for the $S = 0.5$ case is found in Figure 4.13(e) and (f), which is the sudden increase of negative u_θ. The mechanism behind this phenomenon is still uncertain, but from a series of vorticity distributions, it was observed that this is not developed in the z-r plane, but it is transported in the azimuthal direction. However, further analysis is needed to

resolve this issue.

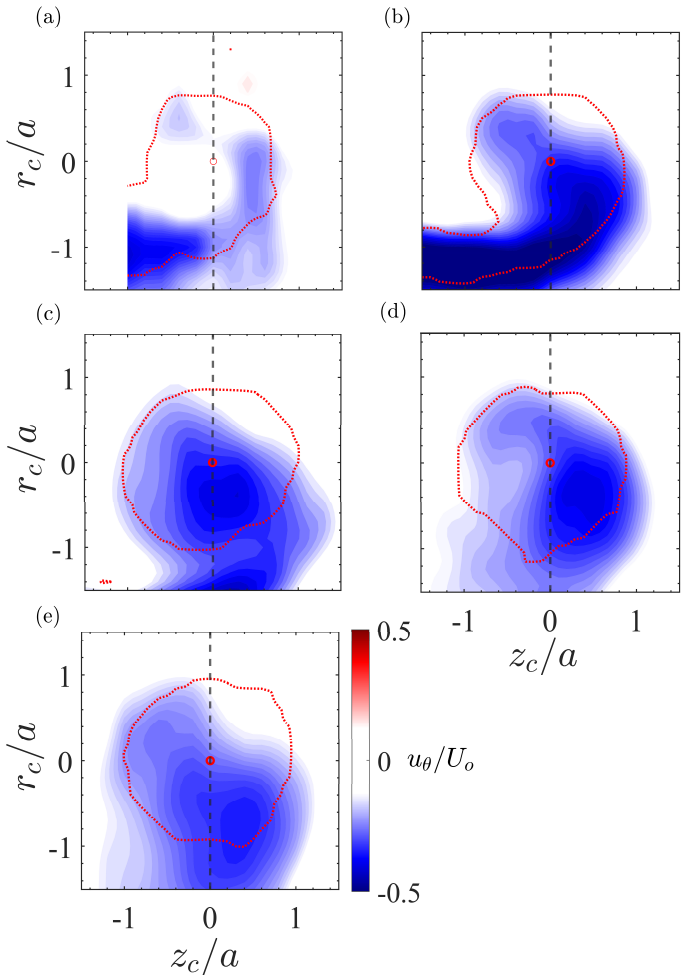

Figure 4.14: The u_θ distribution in the vortex core is represented by a red dashed line for $S = 1$ at different values of T^*, namely (a) $T^* = 1.65$, (b) $T^* = 2$, (c) $T^* = 3$, (d) $T^* = 4$, and (e) $T^* = 5$. The red dot indicates the core centroid and the vertical black dashed line shows where the profile, presented in Figure 4.15, was obtained.

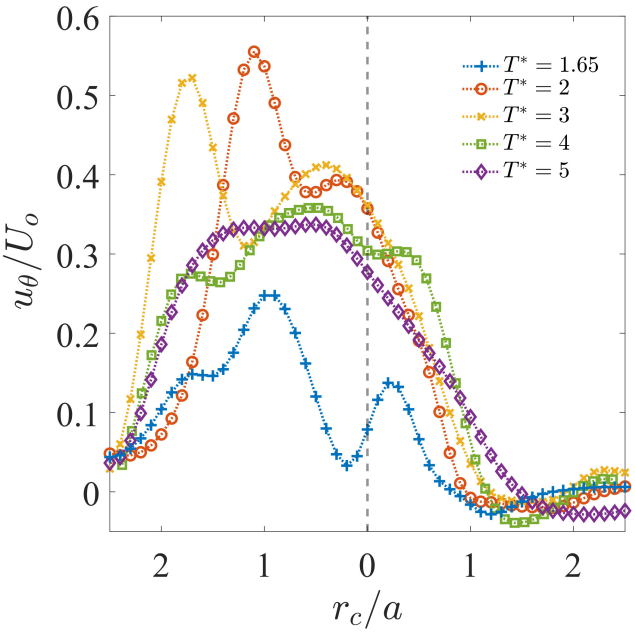

Figure 4.15: u_θ profile evolution at the vortex core. The coordinate system is located at the vortex centroid and scaled with the ring radius, a.

In Figure 4.14, a closer view of the distribution of u_θ in the vortex core for $S = 1$ is shown. The red dashed line represents the core area, and the red dot represents the core centroid. At $T^* = 1.65$, the vortex ring is still in the process of formation. It is observed that u_θ is engulfed in the core via the roll-up of the vortex sheet. Later, u_θ covers most of the core area, but its distribution appears to be independent of the vorticity distribution, leaving zones of low or zero u_θ inside the core.

Figure 4.15 shows the evolution of the u_θ profile in the core, which complements the u_θ distributions. The profiles were extracted from the vertical dashed lines in Figure 4.14 and were plotted on a coordinate system with the core centroid set as the origin and scaled by the core radius, a. A vertical line has been added to indicate the centre of the vortex core.

For $T^* = 1.65$, there are two peaks for u_θ: one for the trailing jet (on the left) and the other for the u_θ that has been engulfed by the vortex core through the roll-up process but has not yet reached the core centre where u_θ is zero. At a later time, u_θ reaches the core centre, but its maximum value was not found at this point for all the times analyzed, as a Gaussian distribution would suggest. Instead, the

u_θ distribution is denser in the half closer to the ring centre, as reported in Chapter 3. u_θ decays abruptly for the other half. This behaviour is observed in Figure 4.14, where a weak zone of u_θ is located mainly in the second half of the core. It appears that the u_θ distribution is more symmetric in the propagation direction.

To quantitatively analyse u_θ in the vortex ring core, the spatial average in the vortex core was calculated, $\overline{u_\theta}$, similar to that which was done in Chapter 3 –see equation(3.28)–. The region from where the data was collected is shown by the dashed lines in Figure 4.13 (excluding the OSV regions), which corresponds to the core area after applying the threshold and representing only a fraction of the u_θ distribution. The results are presented in Figure 4.16 (a), along with the highest value of u_θ in the core for different S, as Naitoh et al. (2014) presented. Both parameters exhibit a noticeable variation among the three cases examined, which corresponds to the difference in angular velocities employed for each case:

$$\bar{u_\theta}(S = 1) \sim 2\bar{u_\theta}(S = 0.5) \sim 4\bar{u_\theta}(S = 0.25). \tag{4.12}$$

In contrast to the findings in Chapter 3, as illustrated in Figure 3.14, no noticeable decay in u_θ was observed for any of the cases or the effect of vortex ring stretching. In Figure 4.16 (a), the three dashed lines represent the time averages of $\overline{u_\theta}$ for each S, and with the exception of the case $S = 0.5$ for $T^* > 7$ where a sudden increment mentioned above takes place, these constant values accurately describe the behaviour of u_θ over the analysed time period. However, applying the dimensionless azimuthal velocity:

$$u_\theta^* = \frac{4\overline{u_\theta}R(t)}{\Omega D_o^2} = \frac{2\overline{u_\theta}R(t)}{\mathrm{S}U_0 D_o}, \tag{4.13}$$

used in Chapter 3 to capture the ring radius effect causes a partial collapse of the different curves shown in Figure 4.16 (c). This partial collapse is more related to the $1/S$ factor, as the effect of the ring radius seems minuscule.

4.1.3 Partially established swirling vortex rings

Previously, it was observed that only a small portion of the u_θ provided by the swirl system contributes to the formation of the vortex ring. This small portion is located

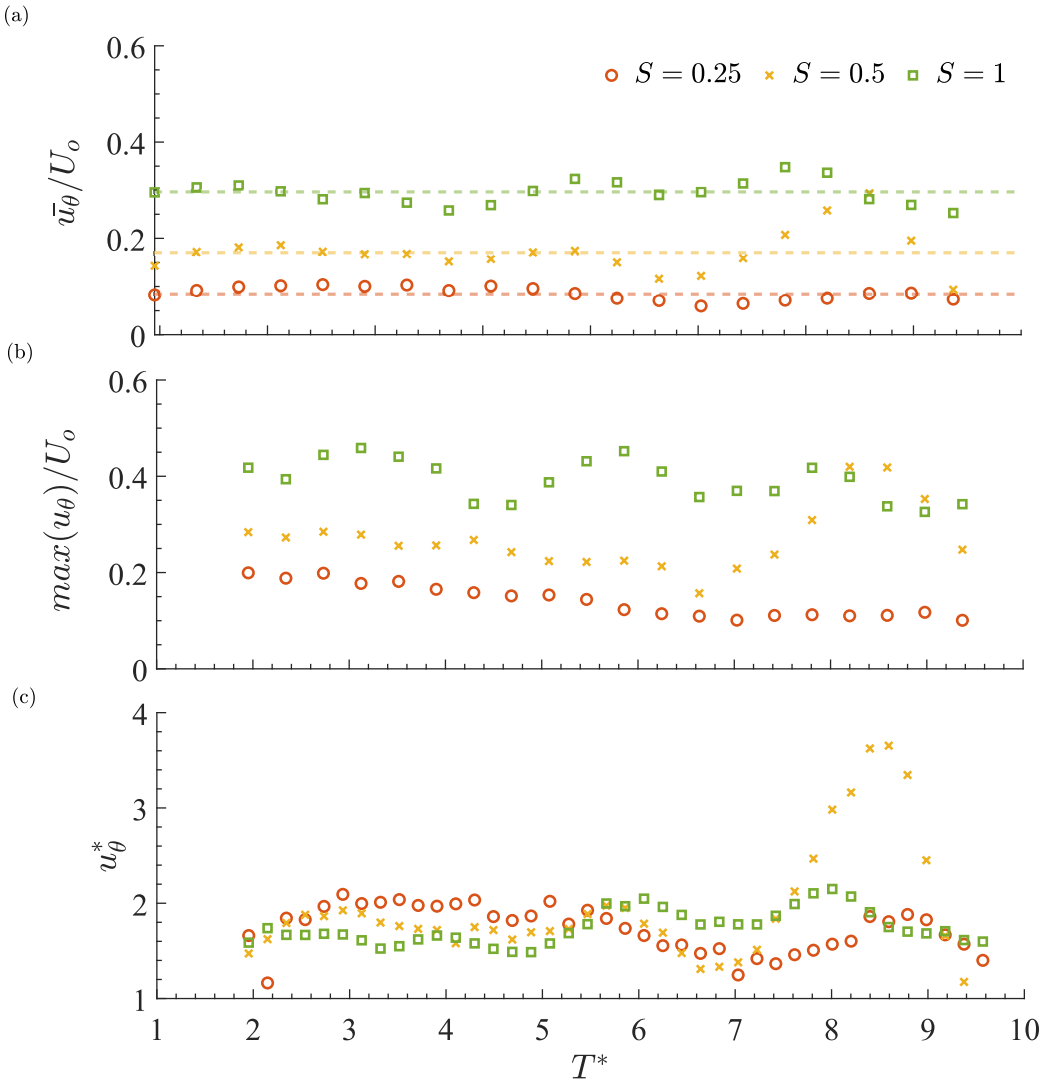

Figure 4.16: Evolution of (a) spatial average u_θ in the vortex core where the dashed lines represent the time average $\overline{u_\theta}$, (b) the maximum u_θ in the core and (c) the dimensionless u^*_θ used in Chapter 3 for all S

in the boundary layer that is created during the flow discharge and becomes a vortex sheet that rolls up to form the vortex ring. Figure 3.4 (a) and 5.17 (b) show that this boundary layer only represents around 10% of the orifice radius. Therefore, using a partially established u_θ profile it is possible to produce a swirling vortex ring with a specific S and with a low u_θ close to the orifice centre, which would reduce the formation of OSV.

The previous section established that the theoretical time required to achieve a solid body rotation profile was approximately 60 seconds, which we refer to as

"preparation time." Assuming that only the flow near the pipe's wall contributes to forming a vortex ring, increasing the pipe's angular speed can reduce the preparation time while maintaining similar flow conditions as in the case of a lower angular speed with a longer preparation time. To quantify this, the average value of u_θ using the theoretical model for the domain of $0.4 < r/D_o < 0.5$ was calculated:

$$\overline{u_\theta}_p = \frac{10}{D_o} \int_{0.8D_o/2}^{D_o/2} u_\theta(r,t)dr. \tag{4.14}$$

In Figure 4.17 (a), two examples of the areas under the u_θ profiles at 5 and 30 seconds are shown, where $\overline{u_\theta}$ was calculated. The selected domain represents 20% of the orifice radius to ensure that most of the u_θ located in the vortex core comes from this region. Figure 4.17 (b) shows the evolution of $\overline{u_\theta}_p$. During the first 10 seconds, it has a higher increment and then reaches an asymptotic state after 20 seconds. For the ideal case where u_θ has a solid body rotation like distribution, the $\bar{u_\theta}$ for a swirling vortex ring is:

$$\overline{u_\theta}_p = \frac{10}{D_o} \int_{0.8D_o/2}^{D_o/2} u_\theta(r,t)dr = \frac{10\Omega}{D_o} \int_{0.8D_o/2}^{D_o/2} rdr = \frac{9}{20} D_o\Omega, \tag{4.15}$$

or in dimensionless form:

$$\overline{u_\theta}_p/U_o = \frac{9}{10}S; \tag{4.16}$$

that is, the value reached by $\overline{u_\theta}_p$ in Figure 4.17 (b) as time goes to infinity. Therefore, to generate a vortex ring with $S = 0.5$, which implies a maximum $\overline{u_\theta}_p/U_o = 0.45$ (ideal case), the preparation time needed is less than 5 seconds for a swirl system set to generate vortex rings with $S = 1$. For that reason, to compare different swirling vortex rings, it is important to characterise them, regardless of the angular speed of the rotating pipe, in terms of how S is defined. The time-averaged angular velocities shown in Figure 4.16(a) were used for this purpose.

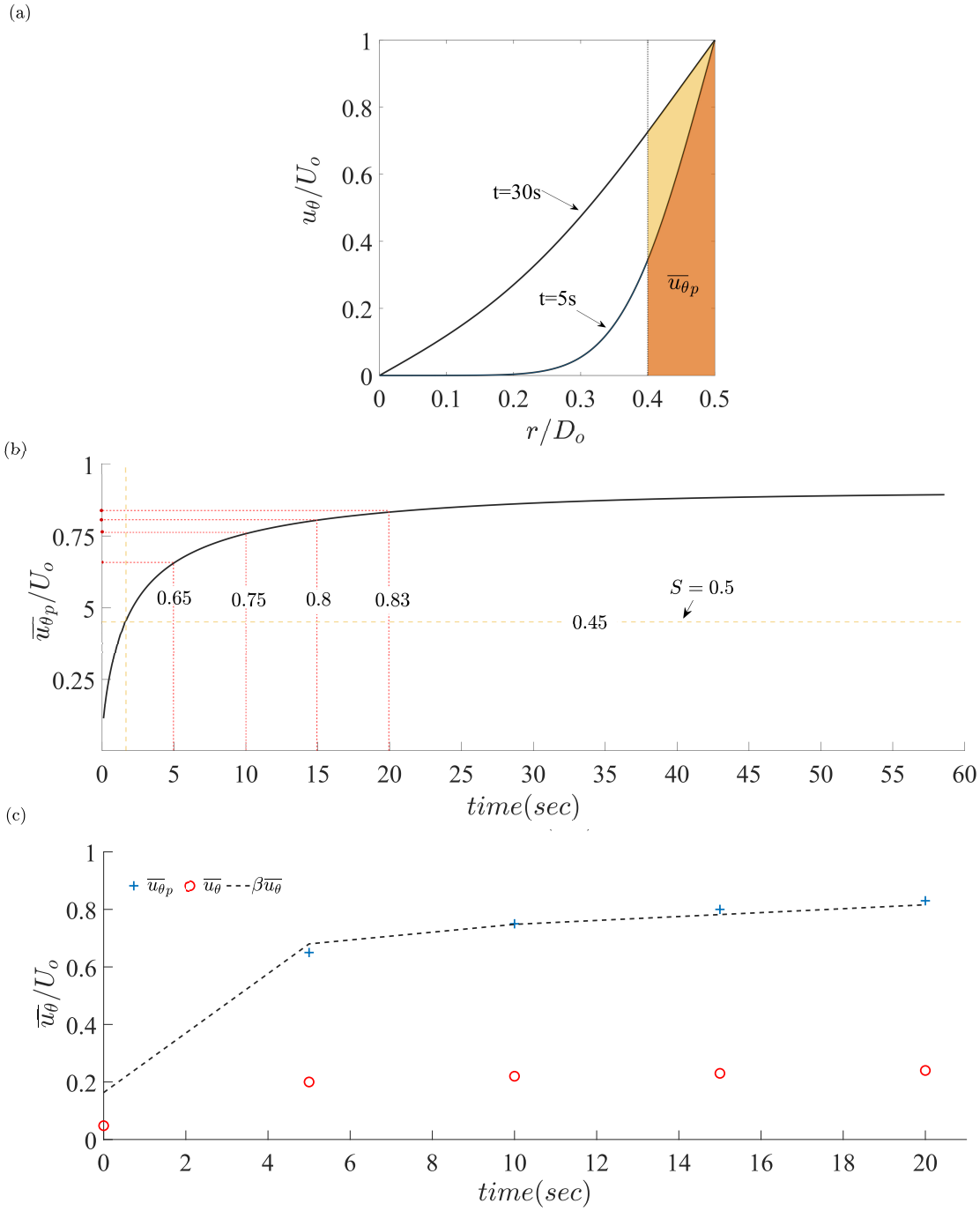

Figure 4.17: (a) Comparison between the two areas under the u_θ profile (based on the theoretical model) at 5 and 30 seconds and for $0.4 < r/D_o < 0.5$, where $\overline{u_\theta}_p$ is calculated. (b) Evolution of $\bar{u}_{\theta p}$ with a Ω set to generated $S = 1$. The red dashed lines mark the different preparation times used in the experiment and their corresponding dimensionless u_θ values. The yellow dashed line indicates the $\overline{u_\theta}_p$ required to create a ring with $S = 0.5$. (c) Comparison between the time-averaged $\overline{u_\theta}$ for different preparation times and their corresponding $\overline{u_\theta}_p$, where the scalar $\beta = 3.4$ is applied to compare the velocity behaviours.

In the upcoming experiment, five distinct preparation times were utilized: 0, 5, 10, 15, and 20 seconds. These times were compared to the previously studied cases of 75 seconds, representing a fully established velocity profile. It is important to note that this time interval did not incorporate the period when the piston stroke occurred, which took approximately 2 seconds. All the other parameters remained the same as in the previous experiment.

Different vorticity contour plots for varying preparation times are shown in Figure 4.18. When the swirl system was only active during the piston stroke, no visible changes occurred in the vortex ring. However, after 5 seconds of preparation time, the onset of OSV formation is observed, increasing with longer preparation times. As shown in Figure 4.18 (a), the ring is initially isolated, but as the preparation time increases, a wake starts to form, despite all the rings having the same $L/D_o = 2$. In Chapter 3, it was discussed that the addition of swirl increases the vorticity flux. However, computing the total circulation for each case at $T^* = 4$ resulted in $\Gamma^*_{Total} = 1.7 \pm 0.1$, suggesting that the observed trailing jet is caused instead by a reduction in the formation number. This phenomenon is also evident when comparing the core sizes in Figure 4.18.

In order to classify the vortex rings generated for each preparation time, Figure 4.19 displays the different values of $\overline{u_\theta}$ as well as the maximum u_θ in the vortex core. The time-averaged $\overline{u_\theta}$ used to characterize the vortex ring are shown as dashed lines, and their respective values are presented in Table 4.1 as well as for different swirl numbers studied in the previous section with the corresponding $\overline{u_{\theta_p}}$ for each case. Only values below $T^* = 5$ were used to compute the time average $\overline{u_\theta}$ due to the interaction between the vortex ring and the OSV, which destabilizes the core affecting the $\overline{u_\theta}$. In both methods of analyzing u_θ, a considerable increase is observed between the 0 and 5 seconds preparation time, equivalent to around 50% of the maximum u_θ obtained for the $S = 1$ case. When the preparation time exceeds 5, the variation between different cases is small. This can be attributed to the rapid growth of $\overline{u_{\theta_p}}$, which is illustrated in Figure 4.17 (b). In the first 5 seconds, $\overline{u_{\theta_p}}$ increases from 0 to 65% of U_o, but subsequently, the increment is only around 15% from 5 to 20 seconds.

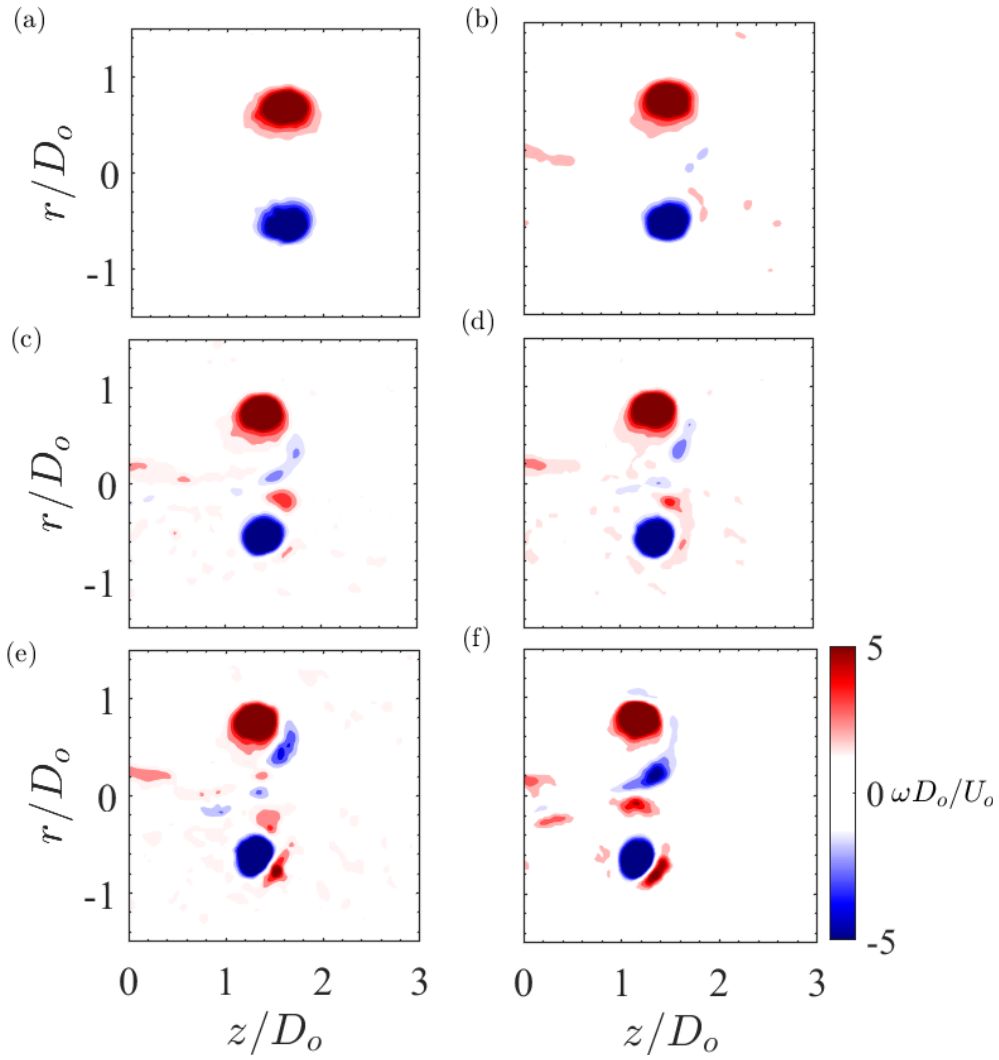

Figure 4.18: Vorticity contour plots at $T^* = 4$ for different preparation times (a) 0, (b) 5, (c) 10, (d) 15, (e) 20 and (f) 75

	S			Preparation time (sec)				
	0.25	0.5	1	0	5	10	15	20
$\overline{u_\theta}/U_o$	0.09	0.17	0.29	0.048	0.2	0.22	0.23	0.24
$\overline{u_{\theta p}}/U_o$	0.225	0.45	0.9	-	0.65	0.75	0.8	0.83

Table 4.1: Time-average azimuthal velocity, $\overline{u_\theta}$, values for different S with a preparation time of 75 sec and for preparation times: 0, 5, 10, 15 and 20 seconds and their corresponding $\overline{u_{\theta p}}$.

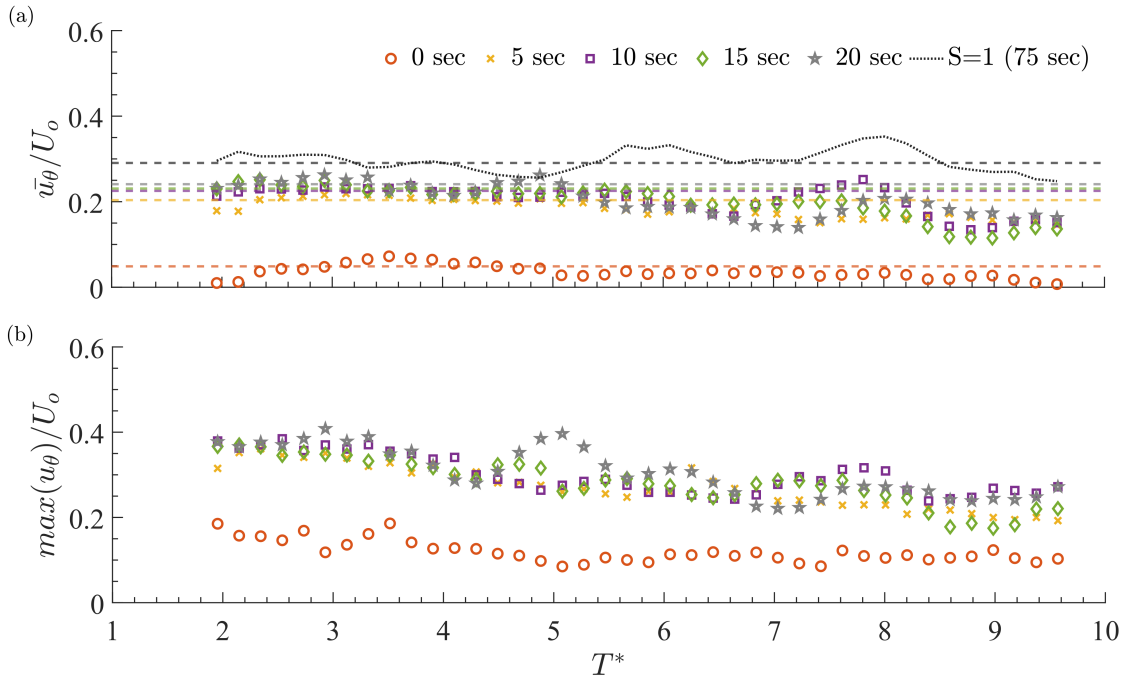

Figure 4.19: Evolution of (a) spatial average u_θ in the vortex core where the dashed lines represent the time average $\overline{u_\theta}$, (b) the maximum u_θ in the vortex core for all S.

According to the model, it estimates that the preparation time required to generate a vortex ring with $S = 0.5$ is around 2.25 seconds. Based on time averaged $\overline{u_\theta}$, the case $S = 0.5$ is in good agreement with the experimentally obtained value of $\overline{u_\theta}$ for a preparation time of 5 seconds. The difference between the preparation times is attributed to the secondary flow generated during the pipe rotation. Besides, the model assumes that all the fluid in the vortex core comes from the flow discharged through the orifice, which is not entirely accurate as some of the fluid comes from the ambient flow with null u_θ. In order to measure the impact of the engulfing of ambient flow, Figure 4.19 (c) compares the estimated $\overline{u_\theta}_p$ for different preparation times with the values obtained in experiments. Although there is a noticeable difference between the cases, the behaviour is similar, increasing slightly after five seconds. By multiplying $\overline{u_\theta}$ by a scalar β of 3.4, represented in a dashed line, both curves coincide, compensating for the decrease in u_θ due to the engulfing of ambient flow.

After 5 seconds of preparation time, $\overline{u_\theta}$ increases to 20% of U_o and then only slightly to 24% over the next 15 seconds. This confirms the effect of the evolution of the $\overline{u_{\theta_p}}$ in the u_θ engulfed by the ring core. Assuming that the $S = 1$ case with a preparation time of 75 seconds has the maximum $\overline{u_{\theta_p}}$ possible, which is 90%, when divided by β, the expected velocity is 26.5% meanwhile, the actual time averaged $\overline{u_\theta}$ was 29%, which shows good agreement with the model.

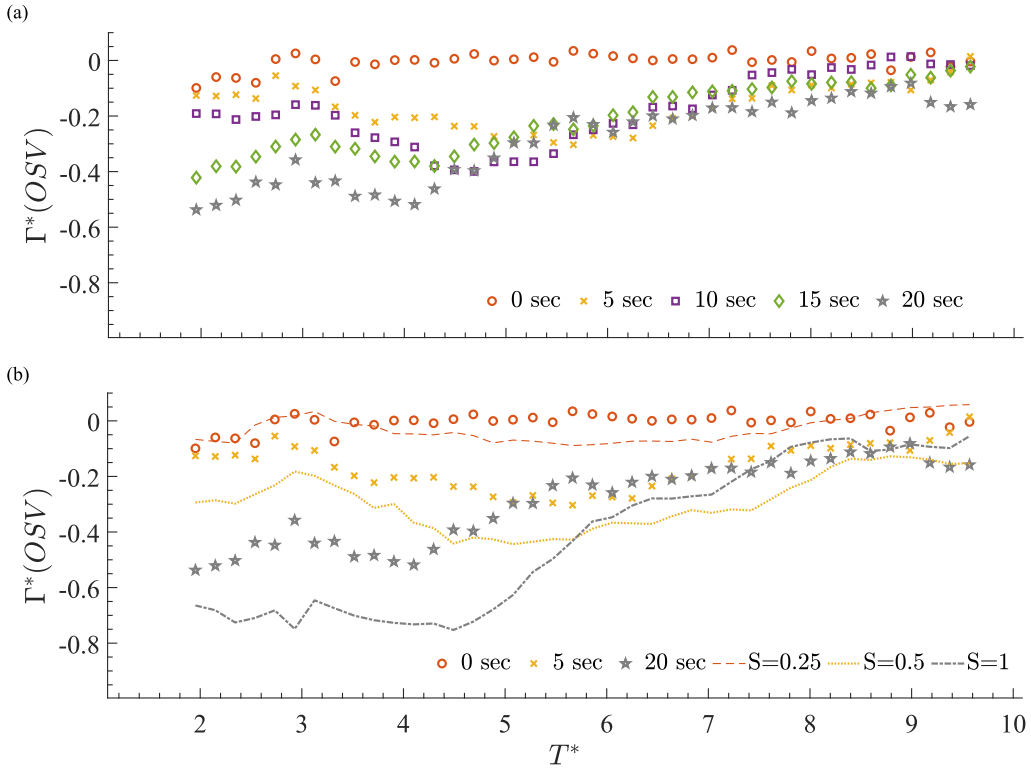

Figure 4.20: Evolution of the dimensionless circulation calculated from the OSV and subtracting it the time averaged OSV circulation for $S = 0$ to reduce that influence of the background noise. (a) For the preparation times: 0, 5, 10, 15 and 20 seconds and (b) comparing $S = 0$, 0.25 and 1 cases (dotted lines) with the preparation times 0, 5 and 20 seconds.

Generating swirling vortex rings with varying preparation times is aimed at reducing the production of OSV. Figure 4.20(a) displays the circulations that are solely calculated from OSV for each preparation time. The average circulation generated by the OSV for the $S = 0$ case was subtracted to avoid the background noise. Similar to $\overline{u_\theta}$, the production of OSV experiences a significant increase between 0 and 5 seconds of preparation time. In the case of zero seconds, OSV production

is weak and comparable to the circulation caused by background noise, as shown in Figure 4.18 (a), where no OSV was detected. For preparation times longer than five seconds and $T^* < 5$, a more notable difference is observed between the various preparation times, unlike $\overline{u_\theta}$, which remains almost constant. This finding supports the hypothesis that the OSV is more strongly related to the u_θ distribution around the centre rather than the 20% near the pipe wall. For $T^* > 5$, all the circulation, except for the zero preparation time, decreases in magnitude due to the vorticity cancellation discussed in the previous section.

Figure 4.20 (b) compares $\Gamma^*(OSV)$ for three preparation times 0, 5 and 20, with the circulation calculated from $S = 0.25$, 0.5 and 1. As expected, the circulation for $S = 0.25$ has a higher magnitude than the zero seconds case. Based on the model, the preparation time to produce a vortex ring with $S = 0.25$ is 2.25 seconds, similar to the duration of a piston stroke ($\sim$ 2 seconds). Therefore, theoretically, a zero preparation time would produce a vortex ring similar to one for $S = 0.25$. However, a period of approximately 1-2 seconds is necessary to achieve a constant angular speed in the swirl system. During a five seconds preparation time, there was a noticeable decrease in circulation magnitude compared to $S = 0.5$ (represented by a dotted line). The time average circulation for $S = 0.5$ is 0.29, while for the five-second preparation time, it is only 0.23. This represents a 25% reduction in $\Gamma^*(OSV)$. As a result, the vortex ring produced by five seconds of preparation time has a $\overline{u_\theta}$ that is 17% higher than that of $S = 0.5$, with 25% less OSV produced. For the case where the preparation time is 20 seconds, the reduction in $\Gamma^*(OSV)$ is approximately 17% compared to the case with $S = 1$. However, it is not reliable to compare these two scenarios as the one with 20 seconds of preparation time produces a vortex ring with $S \approx 0.8$ according to the model. But, it is noteworthy that for the 20 seconds case, the value of $\overline{u_\theta}$ is 20% lower than that of the $S = 1$ case. This suggests that shorter preparation times result in a better combination of reduced $\Gamma^*(OSV)$ and $\overline{u_\theta}$. This supports the hypothesis discussed earlier because u_θ is negligible near the centre in the early stages (see Figure 4.1), and as time progresses, it increases in this region, leading to an increase in the OSV formation.

Although Figure 4.18 showed the formation of a trailing jet, which indicates a

decrease in the formation number, Figure 4.21 does not reveal a clear difference in the ring circulation for the preparation times studied at the early time, $T^* < 3$. However, a clear decay rate is observed in each case due to vorticity cancellation and viscous dissipation. As the preparation time increases, the OSV also increases, which enhances the vorticity cancellation and is reflected in the decay rates of Γ^*_{Ring}. For instance, comparing the ring circulation for a preparation time of five seconds with the $S = 0.5$ case, the latter has a faster decay rate due to a higher production of OSV. Similar behaviour is observed for $S = 1$, represented in a black dotted line.

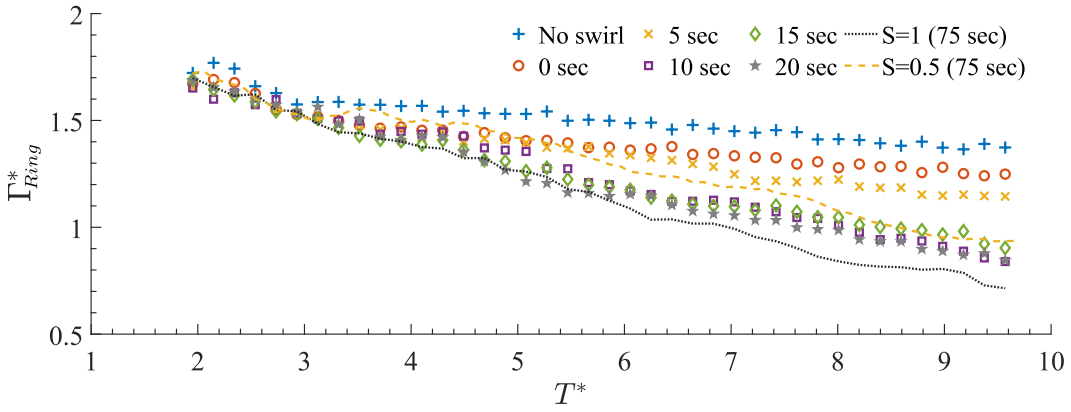

Figure 4.21: Evolution of the ring circulation Γ^*_{ring} for all the time preparations. The dotted line refers to the circulation for $S = 0.5$ and $S = 1$.

Previously, it was found that the production of OSV is responsible for the growth of the ring radius. This is illustrated in Figure 4.22 (a), where the ring radius is shown for different preparation times. As the preparation time increases, the OSV production increases, resulting in an increase in R. The mechanism responsible for this behaviour is discussed in detail in Chapter 3. In the same way that $\overline{u_\theta}$ and $\Gamma^*(OSV)$ vary, there is a significant increase between the zero and five seconds cases. The former has the same values as the no swirl case due to the low production of OSV. When comparing R for $S = 0.5$ (represented by the red dashed line) with the five seconds preparation time, a considerable decrease of about 20% is observed for the latter. The lower OSV production can explain this decrease during the five seconds preparation time, which supports the argument presented in Chapter 3. Besides, due to the higher $\overline{u_\theta}$ of the five seconds case, the centrifugal effect discussed

by He et al. (2020b); Virk et al. (1994) becomes negligible.

Figure 4.22 (b) shows the propagation velocities for different preparation time vortex rings. As in the previous sections, it follows the relation $u_z^{'} \sim 1/R$. In Chapter 3, it was discussed using equation (3.37), which describes the propagation velocity of a vortex ring as well as the importance of each term in the equation, as illustrated in Figure 3.17. Comparing the five seconds case with $S = 0.5$ confirms that the influence of the third term, which involves $\overline{u_\theta}$ is minuscule and $u_z^{'}$ is more sensitive to R.

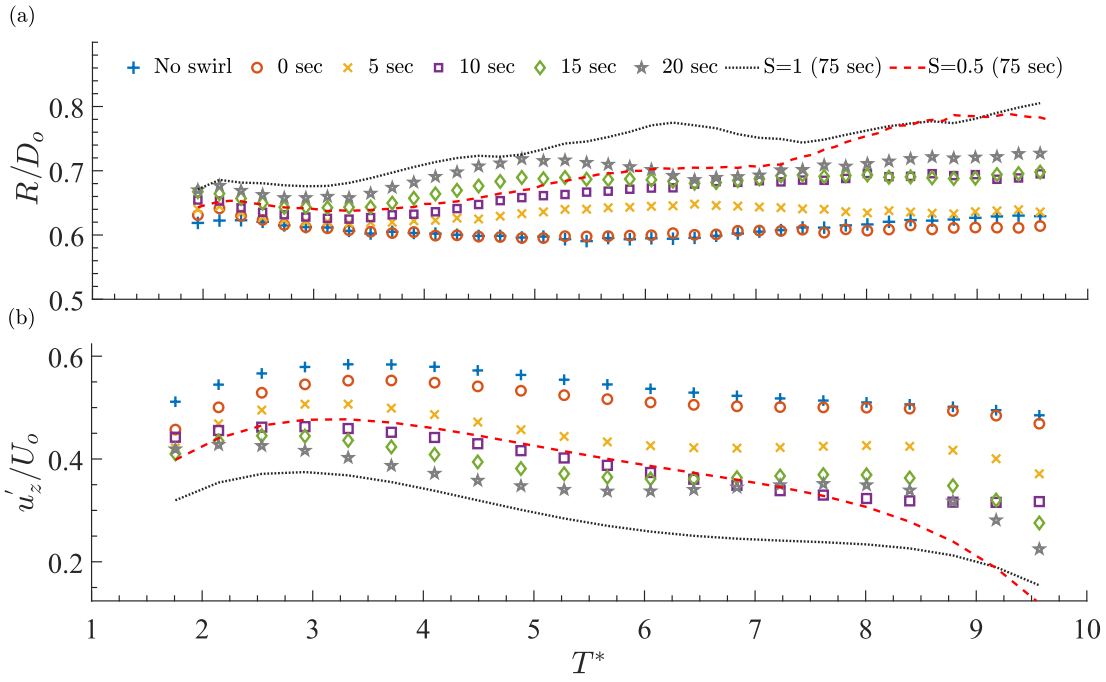

Figure 4.22: (a) Evolution of (a) the ring radius, R and (b) propagation velocity for different preparation times.

4.2 Conclusions

In this chapter, swirling vortex rings were investigated experimentally. It was shown that it is not feasible to replicate a fully developed solid body rotation inlet condition, as employed in numerical simulations, by using a rotating pipe. This is due to the formation of a secondary flow caused by the pressure difference between the flow in the vicinity of the rotating pipe wall (which creates a high-pressure region) and the fluid outside the swirl system. Consequently, as the flow in the high-pressure region is discharged to the tank, the flow from outside the swirl system with zero u_θ is engulfed to replace it, affecting the development of u_θ, especially at the centre of the pipe. The strength of this secondary flow increases with longer periods of pipe rotation and higher angular speeds.

Experimental generation of vortex rings with $L/D_o = 2$ and $S = 0.25$, 0.5, and 1 was carried out. To ensure a fully established inlet flow, the pipe was left rotating for 75 seconds prior to the piston stroke. This period was referred to as the "preparation time." The results obtained show similar characteristics to those of the swirling ring studied numerically. Opposite sign vorticity (OSV) was formed around the centre of the vortex ring, with its magnitude increasing with S. This OSV propagates around the vortex core, leading to vorticity cancellation that destabilised the vortex ring.

Vortex rings with different values of $\overline{u_\theta}$ were produced by varying the preparation time of the swirl system. By increasing the angular speed of the pipe, a vortex ring with a similar u_θ to a $S = 0.5$ case was produced in just five seconds instead of the usual 75 seconds of preparation time. This method generates swirling vortex rings faster and reduces the formation of OSV by shortening the preparation time during which u_θ has not fully developed at the centre of the rotating pipe. When comparing the $\Gamma^*(OSV)$ generated for two vortex rings with similar $\overline{u_\theta}$ but different preparation times and angular speeds, it was found that the shorter preparation time with the higher angular speed resulted in a 25% decrease in OSV formation. However, it was reported that the decrease in OSV diminishes as preparation time increases.

A method has been proposed to determine the average azimuthal velocity, $\overline{u_\theta}$, of a vortex ring based on the preparation time. This method assumes that only the u_θ

located in the boundary layer formed during the piston stroke will be transported by the vortex sheet and ultimately be engulfed by the ring. Therefore, the average u_θ value near the rotating pipe wall, $\overline{u_\theta}_p$, should be similar to the $\overline{u_\theta}$ of the vortex ring. By comparing the u_θ of a vortex ring with $S = 0.5$ generated after 75 seconds of preparation time with another where this method was applied, it was found that there was a difference of 17%. This result shows promise, but the model needs to be more robust and consider the effect of the secondary flow and the angular acceleration of the rotating pipe.

The production of swirling vortex rings with reduced creation of OSV confirms some of the findings of the simulation work in Chapter 3, such as:

- For R growth, the formation of OSV is the dominant factor for a vortex ring, generated by an impulsive discharge of momentum instead of the centrifugal effect discussed in previous research.

- The propagation velocity of the vortex ring is primarily determined by the behaviour of R, with a minor influence from azimuthal velocity $\overline{u_\theta}$ in the vortex core.

- The formation of the OSV for vortex rings, generated by an impulsive discharge of momentum, is related to the u_θ distribution in the swirling jet instead of the $\bar{u_\theta}$ via Dean vortices.

CHAPTER 5

Enhancing a vortex ring's circulation via its interaction with another vortex ring

One of the critical parameters affecting a vortex ring's formation process is its radius, which is related to the kinetic energy of the ring as discussed in Chapter 3. The implication is that to increase the circulation and, consequently, the formation number of a vortex ring, it is necessary to reduce its radius. Dabiri and Gharib (2005) achieved this by varying their nozzle exit diameter; during vortex ring formation they observed an increase of up to 70% in the corresponding formation number. An alternative approach to reducing ring radius during formation, and easier to perform in a laboratory, is due to the effect of a preceeding vortex ring.

The experiment described in this chapter aims to enhance the circulation of the vortex ring by increasing its formation number by manipulating the radius of the ring during formation through its interaction with an earlier discharged vortex ring; unlike previous studies, leapfrogging is avoided as it destabilises the following vortex ring. The study considers the circulation augmentation observed by Qin et al. (2018), but the problem investigated differs in nature.

5.1 Problem specification

The focus is on the interaction of two rings only, with a fixed $Re = (D_o U_o/\nu)$ of around 1900 for all cases; U_o is the time-average velocity of the flow at the orifice with a magnitude of $0.0625 m/s$. This value was obtained by applying continuity to account for the diameter difference between the swirl and piston-cylinder systems, as discussed in Chapter 4. The time difference, $T^*_{off} = t_{off} U_o/D_o$, and the stroke ratio, L/D_o, of the leading ring are the two parameters analyzed. By varying the latter, it is possible to produce vortex rings with different core sizes and propagation velocities, which can significantly alter the ring interaction. The stroke ratio for the following ring is fixed at four, which is greater than the formation number (F $\sim$ 2.73), allowing it to absorb more vorticity from the trailing jet due to interaction with the leading ring.

Previous investigations (Didden, 1979; Lim and Nickels, 1995; Weigand and Gharib, 1997) have reported the formation of a secondary vorticity known as "stopping vortices" during the formation of vortex rings. These vortices are generated when the piston decelerates and a reverse flow region forms at the orifice's edge, with an OSV compared to the primary vortex ring. This secondary vorticity interferes with the formation process of the primary vortex, mainly reflected in the rings' diameter. However, its effect is only relevant during the early formation process, because of its OSV causing it to travel upstream within the tube and reducing its influence on the primary vortex ring over time. It is important to note that the stopping vortex is not related to the vorticity formed at the orifice plate wall, due to the boundary layer formed by the induced velocity of the vortex core at an earlier time, having the same sign as the stopping vortex.

The formation of stopping vortices is critical when two or more vortex rings are generated consecutively. The stopping vortex moves in the reverse direction to the motion of the leading vortex ring, but the new piston stroke that produces the following ring pushes the stopping vortex downstream. As Asadi et al. (2018) observed, in their investigation about the propagation of periodically generated vortex rings, there is a strong interaction between the stopping vortex and the following ring, which triggers instabilities mainly in the stopping vortex, leading to its break-

down, causing a significant impact on the formation and propagation of the following vortex rings as illustrated in Figure 5.1.

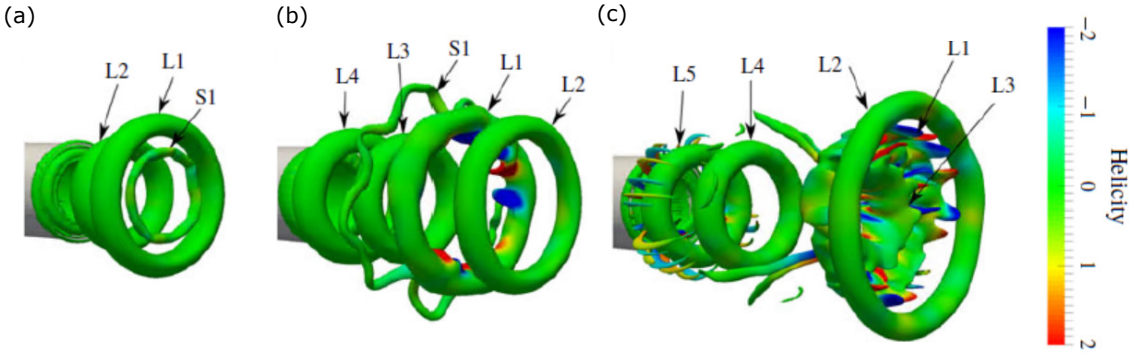

Figure 5.1: Isosurface of vorticity magnitude at three different dimensionless times, t/T, (a) 2, (b) 3.75 and (c) 5. T is the period of the pulsed jet, and the labels "L" and "S" represent the leading rings and stopping vortices, respectively. Figure taken from Asadi et al. (2018).

To prevent the formation of stopping vortices close to the orifice edge, all the vortex rings generated in the tank described in Chapter 2, reported subsequently, follow the velocity programme proposed by Das et al. (2017). This piston time history consists of a trapezoidal velocity programme characterized by a slow deceleration, in this case of around 40% of the time taken by the piston to complete one stroke and an acceleration of 20%. These values are in line with their proposed criteria, where if the ratio of the acceleration impulse I_{acc}, and total impulse I_{total}, namely $I_{acc}/I_{total} < 0.85$ no stopping vortex is formed. The impulse is calculated as $I = \int_0^t U_p^2 dt$ where U_p is the piston velocity and the time, t, defines which impulse has been calculated.

Figure 5.2 provides a visual representation of the parameters and velocity programme applied. The first ring formed is labelled ring B and the second ring A. For the former, three different stroke ratios are studied $L/D_o = 1.5$, 2, 2.5, which allows for the generation of rings with different core areas and strengths. However, the focus here is on ring A, for which stroke ratio is fixed at four as mentioned above. Also, three time differences were implemented, $T^*_{off} = t_{off}U_o/D_o = 1.8$, 3, 6 for every stroke ratio of ring B. The dimensionless time T^*_{off} and $T^*_{on} = t_{on}U_o/D_o$ represent the piston's status. In Figure 5.3, the vorticity contour plots for rings A

and B at $T^* = 2$ are presented to show how the position of ring B varies for each case studied. Table 5.1 summarises all the parameters used in the experiment, and Figure 5.3. A total of 26 experiments were conducted, each repeated five times with a 10-minute interval. Only 10 experiments are presented.

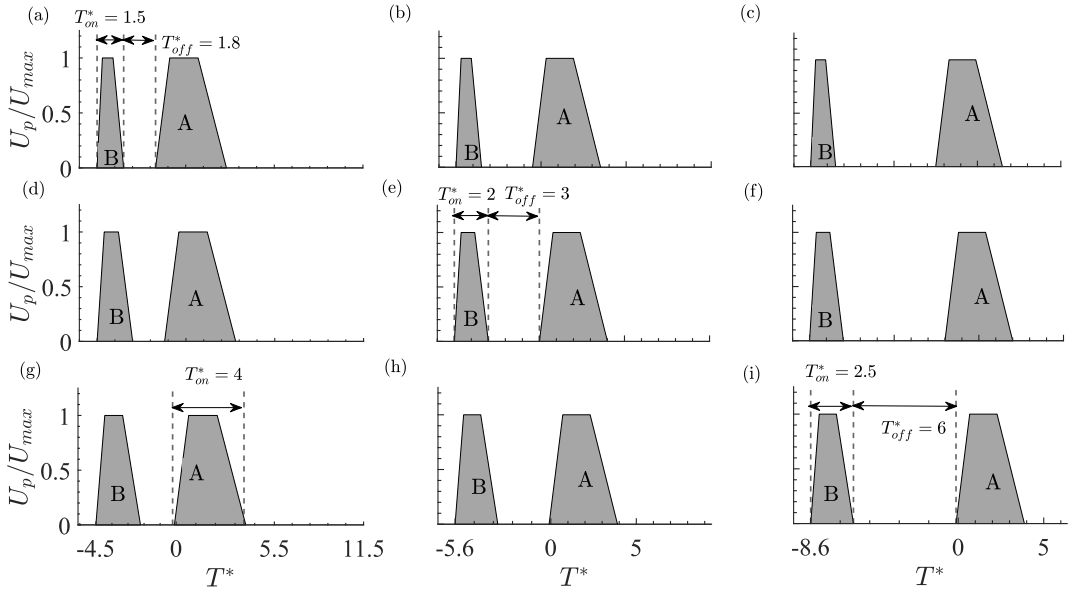

Figure 5.2: Visual representation of all cases studied. Each row shows a different stroke ratio for ring B, (a-c) $L/D_o = 1.5$, (d-f) $L/D_o = 2$, (g-h) $L/D_o = 2.5$; and each column represents a different T^*_{off}, U_p stands for the piston speed and u_{max} is the highest speed reached by the piston.

$R_e(D_oU_o/\nu)$		1900		
$T_{on}(L/D_o)$	Ring A	4		
$T_{on}(L/D_o)$	Ring B	1.5	2	2.5
$T_{off}(t_{off}U_o/D_o)$		1.8	3	6

Table 5.1: Reynolds number and the parameter varied in the experiments performed

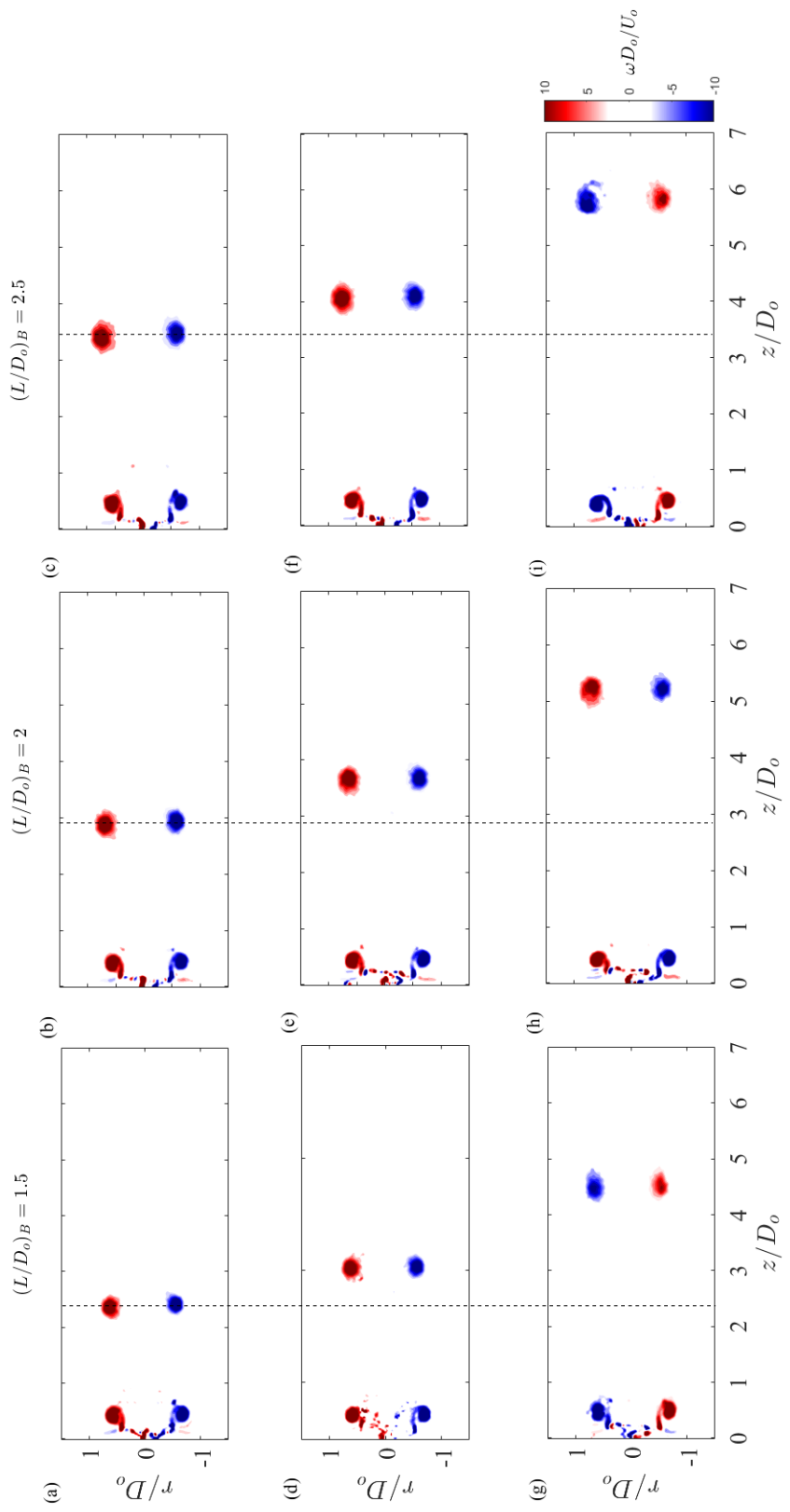

Figure 5.3: Vorticity contour plot of Ring A and B for all the cases studied at $T^* = 2$. Each column represents a different stroke ratio, 1.5, 2.0 and 2.5, for Ring B, and each row represents the time difference T_{off} from top to bottom 1.8, 3, 6, respectively.

5.2 Results and discussion

5.2.1 Alterations in the trajectories of two vortex rings during their interaction.

The trajectory of a pair of vortex rings can be used to identify how strongly they interact. The induced velocity of each ring affects the radius of the other ring, expanding the leading (B) and shrinking the following (A) ring, which in turn affects the propagation velocity of them both as discussed at the beginning of this Chapter. In order to study the propagation of a vortex ring, it is necessary to identify the core's centroid. These are the points where the velocity is zero in a frame of reference that moves with the vortex ring (Limbourg and Nedić, 2021). The same definition as used in Chapter 3 for an axisymmetric vortex is employed here to identify those points:

$$R = \frac{\iint \omega r \, \mathrm{d}r\mathrm{d}z}{\iint \omega \, \mathrm{d}r\mathrm{d}z} \quad Z = \frac{\iint \omega z \, \mathrm{d}r\mathrm{d}z}{\iint \omega \, \mathrm{d}r\mathrm{d}z}. \tag{5.1}$$

For an accurate core centroid estimation, vortex ring cores must be isolated from their trailing jet. When conducting experiments, a distinct technique is required to distinguish and separate the vortex core from the rest of the flow. This is because the experimental data collected is not as consistent as the numerical data collected in Chapter 3. It involves enclosing the vortex core in a box (Fig 5.4 (b)) by following these steps:

- A threshold of 2 S^{-1} is used to remove the background cross-correlation error located mainly in the region where the velocity field is close to zero.
- The highest and lowest vorticity points are manually identified at the start time. Starting from these points, a displacement upstream of Δz is made while evaluating the vorticity magnitude at each step until it reaches zero. This identifies the upstream boundary.
- The centre of the vortex ring is identified as the middle point of the radial

distance between the ring cores from the previous step. One-half of the length is set as the ring radius, R. This value fixes each core's top or bottom boundary.

- A specific length is set for the downstream and the top or bottom boundaries, depending on the core, to ensure the vortex core remains inside the box and excludes vorticity from ring (B).

- For the next time step, a $10\Delta z \times 10\Delta r$ box is placed downstream of the previous points to identify the highest and lowest vorticity points as shown in Figure 5.4(b). These will be the new reference points used to restart the process.

Although this method is easy to implement, it may not be reliable for early times $T^* < 4$. In most cases, the ring has not detached properly from the trailing jet by this time and the box that encloses the core could include parts of the associated trailing jet. For that reason, only values computed for $T^* > 4$ were used for the study of ring circulation.

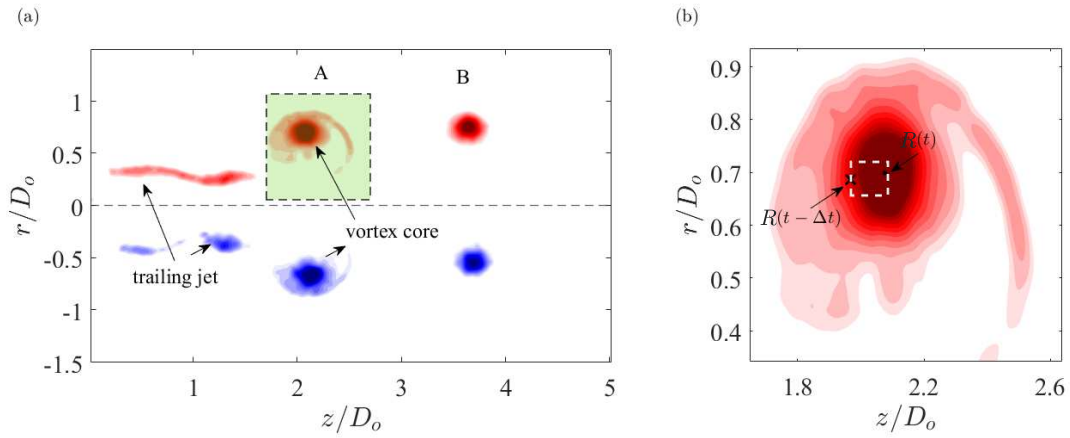

Figure 5.4: (a) Vorticity contour plot of vortex rings A and B, highlighting the box generated to separate the vortex core from the trailing jet. The trailing jet and ring's core are also identified. (b) Visual representation of the method used to identify the new reference point $R(t)$. An area of size $10\Delta z \times 10\Delta r$ is located at the ring core with the reference point from the previous time step $R(t-\Delta t)$ on its upstream side. The point with the maximum or minimum vorticity, depending on the core, in the box becomes $R(t)$.

Once the core of the vortex ring A has been isolated from the trailing jet, equation (5.1) is applied to determine the core's centroid. The trajectories followed for both

rings, A and B, are shown in Figure 5.6 for all the cases studied. The first row shows an intenser interaction when $T^*_{off} = 1.8$, especially for (a), where ring B's radius increases considerably as ring A approaches, causing it to shrink slightly. The different rates of change in the radii of the rings are caused by their circulation. As shown in equation 1.13, the vortex strength Γ, along with the radial distance, determines the induced velocity's magnitude. In this case, the velocity induced by ring A on ring B is greater. Also, the effect of the distance between the rings is observed as the stroke ratio L/D_o of ring B increases. In Figure 5.6 (c), although the circulation of ring A and T^*_{off} are the same as in (a), a weaker interaction is observed due to the increase in the propagation velocity of vortex ring B, which is directly proportional to the ring's circulation [1]. For the rest of the cases, the change in the trajectories of both rings appears negligible, with ring A's trajectory bounded by the equivalent single ring case (blue line).

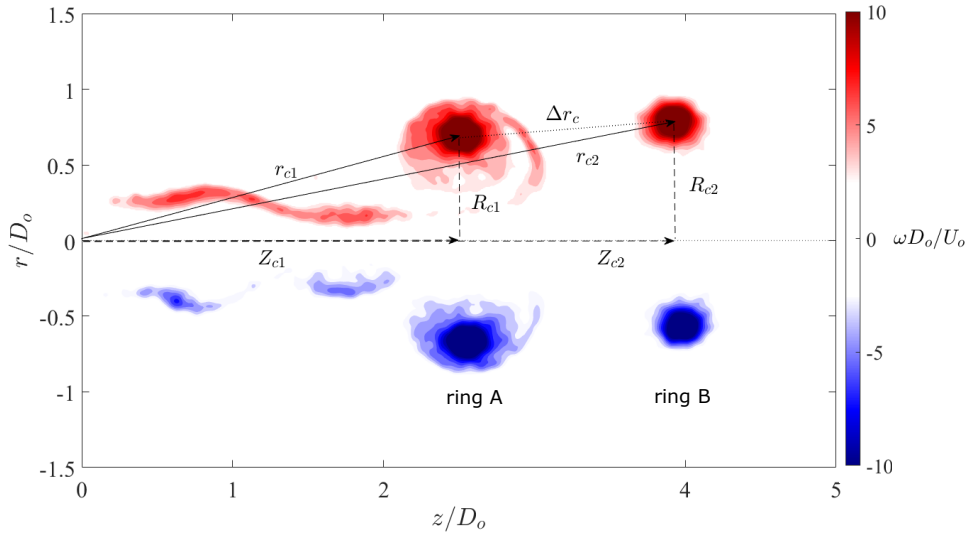

Figure 5.5: Vorticity contour plot where the position of ring A, r_{c1}, and B, r_{c2}, as well as their components (Z, R), used in equation 5.2 , are illustrated.

[1] Since the first model proposed by Kelvin (1867), more complex expressions have been published for modelling the propagation velocity of a vortex ring, but they all share the same common factor $\Gamma/4\pi R$

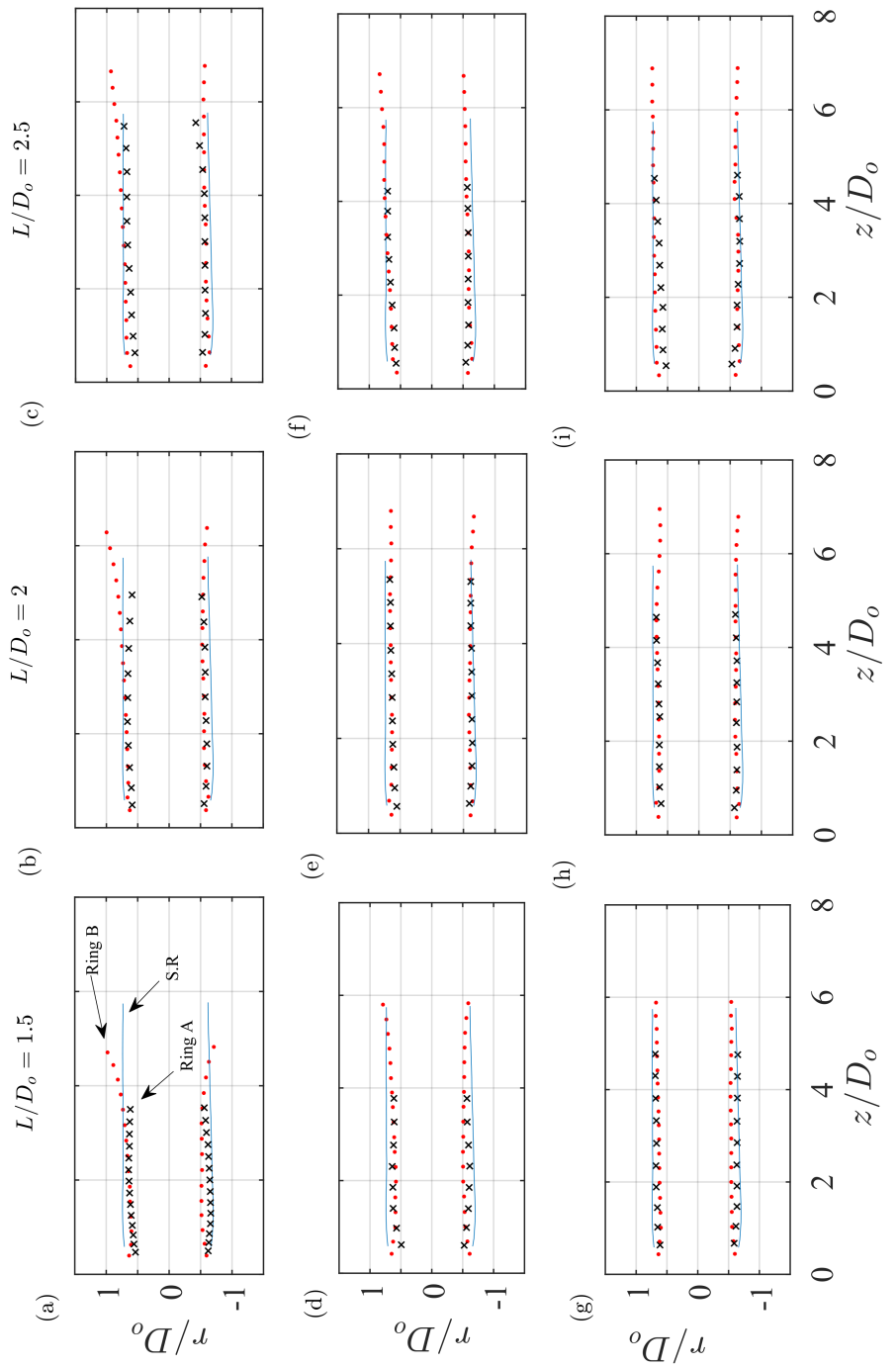

Figure 5.6: Trajectories of the vortex ring based on the vorticity centroids. For rings A (×), B (•) and for the case with a single ring (−). Each column represents a different stroke ratio for Ring B, 1.5, 2.0 and 2.5, and each row represents the time difference T_{off} from top to bottom 1.8, 3.0, 6, respectively.

5.2.2 Evolution and correlation between the ring radius, its circulation and kinetic energy.

As discussed in Chapter 3, the equation (3.40) provided by Shusser and Gharib (2000) relates the dimensionless kinetic energy, α, with the ring radius, R, via the parameter $\epsilon = a/R$, approximating the ring as a member of Norbury's family of vortex rings (Norbury, 1973). An increase in the radius of the vortex ring produces a rise in its kinetic energy, which in turn decreases the amount of time it absorbs vorticity from the trailing jet. This leads to a lower formation number F and the final circulation (Ortega-Chavez et al., 2023). Accordingly, it should be possible to increase the formation number of the ring by reducing its radius during formation. This would decrease the kinetic energy of the ring, allowing it to absorb more vorticity from the trailing jet. Figures 5.7, 5.10 and 5.13 present the evolution of the circulation of vortex ring A, its radius and kinetic energy for the cases mentioned above; see table 5.1.

For $T^*_{off} = 1.8$, where the interaction is stronger according to Figure 5.6, a slight decrease in R is observed for all cases compared to the single ring case, the difference being more pronounced at early times (Figure 5.7 (b)). However, no distinction is observed between the cases involving two rings for $T^* < 4$.

When T^* is greater than 5, the strength of the interaction with ring B increases, leading to a higher rate of shrinkage for ring A as $(L/D_o)_B$ decreases. This behaviour is explained in Figure 5.7 (d) which compares the distance between rings, Δr_c, defined as follow:

$$\Delta r_c = \sqrt{(R_{c2} - R_{c1})^2 + (Z_{c2} - Z_{c1})^2}, \tag{5.2}$$

where Z_{c1} and Z_{c2} are the axial position of each ring. As time passes, Δr_c decreases more rapidly with $(L/D_o = 1.5)_B$ due to its slower propagation velocity, which keeps it closer to ring A, causing a stronger interaction. This explains why the decay of the ring radius occurs when T^* is greater than 4, and it is faster as $(L/D_o)_B$ decreases. The consequences of the interactions are also reflected in the values of α and Γ_{Ring}. Figure 5.7 (c) displays the dimensionless kinetic energy of ring A where α drops below 0.33, which corresponds to the single ring case (Gharib et al., 1998);

also Figure 5.7 (a) confirms the expected increase in ring circulation. For example, the case with $(L/D_o = 2)_B$ has the lowest kinetic energy and gains approximately 13% circulation compared to the single ring case, increasing its formation number from 2.73 to 3 [1]. However, no gain is observed in the circulation of the ring, nor a decrease in its kinetic energy, even though its radius is shrinking as a consequence of the proximity of ring B when $(L/D_o = 1.5)_B$.

Figure 5.8 compares two vorticity contour plots at the same time, $T^* = 5$, for $(L/D_o = 1.5)_B$ and $(L/D_o = 2)_B$. It is evident that the core for $(L/D_o = 1.5)_B$ is detached from the trailing jet, which appears more unstable than the $(L/D_o = 2)_B$ case, where the vortex ring remains attached to the trailing jet. This suggests that the proximity of ring B triggers instabilities in the trailing jet, causing early separation and halting core growth. Nevertheless, a sudden increase in the ring's circulation is observed for $(L/D_o = 1.5)_B$ close to $T^* = 5.6$. After the core detaches, the section of the trailing jet closest to the core breaks, and some vorticity from that section moves around the core until it is engulfed, which increases the ring's circulation. But, this is not enough to surpass the $(L/D_o = 2)_B$ case. The break and engulfing of a section of the trailing jet is illustrated in Figure 5.9. After this, the circulation starts to decay due to the process of leapfrogging beginning, which causes instabilities and vorticity cancellation. The same occurs for $(L/D_o = 2)_B$ and $(L/D_o = 2.5)_B$ but at a slower rate.

[1] To determine F, only the total circulation, Γ_{Total}, from the single ring case is used.

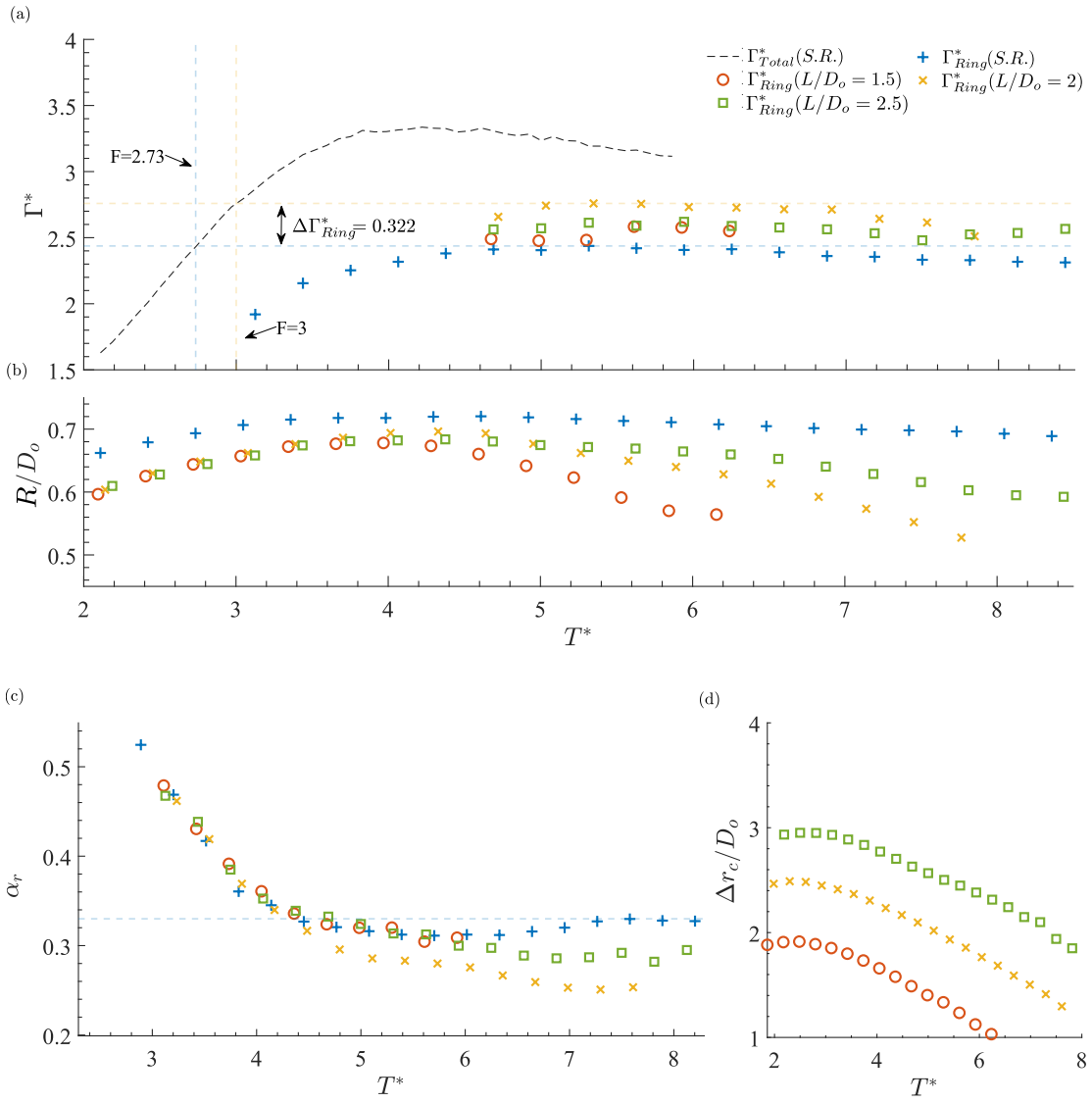

Figure 5.7: Evolution of ring A: (a) Circulation, (b) radius, (c) dimensionless kinetic energy and (d) ring separation for $T^*_{off} = 1.8$.

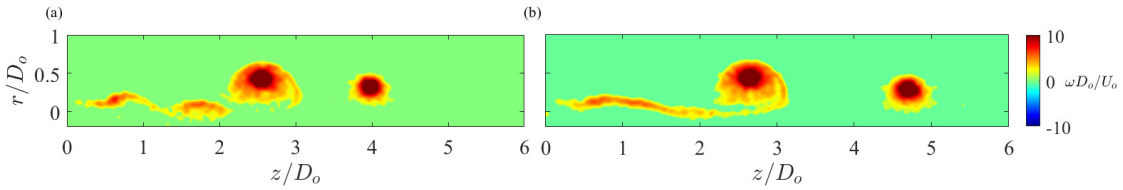

Figure 5.8: vorticity contour plots for (a) $(L/D_o = 1.5)_B$, and (b) $(L/D_o = 2)_B$ for $T^*_{off} = 1.8$ at $T^* = 5$.

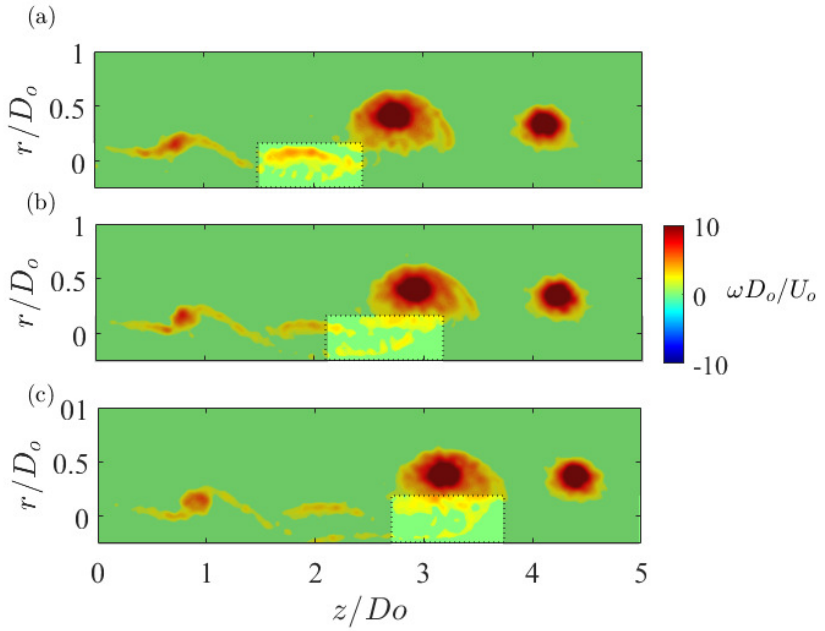

Figure 5.9: vorticity contour plots of the case $(L/D_o = 1.5)_B$ at: (a)$T^* = 5.3$, (b) $T^* = 5.45$ and (c) 5.75 with the section of interest highlighted

For $T^*_{off} = 3$ (Figure 5.10), there is a more significant difference in the evolution of the ring radius than in the previous T^*_{off} value analysed. An interesting factor is that for the cases with $(L/D_o = 1.5)_B$ and $(L/D_o = 2)_B$, the radius has a similar length to the single ring case. However, there is still an increase in the ring circulation. It is precisely this gain of circulation that makes the ring increase its size. During the rolling-up process of a vortex ring, the radius experiences its most significant change, growing as long as the ring core absorbs vorticity from the trailing jet. Therefore, the extra vorticity gained for ring A should also increase its radius. For $T^*_{off} = 1.8$ discussed above, the interaction between the rings is strong enough to counter the ring growth due to the gain of vorticity, keeping it below the single ring case radius. On the other hand, although the interaction is weaker for $T^*_{off} = 3$, it is still strong enough to shrink ring A, gain extra vorticity, and maintain a radius similar to the single ring case despite the increase in ring circulation.

Comparing the interaction strength via Δr_c for $T^*_{off} = 3$ and $T^*_{off} = 6$ reveals differences in the distance between rings, where the latter duplicates the length of the former affecting the strength of the interaction.

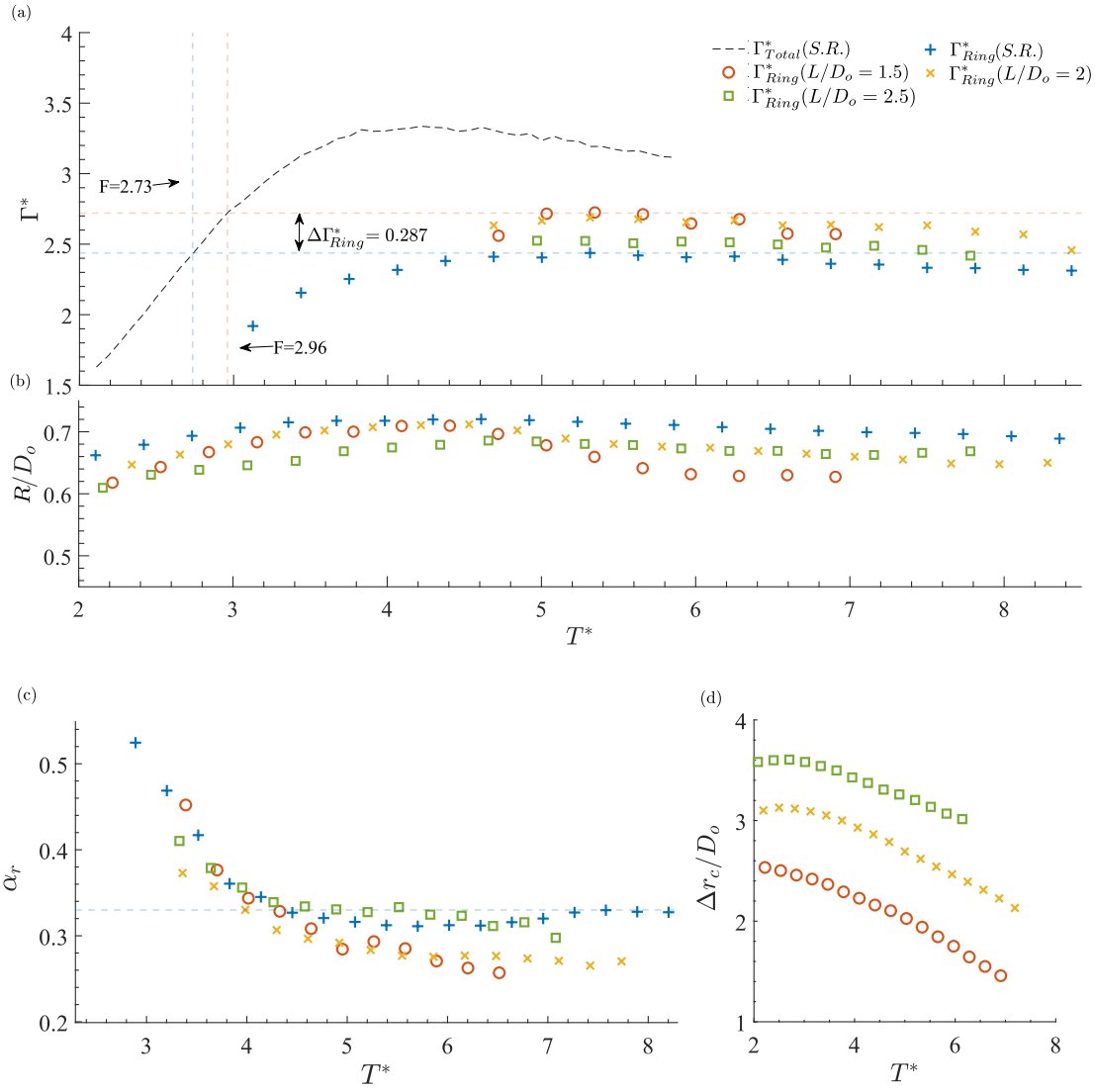

Figure 5.10: Evolution of the ring A: (a) Circulation, (b) radius, (c) dimensionless kinetic energy and (d) ring separation for $T^*_{off} = 3$.

It is interesting to note that in Figure 5.10, the radius of $(L/D_o = 2.5)_B$ does not grow at the same rate as the other $(L/D_o)_B$, and α_r has values even above the single ring case. Based on the earlier ratios explanations, the circulation gain should be lower than in the other cases, as shown in Figure 5.10 (a). This would decrease the ring growth, and with nothing to counteract it, Ring A would be more sensitive to the shrinking generated by Ring B. Also, it is unlike when $T^*_{off} = 1.8$, where the higher circulation gain corresponded to $(L/D_o = 2)_B$. Here, the maximum circulation is for the $(L/D_o = 1,5)_B$ case, which increases its circulation by around 11% pushing the formation number from 2.73 to 2.96. This is due to the rings being further apart than when $T^*_{off} = 1.8$. For instance, over the period studied, the case $(L/D_o = 1,5)_B$ for $T^*_{off} = 3$ exhibits one D_o longer Δz than the $T^*_{off} = 1.8$ case. This leads to a weaker interaction between the rings and reduces the development of instabilities in the trailing jet observed for $T^*_{off} = 1.8$ (see Figure 5.8) that promotes the detachment of rings from the trailing jet, thus constraining its growth. Around $T^* \approx 4.5$, the strength of the interactions between the rings begins to increase. This is reflected in a decrease of R, which follows a similar pattern to that observed for $T^*_{off} = 1.8$, but at a slower rate. The interaction also has an effect on the ring's circulation, which begins to decline around the same time.

The point vortex model is now used to better understand the rings' interaction strength, see Batchelor (1967) Chapter 7. Figure 5.11 (d) illustrates how the system of two vortex rings is changed for a four-point vortices model where the vorticity cores are assumed to be concentrated in a point that induces a velocity with concentric streamlines whose magnitude is giving by equation (1.13). Figures 5.11 (a-c) display the radial velocity induced by two vortex points $\Gamma(B)$ and $-\Gamma(B)$ with one point corresponding to one core of the ring A for different T^*_{off}. The position of the vortex points is based on the core centroids calculated previously. A considerable change is observed in the magnitude of the induced radial velocity, u_{r-i}, as T^*_{off} increases, being almost negligible for $T^*_{off} = 6$. Based on these results, the behavior for $(L/D_o)_B = 2.5$ with $T^*_{off} = 1.8$ should be similar to the case with $(L/D_o)_B = 1.8$ and $T^*_{off} = 3$ due to the similarity of the u_{r-i} values in each case. However, with respect to circulation, the maximum values for each case are 2.62 and

2.72 for $(L/D_o)_B = 2.5$ and $(L/D_o)_B = 1.5$, respectively. Also, there is a noticeable difference in the evolution of the ring radius between the two cases, indicating a complex phenomenon that is not limited only to the radial velocity induced on ring A.

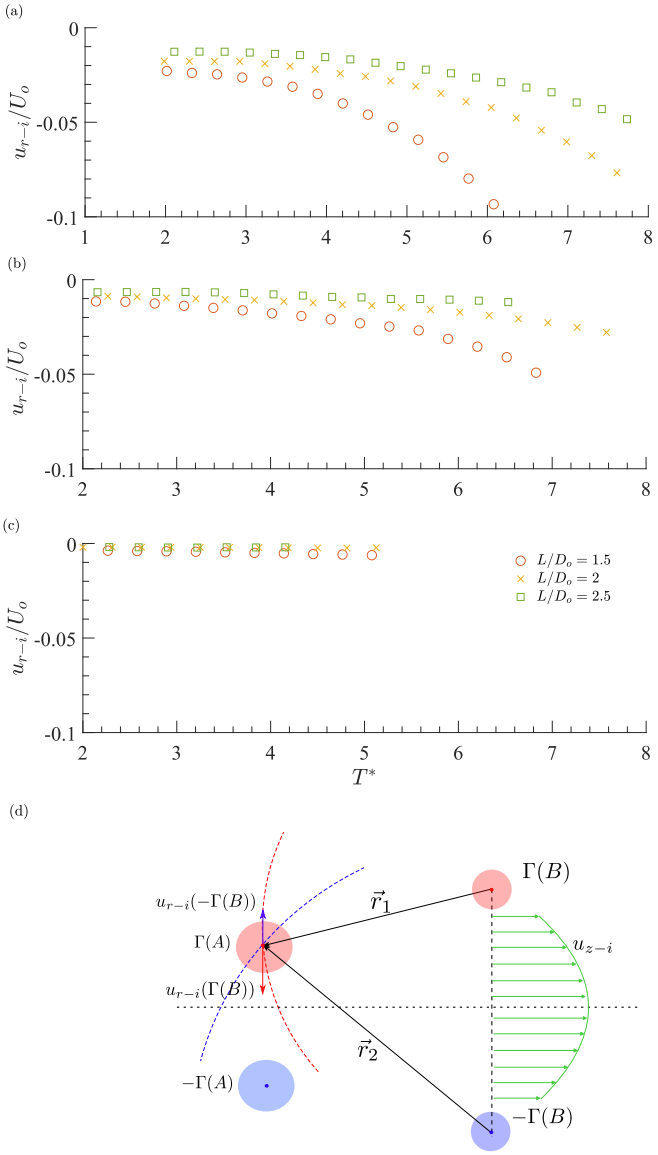

Figure 5.11: Induced radial velocity u_{r-i} from ring B on ring A based on the point vortex model: (a) $T^*_{off} = 1.8$, (b) $T^*_{off} = 3$, (c) $T^*_{off} = 6$, (d) Sketch of the model implemented.

Despite the low u_{r-i} observed at $T^*_{off} = 6$, there is still a gain in the ring's circulation, as shown in Figure 5.13 (a). As expected, the gain of circulation $\Delta\Gamma^*_{Ring}$ drops from 0.32 to 0.22 with a formation number of 2.9 for the case $(L/D_o)_B = 1.5$, which shows the biggest increment. Although the Γ^*_{Ring} difference between the three $(L/D_o)_B$ values is small, it is still interesting to analyse their behaviour. For example, when $(L/D_o)_B = 1.5$, there is a sudden increase in circulation that has also been observed and discussed previously for other T^*_{off} and the same $(L/D_o)_B$. Figure 5.12 shows the evolution of the core of ring A for $(L/D_o)_B = 1.5$ and $T^*_{off} = 6$. It demonstrates the same features as Figure 5.9; described as follows:

- A section of the trailing jet develops instabilities that eventually roll-up, creating zones of high vorticity; see Figure 5.12 (a).

- Following the point vortex model, the induced axial velocity, u_{z-i}, between the vortex cores reaches its maximum value at the centre of the ring as illustrated by the velocity field in Figure 5.14 (a), and its magnitude is increased due to shrinking of the ring. It is important to point out that this method of increasing the circulation of the vortex ring happens when the interaction of the ring A and B increases $T^* > 4$ and R starts to decay.

- The section of the trailing jet with high vorticity is accelerated, travelling around the core with an axial velocity higher than the propagation velocity of the ring until it is subsequently engulfed by the vortex ring.

To quantify the acceleration of flow between the vortex cores mentioned in the second point, the evolution of velocity at the ring's centre, u'_o, is shown in Figure 5.14(b) for $T^*_{off} = 1.8$. It appears that the flow accelerates earlier for higher $(L/D_o)_B$. At $(L/D_o)_B = 1.5$, there is a faster acceleration at $5 < T^* < 6$, which is the same period when Ring A gained extra circulation, which validates the mechanics described. This method of increasing the circulation of the vortex ring is supported by the hypothesis in Shusser and Gharib (2000), which suggests that the vortex ring detaches from the trailing jet and stops its formation process when the velocity of the vortex ring matches the velocity of the jet flow near the ring. However, in Figure 5.12, it is observed that the trailing jet weakens as it approaches

the centre due to vorticity cancellation, decreasing the absorption of vorticity. Although sudden increments were observed for $(L/D_o)_B = 1.5$, this behaviour appears to be general and dependent on the competition between trailing jet acceleration and vorticity cancellation.

For the case $(L/D_o)_B = 2$, ring circulation grows slowly and reaches its maximum vorticity at $T^* \approx 7$, which is similar to the maximum circulation seen at $(L/D_o)_B = 1.5$. This case exhibits unique behaviour extending its formation process longer than any of the other cases studied; even if the maximum circulation decreases by 4% in comparison to the case $(L/D_o)_B = 2$ and $T^*_{off} = 1.8$, it seems that Δr_c is optimal because after reaching its maximum circulation it does not decay as rapidly as the other cases. Table 5.2 shows the maximum circulation of the ring, Γ^*_{Ring}, its corresponding R, and F for each case.

	T^*_{off}								
	1.8			3			6		
$(L/D_o)_B$	Γ^*_r	R_r/D_o	F	Γ^*_r	R_r/D_o	F	Γ^*_r	R_r/D_o	F
1.5	2.61	0.6	2.87	2.76	0.63	2.96	2.67	0.7	2.92
2	2.76	0.64	3	2.69	0.68	2.94	2.68	0.67	2.93
2.5	2.62	0.62	2.88	2.6	0.68	2.86	2.59	0.7	2.85
Single ring case	$\Gamma^*_{Ring} = 2.44$			$R/D_o = 0.71$			F=2.73		

Table 5.2: Maximum ring circulation, Γ^*_{Ring}, its corresponding R and F for each case investigated.

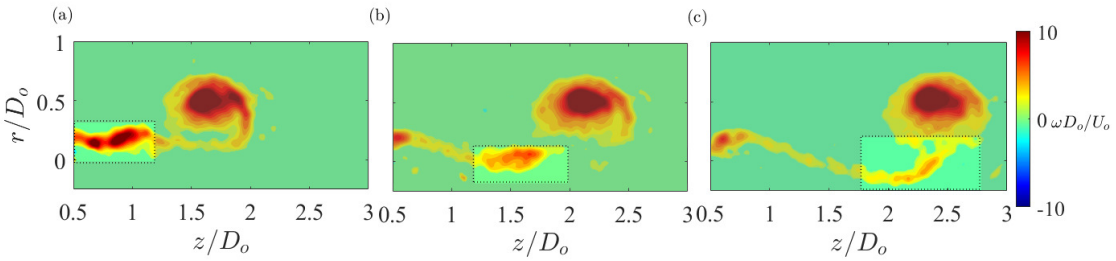

Figure 5.12: vorticity contour plots of the case $(L/D_o = 1.5)_B$ and $T^*_{off} = 6$ at: (a) $T^* = 3.8$, (b) $T^* = 4.4$ and (c) $T^* = 4.8$ with the section of interest highlighted

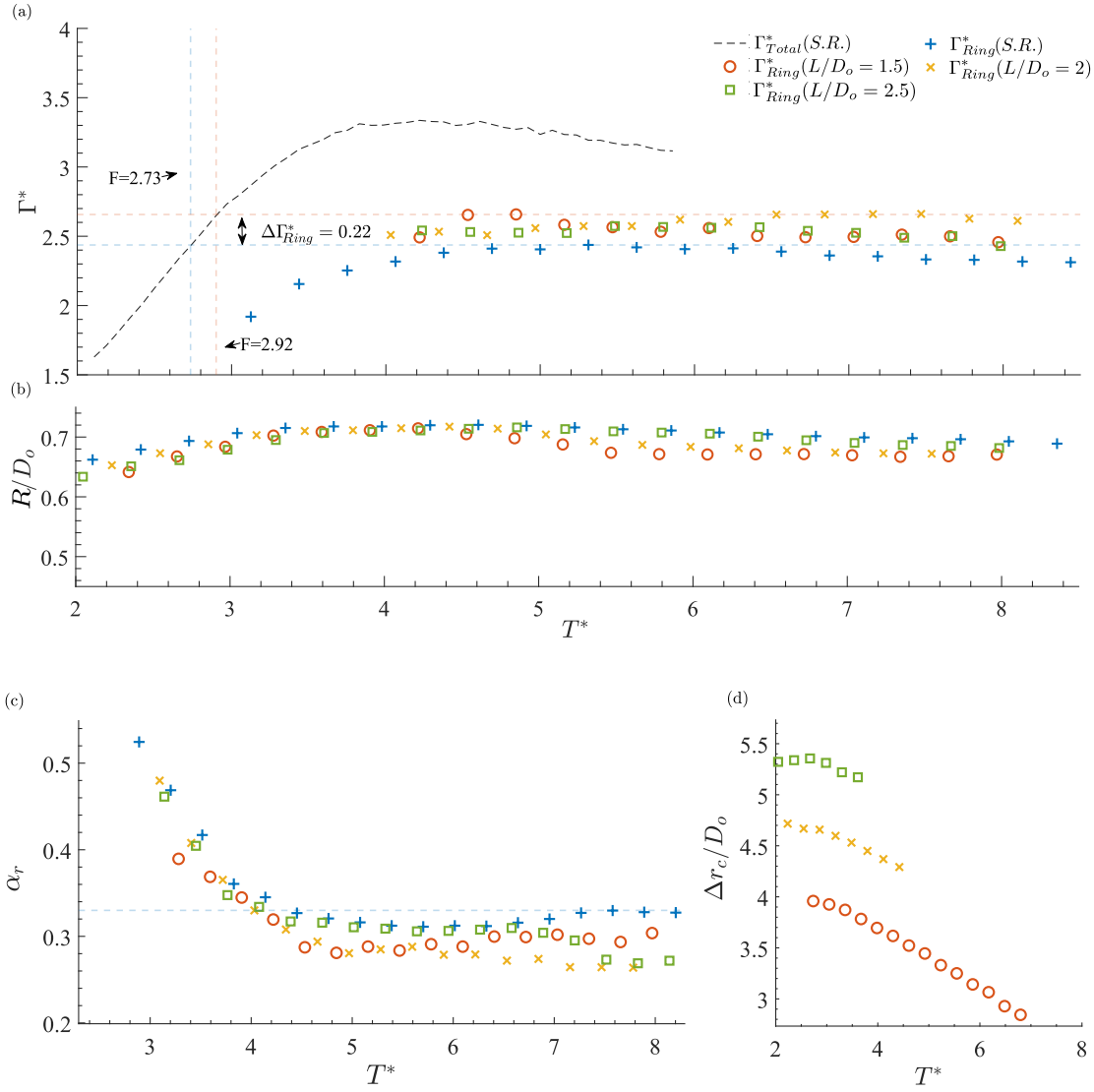

Figure 5.13: Evolution of the ring A: (a) Circulation, (b) radius, (c) dimensionless kinetic energy and (d) ring separation for $T^*_{off} = 6$

5.2.3 Kinematics of the vortex rings interaction

A different way of analysing the interaction between the vortex rings is to examine ring A's propagation velocity and radial velocity. Figure 5.15 shows the velocities calculated using a fifth-degree polynomial fit and central difference scheme for ring A. The fitting technique was implemented to prevent sudden spikes in the graph caused by uncertainty in the experimental data and the program used to isolate the

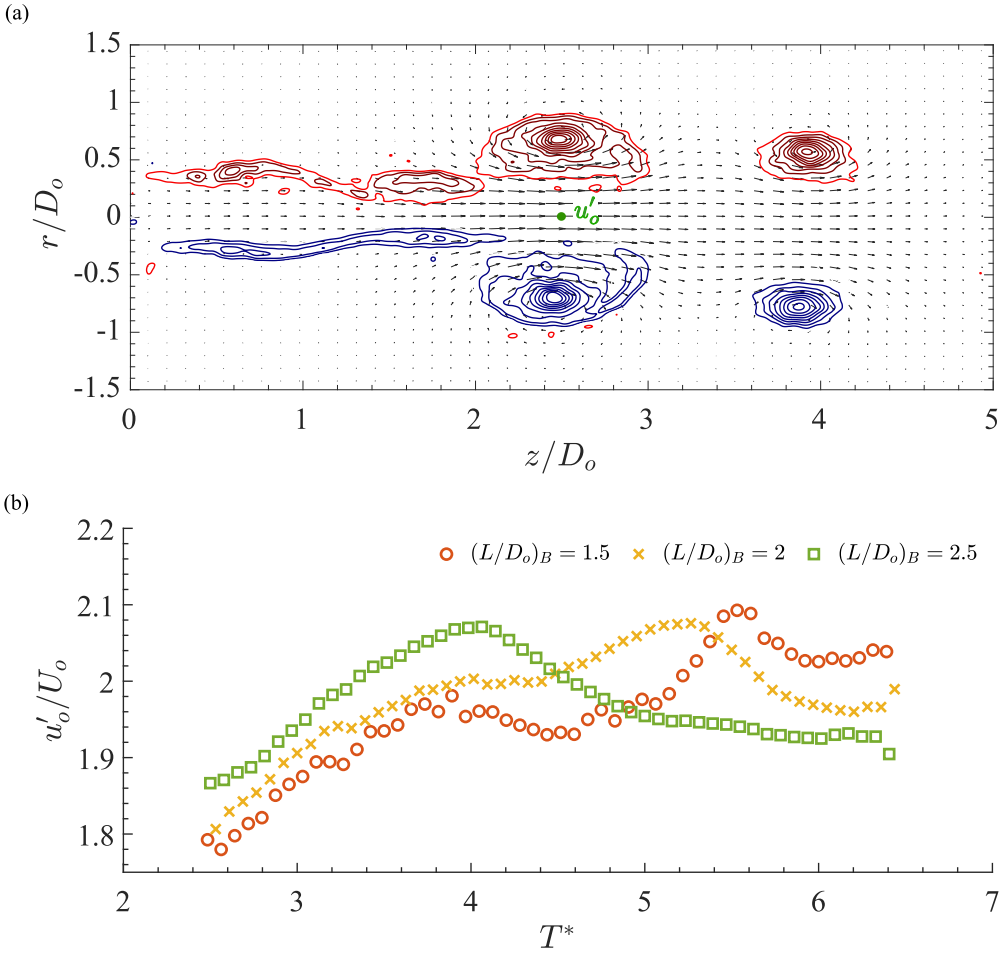

Figure 5.14: (a) Velocity field and vorticity contour plot for $(L/D_o)_B$ at $T^* = 5.3$ and $T^*_{off} = 1.8$ where u'_c is the velocity between the vortex cores. (b) Evolution of the axial velocity at the ring centre, u'_o, for different $(L/D_o)_B$ and $T^*_{off} = 1.8$.

core.

The biggest changes in the velocities are observed for $T^*_{off} = 1.8$ (Figure 5.15 (a,b)) where there is an increase of up to 25% on the propagation velocity for $(L/D_o = 2)_B$. One reason for the increase in propagation velocity is the contraction of ring A, while the other is due to an increase in its circulation, as shown in Figure 5.10 (a). This increase can be explained by the relation $\Gamma/4\pi R$, which accounts for the continuous increment of $u_z^{'}$ for $(L/D_o)_B = 2$. Similar behaviour is observed for $(L/D_o)_B = 1.5$, whose velocity at early times is lower due to its lower circulation.

However, unlike $(L/D_o)_B = 2.5$, which reaches an asymptotic state, its propagation velocity continues to grow until it overtakes $(L/D_o)_B = 2.5$ as a consequence of the circulation gain observed at $T^* > 5$. This phenomenon is also clearly observed when $T^*_{off} = 3$ and the same $(L/D_o)_B$. Besides, all cases with $(L/D_o)_B = 1.5$ show a lower $u_z^{'}$ at $T^* < 4$. This confirms a lower growth rate due to instabilities in the trailing jet and vorticity cancellation discussed in the previous section.

For all cases, including a single ring, radial velocity $u_r^{'}$ decelerates due to the rolling-up process. At early time $T^* < 1$, ring A grows at its maximum rate, reflected in a sudden increase of its radius. Although the ring continues to grow, it does so at a lower rate, explaining the deceleration of $u_r^{'}$. Some of the arguments already discussed can be confirmed based on $u_r^{'}$. For instance, the cases $(L/D_o)_B = 2$ and $(L/D_o)_B = 2.5$ in Figure 5.15 (b) show a different deceleration rate for $3 < T^* < 6$ in comparison with $(L/D_o)_B = 1.5$ where $u_r^{'}$ decays faster, caused by a stronger interaction with ring B and its lower circulation gain that counteracts the drop of $u_r^{'}$. However, for $T^* < 6$, an increase in the circulation is observed in Figure 5.7 (a), which leads to a sudden increase in $u_r^{'}$. This behaviour is also observed for $T^*_{off} = 3$ and 6 in line with the increase of their corresponding $u_z^{'}$ for the $(L/D_o)_B = 1.5$ case, being more pronounced for $T^*_{off} = 3$ where a higher circulation gain was achieved.

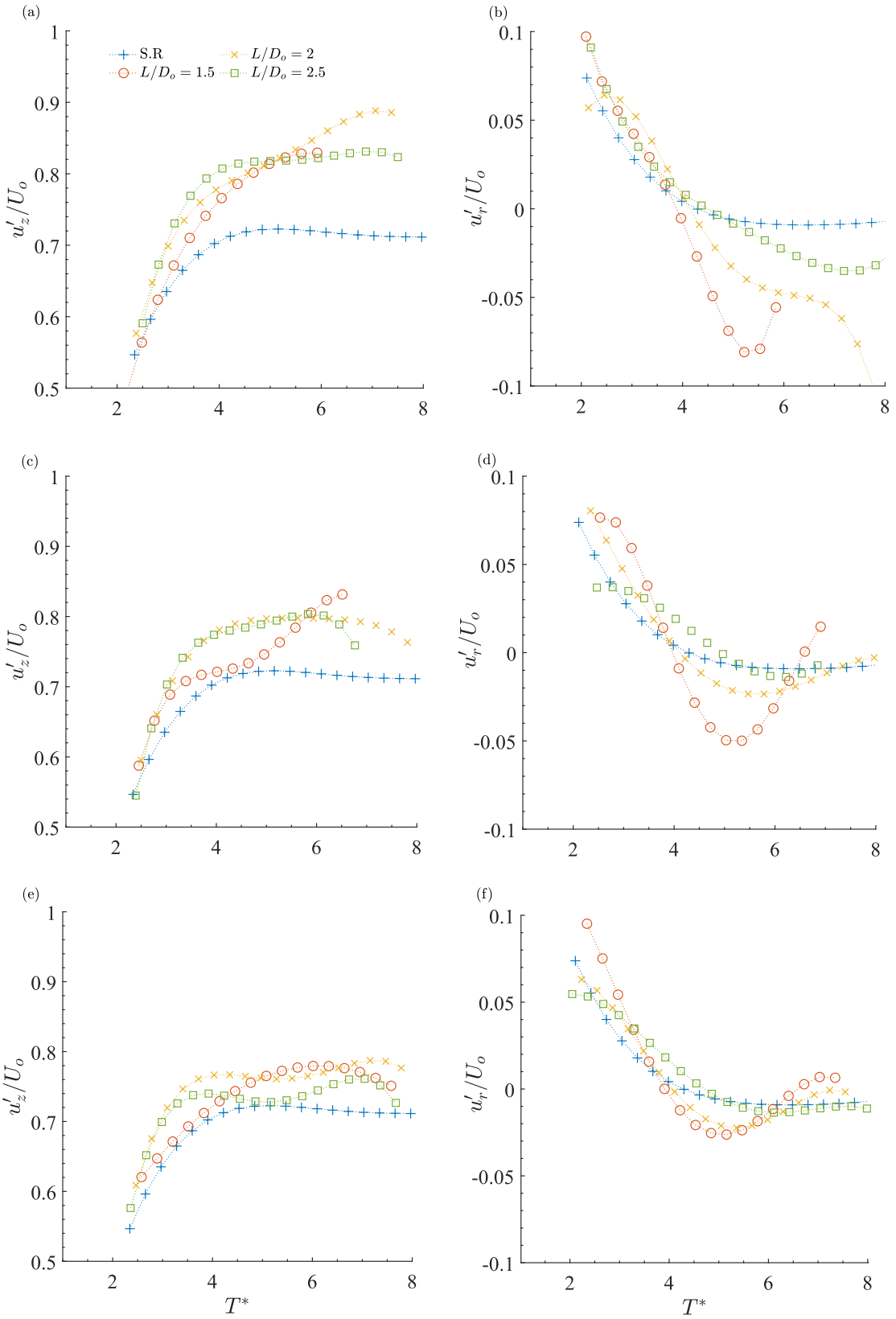

Figure 5.15: Propation velocity $u_z^{'}$ and radius velocity $u_r^{'}$ of ring A for different T^*_{off}: (a) $u_z^{'}$ with $T^*_{off} = 1.8$, (b) $u_r^{'}$ with $T^*_{off} = 1.8$, (c) $u_z^{'}$ with $T^*_{off} = 3$, (d) $u_r^{'}$ with $T^*_{off} = 3$, (e) $u_z^{'}$ with $T^*_{off} = 6$ and (f) $u_r^{'}$ with $T^*_{off} = 6$.

5.2.4 Core distribution

When analyzing the evolution of Δr_c for different T^*_{off} values, it is observed that the strength of interaction between the rings increases as time progresses until leapfrogging is achieved for some cases (for the rest, the FOV is too small to observe it happening). Thus far, the impact of this time-varying interaction has been discussed in terms of significant quantities that describe a vortex ring, including its circulation, energy, and trajectories. However, to better understand the evolution of these quantities, as studied in the last section, it is necessary to analyse the changes in the core via its vorticity distribution and velocity u_c.

In Figure 5.16, the distribution of vorticity and velocity is presented for $T^*_{off} = 1.8$, where the strongest interaction is observed, and all $(L/D_o)_B$. The data was obtained from a line in the axial direction that passes through the centroid of the core of ring A. The radial direction, r_c, origin is located at the core centroid and is scaled with the core radius obtained after applying the threshold $(\omega_{max})e^{-1}$; u_c is the tangential velocity inside the core and like a Rankine vortex (Saffman, 1995) that approaches a solid body rotation.

At $T^* = 2$, no significant difference is observed between the single ring case and the others for both ω and u_c shown in Figure 5.16 (a) and (d). However, at $T^* = 4$, the vorticity distribution spreads out due to shrinking of the ring, and the interaction becomes evident. The same effect was studied in Chapter 2 for swirling rings but with the opposite effect. It is interesting to note that the maximum vorticity, ω_{max}, is basically the same for all cases which oppose the relation:

$$\omega(0,t) \sim \frac{R(t)}{t}, \tag{5.3}$$

studied in Chapter 3 that predicts a decrease in the maximum vorticity as R decreases. The interaction with ring B causes the ring circulation to change, but not the maximum vorticity in the core. Figure 3.6 shows that ω_{max} decreases even during its formation when more vorticity is absorbed; a stronger vortex sheet is the only way to increase ω_{max} and offset the decrease in ω_{max} due to the shrinkage.

Figure 5.16 (e) shows an interesting distribution of u_c that reflects the effect of

the shrinking ring. Assuming that u_c describes a solid body rotation $u_c = \bar{\omega} r_c$, the value $\bar{\omega}$ appears to be the same for all $(L/D_o)_B$ but it is lower than the single ring case which is reflected in the decreases of kinetic energy of the ring:

$$E \sim \frac{1}{2}(u_c)^2 \sim \bar{\omega}^2 r_c^2. \tag{5.4}$$

At $T^* = 6$, ω_{max} decreases for different $(L/D_o)_B$, especially $(L/D_o)_B = 1.5$. Figure 5.7 (b) explains why, for ring A, the decay of ω_{max} is due to its increased interaction with ring B, leading to not only a decreased R but also stronger dissipation. For u_c at $T^* = 6$, the difference of $\bar{\omega}$ between it and the single ring case, and others, is no longer significant.

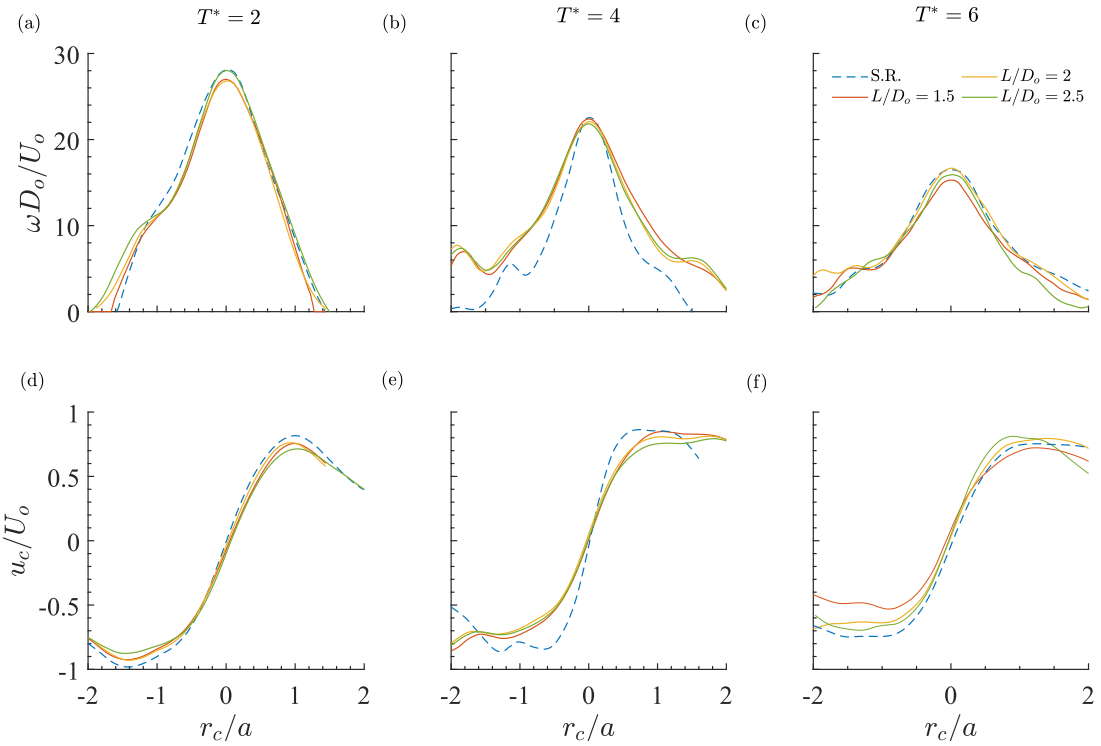

Figure 5.16: Vorticity (a,b,c) and velocity distribution (d,e,f) in the vortex core of ring A at different time T^* for $T^* = 1.8$.

5.2.5 Effect in the vorticity flux

Although the velocity programme used for ring A is consistent across all cases, there was an increase in the vortex flux during the second stroke, as demonstrated by the total circulation of the flow field in Figure 5.17 (a). For each case, the circulation was calculated immediately following the end of the piston stroke that forms ring A, at approximately $T^* = 4.08$, excluding the circulation from the first piston stroke (ring B) and applying a threshold for $\omega < 2$. The most significant increase is observed for $T^*_{off} = 1.8$, where a stronger interaction between the rings occurs, as previously discussed. Interestingly, the case with $(L/D_o)/_B = 1.5$, where it is known that ring B remained closer to the orifice, has the lowest increment of only 8%, compared to a 14% increase for $(L/D_o)_B = 2.5$. The same trend is observed for the other T^*_{off} cases, but with a lower increment in the total circulation.

In the experiments, ring A's stroke ratio was deliberately set higher than its formation number to increase its circulation by absorbing vorticity from the trailing jet. However, Qin et al. (2018) report that the vortex ring circulation increases with certain combinations of parameters such as the number of rings produced, stroke number, the time difference between the piston strokes, and which specific ring is analysed. All the cases with an increase in their circulation have a stroke ratio below their formation number. Unfortunately, the authors did not describe the mechanism involved in this increase. Since there is no trailing jet, the only source of vorticity available to increase the ring's circulation is another vortex ring or a vortex sheet with a higher strength. The former option may be related to the merging of two rings due to leapfrogging. Alternatively, a stronger vortex sheet would involve the induced velocity generated by the leading ring. However, according to Qin et al. (2018), the circulation of the entire flow field does not experience any changes as a result of interaction among multiple vortex rings.

For the results shown in Figure 5.17 (a), the circulation gain is unrelated to including vorticity from ring B. So, the only source could be the induced velocity. However, due to its irrotational nature, the induced velocity can only generate vorticity inside the orifice. For instance, it is well known that the flow ejected by the nozzle's velocity profile changes significantly during the formation process due to the

strong vorticity generated by the roll-up of the vortex sheets at the orifice's edge. The induced velocity from the early vortex ring accelerates the flow near the orifice wall Figure 5.17 (b), increasing its boundary layer and then producing a stronger vortex sheet. As the vortex rings separate from the orifice, the velocity profile tends to be parabolic, as expected for pipe flow (Didden, 1979). This evolution of the velocity profile is similar to the annular effect observed by Richardson and Tyler (1929) in oscillating pipe flow. Prior to the formation of ring A, the ring B for $(L/D_o)_B = 1.5$ has moved downstream a distance equivalent to $1.4D_o$ from the orifice. This indicates that any induced velocity in the axial direction within the orifice would be minimal since it is inversely proportional to the distance from the source of vorticity, rendering it an unlikely possibility. Additionally, if this is true, the case with a $(L/D_o)_B = 1.5$, where ring B is closer to the orifice, would result in a greater increase in total circulation.

A possible alternative explanation is the influence of the induced radial velocity on the circulation increase. In the study of Krieg and Mohseni (2013), the impact of non-zero radial velocity on impulse and kinetic energy of vortex rings is investigated. Their results showed that the impulse and kinetic energy of the flow discharged by the nozzle increase up to 90% for a converging radial velocity, also showing an increase in the total circulation. u_{r-i} also has a converging distribution at the orifice, and even though the induced radial velocity from ring B would be weak, the shrinking that ring A experiences could change the u_{r-i} distribution or magnitude. But, as shown in Figure 5.11 (d), the induced velocity in the radial direction is also stronger for $(L/D_o)_B = 1.5$, contradicting the behaviour observed in Figure 5.17 (a). Although the previous arguments explain the increases in the vortex flux due to the interaction between two rings, the mechanism involved in the higher circulation gain observed as $(L/D_o)_B$ increases remains unclear; further investigation is required.

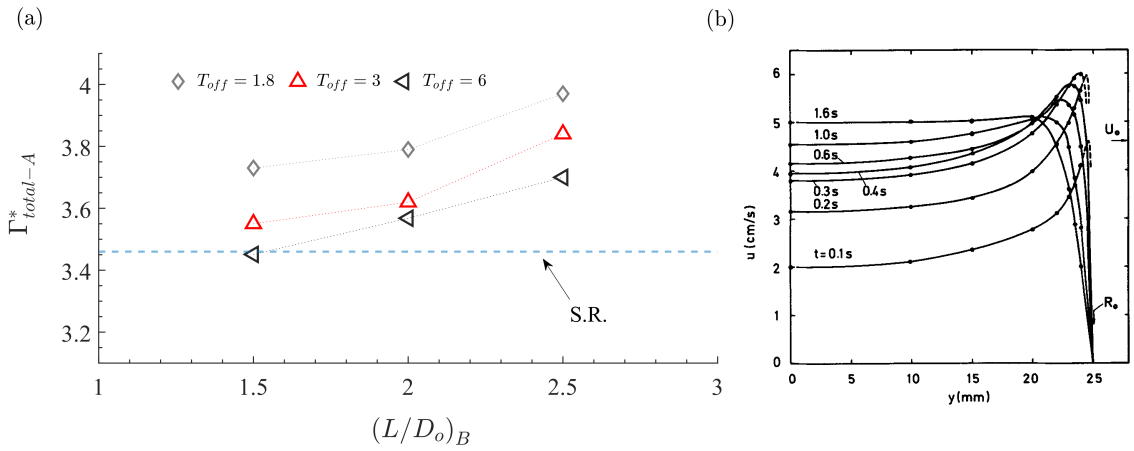

Figure 5.17: (a) Total circulation $\Gamma_{Total-A}$ of ring A at $T^* \approx 4.08$ for all the cases studied. The dashed line represents the single-ring case total circulation. (b) Evolution of the axial velocity profile at the nozzle exit; Figure taken from Didden (1979).

Conclusion

In this chapter, the manipulation of R, which is modified by its interaction with a preceding vortex ring, and its correlation with F has been rigorously investigated for nine cases which correspond to three-time intervals $T^*_{off} = 1.8, 3$ and 6 and three strokes ratios for the leading Ring (B), $(L/D_o)_B = 1.5, 2$ and 2.5. For the following ring (A) L/D_o was fixed to 4. A decrease of R was observed for all the cases but was more pronounced for $T^*_{off} = 1.8$ due to the proximity of ring B. As expected, the shrink of ring A reduced its kinetic energy α, which is reflected in an enhancement of the ring's circulation of up to 13% and increasing F by up to 10% in comparison with the single ring case.

Three different mechanisms were observed for the ring's circulation gain:

- For $T^* < 4$, ring A shrinks, reducing its kinetic energy. This allows it to absorb more vorticity while still attached to the trailing jet.

- For $T^* > 5$, the interaction between rings A and B intensifies as ring B slows down and ring A speeds up due to the evolution of their respective radii, R. This destabilizes the trailing jet of ring A, which generates regions of high vorticity, leading to its detachment. The high vorticity region is partly accelerated by the induced velocity of ring B but mainly by ring A, whose

contraction of its radius accelerates the flow passing through. The vorticity patch travels around the vortex core until it is engulfed by the ring A.

- The formation of a preceding vortex ring increases the vortex flux generated by a following vortex ring.

CHAPTER 6

Conclusions

In this thesis, the effects of adding swirl, S, to vortex rings generated by an impulsive discharge of momentum from an orifice have been investigated both numerically and experimentally. In the numerical analysis, a solid body rotation velocity distribution was used in addition to the discharge velocity to add swirl. The resulting swirling vortex rings were found to exhibit the following characteristics:

1. An increase in the production of opposite sign vorticity (OSV), which increases with S.
2. A growth in the ring radius as S increases.
3. A decrease in the propagation velocity of the vortex ring.
4. An increase in S causes a decrease in the formation number, F, resulting in vortex rings with lower circulation.

The above features for swirling vortex rings have been reported in earlier studies, each addressing the problem from different perspectives and with different degrees of rigour. What is unique about the current work is it considers the formation process, together with the nature of the swirling discharge; the latter being a key feature underpinning the investigation carried out.

From the numerical results generated, three sources of OSV were identified:

- The first is caused by the induced velocity from the ring core interacting with the wall, which creates a boundary layer/vortex sheet with an OSV to that of the vortex core. This source is slightly affected by S but only in terms of the strength and position of the vortex core.

- The second is related to the discharge velocity profile, which again is slightly affected by S.

- The third source is related to the addition of swirl and is described in detail below.

Previous studies have proposed that OSV is produced by the angular velocity, u_θ, within the vortex core, either due to its distribution or through inducing a secondary flow (Dean vortices). However, in the case of a vortex ring created by an impulsive discharge of momentum, OSV is generated instead by the u_θ in the swirling jet. The swirling jet has axial vorticity, ω_z, and due to the roll-up process of the vortex ring, the u_θ distribution of the swirling jet changes, tilting the vorticity vector and generating a new component in the azimuthal direction. This process is captured by the following expression:

$$\left(\frac{\partial \omega_\theta}{\partial t}\right)_{\mathrm{T}} = \frac{1}{2}\frac{\partial}{\partial z}\left(\frac{{u_\theta}^2}{r}\right); \tag{6.1}$$

the subscript 'T' on the *lhs* denoting vortex tilting.

In order to generate the same solid body rotation inlet condition as in the numerical work, a rotating pipe was used in the complementary experimental work undertaken. The theoretical model suggested that it would take approximately 60 seconds to achieve the desired distribution. However, during the experiments, a secondary flow was observed due to the pressure difference between the rotating pipe and the tank. This flow caused fluid to eject from the inside of the pipe and near its wall into the tank, and also entrained fluid from the tank with zero u_θ, preventing the establishment of a fully developed solid body rotation velocity profile. Instead, the steady velocity profile achieved is a partially established solid body rotation only.

As the pipe's angular velocity increases, the secondary flow's intensity increases as well, which affects u_θ.

Nevertheless, instead of being a problem, a partially established solid body rotation profile confirms the physics emerging from the results from the numerical work pertaining to characteristics 1. to 3., as follows:

- A partially established solid body rotation profile has a small u_θ magnitude close to the centre where the gradient in equation (6.1) is stronger. Then, by decreasing the rotation time of the pipe (preparation time) and increasing the angular speed, it is possible to create swirling vortex rings with a higher angular velocity in their core, $\overline{u_\theta}$, and a lower production of OSV.

- Reducing the production of OSV leads to a decrease in the ring radius growth characteristic in swirling vortex rings. This supports the argument that OSV, higher close to the jet centre, induces an axial flow component, u_z, in the opposite direction of the ring's propagation, generating a stagnation point which increases the radial velocity, u_r, due to having to satisfy the continuity equation. This phenomenon was also observed in two vortex rings with similar $\bar{u_\theta}$ but different OSV production, indicating that the centrifugal effect is weaker in the growth of the ring radius.

- The reduction in the velocity of the swirling vortex ring is mainly due to an increase in its radius, where the propagation velocity of the ring axially, $u_z^{'}$, is inversely proportional to the ring radius, R. To investigate the effect of ring velocity on OSV production, two swirling rings with similar $\bar{u_\theta}$ but different R behaviour were compared. The result confirmed that the $\bar{u_\theta}$ has a minor influence on $u_z^{'}$, as illustrated in Figure 3.17.

Estimating the value of $\bar{u_\theta}$ is possible based on the preparation time. This estimation was made by considering that most of the fluid forming a vortex ring comes from the boundary layer inside the orifice during the flow discharge. Only the u_θ in this region will be engulfed by the ring. Therefore, the estimated $\bar{u_\theta}$ is similar to the average u_θ in the vicinity of the rotating pipe wall. Among the preparation times studied, it is estimated that one of five seconds would produce

a $\bar{u_\theta}$ corresponding to a ring with $S = 0.5$. The results show a difference of about 17%, which is explained by the pipe rotation during the piston stroke that was not included in the estimation, as well as the effect of the secondary flow.

In the numerical simulations, the correlation between the variables S and F was explained by the growth of the vortex ring radius, R, and its connection to the ring energy, α. According to Gharib et al. (1998), the vortex ring will continue to grow as long as the energy of the trailing jet is higher than that of the vortex ring. F occurs when both energies are equal. As the vortex ring radius increases, the dimensionless kinetic energy of the vortex ring also increases, decreasing the time available for the vortex ring to absorb vorticity from the trailing jet.

In order to address characteristic 4. an additional experiment was conducted that was not directly related to swirling vortex rings. This experiment aimed to increase the value of F by reducing the growth of R during the formation of a vortex ring through its interaction with a preceding vortex ring. The experiment tested vortex rings with different strengths and separations, resulting in an increase of F up to 10%. Consequently, the ring circulation, Γ_{Ring}, increased by 13%. Furthermore, the value of α was calculated, and it was observed that its value decreases as R decreases and Γ_{Ring} increases, which confirms the finding of the numerical work.

In summary, the schematic on the following page represents the results obtained from both the numerical and experimental studies. A feedback process exists between the formation of OSV and R increase, significantly influencing the vortex ring's kinematics and formation.

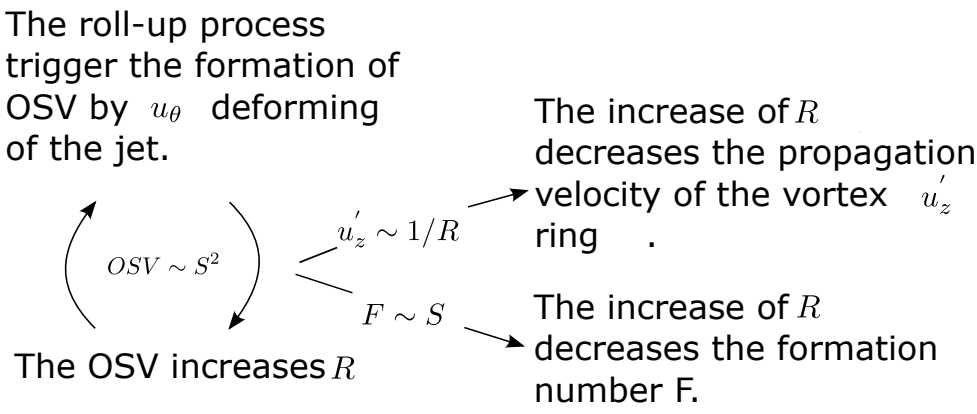

6.1 Future work

The following avenues for further research, investigation and determination are suggested, a number of which are already in progress:

- While experiments have been conducted involving swirling vortex rings with varying preparation times and $L/D_o = 4$, due to time constraints the corresponding in-depth analysis was not performed, but is required. The experiments aimed to establish the relationship between F and the preparation time, and to determine whether the generation of OSV is related to the L/D_o value used, since the dimensionless interpretation of its circulation does not consider this factor.

- Further analysis is needed to describe the relation $S \sim f(R)$.

- Inclusion of the influence of the secondary flow present in a rotating pipe in equation (4.3), to more accurately predict $\bar{u_\theta}$.

- The carrying out of simulations for the cases explored experimentally in Chapter 5, to confirm and explain increased vorticity flux during a second piston stroke.

- Expand and publish the results presented in Chapters 4 and 5.

Bibliography

P. M. Arvidsson, S. J. Kovács, J. Töger, R. Borgquist, E. Heiberg, M. Carlsson, and H. Arheden. Vortex ring behavior provides the epigenetic blueprint for the human heart. *Scientific reports*, 6(1):22021, 2016. (document), 1, 1.1

H. Asadi, H. Asgharzadeh, and I. Borazjani. On the scaling of propagation of periodically generated vortex rings. *Journal of Fluid Mechanics*, 853:150–170, 2018. (document), 5.1, 5.1

P. Bartholomew, F. Denner, M. H. Abdol-Azis, A. Marquis, and B. G. van Wachem. Unified formulation of the momentum-weighted interpolation for collocated variable arrangements. *Journal of Computational Physics*, 375:177–208, 2018. 2.2.1

G. K. Batchelor. *An introduction to fluid dynamics*. Cambridge university press, 1967. (document), 1.2, 1.3, 1.3, 2.1, 4, 4.2, 4.4, 5.2.2

S. Berger, L. Talbot, and L. Yao. Flow in curved pipes. *Ann. Rev. Fluid Mech.*, 15(1):461–512, 1983. 3.3.2, 3.3.2

P. Billant, J. Chomaz, and P. Huerre. Experimental study of vortex breakdown in swirling jets. *J. Fluid Mech.*, 376:183–219, 1998. 1.2, 3.3.3

A. V. Borisov, A. A. Kilin, I. S. Mamaev, and V. A. Tenenev. The dynamics of vortex rings: leapfrogging in an ideal and viscous fluid. *Fluid Dynamics Research*, 46(3):031415, 2014. 1.3

G. Brown and J. Lopez. Axisymmetric vortex breakdown part 2. physical mechanisms. *J. Fluid Mech.*, 221:553–576, 1990. 1.2, 3.3.2, 3.3.2, 3.3.3

S. Candel, D. Durox, T. Schuller, J. Bourgouin, and J. Moeck. Dynamics of swirling flames. *Ann. Rev. Fluid Mech.*, 46:147–173, 2014. 1.2

M. Cheng, J. Lou, and T. Lim. Vortex ring with swirl: A numerical study. *Phys. Fluids*, 22(9):097101, 2010. (document), 1.2, 1.2, 1.5, 3.3.2, 3.3.2, 3.3.2, 3.3.4

M. Cheng, J. Lou, and T. Lim. Leapfrogging of multiple coaxial viscous vortex rings. *Physics of Fluids*, 27(3), 2015. (document), 1.8, 1.3

A. Coussement, O. Gicquel, and G. Degrez. Large eddy simulation of a pulsed jet in cross-flow. *J. Fluid Mech.*, 695:1–34, 2012. 2.2.3

J. O. Dabiri and M. Gharib. Starting flow through nozzles with temporally variable exit diameter. *Journal of Fluid Mechanics*, 538:111–136, 2005. 3.3.6, 5

I. Danaila, F. Kaplanski, and S. Sazhin. Modelling of confined vortex rings. *J. Fluid Mech*, 774:267–297, 2015. 3.2.1

D. Darmofal. The role of vorticity dynamics in vortex breakdown. In *23rd Fluid Dynamics, Plasmadynamics, and Lasers Conference*, page 3036, 1993. 3.3.2, 3.3.2, 3.3.3, 3.3.3

D. Das, M. Bansal, and A. Manghnani. Generation and characteristics of vortex rings free of piston vortex and stopping vortex effects. *Journal of Fluid Mechanics*, 811:138–167, 2017. doi: 10.1017/jfm.2016.733. 4.1.2, 5.1

J. Davila, M. del Pino, M. Musso, and J. Wei. Leapfrogging vortex rings for the 3-dimensional incompressible euler equations. *arXiv preprint arXiv:2207.03263*, 2022. 1.3

N. Didden. On the formation of vortex rings: rolling-up and production of circulation. *Zeitschrift für angewandte Mathematik und Physik ZAMP*, 30:101–116, 1979. (document), 1.1, 3.3.2, 3.3.2, 5.1, 5.2.5, 5.17

J. H. Ferziger, M. Perić, and R. L. Street. *Computational methods for fluid dynamics*. springer, 2019. 2.2.1, 5

L. Fraenkel. Examples of steady vortex rings of small cross-section in an ideal fluid. *J. Fluid Mech.*, 51(1):119–135, 1972. 3.3.6

Z. Fu and H. Liu. Transient force augmentation due to counter-rotating vortex ring pairs. *Journal of Fluid Mechanics*, 785:324–348, 2015. doi: 10.1017/jfm.2015.637. 1.3, 1.3

Z. Fu, S. Qin, and H. Liu. Mechanism of transient force augmentation varying with two distinct timescales for interacting vortex rings. *Physics of Fluids*, 26(1), 2014. 1.3, 1.3

Y. Fukumoto and H. K. Moffatt. Motion and expansion of a viscous vortex ring. part 1. a higher-order asymptotic formula for the velocity. *J. Fluid Mech.*, 417: 1–45, 2000. doi: 10.1017/S0022112000008995. 3.3.2

L. Gan. *An experimental study of turbulent vortex rings using particle image velocimetry*. PhD thesis, University of Cambridge, 2010. 1.1, 2.3.2, 3.2.1, 3.3.3, 3.3.3

L. Gan, T. Nickels, and J. Dawson. An experimental study of a turbulent vortex ring: a three-dimensional representation. *Experiments in Fluids*, 51:1493–1507, 2011. 1.2

L. Gan, J. Dawson, and T. Nickels. On the drag of turbulent vortex rings. *J. Fluid Mech.*, 709:85–105, 2012. 1.1

L. Gao and S. Yu. A model for the pinch-off process of the leading vortex ring in a starting jet. *J. Fluid Mech.*, 656:205–222, 2010. 1.1, 3.3.6

C. Gargan-Shingles, M. Rudman, and K. Ryan. The evolution of swirling axisymmetric vortex rings. *Phys. of Fluids*, 27(8):087101, 2015. 1.2, 1.2, 3.3.2, 3.3.2

M. Germano, U. Piomelli, P. Moin, and W. Cabot. A dynamic subgrid-scale eddy viscosity model. *Phys. Fluids A: Fluid Dynamics*, 3(7):1760–1765, 1991. 2.2.2

M. Gharib, E. Rambod, and K. Shariff. A universal time scale for vortex ring formation. *Journal of Fluid Mechanics*, 360:121–140, 1998. (document), 1.1, 1.3, 1.1, 1.1, 3.3.6, 3.3.6, 3.3.6, 5.2.2, 6

M. Gharib, E. Rambod, A. Kheradvar, D. J. Sahn, and J. O. Dabiri. Optimal vortex formation as an index of cardiac health. *Proceedings of the National Academy of Sciences*, 103(16):6305–6308, 2006. 1

A. Glezer and D. Coles. An experimental study of a turbulent vortex ring. *J. Fluid Mech.*, 211:243–283, 1990. 3.3.3

C. Greenshields and H. Weller. *Notes on Computational Fluid Dynamics: General Principles*. CFD Direct Ltd, Reading, UK, 2022. (document), 2.2.1, 2.3, 3.2.1

R. Gullberg. Computational fluid dynamics in openfoam. *Mesh Generation and Quality. TKP*, 4555, 2017. 2.2.3

D. Hahn and M.-N. Özişik. *Heat Conduction*. John Wiley & Sons, Inc., 2012. 3.3.4

Y. Hattori, F. Blanco-Rodríguez, and S. Le Dizès. Numerical stability analysis of a vortex ring with swirl. *J. Fluid Mech.*, 878:5–36, 2019. 3.3.4

C. He, L. Gan, and Y. Liu. Dynamics of compact vortex rings generated by axial swirlers at early stage. *Phys. Fluids*, 32(4):045104, 2020a. 1.2, 1.2, 3.3.1

C. He, L. Gan, and Y. Liu. The formation and evolution of turbulent swirling vortex rings generated by axial swirlers. *Flow, Turbulence and Combustion*, 104: 795–816, 2020b. (document), 1.2, 1.2, 1.2, 2.2.3, 2.3, 2.7, 2.3.1, 2.3.2, 3.3.2, 3.3.3, 3.3.5, 3.18, 3.3.6, 4.1.3

H. Helmholtz. Über integrale der hydrodynamischen gleichungen, welche den wirbelbewegungen entsprechen. 1858a. 1

L. Helmholtz. Über integral der hydrodynamischen gleichungen welche den wirbelbewegungen entsprechen, journal für reine und angewandte mathematik. 55. 1858b. 1.3

R. I. Issa. Solution of the implicitly discretised fluid flow equations by operator-splitting. *Journal of computational physics*, 62(1):40–65, 1986. 2.2.1

F. P. Kärrholm. Rhie-chow interpolation in openfoam. *Department of Applied Mechanics, Chalmers University of Technology: Goteborg, Sweden*, 2006. 2.2.1

Kelvin. The translatory velocity of a circular vortex ring. *Phil. Mag*, 33:511–512, 1867. 1

A. Kolmogorov. The local structure of turbulence in incompressible viscous fluid for very large reynolds numbers. *Doklady Akademii Nauk*, 30:301–304, 1941. 2.2.2

M. Krieg and K. Mohseni. Modelling circulation, impulse and kinetic energy of starting jets with non-zero radial velocity. *Journal of Fluid Mechanics*, 719:488–526, 2013. 3.3.2, 5.2.5

H. Liang and T. Maxworthy. An experimental investigation of swirling jets. *Journal of fluid mechanics*, 525:115–159, 2005. 1.2, 1.2, 2.3.1, 3.2.1

D. K. Lilly. A proposed modification of the germano subgrid-scale closure method. *Physics of Fluids A: Fluid Dynamics*, 4(3):633–635, 1992. 2.2.2

T. Lim. A note on the leapfrogging between two coaxial vortex rings at low reynolds numbers. *Physics of Fluids*, 9(1):239–241, 1997. (document), 1.7, 1.3, 1.8

T. Lim and T. Nickels. Vortex rings. In *Fluid vortices*, pages 95–153. Springer, 1995. 1.1, 3.3.2, 3.3.5, 5.1

R. Limbourg and J. Nedić. Formation of an orifice-generated vortex ring. *Journal of Fluid Mechanics*, 913:A29, 2021. 1.1, 3.3.6, 5.2.1

Y. Liu and O. Hinrichsen. Cfd modeling of bubbling fluidized beds using openfoam®: Model validation and comparison of tvd differencing schemes. *Computers & chemical engineering*, 69:75–88, 2014. 2.2.1

T. Marić, J. Höpken, et al. The openfoam technology primer. *(No Title)*, 2014. 2.2.1

C. Mavroyiakoumou and F. Berkshire. Collinear interaction of vortex pairs with different strengths—criteria for leapfrogging. *Physics of Fluids*, 32(2), 2020. 1.3

T. Maxworthy. The structure and stability of vortex rings. *Journal of Fluid Mechanics*, 51(1):15–32, 1972. 1.3, 1.3

T. Maxworthy. Some experimental studies of vortex rings. *J. Fluid Mech.*, 81(3): 465–495, 1977. 1.2, 3.3.1

T. Naitoh, N. Okura, T. Gotoh, and Y. Kato. On the evolution of vortex rings with swirl. *Physics of fluids*, 26(6), 2014. (document), 1.2, 1.2, 1.5, 2.3, 2.7, 3.2.1, 3.3.2, 3.3.2, 3.3.3, 3.3.4, 3.3.5, 4.1.2

T. New, G. Gotama, and U. Vevek. A large-eddy simulation study on vortex-ring collisions upon round cylinders. *Phys. Fluids*, 33(9):094101, 2021. 2.2.2

J. Norbury. A family of steady vortex rings. *Journal of Fluid Mechanics*, 57(3): 417–431, 1973. 3.3.6, 5.2.2

OpenCFD. User guide schemes, 2024a. URL `https://www.openfoam.com/documentation/guides/latest/doc/guide-schemes-divergence-lust.html`. 2.2.1

OpenCFD. User guide, 2024b. URL `https://www.openfoam.com/documentation/user-guide/1-introduction`. (document), 2.1, 2.1

R. Ortega-Chavez, L. Gan, and P. H. Gaskell. Formation and evolution of vortex rings with weak to moderate swirl. *Journal of Fluid Mechanics*, 967:A16, 2023. 5.2.2

Y. Oshima. The game of passing-through of a pair of vortex rings. *Journal of the Physical Society of Japan*, 45(2):660–664, 1978. (document), 1.3, 1.8

Y. Oshima, T. Kambe, and S. Asaka. Interaction of two vortex rings moving along a common axis of symmetry. *Journal of the Physical Society of Japan*, 38 (4):1159–1166, 1975. 1.3

S. Pope. Ten questions concerning the large-eddy simulation of turbulent flows. *New J. Phys.*, 6(1):35, 2004. 2.2.3

S. B. Pope. *Turbulent flows*. Cambridge University Press, 2000. 2.2.2

F. Pulvirenti, S. Scollo, C. Ferlito, and F. M. Schwandner. Dynamics of volcanic vortex rings. *Scientific Reports*, 13(1):2369, 2023. (document), 1, 1.1

S. Qin, H. Liu, and Y. Xiang. On the formation modes in vortex interaction for multiple co-axial co-rotating vortex rings. *Physics of Fluids*, 30(1), 2018. (document), 1.3, 1.9, 1.3, 5, 5.2.5

O. Reynolds. On the resistance encountered by vortex rings, and the relation between the vortex rings and streamlines of a disk. *Nature*, 14:477–479, 1876. 1

C. M. Rhie and W.-L. Chow. Numerical study of the turbulent flow past an airfoil with trailing edge separation. *AIAA journal*, 21(11):1525–1532, 1983. 2.2.1

E. Richardson and E. Tyler. The transverse velocity gradient near the mouths of pipes in which an alternating or continuous flow of air is established. *Proceedings of the Physical Society*, 42(1):1, 1929. 3.2.1, 5.2.5

L. F. Richardson. *Weather prediction by numerical process*. Cambridge University Press, 1922. 2.2.2

M. Rosenfeld, E. Rambod, and M. Gharib. Circulation and formation number of laminar vortex rings. *J.Fluid Mech.*, 376:297–318, 1998. (document), 1.1, 2.5, 2.2.3, 3.2.1, 3.2.1, 3.3.6

P. Saffman. On the formation of vortex rings. *Studies in Applied Mathematics*, 54 (3):261–268, 1975. 3.3.2

P. Saffman. The number of waves on unstable vortex rings. *J. Fluid Mech*, 84(4): 625–639, 1978. 1.2, 3.3.2

P. G. Saffman. *Vortex dynamics*. Cambridge university press, 1995. 1.1, 3.3.2, 3.3.5, 5.2.4

J. Satti and J. Peng. Leapfrogging of two thick-cored vortex rings. *Fluid Dynamics Research*, 45(3):035503, 2013. 1.3

K. Shariff and A. Leonard. Vortex rings. *Ann. Rev. Fluid Mech.*, 24(1):235–279, 1992. 1.1

K. Shariff, A. Leonard, and J. H. Ferziger. Dynamics of a class of vortex rings. Technical report, 1989. 1.3, 1.3

M. Shusser and M. Gharib. Energy and velocity of a forming vortex ring. *Physics of Fluids*, 12(3):618–621, 2000. 1.1, 3.3.6, 5.2.2, 5.2.2

J. Smagorinsky. General circulation experiments with the primitive equations: I. the basic experiment. *Monthly Weather Review*, 91(3):99–164, 1963. 2.2.2

A. Sommerfeld. *Lectures on theoretical physics*, volume 2. Academic, 1950. 1.3

J. Taddeucci, J. J. Peña Fernández, V. Cigala, U. Kueppers, P. Scarlato, E. Del Bello, T. Ricci, J. Sesterhenn, and S. Panunzi. Volcanic vortex rings: Axial dynamics, acoustic features, and their link to vent diameter and supersonic jet flow. *Geophysical Research Letters*, 48(15):e2021GL092899, 2021. 1

J. Töger, M. Kanski, M. Carlsson, S. J. Kovács, G. Söderlind, H. Arheden, and E. Heiberg. Vortex ring formation in the left ventricle of the heart: analysis by 4d flow mri and lagrangian coherent structures. *Annals of biomedical engineering*, 40: 2652–2662, 2012. 1

L. Tophøj and H. Aref. Instability of vortex pair leapfrogging. *Physics of Fluids*, 25(1), 2013. 1.3

P. G. Tucker. *Mesh Generation*, page 67–147. Cambridge Aerospace Series. Cambridge University Press, 2016. doi: 10.1017/CBO9781139872010.004. 2.2.3

R. Verzicco, P. Orlandi, A. Eisenga, G. Van Heijst, and G. Carnevale. Dynamics of a vortex ring in a rotating fluid. *Journal of Fluid Mechanics*, 317:215–239, 1996. (document), 1.2, 2.3, 2.7

D. Virk, M. Melander, and F. Hussain. Dynamics of a polarized vortex ring. *J. Fluid Mech.*, 260:23–55, 1994. 1.2, 1.2, 3.3.3, 3.3.5, 4.1.3

A. Weigand and M. Gharib. On the evolution of laminar vortex rings. *Experiments in Fluids*, 22(6):447–457, 1997. 3.3.2, 5.1

A. Wimshurts. [cfd] the piso algorithm, 2019. URL https://www.youtube.com/watch?v=ahdW5TKacok. 5

H. Yamada and T. Matsui. Preliminary study of mutual slip-through of a pair of vortices. *The Physics of Fluids*, 21(2):292–294, 1978. 1.3

W. Zhao, S. Frankel, and L. Mongeau. Effects of trailing jet instability on vortex ring formation. *Phys. Fluids*, 12(3):589–596, 2000. 3.3.2, 3.3.6

APPENDIX A

OpenFOAM user script

,

A.1 0 folder

U

p

k

nut

A.2 constant folder

transportProperties

turbulenceProperties

A.3 system folder

BlockMeshDict

controlDict

fvSchemes

fvSolution

```
/*--------------------------------*- C++ -*----------------------------------*\
  =========                 |
  \\      /  F ield         | OpenFOAM: The Open Source CFD Toolbox
   \\    /   O peration     | Website:  https://openfoam.org
    \\  /    A nd           | Version:  7
     \\/     M anipulation  |
\*---------------------------------------------------------------------------*/
FoamFile
{
    version     2.0;
    format      ascii;
    class       volVectorField;
    location    "0";
    object      U;
}
// * * * * * * * * * * * * * * * * * * * * * * * * * * * * * * * * * * * * * //
dimensions      [0 1 -1 0 0 0 0];
internalField   uniform (0 0 0);
boundaryField
{
     inlet
    {
        type            cylindricalInletVelocity;
        origin          (0 0 0);
        axis            (0 0 1);
        axialVelocity   table
(
(0 0.1)
(1.49 0.1)
(1.5 0)
);
        radialVelocity  constant 0;
        rpm             constant 76.4;
        value           uniform (0 0 0);
    }
    pipe
    {
        type           noSlip;
    }
    tapa
    {
        type            noSlip;
    }
    outlet
    {
        type            zeroGradient;
    }
    tank
    {
        type            noSlip;
    }
}
// ************************************************************************* //
```

```
/*--------------------------------*- C++ -*----------------------------------*\
  =========                 |
  \\      /  F ield         | OpenFOAM: The Open Source CFD Toolbox
   \\    /   O peration     | Website:  https://openfoam.org
    \\  /    A nd           | Version:  7
     \\/     M anipulation  |
\*---------------------------------------------------------------------------*/
FoamFile
{
    version     2.0;
    format      ascii;
    class       volScalarField;
    location    "0";
    object      p;
}
// * * * * * * * * * * * * * * * * * * * * * * * * * * * * * * * * * * * * * //
dimensions      [0 2 -2 0 0 0 0];

internalField   uniform 0;
boundaryField
{
    inlet
    {
        type            zeroGradient;
    }
    pipe
    {
        type            zeroGradient;
    }
    tapa
    {
        type            zeroGradient;
    }
    outlet
    {
        type            fixedValue;
        value           uniform 0;
    }
    tank
    {
        type            zeroGradient;
    }
}
// ************************************************************************* //
```

```
/*--------------------------------*- C++ -*----------------------------------*\
  =========                 |
  \\      /  F ield         | OpenFOAM: The Open Source CFD Toolbox
   \\    /   O peration     | Website:  https://openfoam.org
    \\  /    A nd           | Version:  7
     \\/     M anipulation  |
\*---------------------------------------------------------------------------*/
FoamFile
{
    version     2.0;
    format      ascii;
    class       volScalarField;
    location    "0";
    object      nut;
}
// * * * * * * * * * * * * * * * * * * * * * * * * * * * * * * * * * * * * * * * //

dimensions      [0 2 -1 0 0 0 0];

internalField   uniform 0;

boundaryField
{
    inlet
    {
        type         nutUWallFunction;
        value           uniform 0;
    }
    pipe
    {
        type            nutUWallFunction;
        value           uniform 0;
    }
    tapa
    {
        type            nutUWallFunction;
        value           uniform 0;
    }
    outlet
    {
        type            nutUWallFunction;
        value           uniform 0;
    }
    tank
    {
        type            nutUWallFunction;
        value           uniform 0;
    }
}


// ************************************************************************* //
```

```
/*--------------------------------*- C++ -*----------------------------------*\
  =========                 |
  \\      /  F ield         | OpenFOAM: The Open Source CFD Toolbox
   \\    /   O peration     | Website:  https://openfoam.org
    \\  /    A nd           | Version:  7
     \\/     M anipulation  |
\*---------------------------------------------------------------------------*/
FoamFile
{
    version     2.0;
    format      ascii;
    class       volScalarField;
    location    "0";
    object      k;
}
// * * * * * * * * * * * * * * * * * * * * * * * * * * * * * * * * * * * * * //
dimensions      [0 2 -2 0 0 0 0];
internalField   uniform 0
boundaryField
{
    inlet
    {
        type            fixedValue;
        value           uniform 0.000025;
    }
    pipe
    {
        type            fixedValue;
        value           uniform 0;
    }
    tapa
    {
        type            fixedValue;
        value           uniform 0;
    }
    outlet
    {
        type            inletOutlet;
        inletValue      uniform 0;
        value           uniform 0;
    }
    tank
    {
        type            fixedValue;
        value           uniform 0;
    }
}
// ************************************************************************* //
```

```
/*--------------------------------*- C++ -*----------------------------------*\
  =========                 |
  \\      /  F ield         | OpenFOAM: The Open Source CFD Toolbox
   \\    /   O peration     | Website:  https://openfoam.org
    \\  /    A nd           | Version:  7
     \\/     M anipulation  |
\*---------------------------------------------------------------------------*/
FoamFile
{
    version     2.0;
    format      ascii;
    class       dictionary;
    location    "constant";
    object      transportProperties;
}
// * * * * * * * * * * * * * * * * * * * * * * * * * * * * * * * * * * * * * //

transportModel  Newtonian;

nu              [0 2 -1 0 0 0 0] 1e-06;

// ************************************************************************* //
```

```
/*--------------------------------*- C++ -*----------------------------------*\
| =========                 |                                                 |
| \\      /  F ield         | OpenFOAM: The Open Source CFD Toolbox           |
|  \\    /   O peration     | Version:  2.3.0                                 |
|   \\  /    A nd           | Web:      www.OpenFOAM.org                      |
|    \\/     M anipulation  |                                                 |
\*---------------------------------------------------------------------------*/
FoamFile
{
    version     2.0;
    format      ascii;
    class       dictionary;
    location    "constant";
    object      turbulenceProperties;
}
// * * * * * * * * * * * * * * * * * * * * * * * * * * * * * * * * * * * * * //

simulationType  LES;

LES
{
turbulence      on;
LESModel       Smagorinsky;

delta          cubeRootVol;

printCoeffs     on;

cubeRootVolCoeffs
{
    deltaCoeff      1;
}

maxDeltaxyzCoeffs
{
    deltaCoeff      1;
}

SmagorinskyCoeffs
{
    filter          simple;
}

}

// ************************************************************************* //
```

```
/*--------------------------------*- C++ -*----------------------------------*\
  =========                 |
  \\      /  F ield         | OpenFOAM: The Open Source CFD Toolbox
   \\    /   O peration     | Website:  https://openfoam.org
    \\  /    A nd           | Version:  7
     \\/     M anipulation  |
\*---------------------------------------------------------------------------*/
FoamFile
{
    version     2.0;
    format      ascii;
    class       dictionary;
    object      blockMeshDict;
}
// * * * * * * * * * * * * * * * * * * * * * * * * * * * * * * * * * * * * * //

scale 0.01;

vertices
(
     (0.5 0 -0.25)   //0
    (0 0.5 -0.25)    //1
    (-0.5 0 -0.25)    //2
    (0 -0.5 -0.25)    //3
    (0.5 0 0)         //4
    (0 0.5 0)         //5
    (-0.5 0 0)         //6
    (0 -0.5 0)      //7

    (1.25 0 -0.25)   //8
    (0 1.25 -0.25)    //9
    (-1.25 0 -0.25)    //10
    (0 -1.25 -0.25)    //11
    (1.25 0 0)         //12
    (0 1.25 0)         //13
    (-1.25 0 0)         //14
    (0 -1.25 0)      //15


    (0.5 0 0)         //16
    (0 0.5 0)         //17
    (-0.5 0 0)         //18
    (0 -0.5 0)      //19

    (0.5 0 50)         //20
    (0 0.5 50)         //21
    (-0.5 0 50)         //22
    (0 -0.5 50)      //23


    (1.25 0 0)   //24
    (0 1.25 0)    //25
    (-1.25 0 0)    //26
    (0 -1.25 0)    //27
```

```
    (1.25 0 50)         //28
    (0 1.25 50)         //29
    (-1.25 0 50)         //30
    (0 -1.25 50)      //31

    (3.25 0 0)   //32
    (0 3.25 0)    //33
    (-3.25 0 0)    //34
    (0 -3.25 0)    //35
    (3.65 0 50)         //36
    (0 3.65 50)         //37
    (-3.65 0 50)         //38
    (0 -3.65 50)      //39
    (12.5 0 0)   //40
    (0 12.5 0)    //41
    (-12.5 0 0)    //42
    (0 -12.5 0)    //43
    (12.5 0 50)         //44
    (0 12.5 50)         //45
    (-12.5 0 50)         //46
    (0 -12.5 50)      //47
);

blocks
(
    hex (0 1 2 3 4 5 6 7) (32 32 25) simpleGrading (1 1 1)
    hex (8 9 1 0 12 13 5 4) (32 45 25) simpleGrading (1 1.5 1)
    hex (9 10 2 1 13 14 6 5) (32 45 25) simpleGrading (1 1.5 1)
    hex (10 11 3 2 14 15 7 6) (32 45 25) simpleGrading (1 1.5 1)
    hex (11 8 0 3 15 12 4 7) (32 45 25) simpleGrading (1 1.5 1)
    hex (16 17 18 19 20 21 22 23) (32 32 450) simpleGrading (1 1 43)

    hex (24 25 17 16 28 29 21 20) (32 45 450) simpleGrading (1 1.5 43)
    hex (25 26 18 17 29 30 22 21) (32 45 450) simpleGrading (1 1.5 43)
    hex (26 27 19 18 30 31 23 22) (32 45 450) simpleGrading (1 1.5 43)
    hex (27 24 16 19 31 28 20 23) (32 45 450) simpleGrading (1 1.5 43)

    hex (32 33 25 24 36 37 29 28) (32 80 450) simpleGrading (1 0.3 43)
    hex (33 34 26 25 37 38 30 29) (32 80 450) simpleGrading (1 0.3 43)
    hex (34 35 27 26 38 39 31 30) (32 80 450) simpleGrading (1 0.3 43)
    hex (35 32 24 27 39 36 28 31) (32 80 450) simpleGrading (1 0.3 43)

    hex (40 41 33 32 44 45 37 36) (32 30 450) simpleGrading (1 0.05 43)
    hex (41 42 34 33 45 46 38 37) (32 30 450) simpleGrading (1 0.05 43)
    hex (42 43 35 34 46 47 39 38) (32 30 450) simpleGrading (1 0.05 43)
    hex (43 40 32 35 47 44 36 39) (32 30 450) simpleGrading (1 0.05 43)

);

edges
(
arc 8 9 (0.8838 0.8838 -0.25)
arc 12 13 (0.8838 0.8838 0)
arc 9 10 (-0.8838 0.8838 -0.25)
```

```
arc 13 14 (-0.8838 0.8838 0)
arc 10 11 (-0.8838 -0.8838 -0.25)
arc 14 15 (-0.8838 -0.8838 0)
arc 11 8 (0.8838 -0.8838 -0.25)
arc 15 12 (0.8838 -0.8838 0)

arc 0 1 (0.30177 0.30177 -0.25)
arc 4 5 (0.30177 0.30177 0)
arc 1 2 (-0.30177 0.30177 -0.25)
arc 5 6 (-0.30177 0.30177 0)
arc 2 3 (-0.30177 -0.30177 -0.25)
arc 6 7 (-0.30177 -0.30177 0)
arc 3 0 (0.30177 -0.30177 -0.25)
arc 7 4 (0.30177 -0.30177 0)

arc 16 17 (0.30177 0.30177 0)
arc 20 21 (0.30177 0.30177 50)
arc 17 18 (-0.30177 0.30177 0)
arc 21 22 (-0.30177 0.30177 50)
arc 18 19 (-0.30177 -0.30177 0)
arc 22 23 (-0.30177 -0.30177 50)
arc 19 16 (0.30177 -0.30177 0)
arc 23 20 (0.30177 -0.30177 50)

arc 24 25 (0.8838 0.8838 0)
arc 28 29 (0.8838 0.8838 50)
arc 25 26 (-0.8838 0.8838 0)
arc 29 30 (-0.8838 0.8838 50)
arc 26 27 (-0.8838 -0.8838 0)
arc 30 31 (-0.8838 -0.8838 50)
arc 27 24 (0.8838 -0.8838 0)
arc 31 28 (0.8838 -0.8838 50)

arc 32 33  (2.298 2.298 0)
arc 36 37 (2.5809 2.5809 50)
arc 33 34 (-2.298 2.298 0)
arc 37 38 (-2.5809 2.5809 50)
arc 34 35 (-2.298 -2.298 0)
arc 38 39 (-2.5809 -2.5809 50)
arc 35 32 (2.298 -2.298 0)
arc 39 36 (2.5809 -2.5809 50)

arc 40 41  (8.8388 8.8388 0)
arc 44 45 (8.8388 8.8388 50)
arc 41 42 (-8.8388 8.8388 0)
arc 45 46 (-8.8388 8.8388 50)
arc 42 43 (-8.8388 -8.8388 0)
arc 46 47 (-8.8388 -8.8388 50)
arc 43 40 (8.8388 -8.8388 0)
arc 47 44 (8.8388 -8.8388 50)
);

boundary
(
```

```
inlet
{
    type wall;
    faces
    (
        (0 1 2 3)
        (8 9 1 0)
        (9 10 2 1)
        (10 11 3 2)
        (11 8 0 3)
    );
}
out1
{
    type wall;
    faces
    (
        (5 4 7 6)
        (13 12 4 5)
        (14 13 5 6)
        (15 14 6 7)
        (12 15 7 4)

    );
}

pipe
{
    type wall;
    faces
    (
        (12 13 9 8)
        (13 14 10 9)
        (14 15 11 10)
        (15 12 8 11)

    );
}
 tapa
{
    type wall;
    faces
    (
        (16 17 18 19)
        (24 25 17 16)
        (25 26 18 17)
        (26 27 19 18)
        (27 24 16 19)
        (32 33 25 24)
        (33 34 26 25)
        (34 35 27 26)
        (35 32 24 27)
        (40 41 33 32)
        (41 42 34 33)
```

```
            (42 43 35 34)
            (43 40 32 35)
        );
    }

  outlet
    {
        type wall;
        faces
        (
            (21 20 23 22)
            (21 29 28 20)
            (22 30 29 21)
            (23 31 30 22)
            (20 28 31 23)
            (37 36 28 29)
            (30 38 37 29)
            (31 39 38 30)
            (28 36 39 31)
            (45 44 36 37)
            (46 45 37 38)
            (47 46 38 39)
            (44 47 39 36)
        );
    }

      tank
    {
        type wall;
        faces
        (
            (44 45 41 40)
            (45 46 42 41)
            (46 47 43 42)
            (47 44 40 43)
        );
    }

);

mergePatchPairs
(
(out1 tapa)
);
// ************************************************************************* //
```

```
/*--------------------------------*- C++ -*----------------------------------*\
  =========                 |
  \\      /  F ield         | OpenFOAM: The Open Source CFD Toolbox
   \\    /   O peration     | Website:  https://openfoam.org
    \\  /    A nd           | Version:  7
     \\/     M anipulation  |
\*---------------------------------------------------------------------------*/
FoamFile
{
    version     2.0;
    format      ascii;
    class       dictionary;
    location    "system";
    object      controlDict;
}
// * * * * * * * * * * * * * * * * * * * * * * * * * * * * * * * * * * * * * //

application     pisoFoam;

startFrom       latestTime;

startTime       0;

stopAt          endTime;

endTime        1;

deltaT         1e-04;

writeControl    timeStep;

writeInterval   1000;

purgeWrite      0;

writeFormat     ascii;

writePrecision  6;

writeCompression off;

timeFormat      general;

timePrecision   6;

runTimeModifiable true;

functions
{
 turbulenceFields1
    {

        type        turbulenceFields;
        libs        ("libfieldFunctionObjects.so");
```

```
        // Either field or fields entries

        fields                  (k R);

        enabled                 true;

        writeControl            writeTime;

        executeControl          timeStep;

        executeInterval         1;

    }

    fieldAverage1
    {
        type            fieldAverage;
        libs            ("libfieldFunctionObjects.so");
        writeControl    writeTime;

        fields
        (
            U
            {
                mean        on;
                prime2Mean  on;
                base        time;
            }
        );
    }

}

// ************************************************************************* //
```

```
/*--------------------------------*- C++ -*----------------------------------*\
  =========                 |
  \\      /  F ield         | OpenFOAM: The Open Source CFD Toolbox
   \\    /   O peration     | Website:  https://openfoam.org
    \\  /    A nd           | Version:  7
     \\/     M anipulation  |
\*---------------------------------------------------------------------------*/
FoamFile
{
    version     2.0;
    format      ascii;
    class       dictionary;
    location    "system";
    object      fvSchemes;
}
// * * * * * * * * * * * * * * * * * * * * * * * * * * * * * * * * * * * * * //

ddtSchemes
{
    default         backward;
}

gradSchemes
{
     default         Gauss linear;
}

divSchemes
{
    default         none;
    div(phi,U)      Gauss LUST unlimitedGrad(U);
    div(phi,k)      Gauss limitedLinear 1;
    div(phi,nuTilda) Gauss limitedLinear 1;
    div(phi,s1)     Gauss linearUpwind grad(s1);
    div((nuEff*dev2(T(grad(U))))) Gauss linear;
}

laplacianSchemes
{
    default         Gauss linear corrected;
}

interpolationSchemes
{
    default         linear;
}

snGradSchemes
{
    default         corrected;
}
fluxRequired
{
default  no;
```

```
   p        ;
   pcorr    ;
}

// ************************************************************************ //
```

```
/*--------------------------------*- C++ -*----------------------------------*\
  =========                 |
  \\      /  F ield         | OpenFOAM: The Open Source CFD Toolbox
   \\    /   O peration     | Website:  https://openfoam.org
    \\  /    A nd           | Version:  7
     \\/     M anipulation  |
\*---------------------------------------------------------------------------*/
FoamFile
{
    version     2.0;
    format      ascii;
    class       dictionary;
    location    "system";
    object      fvSolution;
}
// * * * * * * * * * * * * * * * * * * * * * * * * * * * * * * * * * * * * * //

solvers
{
    p
    {
        solver          GAMG;
        tolerance       1e-04;
        relTol          0.01;
        smoother        GaussSeidel;
        nPreSweeps      0;
        nPostSweeps     2;
        cacheAgglomerarion true;
        nCellsInCoarsestLevel 10;
        agglomerator    faceAreaPair;
        mergeLevels     1;
    }

    pFinal
    {
        $p;
        smoother        DICGaussSeidel;
        tolerance       1e-05;
        relTol          0;
    }

    pcorr
    {
        $p;
        tolerance       1e-05;
        relTol          0.01;
    }

    "(U|k|B|nuTilda)"
    {
        solver          smoothSolver;
        smoother        symGaussSeidel;
        tolerance       1e-05;
        relTol          0.01;
```

```
    }
    "(U|k|B|nuTilda)Final"
    {
        $U;
        tolerance       1e-05;
        relTol          0.01;
    }
     "s.*"
    {
        solver          PBiCGStab;
        preconditioner  DILU;
        tolerance       1e-08;
        relTol          0;
        minIter                 1;
    }
}

PISO
{
    nCorrectors     2;
    nNonOrthogonalCorrectors 3;
    pRefCell    0;
    pRefValue    0;
}


// ************************************************************************* //
```